DOCTOR OF PHILOSOPHY

Numerical simulations of MHD flows past obstacles in a duct under externally applied magnetic field

Dousset, Vincent

Award date:
2009

Awarding institution:
Coventry University

Numerical simulations of MHD flows past obstacles in a duct under externally applied magnetic field

Dousset, V.

Coventry University

Numerical simulations of MHD flows past obstacles in a duct under externally applied magnetic field

Vincent DOUSSET

A thesis submitted in partial fulfilment of the University's requirements for the Degree of Doctor of Philosophy

–December 2009–

À Marie et Marie,

Abstract

In this thesis, we simulate the flow of an electrically conducting fluid past an obstacle placed inside a duct under the influence of an externally applied magnetic field. Three different obstacles are considered: a circular and a square cylinder spanning over the full height of the duct and a square cylinder spanning over the half height of the duct. The magnetic field is oriented along the cylinder axis and the duct is electrically insulating.

In a first stage of the thesis, we perform a parametric study over both Ha and Re in the case where both $Ha \gg 1$ and $N \gg 1$ with 2D simulations using the quasi-2D flow model by [165]. In particular, we provide the first explanation of the collapse of the regular Kármán vortex street observed experimentally by [180]. We also derive two different scaling laws linking the evolutions of the flow coefficients and either Re/Ha or $Re/Ha^{0.8}$.

The second phase of the thesis is dedicated to the development of a 3D MHD capable code to solve the flow equations with the inductionless approximation. This code is used to investigate the 3D MHD flow past a truncated square cylinder in a duct. We explain the different stages of elaboration of our code and validate its performances to MHD duct flows and cylinder wakes. We also implement a wall function at the interface between the Hartmann layers and the bulk flow.

The non-MHD flow past the truncated cylinder is simulated for $10 \leq Re \leq 400$. In particular, the early stages of the unsteady flow regime is characterised by a regular symmetric procession of hairpin vortices. We explain the formation mechanism of these vortices and its evolution when Re is increased. Finally, we investigate the MHD flow past the electrically insulating truncated cylinder at $Ha = 100$ and 200 for Re up to 1000. The flow dynamics is strongly 2D with the presence of a Hunt's wake at very low Re. The unsteady regime leads to the development of a Kármán vortex street. Switching to a perfectly conducting truncated square cylinder enhances the braking of the flow by the Lorentz force in the region above the cylinder tip.

Acknowledgements

This dissertation is both exhaustive and incomplete. It describes with much detail the scientific achievements, but does not acknowledge the conditions and the people that contribute to it. This is the scope of this page.

I am very much indebted to my supervisor Alban Pothérat. Thank you for this opportunity to work with him, for his constant support, his precious indications and his patience. Thank you for having always made sure that I could work in the best possible conditions. I hope that my work matched his expectations in me. Enfin, merci de m'avoir offert un toit quand j'avais froid et pour ses nombreuses soirées passées à discuter de tout et de rien...

Part of the work is the result of a close collaboration with Elisabet Mas de les Valls from the Technical University of Catalonia. Gràcies Elisabet. Also the contribution made by Naïck Maurice during her internship was very much appreciated. Merci à toi Naïck.

Thanks to the team of examinators who accepted to be part of my jury and read this long thesis. This dissertation greatly benefited from their feedback and comments.

This PhD was started at Ilmenau in Germany. I was touched by the reception I had from the people at Ilmenau where I always travel back with much pleasure. Danke Prof. Schulze, Cornelia, Gabi, Artjem, Eckhardt, Lupo, Stefan, Uli und Vaclav. Danke Prof. Thess, Prof. Kolesnikov, Dmitri und Irina, Egbert, Oleg und Thomas.

This PhD was finished at Coventry in Great Britain. I have also been very lucky to be welcomed in such a friendly and talented research team. Thanks Sveta, Alex, Janis, Jim and Sergei.

Also, during this long adventure, I was accompanied by two great guys: Rico and Vitali. We shared many things together and we lived under the same roof a long time. Thanks guys for having been there and supported my moods sometimes.

Thanks Leslie for your help, for checking my English, for your tips on how not to get fooled by a real estate agency and for your cooking skills.

Thanks to my favourite chemist. Her sweet words and her smile have always been a big help for me.

Of course, I thank my family and my friends for their support and their presence throughout the last 4 years. J'ai une pensée pour ceux qui ont disparu pendant cette période et j'en ai une autre tout aussi forte pour ceux qui sont nés pendant cette même période. Un grand merci à eux.

Contents

Introduction

Back in January 1832, Michael Faraday set up a rudimentary magnetohydrodynamic power generator. He placed two copper electrodes in the river Thames in London and measured a voltage between them. Although the demonstration was not fully successful, Faraday thus demonstrated that the motion of an electrically conducting fluid, here the salty water of river Thames, under the influence of a magnetic field, here the Earth's magnetic field, induces an electric current.

The principle shown by Faraday offered an opportunity to produce electricity at a low environmental cost. A simple analysis of orders of magnitude hovewer dismisses a straightforward application of magnetohydrodynamic power generator relying on salty water and the Earth's magnetic field. A reasonable power generator would require a much stronger conducting fluid like mercury and a very intense magnetic field, at least 10^{10} as high as that of the Earth. Magnetohydrodynamics (MHD) is however at the heart of a promising technology to produce electricity with potentially little effect on the environment. The objective is to harness nuclear fusion into a reactor, *i.e.* to reproduce the nuclear reactions occurring in the Sun into a reactor. This technology shall eventually take over to nuclear fission at the basis of the current nuclear plants, while tackling most of its flaws.

Different projects are devised to eventually deliver a prototype reactor by 2030. We shall discuss in more detail the ITER project [1]. Figure 1 presents a general overview of ITER reactor. The fusion reactions involving deuterium and tritium occur in a very hot plasma confined inside a toroidal shell by a set of superconducting magnet coils. Blankets modules form the walls of the shell. They are designed to absorb high-energy neutrons from the fusion reaction, feed it with tritium and transfer the heat generated by the reaction to a water-cooling loop to produce steam, that eventually drives an electric turbine to generate electricity.

Several designs of blankets are investigated. In the Helium Cooled Lead Lithium (HCLL) blanket for example [148], liquid metal $PbLi$ circulates in an array of rectilinear rectangular ducts connected by U-shaped ducts under the influence of the magnetic field. In particular, heat transfer inside these blankets is more efficient if the flow is turbulent and a technique to promote turbulence consists in placing obstacles inside the blankets. This is the most straightforward application of the outcomes of

[1] http://www.iter.org

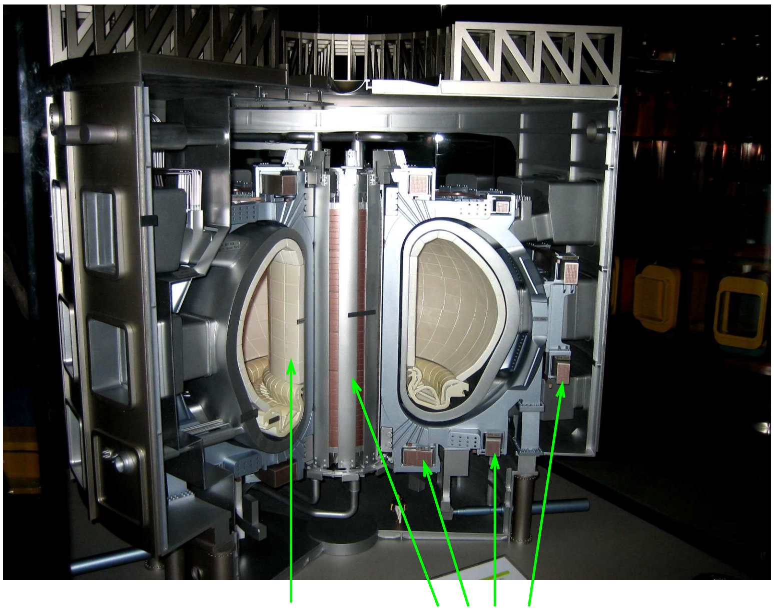

Figure 1: General overview of ITER fusion reactor.

this thesis.

We study the flow of an electrically conducting fluid in a rectangular duct past an obstacle under the influence of an externally applied magnetic field. This topic combines two main bodies of interests. On the one hand, it deals with the dynamics of a fluid past an obstacle. Although the shape of the obstacle may have a dramatic influence, the flow features and dynamics present many similarities whatever this shape is. A very large amount of research has been performed on the flow past a circular cylinder for more than a century. We shall therefore introduce this case in more detail. On the other hand, our configuration requires to describe the interaction between the flow motion and the induced electric currents. The presence of a magnetic field has indeed a dramatic influence on the flow dynamics and it requires a thorough review too.

This thesis has two principal objectives. Firstly, we shall present an extensive study of the MHD flow past a cylindrical obstacle under a magnetic field orientated along the cylinder axis. We perform parametric studies on the flow parameters. We vary the shape, the height and the electrical conductivity of the cylinder. We shall also systematically describe the evolution of flow coefficients to assess the physical mechanisms underlying the flow dynamics. Secondly, we shall develop a 3D MHD numerical code based on an open source framework. This code is designed to be accurate, consistent, robust and flexible, but its optimisation has not been our main concern. The ultimate goal of this thesis is to investigate the physical effects featured in MHD flows past an obstacle under the influence of an axial magnetic field. We systematically investigate the non-MHD case to identify the related flow patterns and dynamics. We then consider the MHD case to devise the effects of the magnetic fields by comparison to the non-MHD study.

Here are the outlines of this thesis. In part I, we review the principles of magnetohydrodynamics and a set of classical MHD flows. Then, we make a survey of the flow past a cylinder: firstly in the absence of a magnetic field 2 and 3 and secondly with its presence in chapter 4. In a first stage of the thesis, we consider a configuration in which the effects of the magnetic field are utterly dominant in the flow. Under some assumptions which we shall be defined, we perform two-dimensional (2D) numerical computations of the MHD cylinder wake using a theoretical quasi-2D flow model by [165]. Doing this, we will describe the flow dynamics, identify flow regimes and the evolution of the flow patterns within these regimes. This quasi-2D study is the subject of part II.

In a second phase of the thesis which part III is dedicated to, we develop our own three-dimensional (3D) MHD code to investigate the 3D flow dynamics of MHD cylinder wakes. We describe the successive steps of the elaboration of the code in chapter 7. The code is then validated to a series of non-MHD and MHD typical flow configurations in chapter 8. In the latter chapter also, we implement a wall function to investigate 3D MHD flows in very intense magnetic fields. Finally, we perform 3D numerical computations to investigate the MHD flow past a truncated square cylinder in a duct. Chapter 9 is devoted to the case where no magnetic field is imposed and chapter 10 to the case where it is present.

Part I

State-of-the-art

Chapter 1

Introduction to magnetohydrodynamics

Magnetohydrodynamics (MHD) investigates the coupled effects of the dynamics of electrically conducting fluids and electromagnetism. We shall first introduce fluid mechanics and electromagnetism laws separately. Then we will review the coupling effects through a set of fundamental MHD flows. An extensive introduction to MHD is available in [16, 18, 20].

1.1 MHD equations

1.1.1 Navier-Stokes equations

Fluid dynamics are governed by the Navier-Stokes equations (for a comprehensive review of fluid mechanics, see e.g. [14] or [17]). The fluids under consideration in this thesis are assumed to be incompressible with density ρ and kinematic viscosity ν. In this context, the Navier-Stokes equations express the mass conservation (1.1) and the momentum conservation (1.2):

$$\nabla \cdot \mathbf{u} = 0 \tag{1.1}$$

$$\rho \partial_t \mathbf{u} + \rho(\mathbf{u} \cdot \nabla)\mathbf{u} = -\nabla p + \rho\nu\nabla^2\mathbf{u} + \mathbf{F_{vol}} + \mathbf{j} \times \mathbf{B} \tag{1.2}$$

where $\mathbf{u}$ is the velocity field, p the dynamic pressure, $\mathbf{j}$ the current density, $\mathbf{B}$ the magnetic field and $\mathbf{F}_{vol}$ represents volumetric forces other than of electromagnetic nature (e.g. gravitational force, externally imposed pressure gradient,...).

The fluid's incompressibility means that the fluid density ρ can be considered as constant, hence equation (1.1). Equation (1.2) corresponds to the assessment of the force balance on a given fluid particle. The left-hand side is the momentum's particular derivative, which is decomposed into its time variations $\rho\partial_t\mathbf{u}$ and the advection term $\rho(\mathbf{u}.\nabla)\mathbf{u}$. Both terms correspond to the inertia term. On the right-hand side, one recognises the pressure force $-\nabla p$, the viscous friction $\rho\nu\nabla^2\mathbf{u}$, the Lorentz force $\mathbf{j}\times\mathbf{B}$ resulting from the interactions between the currents and the electromagnetic field, and additional external forces $\rho\mathbf{F}_{vol}$.

1.1.2 Electromagnetic equations

Electromagnetism's laws model the interactions between an electric field $\mathbf{E}$ and a magnetic field $\mathbf{B}$ in a continuous medium where electric charges or current are present. They are summarised into a set of 4 equations dubbed *Maxwell's equations*. In a continuous medium characterised by an electric charge density q, a current density $\mathbf{j}$, a magnetic permeability μ and an electric permittivity ϵ, Maxwell's equations read:

$$\nabla\cdot\mathbf{E} = \frac{q}{\epsilon} \tag{1.3}$$

$$\nabla\cdot\mathbf{B} = 0 \tag{1.4}$$

$$\nabla\times\mathbf{E} = -\partial_t\mathbf{B} \tag{1.5}$$

$$\nabla\times\mathbf{B} = \mu\mathbf{j}+\mu\epsilon\partial_t\mathbf{E} \tag{1.6}$$

Equation (1.3) describes how electric charges distributed within the medium generate an electric field. Equation (1.4) means that the magnetic field is solenoidal so that the magnetic field lines are closed possibly at infinity. Equation (1.5) (*resp.* (1.6)) characterises how a changing magnetic (*resp.* electric) field induces an electric (*resp.* magnetic) field. Equation (1.6) furthermore expresses how a current density generates a magnetic field.

Following equation (1.4), $\mathbf{B}$ can be defined as a purely rotational field so that: $\mathbf{B}=\nabla\times\mathbf{A}$ with *potential-vector* $\mathbf{A}$. Subsequently, using (1.5), the electric field can be expressed with an electric potential field ϕ as:

$$\mathbf{E} = -\nabla\phi-\partial_t\mathbf{A} \tag{1.7}$$

In the case of the flow of an electrically conducting fluid with an electric conductivity σ, the current density is given by Ohm's law as:

$$\mathbf{j} = q\mathbf{u}+\sigma(\mathbf{E}+\mathbf{u}\times\mathbf{B}) \tag{1.8}$$

Ohm's law expresses the current density as the sum of the convection current ($q\mathbf{u}$) and the conduction current ($\sigma(\mathbf{E}+\mathbf{u}\times\mathbf{B})$).

At this point, we shall introduce the so-called *quasi-static approximation*. It relies on a set of 4 conditions: (i) typical fluid velocities are much smaller than the speed of light, (ii) velocity of the charge carriers (electrons or ions) remains small with respect to fluid velocity, (iii) the charge carriers move within the fluid without inertia and (iv) no thermo-electric voltage sources are present [19]. As a straightforward implication of this approximation, the charge relaxation time defined as $\tau_r = \epsilon/\sigma$ is extremely short. In the case of the fluids under consideration in this thesis, *i.e.* liquid metals and eutectic alloys, a typical value for τ_r is 10^{-18} s [16].

In Ohm's law (1.8), a simple analysis of the respective orders of magnitude of the convection current and $\sigma\mathbf{E}$ leads to $(q\mathbf{u})/(\sigma\mathbf{E}) \sim \tau_r U_0/L$, where U_0 is the fluid typical velocity and L is a characteristic length of the fluid domain. In the frame of the quasi-static approximation, the convection current $q\mathbf{u}$ can then be neglected with respect to $\sigma\mathbf{E}$ so that Ohm's law is eventually reformulated as:

$$\mathbf{j} = \sigma(\mathbf{E} + \mathbf{u} \times \mathbf{B}) \tag{1.9}$$

The conservation of electric charge is a principle universally accepted and can be obtained from the particular derivative of the total charge which must be zero [18], it can also be recovered from Maxwell's equations using (1.3) and the divergence of (1.6):

$$\nabla \cdot \mathbf{j} + \partial_t q = 0 \tag{1.10}$$

By taking the divergence term by term of equation (1.9) and introducing the result into equation (1.10), one obtains:

$$\partial_t q + \frac{q}{\tau_r} + \sigma\nabla \cdot (\mathbf{u} \times \mathbf{B}) = 0 \tag{1.11}$$

Accounting for the typical value of τ_r, the last-term on the left-hand side of the previous equation can be neglected with respect to q/τ_r so that $\partial_t q + q/\tau_r = 0$. The charge density q can then be considered as constant and the current conservation is satisfied when:

$$\nabla \cdot \mathbf{j} = 0 \tag{1.12}$$

Consequently the current density lines are closed, which characterises a solenoidal field.

Similarly, in conducting media like liquid metal, eutectic alloy and electrolytes, the displacement current ($\epsilon\mu\partial_t\mathbf{E}$) can be neglected [18] and (1.6) becomes:

$$\nabla \times \mathbf{B} = \mu\mathbf{j} \tag{1.13}$$

1.1.3 Induction equation

The coupling between the magnetic field **B** and the velocity field **u** appears in Ohm's law but also in the *induction equation*. It is obtained from equation (1.5) using (1.4) and the curl of (1.8):

$$\partial_t \mathbf{B} = \nabla \times (\mathbf{u} \times \mathbf{B}) + \frac{1}{\sigma\mu}\nabla^2 \mathbf{B} \tag{1.14}$$

The induction equation links the time variations of the magnetic field with the sum of the advection of the magnetic field by the velocity field and the diffusion of the magnetic field within the domain. Two mechanisms are involved in the advection process: the deformation of the magnetic field lines by the velocity field and the stretching of the velocity field lines by the magnetic field. The former mechanism is especially significant when the direction of greatest change of the magnetic field is parallel to streamwise direction, such as in problems featuring a fringing magnetic field or when the region under consideration is located at the extremities of a magnet.

Let us consider that the magnetic field is pulsating at a pulsation ω and we denote B_0, U_0, and L as the respective characteristic magnetic field, velocity and length. We derive the non-dimensional form of the induction equation using the magnetic Reynolds number $Rm = \sigma\mu U_0 L$ and the shielding parameter $R_\omega = \sigma\mu L^2\omega$:

$$R_\omega \partial_t \mathbf{B}^\star = Rm \nabla \times (\mathbf{u}^\star \times \mathbf{B}^\star) + \nabla^2 \mathbf{B}^\star \tag{1.15}$$

where non-dimensional quantities are indicated by a $\star$ superscript.

When $Rm \gg 1$, the magnetic field is non-dissipative, instead its time variations result only from its advection by the velocity field. If furthermore $Rm \gg R_\omega$, the magnetic field lines are instantaneously deformed by the velocity field and remains frozen in the medium. This situation is common for MHD phenomena at the scale of the Earth ($Rm \simeq 10^4$ [18]) and in astrophysics.

When $Rm \ll 1$, no advection phenomenon is present in the medium and only the diffusion process shall be taken into account. Two cases must then be distinguished:

- (i) $Rm \ll R_\omega$,
- (ii) $Rm \gg R_\omega$.

In case (i), the time variations of the magnetic field have to be carefully addressed. Let us consider that an oscillating magnetic field with pulsation ω is applied at the surface of an electrically conducting medium. The magnetic field will not instantaneously propagate into the interior of the medium, but it will diffuse from the surface of the medium inwards. Neglecting advection in equation (1.14) results in $\partial_t \mathbf{B} \simeq \frac{1}{\sigma\mu}\nabla^2 \mathbf{B}$. The characteristic diffusion length of the magnetic field can be derived by dimensional analysis of the latter approximation and:

$$\delta_m = \sqrt{2/(\mu\sigma\omega)} \tag{1.16}$$

δ_m is the called *the magnetic skin depth*. The diffusion of the magnetic field therefore generates electric currents within a thin surface layer of thickness δ_m. This layer shields the interior of the medium from the external magnetic field, but the outer surface may turn very unstable. For example, oscillations may appear at the surface of a droplet of liquid metal submitted to an alternating magnetic field [136, 143] and pinch-effect may be observed at the surface of a channel flow of liquid metal [150, 169]. If the electrically conducting medium does not involve any free surface, then there is no coupling between the velocity and magnetic field and the latter can be considered as given in the problem.

In case (ii) where $Rm \ll 1$ and $Rm \gg R_\omega$, it follows from (1.13) that the induced magnetic field B_i scales as RmB_0, so that B_i can be considered as negligible. Similarly the time variations of the magnetic field can also be neglected so that the electric field is irrotational and derived only from the electric potential ϕ as shown by (1.7). As a result, the velocity field and the magnetic field are not coupled anymore and Maxwell's equations are only reduced to the current conservation (1.12). Once the latter is associated with the Navier-Stokes equations (1.1) and (1.2), the resulting set of equations corresponds to the so-called *inductionless* or *low-Rm* approximation. In numerical simulations, this approximation implies crucial simplifications, which result in a dramatic gain in efficiency of the involved numerical methods [178].

1.2 MHD equations within the low-Rm approximation

The MHD flow of an electrically conducting, incompressible fluid under the influence of an externally applied, steady magnetic field $\mathbf{B}_0$ within the inductionless approximation is fully defined by the determination of the velocity field $\mathbf{u}$, pressure field p and electric potential ϕ provided adequate boundary conditions are given at the limits of the fluid domain together with initial conditions. The inductionless approximation yields a simplified set of equations. Using U_0, ρU_0^2, $\sigma U_0 B_0$ and $U_0 B_0 L$ as respective typical velocity, pressure, current density and electric potential, the non-dimensional formulation of the MHD equations within the inductionless approximation is:

$$\nabla \cdot \mathbf{u}^\star = 0 \tag{1.17}$$

$$\partial_t \mathbf{u}^\star + (\mathbf{u}^\star \cdot \nabla)\mathbf{u}^\star = -\nabla p^\star + \frac{1}{Re}\nabla^2 \mathbf{u}^\star + \frac{Ha^2}{Re}(\mathbf{j}^\star \times \mathbf{B}^\star) \tag{1.18}$$

$$\nabla \cdot \mathbf{j}^\star = 0 \tag{1.19}$$

and

$$\mathbf{j}^\star = -\nabla\phi^\star + \mathbf{u}^\star \times \mathbf{B}^\star \tag{1.20}$$

$$\mathbf{E}^\star = -\nabla\phi^\star \tag{1.21}$$

where the quadratic norm of $\mathbf{B}_0$ is used in $\mathbf{B}^\star = \mathbf{B}_0/||\mathbf{B}_0||$, $Re = U_0 L/\nu$ is the Reynolds number and $Ha = LB_0\sqrt{\sigma/(\rho\nu)}$ is the Hartmann number. Re is the ratio of the inertial to the viscous forces, while Ha is the square root of that of the Lorentz to the viscous forces. A further non-dimensional number expresses the ratio of the Lorentz to the inertial forces: it is the magnetic interaction parameter or Stuart number $N = \sigma B_0^2 L/(\rho U_0)$, which can be also formulated using Re and Ha as: $N = Ha^2/Re$.

1.3 Boundary conditions

Initial conditions are required to define all the flow variables at the initial time instant in the whole domain. Boundary conditions must be defined at all the boundaries of the fluid domain under consideration. The boundaries may be located at the interface between two materials such as at the interface between the fluid and a solid surface or at the interface between two different media (e.g. free surface). In the case of an infinite fluid domain, the boundary conditions must accurately characterise the fluid at infinity (e.g. inlet and outlet boundaries of duct flows). Whatever the nature of the boundary, the expression of the condition at the interface is obtained after considering a infinitesimal control volume enclosing the interface. Then one applies the flow equations on this control volume in the limiting case where the control volume is of zero thickness and matches exactly the interface. Free-surface problems are out of the scope of this thesis so that the boundary condition relevant with these problems will not be described thereafter but shall be found in e.g. [18]. We shall determine only the boundary condition at the interface between the fluid and a wall. The kinematic and electric boundary conditions at the inlet and outlet of a duct or a channel are introduced in sections 5.2 and 8.4, respectively. We shall now introduce separately the kinematic and electronic boundary conditions.

1.3.1 Kinematic boundary conditions

The mass conservation (1.1) requires that the velocity component normal is continuous at the interface between the fluid and another medium. In the case of the boundary at an impermeable, rigid and non-moving wall, due to viscosity, the velocity is uniformly zero at interface Γ between the fluid and the wall:

$$\mathbf{u}^\star = \mathbf{0} \quad \text{at } \Gamma \tag{1.22}$$

This condition is referred to as the *no slip* condition. By contrast, the *slip* condition is defined as:

$$\begin{cases} \mathbf{u}^\star \cdot \mathbf{n}_w = 0 \\ \partial_n(\mathbf{u}^\star \cdot \mathbf{t}_w) = 0 \end{cases} \tag{1.23}$$

where $\mathbf{n}_w$ (*resp.* $\mathbf{t}_w$) is the vector normal (*resp.* tangential) to Γ and $\partial * /\partial n = (\nabla *) \cdot \mathbf{n}_w$. This condition expresses that the normal component of the velocity is continuous at the interface Γ without any fluid transfer across it. If the fluid is assumed as non-viscous, this condition is applied at an interface between the fluid and an impermeable wall. In open flow problems, this condition may also be imposed to model a plane of symmetry inside the fluid domain. For example, in non-MHD 2D cylinder wakes in an infinite fluid domain, the slip condition may be imposed at the boundaries located on either sides of the cylinder.

1.3.2 Electromagnetic boundary conditions

Both the magnetic and the current density fields are solenoidal so that (1.4) and (1.12) require that the normal component of both fields is continuous at the interface. If the wall is electrically insulating ($\sigma_w = 0$), no current can penetrate into the wall, which imposes that the component of the current density normal to the interface vanishes at the wall. If the wall is perfectly conducting ($\sigma_w \to \infty$), the whole current enters the wall and the component of the current density tangential to Γ vanishes at the wall. The two previous cases then respectively require at the interface fluid/wall:

$$\mathbf{j}^\star \cdot \mathbf{n}_w = 0 \text{ if the wall is electrically insulating at } \Gamma \tag{1.24}$$

$$\mathbf{j}^\star \cdot \mathbf{t}_w = 0 \text{ if the wall is perfectly conducting at } \Gamma \tag{1.25}$$

The previous boundary conditions are related to two ideal situations. Industrial applications often feature walls with a finite non-zero electric conductivity σ_w. A general boundary condition for the current density field can be derived using (1.5) and Ohm's law (1.9):

$$\mathbf{j}^\star \cdot \mathbf{n}_w = \frac{\sigma}{\sigma_w} \mathbf{j}_w^\star \cdot \mathbf{n}_w \quad \text{at } \Gamma \tag{1.26}$$

1.4 Fundamental MHD flows

In this thesis, we investigate the MHD flow past a cylindrical obstacle in a duct of rectangular cross-section. We shall now introduce the fundamental results about the MHD flow between two parallel infinite walls. Then we present the flow dynamics when the fluid is confined in a rectangular duct. We briefly review the influence of a magnetic field on an isolated vortex.

1.4.1 MHD flow between two infinite walls perpendicular to the magnetic field

We consider the flow of an electrically conducting fluid between two infinite planar rigid parallel walls under the influence of a steady, uniform, homogeneous, externally applied magnetic field $\mathbf{B}_0$ normal to the walls. Two cases will be included in this presentation: either both walls are electrically insulating or both are perfectly conducting. The former case refers to the *Hartmann flow*, named after J. Hartmann who described the flow dynamics involved in this configuration back in 1937 [137, 138].

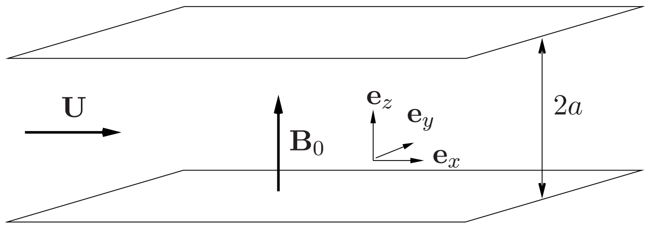

Figure 1.1: Configuration of the MHD flow between two infinite walls normal to the magnetic field

The exact configuration is sketched on figure 1.1. The $x-$axis is the streamwise direction and the walls are located at $z = \pm a$. In this configuration, the flow variables depend only on the $z-$coordinate. $\mathbf{B}_0$ is applied along the $z-$axis such that: $\mathbf{B}_0 = B_0\mathbf{e}_z$. The velocity $\mathbf{u}$ has only one component $u_x(z)$ parallel to the streamwise direction.We consider that the fully developed steady state has been reached for both the velocity and the magnetic fields, but without any restriction on the value of the magnetic Reynolds number. The flow is unidirectional and perpendicular to $\mathbf{B}_0$ so that it follows from the induction equation (1.14) that the induced magnetic field $\mathbf{B}_i$ is of the form: $\mathbf{B}_i = B_i(z)\mathbf{e}_x$. The pressure gradient is also unidirectional, parallel to the $x-$axis and constant so that a positive force per unit volume G is defined as: $\nabla p = -\rho G\mathbf{e}_x$.

If one expresses the current density $\mathbf{j}$ using the curl of the magnetic field (1.13), one deduces that $\mathbf{j} = j_y(x)\mathbf{e}_y$. Then, using Ohm's law (1.9) to determine the electric current, one derives that the electric potential is invariant along both $\mathbf{e}_x$ and $\mathbf{e}_z$. On the other hand, the conservation of electric current (1.12) yields: $\partial^2_{yy}\phi = 0$, which means that the electric field $\mathbf{E}$ is uniform and $\mathbf{E} = E\mathbf{e}_y$.

We use a, a^2G/ν, $aG\sqrt{(\sigma\rho/\nu)}$ as respective characteristic length, velocity, current density [18]. We express the current density using Ohm's law (1.20):

$$j^\star_y = \tilde{E} - Hau^\star_x \quad \text{for } -1 \leq z^\star \leq 1 \tag{1.27}$$

with $\tilde{E} = \frac{E}{aG}(\sigma\nu/\rho)^{1/2}$.

and we put (1.27) into the equation of the momentum conservation (1.18):

$$\partial^2_{z^\star z^\star}u^\star_x - Ha^2u^\star_x = -1 - Ha\tilde{E} \quad \text{for } -1 \leq z^\star \leq 1 \tag{1.28}$$

with a no-slip boundary condition (1.22) imposed on $u_x^\star$ at $z^\star = \pm 1$.

The solution for $u_x^\star$ is then, for $-1 \leq z^\star \leq 1$:

$$u_x^\star = u^c \left[1 - \frac{\cosh{(Ha z^\star)}}{\cosh{(Ha)}}\right] \quad \text{with } u^c = \frac{1}{Ha^2}(1 + Ha\tilde{E}) \tag{1.29}$$

The current density is deduced by inserting (1.29) into (1.27):

$$j_y^\star = -Ha^{-1} + Ha\frac{\cosh{(Ha z^\star)}}{\cosh{(Ha)}}u^c \tag{1.30}$$

The first term on the right-hand side of (1.30) is the current density generated in the core flow. The latter is of order Ha^{-1} whatever the conductivity of the wall is. It drives Lorentz forces opposing the free stream. The second term corresponds to the current circulating inside the boundary layers. If the walls are insulating, the current density then turns positive in the vicinity of the walls so that the Lorentz forces accelerate the flow in the boundary layers. This mechanism is active until the Lorentz forces balance the pressure gradient (*resp.* the viscous forces) in the core flow (*resp.* boundary layers).

This academic problem highlights one of the most striking features of MHD flows: how the boundary layer controls the core flow through the generation of electric currents. This remarkable boundary layer is the *Hartmann layer* and the wall at which this layer arises the *Hartmann wall.* It characterises the boundary layer arising at a wall whose normal is parallel to one non-zero component of the magnetic field. Also, while the typical Poiseuille velocity profile can be recovered from (1.29) when $Ha \to 0$, an asymptotic development of (1.29) for $Ha \gg 1$ and $-1 < z^\star < 0$ yields (an equivalent expression can be obtained for $0 < z^\star < 1$):

$$u_x^\star = u^c\{1 - \exp{[-Ha(1 + z^\star)]}\} \tag{1.31}$$

For $Ha \gg 1$, the velocity decreases exponentially within the Hartmann layers whose thickness δ_H scales with Ha^{-1}. u^c can then be interpreted as the velocity reached outside the Hartmann layer in the core flow so that it is called the *core velocity.* A remarkable outcome is that the electric conductivity of the walls does not affect the velocity profile, but only the core velocity u^c. If the walls are perfectly conducting, no electric field exists between the walls. The flow is driven only by the pressure gradient and u^c scales with Ha^{-2} [see equation (1.29)]. Instead, if the walls are insulating, a uniform electric field $\tilde{E}$ remains in the flow and u^c scales with Ha^{-1}.

1.4.2 MHD flows in rectangular ducts

In this configuration (see figure 1.2), the fluid flows in a rectangular duct under the influence of an externally applied steady, uniform and homogeneous magnetic field $\mathbf{B}_0 = B_0\mathbf{e}_z$. The distance between the walls normal (*resp.* parallel) to $\mathbf{B}_0$ is equal to $2a$ (*resp.* $2b$) and the origin of the frame of reference is located at the centre of the duct cross-section. The streamwise direction corresponds to the $x-$axis, both pairs of opposite walls are parallel and normal to the $y-$axis (*resp.* $z-$axis). The flow is driven by a uniform pressure gradient: $\nabla p = -\rho G \mathbf{e}_x$. Since the flow is unidirectional and perpendicular to the magnetic field, it follows from the induction equation (1.14) that the induced magnetic field $\mathbf{B}_i$ has only one non-zero component along the streamwise direction. Both the velocity $\mathbf{u}$ and the induced magnetic field $\mathbf{B}_i$ are independent of the streamwise coordinate x so that: $\mathbf{u} = u(y,z)\mathbf{e}_x$ and $\mathbf{B}_i = B_i(y,z)\mathbf{e}_x$. Only the configuration where all walls are electrically insulating is detailed thereafter. We consider that both the velocity and magnetic fields have reached a fully developed stationary state, but no restriction is made on the magnetic Reynolds number.

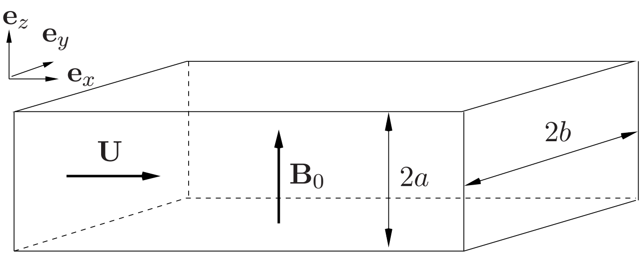

Figure 1.2: Configuration of the MHD flow in a rectangular duct

We use a, (Ga^2/ν) and $(\mu G a^2\sqrt{\sigma\rho/\nu})$ as respective characteristic length, velocity and induced magnetic field. We obtain the non-dimensional form of both induction equation and momentum conservation for $-\chi \leq y^\star \leq \chi$ and $-1 \leq z^\star \leq 1$ $(\chi = b/a)$:

$$\nabla^2 B_i^\star + Ha\partial_{z^\star} u^\star = 0 \tag{1.32}$$

$$\nabla^2 u^\star + Ha\partial_{z^\star} B_i^\star = -1 \tag{1.33}$$

At $z^\star = \pm 1$ and $y^\star = \pm\chi$, a no-slip condition (1.22) is imposed for $u^\star$. The boundary conditions for the induced magnetic field $B_i^\star$ at $z^\star = \pm 1$ and $y^\star = \pm\chi$ shall be derived from equation (1.24). To this end, we use equation (1.13):

$$\mathbf{j}^\star = \frac{1}{Ha}\nabla \times \mathbf{B}_i^\star = \frac{1}{Ha}\left(\frac{\partial B_i^\star}{\partial z^\star}\mathbf{e}_y - \frac{\partial B_i^\star}{\partial y^\star}\mathbf{e}_z\right) \tag{1.34}$$

This equation means that $(1/Ha)\mathbf{B}_i^\star$ is the streamfunction for the current density $\mathbf{j}^\star$ in the plane of the duct cross-section, *i.e* lines of constant induced magnetic field are the electric current streamlines. As the duct is assumed as insulating, the contours of the duct cross-section match an isoline of current density along which the streamfunction $\mathbf{B}_i^\star$ is equal to a constant. We can fix the value of this constant to any value without loss of generality. By convenience, we set it to zero and the boundary conditions for $\mathbf{B}_i^\star$ at $z^\star = \pm 1$ and $y^\star = \pm\chi$ read:

$$\mathbf{B}_i^\star = 0 \text{ at } z^\star = \pm 1 \tag{1.35}$$

$$\mathbf{B}_i^\star = 0 \text{ at } y^\star = \pm\chi \tag{1.36}$$

Both equations (1.32) and (1.33) can be decoupled using Elsasser variables: $\zeta = u^\star + B_i^\star$ and $\xi = u^\star - B_i^\star$, so that only the solution for ζ is required to deduce ξ, $u^\star$ and $B_i^\star$. We omit the $\star$ superscript for simplicity's sake and we express u and B_i as Fourier series on $-\chi \leq y \leq \chi$ and $-1 \leq z \leq 1$:

$$u(y,z) = \sum_{n=1,3,5}^{\infty} u_n(z)\cos(\lambda_n y) \tag{1.37}$$

$$B_i(y,z) = \sum_{n=1,3,5}^{\infty} b_n(z)\cos(\lambda_n y) \tag{1.38}$$

with:

$$\begin{aligned}
u_n(z) &= (k_n/\lambda_n^2)\left[1 - \frac{\sinh p_{n_2}\cosh(p_{n_1}z) - \sinh p_{n_1}\cosh(p_{n_2}z)}{\sinh(p_{n_2} - p_{n_1})}\right] \\
b_n(z) &= (k_n/\lambda_n^2)\left[\frac{\sinh p_{n_1}\sinh(p_{n_2}z) - \sinh p_{n_2}\sinh(p_{n_1}z)}{\sinh(p_{n_2} - p_{n_1})}\right] \\
p_{n_1} &= \frac{1}{2}\left(Ha - \sqrt{Ha^2 + 4\lambda_n^2}\right) \\
p_{n_2} &= \frac{1}{2}\left(Ha + \sqrt{Ha^2 + 4\lambda_n^2}\right) \\
\lambda_n &= n\pi/(2\chi) \\
k_n &= 2\frac{\sin(\lambda_n\chi)}{\lambda_n\chi}
\end{aligned}$$

This solution was first computed by Shercliff [161] so that this configuration is referred to the *Shercliff flow*. For $Ha \gg 1$, both expressions for $u(y,z)$ and $B_i(y,z)$ can be further simplified [18, 19, 20].

In the vicinity of the wall parallel to $\mathbf{B_0}$ and away from the Hartmann layers, $\nabla^2 B_i \simeq \partial_{yy}^2 B_i$. Equations (1.32) and (1.33) then yield the characteristic thickness δ_S of the boundary layers at the walls parallel to $\mathbf{B_0}$: $\delta_S \sim (Ha)^{-1/2}$. These boundary layers are the *Shercliff* or *parallel layers* and the walls at which these layers arise are the *Shercliff walls*.

Equation (1.34) shows that the current density has two non-zero components along $\mathbf{e}_y$ and $\mathbf{e}_z$. Following (1.38) and (1.34), the $z-$component (*resp.* $y-$component) of $\mathbf{j}$ is antisymmetric (*resp.* symmetric) with respect to both the $z-$ and $y-$axes. Therefore, due to symmetry considerations, two sets of identical electric current loops are located on either side of the plane ($z = 0$) in the duct cross-section. The current density is mainly perpendicular (*resp.* parallel) to $\mathbf{B}_0$ in the Hartmann (*resp.* Shercliff) layers. Consequently, the Lorentz forces are efficient in the Hartmann layers and of little influence in the Shercliff layers. The thickness of the Shercliff layer is thus bigger than that of the Hartmann layers.

For $Ha \gg 1$, the velocity profile becomes flat in the core region, while it exhibits an exponential decay in the Hartmann layers (see equation (1.29)). As a result, all boundary layers are very thin, the core flow spreads out over a very large part of the cross section and the velocity gradients are steep in the boundary layers. We shall see later that mesh-based direct numerical simulations experience difficulties to deal with MHD flows in ducts at very high Ha as the CPU cost of solving the flow equations in the Hartmann layers can become prohibitive.

The integration of the velocity over the duct cross-section yields the flow rate Q_r and it follows from equation (1.37) that:

$$Q_r = 2\chi \sum_{n=1,3,5}^{\infty} k_n \int_0^1 u_n(z)dz \tag{1.39}$$

This equation can be reformulated to provide an expression of the non-dimensional pressure drop $K = Ga^2/(\nu U_0)$ as a function of the flow rate $K = 4\chi/Q_r$. Interestingly, an asymptotic expansion of the expression of the non-dimensional pressure drop yields for $Ha \gg 1$ [19, 161]:

$$K = \frac{Ha}{1 - (\alpha_c/\chi)Ha^{-1/2} - Ha^{-1}} \tag{1.40}$$

where α_c is a coefficient depending on the conductivity of the Shercliff walls. If these walls are insulating (*resp.* perfectly conducting), $\alpha_c = 0.825$ (*resp.* 0.95598). The first term in the denominator in (1.40) represents the velocity deficit in the core flow and reflects the balance between the pressure gradient and the Lorentz force in the core flow. The second and last terms represent the pressure loss in the Shercliff and Hartmann layers, respectively. These contributions scale with the thickness of the respective boundary layers.

In the Shercliff flow, the duct walls are all insulating. The configuration where all walls are perfectly conducting and that with insulating (*resp.* perfectly conducting) Hartmann walls and perfectly conducting (*resp.* insulating) Shercliff walls are investigated in [139]. In summary, the velocity profile depends mostly on the electric conductivity of the Hartmann walls. The latter indeed rules the order of magnitude of the core velocity: Ha^{-1} if the walls are insulating and Ha^{-2} if the walls are perfectly conducting, whereas the velocity in the Shercliff layers is always of order Ha^{-1} [139]. As a result, in the configuration with perfectly conducting Hartmann walls, the velocity exhibits a very unstable M-shape profile with a uniform velocity of order Ha^{-2} in the core region and an overspeed flow region of order Ha^{-1} in each Shercliff layer. The case with perfectly conducting Hartmann walls and insulating Shercliff walls is referred as to the *Hunt's flow*. Its stability is investigated in e.g. [141, 160]. In the configuration with insulating Hartmann walls, the velocity profile is smoother since the order of magnitude of the velocity is the same in the whole flow.

On the other hand, the conductivity of the Shercliff walls has little influence on the flow. In the case with perfectly conducting Shercliff walls, away of the Hartmann layers, the electric current streamlines are straight and uniform. Consequently, perfectly conducting Shercliff walls only induce a slight additional damping to the flow in the Shercliff layers since non-zero Lorentz forces are maintained in these layers due to electric currents perpendicular to $\mathbf{B}_0$.

1.4.3 Isolated vortex under the influence of a magnetic field at low Rm

So far, we have studied the interactions between the Lorentz and the viscous forces governed by the Hartmann number Ha. We will now investigate the comparative effects between inertia and Lorentz forces in the simple configuration of an isolated vortex located between two infinite walls perpendicular to the magnetic field $\mathbf{B}_0$ (see figure 1.3). By convenience, we suppose that the vortex axis is parallel to the magnetic field along the $z-$axis. We still consider that the fully developed stationary state is reached for the magnetic field, but the velocity field is now assumed to be time-dependent. The characteristic length scale of the vortex is denoted as l_v, the one along $\mathbf{B}_0$ as l_z and its characteristic velocity is U_v. The time scale of the vortex is the *turnover time* defined as $t_v = l_v/U_v$.

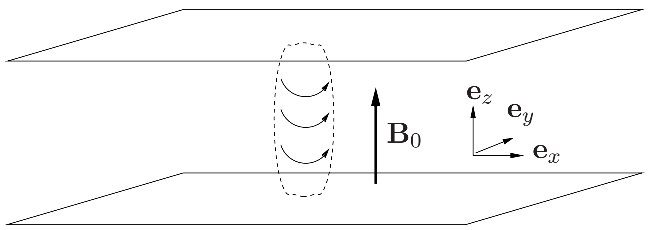

Figure 1.3: Isolated vortex between two infinite walls perpendicular to $\mathbf{B}_0$

We express the current density using equation (1.13) to derive the Lorentz force $\mathbf{F}_L$ with the induced magnetic field $\mathbf{B}_i$:

$$\mathbf{F}_L = N_v[\partial_z \mathbf{B}_i - \nabla(\mathbf{B}_{i,z})] = N_v[\partial_z \mathbf{B}_{i,\perp} - \nabla_\perp B_{i,z}] \tag{1.41}$$

where $N_v = t_v/t_J$ and $t_J = \rho/(\sigma B_0^2)$ is the *Joule dissipation time*. The subscript $\perp$ indicates the component in the plane normal to $\mathbf{B}_0$.

On the one hand, the second term on the right-hand side of this equation is irrotational and can be included into the pressure gradient term of the momentum conservation to form the augmented pressure $\tilde{p}$. On the other hand, from the induction equation of the form of (1.32), it follows that $\mathbf{B}_i$ can be expressed with $\mathbf{u}$ using the inverse of the Laplacian operator ∇^{-2} via the Biot-Savart law

[20] provided adequate boundary conditions for the problem are defined to ensure that the Laplacian operator is invertible. As a result, one obtains the momentum conservation (1.18) as:

$$\partial_t \mathbf{u} + (\mathbf{u} \cdot \nabla)\mathbf{u} = -\nabla \tilde{p} + \frac{1}{Re_v}\nabla^2 \mathbf{u} - N_v \left(\frac{l_v}{l_\parallel}\right)^2 \nabla^{-2}(\partial^2_{zz}\mathbf{u}_\perp) \tag{1.42}$$

where $Re_v = U_v l_v/\nu$.

The last term on the right-hand side of equation (1.42) corresponds to the damping action of the Lorentz forces on the vortex. One observes that this damping is effective only on the velocity components normal to the magnetic field and fuels a diffusion mechanism of the vortex along the direction of the magnetic field. The efficiency of this anisotropic damping depends on the value of N_v. If the Joule dissipation time t_J is much larger than the vortex turnover time t_v, *i.e.* $N_v \gg 1$, then the vortex is elongated within a time of the order of t_J and its final size along the magnetic field scales with $l_z \sim l_\perp N_v^{1/2}$ where $l_\perp$ is the initial length of the vortex in the plane normal to $\mathbf{B}_0$. At this stage, the vortex is elongated and uniform along the direction of the magnetic field except in the Hartmann layers. On the contrary, if $t_J \ll t_v$, *i.e.* $N_v \ll 1$, inertial forces dominate the Lorentz forces. Non-linearities develop in the flow causing disruptions of the vortex and its collapse into smaller vortices. Nevertheless, whatever the value of N_v, the last term on the right-hand side of equation (1.42) indicates that the vortex ends immersed into the Hartmann layers are always perpendicular to the walls, provided inertia is negligible at the scale of these layers.

This anisotropic action of the magnetic field has been observed in numerous experimental investigations [132, 186, 166, 164] and recovered by other approaches. Theoretical arguments in [135] have shown that the component of the angular momentum parallel to the magnetic field is conserved while other components tend to quickly vanish, even though experimental results are still lacking to support this result. Energetic considerations [142, 149, 156] also confirm that the flow structures are strongly dissipated in the plane normal to the magnetic field, while dissipation along the magnetic field lines is much weaker.

1.5 Quasi-two-dimensional MHD flow and shallow water model for $Ha \gg 1$ and $N \gg 1$

We consider the configuration of the Hartmann flow as sketched in figure 1.1. We suppose furthermore that both the Hartmann and Stuart numbers are much bigger than unity and the Lorentz forces dominate both the viscous and inertial forces. Under these conditions, the Hartmann layers are very thin so that the flow exhibits a quasi-two-dimensional profile. In the core flow, the velocity profile hardly depends on the coordinate along the magnetic field and the flow structures can be considered as fully invariant along this magnetic field. In the Hartmann layers, flow patterns are fully three-dimensional and the velocity decays exponentially to zero.

Assuming that both $Ha \gg 1$ and $N \gg 1$, Sommeria and Moreau [165] have elaborated a theoretical model of the quasi-2D flow by averaging the flow equations along the magnetic field lines. In this model, called thereafter *SM82 model*, the core flow is perfectly two-dimensional, the Hartmann layers are modelled by the exponential profile given in (1.29) and walls are electrically insulating.

Since the velocity vanishes at the walls and the walls are electrically insulating, the averages of the mass conservation (1.17) and the current conservation (1.19) along the magnetic field between $z = -1$ and $z = 1$ yield:

$$\nabla_\perp \cdot \bar{\mathbf{u}}_\perp = 0 \tag{1.43}$$

$$\nabla_\perp \cdot \bar{\mathbf{j}}_\perp = 0 \tag{1.44}$$

where $\bar{\mathbf{u}}_\perp$ (*resp.* $\bar{\mathbf{j}}_\perp$) is the component of the velocity (*resp.* current density) normal to $\mathbf{B_0}$ averaged over the direction of the magnetic field.

Similarly, averaging the momentum conservation (1.2) on $-1 \leq z \leq 1$ results in:

$$(1/N)[\partial_t \bar{\mathbf{u}}_\perp + (\bar{\mathbf{u}}_\perp \cdot \nabla_\perp)\bar{\mathbf{u}}_\perp + \overline{(\mathbf{u}'_\perp \cdot \nabla_\perp)\mathbf{u}'_\perp} + \nabla_\perp \bar{p}] = (1/Ha^2)\nabla^2_\perp \bar{\mathbf{u}}_\perp + (1/Ha^2)\mathbf{F}_W \tag{1.45}$$

where $\mathbf{u}'_\perp = \mathbf{u}_\perp - \bar{\mathbf{u}}_\perp$ and $\mathbf{F}_W = [\partial_z \mathbf{u}_\perp(z = 1) - \partial_z \mathbf{u}_\perp(z = -1)]$. $\mathbf{F}_W$ corresponds to the total wall friction at both walls. It can be derived from the velocity profile inside the Hartmann layer (1.29) so that $\mathbf{F}_W = -2Ha\bar{\mathbf{u}}_\perp$. The factor 2 appearing in the definition of $\mathbf{F}_W$ is due to the presence of 2 Hartmann layers in this configuration.

From the integration of the mass conservation (1.17) over the Hartmann layer, it follows that the term $\overline{(\mathbf{u}'_\perp \cdot \nabla_\perp)\mathbf{u}'_\perp}$ is of order $(Ha^{-1}N^{-1})$ [154]. SM82 model neglects the inertial effects occurring inside the Hartmann layers so that this model is accurate down to the order $O(Ha^{-1}, N^{-1})$. As a result, (1.45) in the SM82 model turns into

$$(1/N)[\partial_t \bar{\mathbf{u}}_\perp + (\bar{\mathbf{u}}_\perp \cdot \nabla_\perp)\bar{\mathbf{u}}_\perp + \nabla_\perp \bar{p}] = (1/Ha^2)\nabla^2_\perp \bar{\mathbf{u}}_\perp - (2/Ha)\bar{\mathbf{u}}_\perp \tag{1.46}$$

In this quasi-2D flow model, the magnetic field on the flow imposed a linear damping of the flow from both Hartmann layers with a related non-dimensional characteristic time:

$$t_H = Ha/(2N) \tag{1.47}$$

t_H shall be thereafter denoted as *Hartmann* time. This model can also account for possible current injections at the wall from electrodes. Current conservation (1.44) is then $\nabla_\perp.\bar{\mathbf{j}}_\perp = \mathbf{j}_W$ and the curl of electric current is $\nabla_\perp \times \bar{\mathbf{j}}_\perp = \mathbf{0}$ where $\mathbf{j}_W$ is the current injected at both walls. The effect of current injection can be expressed as a forcing velocity $\mathbf{u}_f = \nabla\Psi_0 \times \mathbf{e}_z$ imposed on the flow where Ψ_0 is defined as:

$$
\begin{aligned}
\bar{\mathbf{j}}_\perp &= -Ha^{-1}\nabla_\perp\Psi_0 \times \mathbf{e}_z \\
Ha^{-1}\nabla_\perp^2\Psi_0 &= -\mathbf{j}_W
\end{aligned}
$$

This modification has been proposed in [157] and leads to a reformulation of (1.46):

$$
(1/N)[\partial_t\bar{\mathbf{u}}_\perp + (\bar{\mathbf{u}}_\perp \cdot \nabla_\perp)\bar{\mathbf{u}}_\perp + \nabla_\perp\bar{p}] = (1/Ha^2)\nabla_\perp^2\bar{\mathbf{u}}_\perp + (1/Ha)(\mathbf{u}_f - 2\bar{\mathbf{u}}_\perp) \tag{1.48}
$$

When applied to the Shercliff flow, the three-dimensional nature of the Shercliff layers is not specifically addressed by the SM82 model, as it assumes that diffusion along the field lines is an order of magnitude faster than the lateral diffusion of the angular momentum. Nevertheless, the related error has been shown to be of the order of 10% in the Shercliff flow. In addition, this error is significant only in the vicinity and inside the Shercliff layers [157]. Besides, the SM82 model requires electrically insulating perpendicular walls, as the assumption of a quasi-2D flow fails if strong velocity jets at the lateral extremities of the Hartmann layers are present. Finally, this model assumes that no fluid transfer exists at the interface between the Hartmann layers and the core flow. As a result, Ekmann-like recirculation flow, which is the basic formation mechanism of cyclones for example, is forbidden in the SM82 model. This flaw can be corrected by taking into account the inertial effects in Hartmann layers, *i.e.* the terms of order Ha^{-1} in (1.45). This has been achieved in [157] leading to a gain in the model accuracy equal to $Ha^{-i}N^{-j}$ with $i + j = 3$.

In conclusion, provided $Ha \gg 1$ and $N \gg 1$, the implementation of the SM82 model in a numerical code is an effective and accurate method to investigate the flow dynamics. The involved CPU cost is much lower compared to 3D direct numerical simulations. In chapter 6, we implement this model to study a MHD cylinder wake inside a square duct.

Chapter 2

Flow past a circular cylinder

In this chapter, we introduce the flow features of the cylinder wake in the case where no magnetic field is present. Firstly, we consider an unbounded fluid domain and an infinitely long cylinder. The flow regimes and related patterns are described until the 3D features are settled in the flow. The nature of the successive transitions are given and the critical thresholds provided. The evolutions of the flow coefficients are linked to the flow dynamics. We assess the influence of the confinement of the flow domain by parallel side walls. From now on, the streamwise direction indicates the direction parallel to the free stream, the spanwise direction is the one parallel to the cylinder axis and the transverse direction that across both the cylinder axis and the streamwise direction. A very comprehensive review of the flow dynamics in cylinder wakes is available in [92, 93].

2.1 Two-dimensional features of flow past a circular cylinder

We consider the flow of an incompressible Newtonian fluid past a smooth, infinitely long, straight, circular cylinder in an unbounded fluid domain in which the streamwise direction is perpendicular to the cylinder axis. In this reference case sketched on figure 2.1 (a), the flow is governed only by the Reynolds number $Re = U_0 d/\nu$ defined with the free stream velocity U_0, the cylinder diameter d and the kinematic viscosity ν. A review of experimental works investigating the reference case is given in [38]. The respective critical Re for the successive transitions between flow regimes have been well established by experiments, but due to the unavoidable perturbations present in any set-up, they often exhibit some discrepancy from one experimental campaign to the other. Therefore, instead of one single value for a critical Re, we provide a interval of Re.

When increasing Re from zero on, the flow exhibits a sequence of three 2D flow regimes, in which the features are invariant along the cylinder span. For Re up to Re_{cS}, $4 < Re_{cS} < 5$, the flow sticks to the whole cylinder surface and no separation is visible [30] (see figure 2.2 (a)). This regime is referred to the *creeping flow* or *Stokes flow* and corresponds to a viscous-dominated flow in which

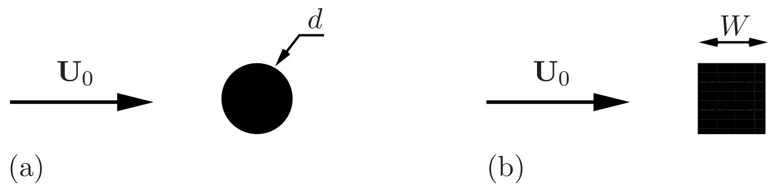

Figure 2.1: Reference cases: Circular cylinder wake (a); Square cylinder wake (b).

inertia has little influence. When further increasing Re, flow separation appears and two steady recirculation regions symmetric with respect to the wake centreline develop at the rear of the cylinder [37, 61, 79, 84] and lengthen downstream. Figure 2.2 (b) presents a schematic view of the resulting flow. This is the regime of the steady recirculation regions, it is the second and last steady flow regime before unsteadiness appears at Re_{cU}, $50 < Re_{cU} < 60$.

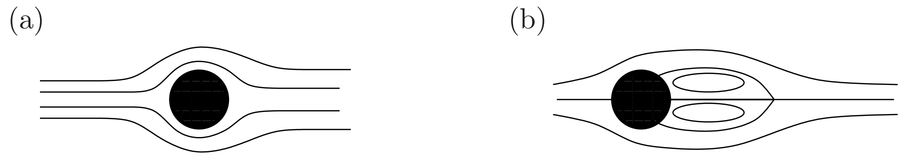

Figure 2.2: Steady flow regimes of the unbounded cylinder wake: Creeping flow (a); Regime of the steady recirculation regions (b). Flow from left to right.

In the vicinity of Re_{cU}, the steady recirculation regions reach their maximum length. Their tails undergo transverse undulations which gradually move upstream, reach the near-wake and destabilise the whole recirculation regions. The free shear layers on both sides of the cylinder alternatively roll up at the cylinder back and clockwise (*resp.* anticlockwise) vortices are generated by the upper (*resp.* lower) free shear layer. These vortices eventually detach and flow downstream along two parallel trajectories, themselves parallel to the wake centreline [37, 43, 64, 69, 71, 84, 91]. This regime is the periodic laminar flow regime (see figure 2.3 (a)) and probably the most remarkable one, as the shedding process fuels a procession of alternate counter-rotating vortices, also known as *Kármán vortex street*, first described by Bénard [26, 28, 27] and von Kármán [82, 83].

2.2 Route to three-dimensionality: mode-A and mode-B flow regimes

The cylinder wake remains truly 2D as long as the Kármán vortices remain invariant along the cylinder axis. When Re is further increased, 3D features appear as streamwise vortices settle in the flow. Two phases in the route to three-dimensionality have been identified by Williamson [86]. They are characterised by the appearance of so-called *mode-A* and *mode-B* streamwise vortices, both depicted in figure 2.3 (b).

Mode-A regime is a regularly spaced, out-of-phase pattern of counter-rotating streamwise vortices

This image has been removed due to third party copyright. The unabridged version of the thesis can be viewed at the Lanchester Library, Coventry University.

Figure 2.3: Experimental observations of the laminar periodic flow regime at $Re = 120$ [43] (a); Schematic view of the modes A and B flow patterns [34] (b).

with a spanwise wavelength of about 4 cylinder diameters and strongly distorted Kármán vortices along the spanwise direction [34, 48, 54, 65, 81, 86, 94]. This regime appears according to a hysteretical transition, *i.e.* the critical threshold Re_{cA} differs whether Re is increased or decreased, for $180 < Re_{cA} < 190$ [24]. In mode B, one can observe a continuous sheet of counter-rotating streamwise vortices alternately distributed over the spanwise direction with a spanwise wavelength of about 1 cylinder diameter. This vorticity sheet undulates between the Kármán vortices whose shape is almost invariant along the spanwise direction [34, 48, 54, 65, 81, 86, 94]. Unlike mode A, the transition to mode B is supercritical and with a critical Re noted Re_{cB}, this flow regime appears at $250 < Re_{cB} < 270$ [24, 87]. Mode-B pattern has been observed in flows for Re up to 10^4 [87]. The formation mechanisms of mode-A and mode-B structures are described in [33, 34, 57, 80, 87].

Once the mode-A flow structures are wiped out by the mode-B one from Re_{cB} on, the cylinder wake is truly 3D. When Re is increased, the flow dynamics further evolve and new flow regimes with characteristic pattern can be observed. These features are out of the scope of this thesis, but detailed information can be found in [92].

2.3 Flow coefficients

2.3.1 Definitions

We still consider the reference configuration and we now introduce a set of flow coefficients whose respective evolutions with Re reflect various aspects of the flow dynamics.

In the second steady regime, L_b is defined as the length of the steady recirculation regions. It is measured along the wake centreline, between the rear of the cylinder and the tail of the recirculation regions. In the unsteady flow regimes, L_b is defined as the distance between the rear point of the cylinder and that where the RMS velocity fluctuations reach a maximum [88]. It is rather difficult to measure L_b in experiments at Re in the lower range of the regime of the steady recirculation regions.

The rear point of the cylinder along the wake centreline is the base point. It is used in the definition of the base pressure coefficient C_{pb}:

$$C_{pb} = \frac{2(p_b - p_0)}{\rho U_0^2} \tag{2.1}$$

where p_b is the static pressure at the base point and p_0 the free stream static pressure. In the unsteady flow regimes, a time average value is used. Systematic pressure measurements are widespread in experiments, since the measurement methods are reliable and easy to integrate into the experimental set-up.

As the fluid flows around the cylinder, it exerts a force on the cylinder due to both pressure and viscous forces. The projection of this force along the streamwise (*resp.* transverse) direction is the drag (*resp.* lift) force. In the reference case, the cylinder is considered as infinitely long, so F_D (*resp.* F_L) represents the drag force (*resp.* lift force) per unit span length. One subsequently defines the drag coefficient C_D and the lift coefficient C_L as:

$$C_D = 2F_D/(\rho U_0^2 d) \tag{2.2}$$

$$C_L = 2F_L/(\rho U_0^2 d) \tag{2.3}$$

Furthermore, one can distinguish the pressure (*resp.* viscous) component of the drag coefficient $C_{D,p}$ (*resp.* $C_{D,v}$) along with the relationship $C_D = C_{D,p} + C_{D,v}$. In the steady flow regimes, the drag and lift coefficients are measured once the flow is fully established while their time average values are used in the unsteady flow regimes. The transition to 3D flow should be addressed in the definition of the drag and lift coefficients. As mode-A and mode-B flow regimes are periodic along the cylinder span, we consider that the drag and lift forces are acting on a typical spanwise length, defined by the respective spanwise lengths of mode-A and mode-B. The definitions for drag and lift coefficients can then be considered as unchanged. Note that force coefficients are delicate to obtain in experiments, especially in the 3D flow regimes. In this matter, numerical experiments provide more reliable data.

An adequate flow coefficient is used to characterise the vortex shedding in the unsteady flow regimes. This is the Strouhal number St which is base on the frequency f of the vortex shedding:

$$St = fd/U_0 \tag{2.4}$$

In experiments, St curves are very often derived from the time history of velocity at given locations in the cylinder wake. In numerical computations, one can obtain them from the time history of C_L.

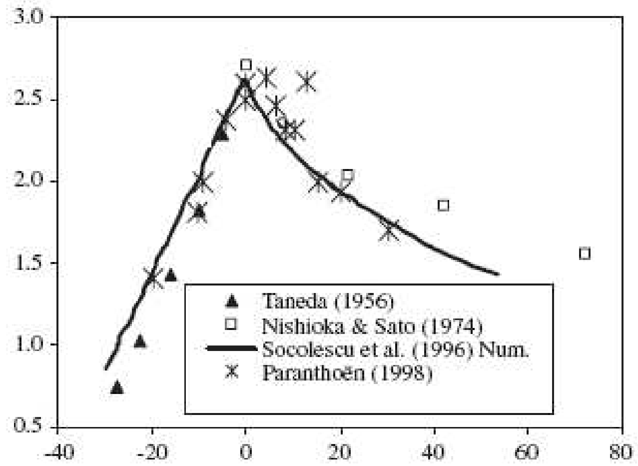

Figure 2.4: Circular cylinder wake in the reference case: L_b/d versus $(Re - Re_{cU})$ [67]

2.3.2 Evolutions of the flow coefficients against Re

Figure 2.4 is extracted from [67]. It presents the evolution of L_b/d with increasing Re before and after the transition to unsteadiness. Figures 2.5 and 2.6 are taken from [47] and [66]. The former reports the evolution of $-C_{pb}$ versus Re for Re up to 350; the latter presents the respective curves of the viscous, pressure and total drag coefficient in the steady regime, but only the evolution of the total drag coefficient in the unsteady flow regime.

In the steady flow regimes, L_b increases linearly with Re as reported in various experimental investigations [37, 45, 61]. This increase in L_b corresponds to a decrease in both C_{pb} and C_D. The appearance of the steady recirculation regions corresponds to that of an adverse pressure gradient at the rear of cylinder. As a consequence, the pressure at the base point increases and gets closer to p_0, hence the decrease in C_{pb} in the regime of the steady recirculation regions. Similarly, both the pressure and viscous part of the drag coefficient decrease with increasing Re. The total drag coefficient $C_D = C_{Dp} + C_{Dv}$ therefore decreases in the steady flow regimes [29, 55].

The transition to unsteadiness occurring at Re_{cU} is characterised by a discontinuity in the respective evolutions of all coefficients. In the unsteady regime, L_b measures the length of the formation region of the Kármán vortices. Experiments have shown that this region shrinks as Re becomes higher [44, 62, 87]. Indeed, at the onset of the vortex shedding, the Kármán vortices are released at the back of the remaining steady recirculation regions and vortices gradually shed closer to the cylinder as Re is increased. As the Kármán vortices are formed closer from the base point, the kinematic streamline linking the point where the reference pressure is measured and the base point becomes shorter so that velocity at the vicinity of the base point increases and in return, pressure p_b decreases. As a result, C_{pb} decreases after the transition to unsteadiness. Here it is important to notice that L_b and C_{pb} have opposite variations in both steady and unsteady flow regimes.

This is in contrast with C_{Dp} which starts increasing after the onset of vortex shedding as the results

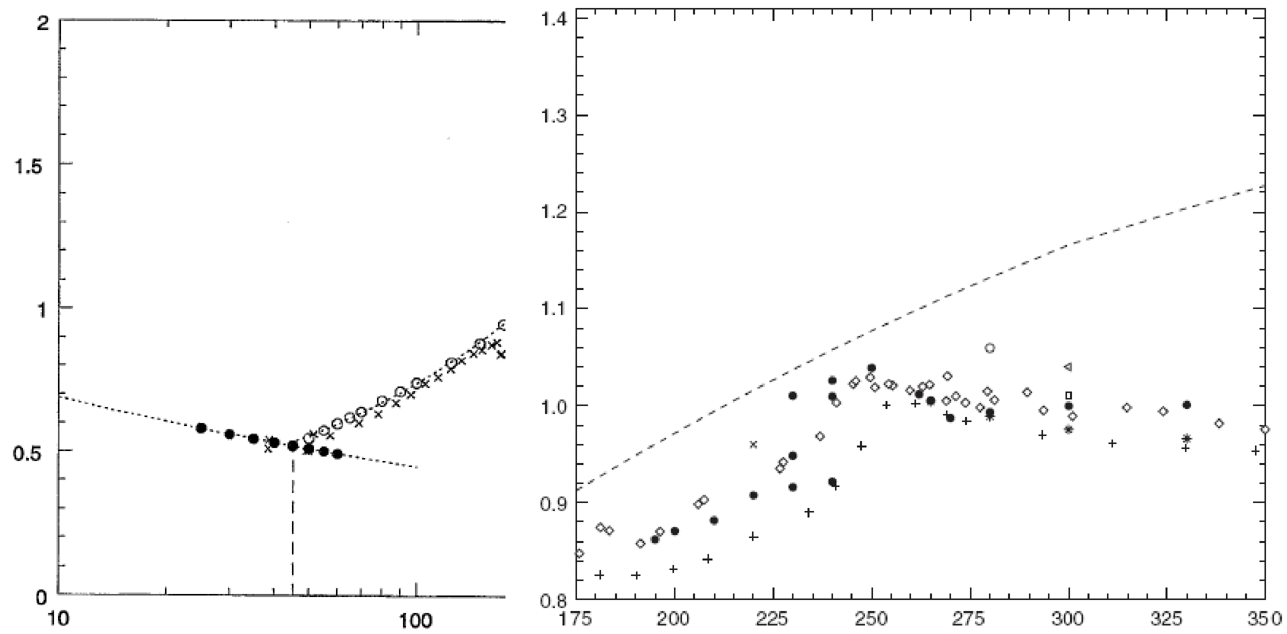

Figure 2.5: Circular cylinder wake in the reference case: C_{pb} versus Re. (Left) 2D flow regimes [47]. (Right) 3D flow regimes [66]. The dash line is the prolongation of the 2D curve from [47].

of the modification of the pressure distribution in the near wake of the cylinder. The same event does not affect the evolution of C_{Dv} which keeps on decreasing. In the first stage of the unsteady regime, its decrease still outweighs the increase in C_{Dp} so that the total drag coefficient C_D only exhibits a change in its decreasing slope initiated throughout the steady regime.

Figure 2.7 is extracted from [88] and shows the evolution of the Strouhal number St with increasing Re. One can observe that St increases with Re within the laminar periodic flow regime for Re up to about 180. The shedding frequency can be seen as the ratio of the typical velocity U_v of the Kármán vortices to the typical distance l_v between 2 successive clockwise (or anti-clockwise) vortices. The Strouhal number can then be written as:

$$St = \frac{U_v}{U_0}\frac{d}{l_v} \tag{2.5}$$

As the formation region of the Kármán vortices shrinks, the inertia of the vortices dragged by the free stream diminishes so that U_v gradually catches up the free stream velocity as Re is increased. On the other hand, the shedding process is accelerated by the increase of the free stream velocity on the outside of the free shear layers. The shedding frequency therefore increases and the distance l_v shrinks. Both the increase in U_v and the decrease in l_v were observed experimentally [69, 70] and explain why St increases within the periodic laminar regime.

The appearance of mode-A regime at the critical threshold Re_{cA} is clearly detected in the evolutions of each flow coefficient. Due to the formation of streamwise vortices, the Kármán vortices exhibit

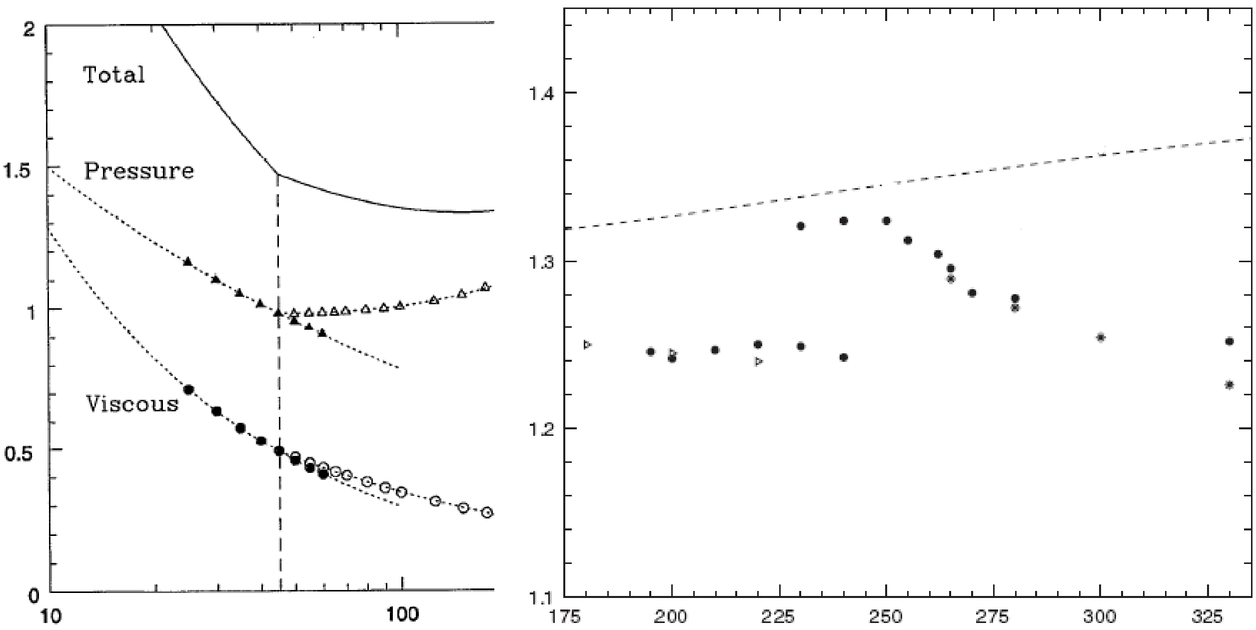

Figure 2.6: Circular cylinder wake in the reference case: C_D versus Re. (Left) 2D flow regimes: viscous, pressure and total drag coefficient from bottom to top [47]. (Right) 3D flow regimes: Total drag coefficient only [66]. The dash line is the prolongation of the 2D curve for the total drag coefficient from [47].

a distorted shape along the cylinder span. The whole columnar Kármán vortex does not separate from the free shear layer as a single block, instead the shedding process is delayed at the locations where the streamwise vortices are formed. As a result, the St-curve exhibits a discontinuity at the transition to mode-A regime as St undergoes a sudden decrease. Further for $Re_{cA} < Re < Re_{cB}$, the respective evolutions of both mode A and B structures can be tracked down on the St time histories [48, 66, 86]. The formation of streamwise vortices also modifies the pressure distribution in the cylinder near wake so that a break in the decreasing slope of C_{pb}-curve is seen at Re_{cA}. Accurate 3D numerical simulations [48, 66] have shown that the transition to mode-A regime also causes a discontinuity in the C_D-curve as C_D starts increasing after Re_{cA}. Note that, for $Re_{cU} \leq Re \leq Re_{cA}$, the rate of increase in C_{Dp} gradually levels out the rate of decrease in C_{Dv} so that the total drag coefficient $C_D = C_{Dp} + C_{Dv}$ reaches a minimum value just before Re_{cA}. For higher values of Re, C_{Dv} is very low in comparison to C_{Dp}. The variations of C_D therefore follow from those of C_{Dp} and C_D increases.

2.4 Flow past a circular cylinder confined between two parallel walls

The reference case of the unbounded flow domain involves a flow dynamics free of any kind of external disturbances. This remains however an idealised configuration. Any experimental set-up necessarily

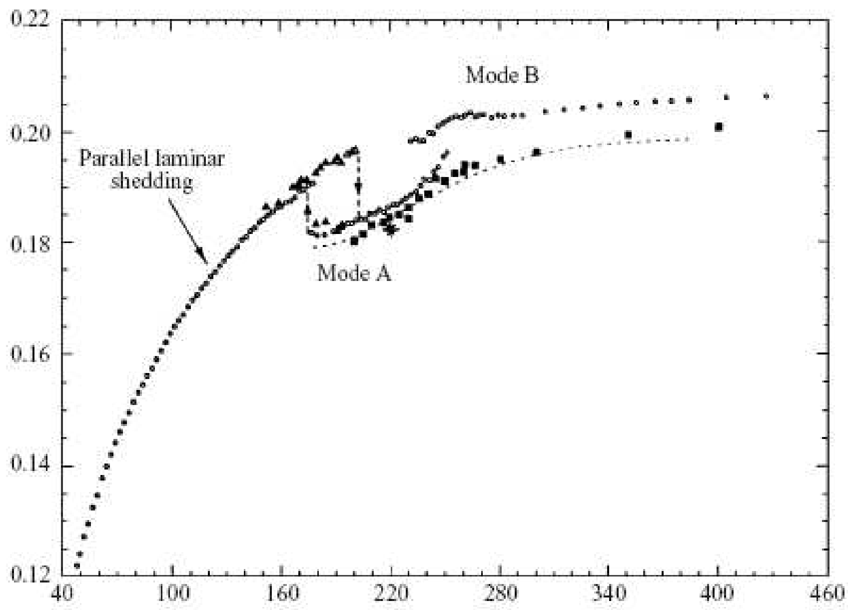

Figure 2.7: Circular cylinder wake in the reference case: St versus Re [88]

imposes a set of limits to the flow and perturbations can not be totally driven out. In particular, the flow domain is never unbounded, so that it is important to assess the influence of confinement on the flow dynamics. Here we consider only the blockage effects on the flow by two parallel side walls.

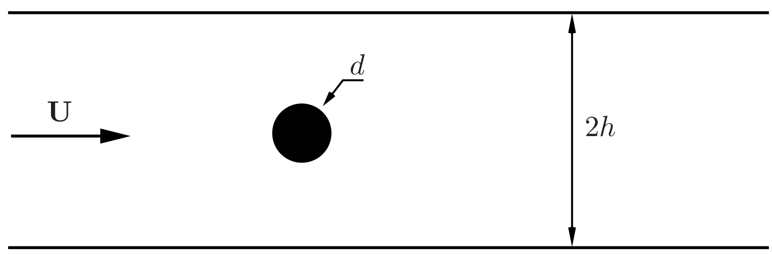

Figure 2.8: Configuration of the flow past a circular cylinder between two parallel walls

In this configuration sketched in figure 2.8, the flow domain is still assumed as unbounded in both streamwise and spanwise directions, but confined in the transverse one. Two infinite parallel walls are located on each side of the cylinder, at equal distance h from the wake centreline and normal to the transverse direction. The inflow velocity is no longer invariant along the transverse direction, but corresponds to a parabolic velocity profile, also known as *Poiseuille* velocity profile. In addition, due to the restriction of the channel cross-section by the cylinder, the free stream is accelerated between the cylinder and the walls. Another important feature is the presence of a boundary layer along each wall which may interact with cylinder wake. The influence of the confinement of the flow by parallel side walls is evaluated through the *blockage ratio* β defined as the ratio of the cylinder diameter d to the distance between the side walls $2h$ so that $\beta = d/(2h)$.

2.4.1 Influence on the flow dynamics

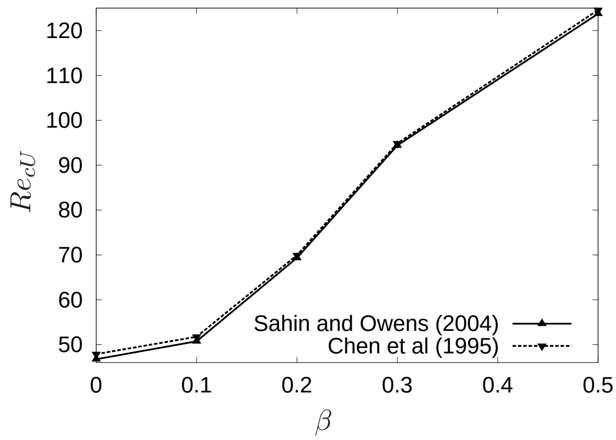

Figure 2.9: Critical Re at the onset of vortex shedding versus blockage ratio $\beta = d/(2h)$

For $\beta < 0.1$, flow confinement has little influence on the flow dynamics. In the range $0.1 < \beta < 0.6$, the acceleration due to flow confinement causes noticeable changes in the flow. Flow separation occurs at higher Re [35, 37, 45, 67] and the lengthening of the steady recirculation regions is slower in the sense that their length still grows linearly with Re, but at a given Re the steady recirculation regions are shorter if β is higher [35, 37, 45, 67, 73]. At a given Re, increasing β pushes downstream the point where the free shear layer separates from the cylinder surface [89]. Another effect of the flow confinement is the stabilisation of the free shear layers. The onset of vortex shedding is initiated by oscillations of the recirculation regions in the transverse direction. According to [45], the development of these oscillations is impeded by the presence of the side walls. As a result, as shown on figure 2.9, the transition to unsteadiness is shifted to significantly higher Re as β is increased [35, 59, 69, 72, 74].

Also, for $Re \geq 200$, the development of Kármán vortices initiates the separation of the side wall boundary layers and the generated secondary vortices then interact with the Kármán vortices [59, 67, 72]. For $0.6 < \beta < 1$, the flow dynamics are very peculiar and differ in many aspects from the typical cylinder wake [36, 72]. The separation of the side wall boundary layers influences the flow very much. New flow patterns are detected and the nature of the transitions between the flow regimes have nothing in common with the ones described up to now. For example, one may observe vortex shedding induced only by the separation of the side wall boundary layers, but not by the cylinder itself [72].

2.4.2 Influence on the evolutions of the flow coefficients

Figure 2.10 is extracted from [59] and shows the respective evolutions of the total drag coefficient C_D and St with increasing Re for several values of the blockage ratio β. The presence of side walls introduces an additional pressure gradient along the transverse direction as well as an increase of the flow friction from viscous forces within the side wall boundary layers. As a result, the drag coefficient C_D increases with β [52, 59, 72, 73]. In the creeping flow regime where viscosity dominates the flow, experiments have shown that C_D is constant for $Re < 0.1$ [85] and the value of the constant C_D increases with β [68, 30, 29, 77]. In further regimes, the respective C_D curves for increasing β have a roughly similar shape, but are shifted to higher values of C_D. For $\beta < 0.8$ in the range $0 < Re < 10^4$, C_D significantly decreases and increases very slightly after the onset of vortex shedding [1, 52, 59, 72, 95]. Note that, as the blockage delays the transition to unsteadiness, the decrease of the viscous component of the drag coefficient C_{Dv} over the steady flow regimes is prolonged over a longer Re interval. Consequently, at the onset of vortex shedding, when the pressure-based drag coefficient C_{Dp} starts to increase while C_{Dv} keeps on decreasing, the decrease in C_{Dv} is too weak to counteract the increase in C_{Dp}. C_D therefore starts increasing as soon as the transition to unsteadiness is reached.

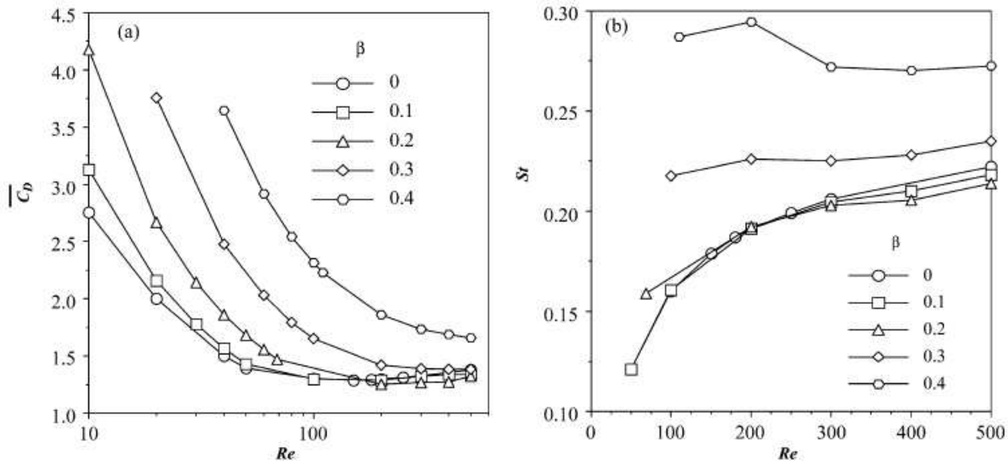

Figure 2.10: Circular cylinder wake between parallel walls β: C_D (a) and St (b) versus Re at different blockage ratio β [59]

Similar observations can be made on the St-evolution with Re for different values β in the range $0 < Re < 500$. The value of St at the onset of vortex shedding increases with β [35, 59, 72]. Indeed, due to the confinement, at a given Re, the ratio of the typical vortex velocity to the free stream velocity is higher for higher β and the typical distance between two successive clockwise vortices is smaller [69]. Also, the evolution of the Strouhal number as defined in (2.5) is the same as that relevant with the unconfined cylinder wake. As long as the Kármán vortex street is not disturbed by secondary vortices released after the separation of side wall layers, St increases with Re and higher St are obtained for higher β at a given Re [59]. Nevertheless, as soon as the secondary vortices interact with the Kármán vortex street, St decreases (see curve for $\beta = 0.3$ in [59]).

Broadly speaking, relatively little attention has been paid in the literature on the influence of flow confinement in comparison with the large amount of publications on the reference case. For example, it could be of interest to identify the influence of the blockage on the appearance of streamwise vortices. To our knowledge, only the experiments of [67] with $\beta = 0.3$ have shown that mode A (*resp.* mode B) appears at a lower (*resp.* higher) critical Re than when no blockage is involved. In addition, the spanwise lengthwave of mode-A is one cylinder diameter shorter while that of mode-B is the same as in the unconfined cylinder wake. Also, an investigation of the interactions between the Kármán vortices and the secondary vortices initiated by the separation of the side wall layer would bring useful insight in this particular flow dynamics.

Chapter 3

Flow around more complex obstacles

In this chapter, we modify the geometry of the cylinder. Firstly, we consider the flow past a cylinder of square cross-section. Secondly, we review the case where the cylinder does not span over the full height of the fluid domain: one end is mounted on a wall normal to the cylinder axis and the other one is free.

3.1 Flow past a square cylinder

The shape of the cylinder cross-section is important in the flow dynamics. Flow separation is promoted at sharp angles of the cross-section. In case no such angle exists as for the circular cylinder, the separation point fluctuates along the cylinder cross-section and even along the cylinder span such that the separation line can be wavy [90]. Also, the cross-section shape defines the typical width of the wake, which has an influence on the stability of the steady flow regime and affects the critical size of the steady recirculation regions. Finally, the stability of the free shear layers is significantly influenced by their curvature [58]. We shall introduce in detail the flow past a square cylinder using the width W of the square cross-section as unit length used to define Re. The square cylinder is oriented such that the streamwise direction is normal to the upstream cylinder face. This reference configuration is sketched on figure 2.1 (b). The flow domain is unbounded and the cylinder is infinitely long. We will describe the flow dynamics in this configuration until three-dimensionality has settled into the flow.

3.1.1 Flow dynamics

When increasing Re from zero on, the flow exhibits a sequence of 2 steady regimes and 3 unsteady regimes before three-dimensional instability appears in the flow. The steady flow regimes are similar to the circular cylinder wake. Flow separation appears in flow at $2 < Re_{cS} < 3$ and two symmetric steady recirculation regions lengthen in the wake as Re is increased [104]. Free shear layers separate at the downstream corners of the cylinder. The transition to unsteadiness occurs at $40 < Re_{cU} < 50$ [104, 106] and vortex shedding fuels a regular Kármán vortex street. The successive stages of the unsteady flow regimes with increasing Re is presented on figure 3.1 extracted from [101]. At $100 < Re < 120$, the free shear layers separate from both upstream and downstream corners [101, 104]. The separation at the downstream corners generates Kármán vortices, while separation at the upstream corners gives rise to an unsteady recirculation region which slightly moves along the lateral face of the cylinder but its reattachment point always remains away from the downstream corner. The appearance of this lateral recirculation region has no effect on the formation process of Kármán vortices. For $150 < Re < 160$, the junction between the lateral and the rear recirculation regions is effective [101, 104].

Figure 3.1: Square cylinder wake in the reference case: Time-averaged mean streamlines in the 2D unsteady flow regimes [101]. Separation only at the rear edges $100 \leq Re \leq 120$ (a). Separation at both front and rear edges, appearance of two lateral recirculation regions $120 \leq Re \leq 150$(b). Separation only at the front edge, junction between both side and rear recirculation regions $150 \leq Re \leq 160$(c).

The route to three-dimensionality is also characterised by the successive appearances of mode-A and mode-B regimes. Respective flow patterns have the same properties as in the circular cylinder wake with a spanwise wavelength of about $5W$ and $1W$ for mode A and mode B respectively [99, 101]. A hysteretical transition characterises also the appearance of mode-A regime at $160 < Re_{cA} < 170$ [99, 101], but the hysteresis is weak and spans over a narrow Re range less than 6 [99]. The Kármán vortices are strongly distorted and vortex dislocations develop in the very first stages of mode-A regime. As in the circular cylinder wake, mode-B regime appears also after a supercritical transition at $190 < Re_{cB} < 200$ [99, 101] and Kármán vortices are almost invariant along the spanwise direction.

The respective formation mechanisms of both modes are very similar to the ones observed in the circular cylinder (see [99] for a detailed analysis).

3.1.2 Evolution of the flow coefficients against Re

Using the same definitions as previously, the flow coefficients exhibit similar variations as in the circular cylinder wake [99, 100, 101, 104, 106]. Striking changes are observed in the evolution of the different drag coefficients. On figure 3.2, we reproduce the respective curves of the pressure and total drag coefficient given in [104]. The steady regime results in a decrease in both C_{Dp} and C_{Dv} and subsequently also in C_D, as in the circular cylinder case [104]. In the laminar periodic flow regime up to about Re_{cA}, C_D monotonically decreases [106, 104] while C_{Dp} first decreases for $Re \leq 90$ and then increases until it becomes finally bigger than C_D at Re about 140 [104, 107]. The appearance of the unsteady recirculation regions along the lateral faces of the cylinder causes C_{Dv} to turn negative. Further within the 3D vortex shedding regime, as in the circular cylinder case, the influence of C_{Dv} wanes as C_D follows the variations of C_{Dp} and a slight increase in C_D is observed [102, 107].

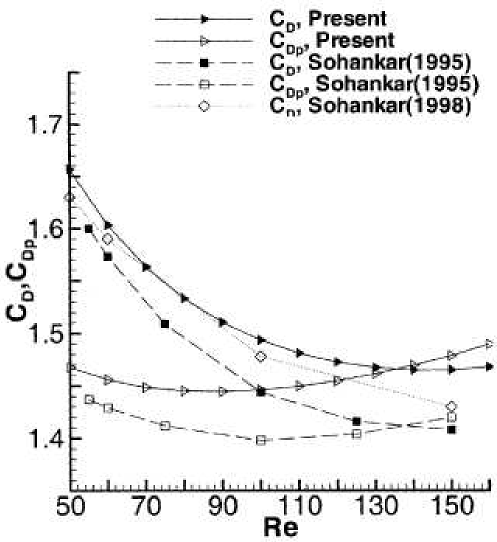

Figure 3.2: Square cylinder wake in the reference case: C_D and $C_{D,p}$ versus Re [104]. The intersection of the curves with the same symbol, filled and open, corresponds to the appearance of the lateral recirculation region

The influence of the blockage by parallel walls located symmetrically on both sides of the cylinder is studied in [96, 97, 98, 105, 106] for moderate values of Re up to about 10^3. Similar effects as in the circular cylinder case are observed.

In conclusion, the flow dynamics of the square cylinder wake are very similar to that of the circular cylinder. Actually, the main change is provided by the appearance of recirculation regions along the lateral faces of the cylinder when the flow separates at the leading edge of the square cylinder. As a result, the typical size of the square cylinder is then bigger than the cylinder width by about 10 to

20%. If one accounts for this change in the unit length in the definitions of Re and St, one roughly recovers the curves relative to the circular cylinder wake as well as about the same values for the critical thresholds of modes A and B [101]. Also, one can notice that the Re value at which the lateral recirculation regions reattached at the trailing edge of the cylinder corresponds more or less to the appearance of mode A.

3.2 Flow past a cylinder with one free end

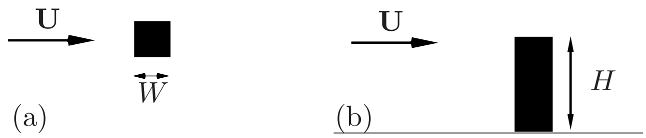

Figure 3.3: Configuration of the flow past a truncated square cylinder: Top view (a); Side view (b).

In this configuration, the fluid domain is bounded by an infinite bottom wall and unbounded in the other directions. Figure 3.3 shows the configuration of the flow past a truncated square cylinder. A square or circular cylinder is mounted on the bottom wall and its axis is normal to this wall. In the case of the square cylinder wake, the streamwise direction is normal to the cylinder upstream face. The unit length for the circular (*resp.* square) cylinder case is the cylinder diameter d (*resp.* width W). The cylinder aspect ratio γ is the ratio of the cylinder height H to its diameter d (*resp.* width W) in the circular (*resp.* square) cylinder case.

The flow dynamics relevant to this configuration have been thoroughly studied for $Re > 10^4$ to give insight on a wide variety of industrial problems such as smoke flow from chimney stack or ship funnel and wind flow past a building. For moderate values of Re, *i.e.* $Re < 10^3$, works are very scarce in the literature although valuable insight may be provided on the influence of probes used in intrusive measurements methods [177] or on heat transfer in electronic circuit boards [119].

In these regimes, the cylinder wake consists of the combination of four main structures: the horseshoe pattern, a system of trailing vortices and the free shear layer arising at the cylinder free end and those stretching from both cylinder lateral faces. The latter feature is similar to those forming in the non-truncated cylinder wake. We shall describe in more detail the former three structures.

The boundary layer arising at the bottom wall is disturbed by the presence of the cylinder. At the junction between the cylinder and the bottom wall, the instability of the bottom wall boundary layer causes flow separation some distance upstream the cylinder and gives rise to a system of swirls [108, 114, 116, 117] as shown on figure 3.4(a). The swirl system then spirals around the cylinder and forms a *horseshoe* pattern named after its remarkable shape. The number of swirls and its stability depend on the cylinder cross-section, Re and the thickness of the bottom wall boundary layer. In the case of a square cylinder, experiments [117] showed that the horseshoe pattern was steady for Re up

This image has been removed due to third party copyright. The unabridged version of the thesis can be viewed at the Lanchester Library, Coventry University.

Figure 3.4: (a) Streamline patterns at the front of a plate at $Re = 1200$ exhibiting the presence of a system of swirls at the origin of the horseshoe pattern obtained from PIV measurements [116]. The $x-$axis corresponds to the bottom wall, the front edge of the plate is located at $x = 0$ and the y-axis is here parallel to the cylinder axis. (b) Snapshot of the vortex generated at the cylinder free end at $Re = 100$. Experiments by [118] achieved for a truncated circular cylinder.

to 1500 without any restriction on the thickness of the bottom boundary layer. Also, the main swirl is slightly shifted upstream when Re is increased [108, 114, 123].

The system of trailing vortices consists of two pairs of counter-rotating streamwise vortices located below the cylinder tip and above the cylinder base, respectively. According to their location, they are referred to as *tip* and *base vortices*. The origin of the both vortices still remains controversial. From experimental flow visualisations in the wake of a truncated circular cylinder at $Re > 10^4$, [112] and [120] suggested that the tip vortices are generated above the upper cylinder face from the rolling-up of the lateral ends of the upper free shear layer, while [115] interpreted these tip vortices as the result of the tilting of the lateral free shear layers in the vicinity of the cylinder free end. From experimental measurements in the same configuration at $Re = 6.10^4$, [125] suggested that the tip vortices have nothing to do with the lateral free shear layers. Investigating experimentally the flow past a truncated square cylinder for $200 < Re < 10^4$, [126] drew the same conclusions as [115]. On the other hand, little information is available on the base vortices. [112], [125] and [126] agreed that they resulted from the tilting of the lateral free shear layers in the vicinity of the bottom wall. [112] furthermore indicated that the base vortices were initially aligned along the spanwise direction and then tilted along the streamwise between the mid-span and the free end. The cylinder aspect ratio γ determines which of the tip or the base vortices prevail in the wake [125, 126]. Also, increasing the thickness of the boundary layer at the bottom wall strengthens the base vortices [127].

A free shear layer is generated by the boundary layer arising at the cylinder free end. According to many researchers [114, 118, 129], it separates at the trailing edge of the cylinder free end to form a transverse vortex as shown on figure 3.4(b). We shall see in section 9.3 that the latter vortex does not necessarily result from the the separation of this free shear layer, but can be fed by streamlines flowing under the lateral free shear layers. At low Re, the tail of the top free shear layer however washes down behind the cylinder tip and interferes with the upper part of the cylinder wake [115, 118, 124].

The flow is governed by two parameters: the Reynolds number Re and the cylinder aspect ratio γ. For moderate values of Re, *i.e.* up to 1500, the horseshoe system remains steady so that vortex shedding is generated only by the free shear layers. For high values of γ, the flow dynamics are dominated by the lateral free shear layers and the onset of vortex shedding results in an asymmetric Kármán-like vortex street [118, 121, 124, 126]. For intermediate values of γ, the transition to unsteadiness leads to a combination of both top and lateral free shear layers to yield a symmetric vortex shedding formed by hairpin vortices released along the wake centreline [121, 122, 128, 129]. The latter mode of vortex shedding eventually turns asymmetric for higher Re as the hairpin vortices are released alternately on each side of the wake [128]. If γ is close to zero, both free shear layers at the cylinder top and lateral faces are entangled into a single swirl flow and prevent any vortex shedding from developing [115, 119, 123]. The respective critical values of γ separating these regimes depend on the shape of the cylinder cross-section and on the flow confinement. For instance, experiments by [121] detected a symmetric wake for $\gamma < 2$ (*resp.* $\gamma < 2.5$) in the configuration featuring a truncated square (*resp.* circular) cylinder. [122] observed a symmetric vortex shedding in the wake of a truncated circular cylinder for γ up to 4. Also, the onset of vortex shedding is shifted to higher Re as γ is decreased [122].

A topological approach of the flow has proved to being an efficient means to infer the flow patterns [113, 123]. In particular, the number of saddle and node points is linked by a simple relationship which can be used to check the validity of the results obtained from a numerical or analytical approach [113].

The formation mechanism of the Kármán vortices relies on the alternate roll-up and shedding of the lateral free shear layers as in non-truncated cylinder wakes (see figure 2.3). In contrast, there has not been yet any clear agreement on the scenario leading to the symmetric hairpin vortex street. From experimental investigations, [121] suggested that both lateral free shear layers join the top one to form a single entity in the near-wake and as the latter becomes unstable, an arch-type vortex is formed and released in the wake. This view is supported by [114] who performed numerical simulations of the flow past a truncated square cylinder with $\gamma = 0.5$ for $Re \leq 2000$ and by experimental flow visualisations by [126] at $Re = 221$. The latter authors also included the tip and base vortices within the arch-vortices released in the wake. [129] simulated the flow past a truncated square cylinder featuring $\gamma = 1$ at $Re = 500$ and claimed that hairpin vortices were originally vortices that detach from the free shear layer stretching from the cylinder free end and then grow into hairpin vortices. Until now though, the generation mechanism of hairpin vortices in the wake of a truncated cylinder has never been the object of any dedicated study so it remains rather unclear.

The respective evolutions of the flow coefficients with Re are roughly similar to those relevant with the non-truncated cylinder wake. We shall yet emphasise that the difference in the mode of

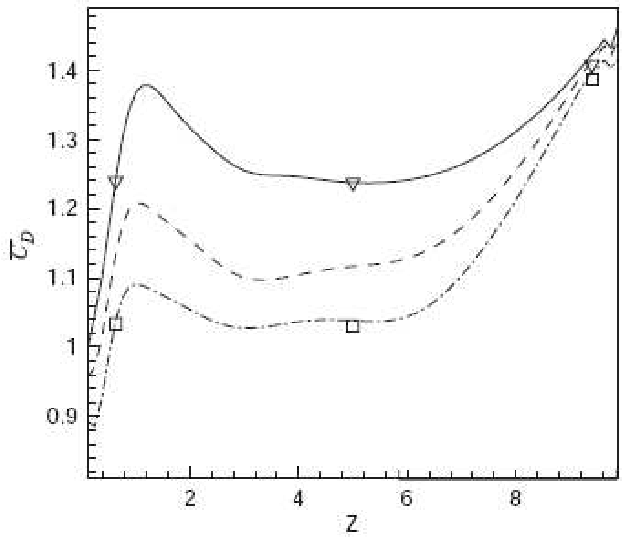

Figure 3.5: Time-averaged total drag coefficient versus spanwise position on the cylinder obtained in the numerical simulations achieved by [118] at $Re = 100, 150$ and 200 from top to bottom curve. Circular cylinder wake. The cylinder bottom (*resp.* top) is located at $z = 0$ (*resp.* $z = 10$)

vortex shedding is reflected by the Strouhal number. Symmetric vortex shedding yields values of St lower than those relevant with the asymmetric one [121]. On the one hand, in the case of the symmetric vortex shedding, experiments [122] performed with a circular cylinder at $\gamma = 3$ reported that St increased in the early stages of the unsteady regime up to $Re \simeq 200$, then decreased slightly and eventually rose again for $Re \geq 300$. On the other hand, in the configuration in which only an asymmetric vortex street is detected at $\gamma = 6$, St monotonically increases for $70 \leq Re \leq 300$ [122].

A further remarkable aspect of the flow coefficients is their variation along the cylinder span at a given Re. Three main regions can be identified: two narrow ones at both cylinder ends and a larger inbetween. For example, figure 3.5 gives the variations of the mean total drag coefficient at $Re = 100, 150, 200$ obtained in the numerical simulations achieved for a truncated circular cylinder with $\gamma = 10$ [118]. One observes that the mean drag coefficient is higher in both end regions where the fluid flows faster, while it is lower and rather constant in the mid-span region of the cylinder where the flow motion is much slower. Also, [118] detected two distinct shedding frequencies at both end regions and only one in the mid-span region at $Re = 100$. Simulations performed at a similar cylinder aspect ratio $\gamma = 10.7$ by [110] also recovered a two-frequency frequency spectrum at $Re = 100$ yielding a primary $St \simeq 0.15$ and a secondary $St \simeq 0.013$, *i.e.* the secondary St was one order of magnitude lower than the primary one.

Chapter 4

MHD cylinder wake

In this chapter, we introduce the features of MHD cylinder wakes in the case where the magnetic Reynolds number is much lower than unity. We consider only studies in which the magnetic field is externally applied, homogeneous, steady and unidirectional. The different configurations under consideration in this section are sketched on figure 4.1.

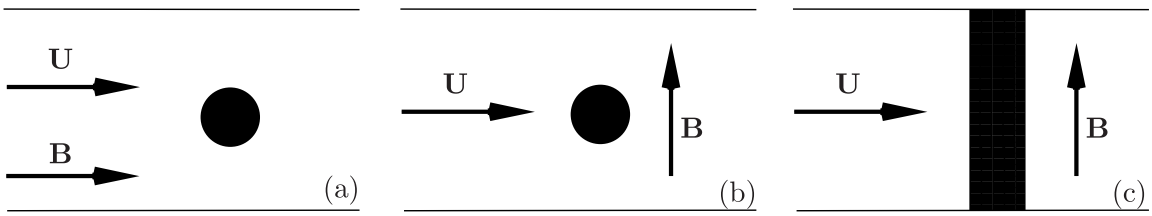

Figure 4.1: Orientation of the magnetic field in MHD cylinder wakes: Streamwise magnetic field (a); Transverse magnetic field (b); Spanwise magnetic field (c).

Configurations where the direction of the magnetic field **B** is along the streamwise direction are considered in [176, 182, 188] (experiments) and [190, 191, 195] (numerics). The magnetic field is oriented along the transverse direction in [183, 193] (experiments) and [191, 192] (numerics). Studies in which the cylinder axis and the magnetic field are parallel are featured in experiments [174, 175, 179, 184, 185, 187, 180] and in numerical computations [189, 194].

The orientation of the magnetic field has a dramatic influence. In all configurations, the magnetic field stabilises the flow, shifts the appearance of flow separation and the transition to unsteadiness to higher critical thresholds and promotes vortices whose axis is aligned with the magnetic field lines. In addition, the location of the Hartmann and Shercliff layers depends on the orientation of **B**.

In cases where **B** is parallel to the free stream and points in the same sense, an effect of the magnetic field is to push the separation point downstream [182, 188] until the latter becomes stagnant and slightly moves upstream for Stuart numbers N higher than 5 [191, 195]. Similarly, the reattachement point is located closer to the cylinder base point and vortex shedding is impeded as the vortices have little room to develop [188, 191, 195]. An important feature is the existence of a 3D steady flow, *i.e.* the transition to unsteadiness which characterises the 2D instability occurs at a higher Re than the transition to three-dimensionality effective when streamwise vortices appear in the flow [190, 191]. Actually, the magnetic field promotes the development of vortices aligned with $\mathbf{B}$ and damps all other vortices. In the cylinder wake, unsteadiness is initiated by transverse undulations of the recirculation regions and three-dimensionality is initiated by the appearance of streamwise vortices. A streamwise magnetic field then shifts the onset of the transverse oscillations at a higher Re and allows the formation of streamwise vortices at a lower Re. Consequently, under the influence of a streamwise magnetic field, the cylinder wake may exhibit 3D steady flow patterns.

The base pressure coefficient C_{pb} has a non-monotonic evolution against N. C_{pb} is maximum at $N = 1.5$ and its subsequent decrease scales with $N^{1/2}$ [182]. The pressure drag coefficient C_{Dp} has opposite variations as C_{pb} with a minimum also at $N = 1.5$ [182]. Numerical investigations featuring a circular cylinder [195] recovered the same trend for C_{Dp} but isolated the minimum value at $N = 0.2$. This study also showed that the magnetic field had little influence on the viscous component of the drag coefficient, although a slight increase in C_{Dv} was observed for $N > 2$. Finally, St monotonically decreases with increasing N for $0 < N < 0.16$.

The configuration where $\mathbf{B}$ is oriented along the transverse direction has been little investigated. The onset of vortex shedding is shifted to higher Re, but smaller than in the case when $\mathbf{B}$ is aligned with the streamwise direction [192].

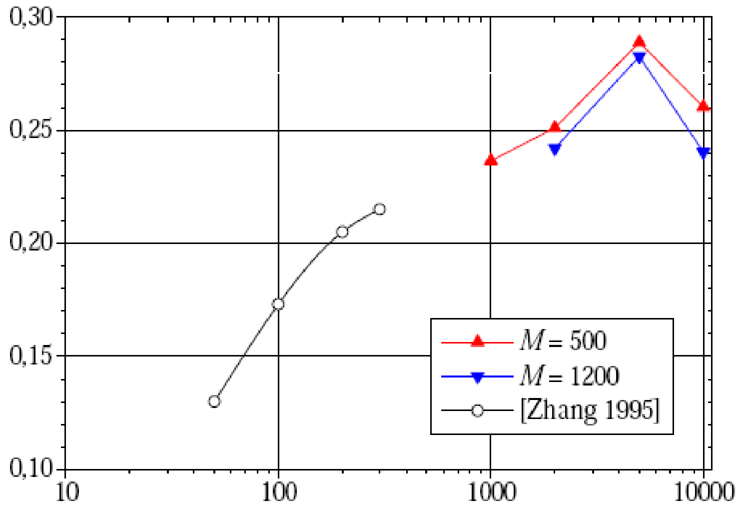

Figure 4.2: MHD circular cylinder wake with a spanwise magnetic field: St versus Re [179]

When the magnetic field is aligned with the cylinder axis, similar stabilising effects of the wake by the magnetic field are observed [174, 176, 180, 189]. The critical Re for the transition to unsteadiness increases following a linear dependency with Ha [175, 180]. In addition, Kármán vortices have a cigar-like shape near the Hartmann walls for $N \geq 2$ [189]. This feature has been theoretically predicted by [157]. The vortex extremities are immersed into the Hartmann layers where the electric current is sucked into the vortex core. A vertical current density pointing outwards the Hartman layer is generated. It depends linearly on the vertical coordinate. This results in a quadratic profile of the velocity field and cigar-like vortex ends. Also, for both high Re and Ha, *i.e.* $Ha > 10^3$ and $Re > 2000$, experiments [180] detected an unsteady flow regime with an irregular Kármán vortex street and secondary vortices appearing at positions outside the rows of Kármán vortices. Moreover the loss of regularity of the Kármán vortex street involves a sudden decrease in St [179] (see figure 4.2). The pressure drag coefficient is constant for N up to about 20 and then decreases in the range $20 < N < 220$ [175].

Part II

Two-dimensional numerical computations

Chapter 5

Numerical set-up in 2D simulations of cylinder wakes

Two-dimensional numerical simulations have been performed both with the commercial software FLUENT/UNS (version 6.2) [199] and the open source code OpenFOAM [205, 206, 210]. Both codes are based on the finite-volume method. An extensive introduction to this numerical method is available in [209]. The general concepts and methods used in numerical computations are introduced in e.g. [198, 207]. We shall however very briefly introduce the finite-volume method in section 5.1.

Cylinder wakes have become a benchmark configuration to assess the performance of a given numerical code. Indeed, the geometrical configuration is very simple, the flow regimes and patterns are well identified, turbulent flows foollow on from laminar flow in a rather narrow *Re* interval and a large amount of data is available in the literature. In section 5.2, we review the influence of the respective components of the numerical set-up used in 2D computations. The PISO scheme designed to address the coupling between the pressure and the velocity fields is described in section 5.3. Section 5.4 is dedicated to the implementation of the SM82 model into the numerical code. The consequences of the choice of a segregated or a coupled solver are shown in a simple example in section 5.5. Finally we present the perturbation method required to make sure the numerical code recovers the critical threshold of the transition to unsteadiness in section 5.6.

5.1 Introduction to the finite-volume method

The finite-volume method is one of the most popular methods in Computational Fluid Dynamics (CFD). A mesh is designed to decompose the fluid domain into a set of adjacent control volumes or cells. The flow equations are applied to each cell and averaged over its volume. To this end, the finite-volume method uses the integral formulation of the conservation equations. For example, the

Navier-Stokes equations are written under the following non-dimensional integral formulation:

$$\int_V \left[\frac{\partial \mathbf{u}}{\partial t} + \nabla \cdot (\mathbf{u}\mathbf{u})\right] dV = \int_V \left[\nabla p + \frac{1}{Re}\nabla^2 \mathbf{u}\right] dV \tag{5.1}$$

$$\int_V (\nabla \cdot \mathbf{u}) dV = 0 \tag{5.2}$$

where the fluid is considered as incompressible and V denotes the volume of a given mesh cell.

These equations are then simplified using the Gauss' theorem and volume integrals can then be transposed into surface integrals over the volume surface on the form of:

$$\int_V \nabla \star \vartheta dV = \oint_{\partial V} d\mathbf{S} \star \vartheta \tag{5.3}$$

where ∂V denotes the surface of a given cell of volume V, $\star$ stands for any tensor operation and ϑ denotes any tensor field.

Under the finite volume method, each term of the flow equation is then reformulated using Gauss' theorem. For example, the mass conservation (5.2) is reformulated as:

$$\int_V (\nabla \cdot \mathbf{u}) dV = \oint_{\partial V} \mathbf{u} \cdot d\mathbf{S} = \sum_{faces} \mathbf{u}^f \cdot \mathbf{S}^f \tag{5.4}$$

where the f superscript indicates quantities taken at the cell faces. The mass conservation is then written as the discrete sum of the velocity fluxes over the cell faces.

This example shows that the finite volume formulation requires the definition of where the variable is located in the cells. According to the arrangement of the variable in the control volumes, interpolation schemes may be required to implement Gauss' theorem.

Using Gauss' theorem for each term when possible, the flow equations are finally expressed as equations involving volume, surface and contour integrals. The final step is then to linearise the latter integrals when necessary. To this end, one uses discretization schemes in time for time derivative terms and in space for spatial derivative terms (see e.g. [198, 199, 205] for an exhaustive list of existing discretization schemes). The order of accuracy of the numerical simulations depends on those of both the discretization and interpolation schemes. Mesh skewness may also require a special care as it may greatly deteriorate the order of accuracy of the whole simulation [202].

5.2 Influence of the 2D numerical set-up

The first computations of the flow past a circular cylinder were performed by hand by Thom [79] in the late 1920's and later by Kawaguti [51]. For information, it took a year and a half to Kawaguti to compute the flow at $Re = 40$. Early 2D simulations were limited due to low resolution, convergence problems and small domain size [42]. As computers have gained in performance and reliability, numerical techniques have become more sophisticated and numerical set-ups more realistic. Cylinder wakes were simulated with the lattice-Boltzmann method in [76, 118], finite element method in [22, 23, 25, 35, 40, 41, 48, 60, 73, 78, 95], finite difference or volume method in [31, 36, 98, 39, 42, 49, 54, 56, 59, 63, 65, 101, 72, 107, 94] and spectral methods [47, 50, 66, 81] to mention the most common numerical techniques.

In the finite volume method, the flow equations can be written in a formulation involving the vorticity field and the kinematic stream function as variables. In this case, polar meshes are used, but special care is required for the outer boundary since it characterises both the inflow and outflow boundaries. In particular, the distance at which the outer boundary is located strongly influences the reliability of the results. Oseen's approximation can be used at this boundary. This technique consists in neglecting inertial terms in regions where their order of magnitude is comparable to that of the viscous terms. The Navier-Stokes equations are then modified to account for this approximation and an expression as a series can be derived for both the stream function and the vorticity at a large distance from the cylinder axis [14]. As long as the flow remains steady, this technique provides results in reasonable agreement with experimental data [17, 39]. For unsteady flows, the equations derived with Oseen's approximation may be modified by the addition of a small linear periodic disturbance on the free stream velocity. In addition, the definition of the boundary condition for the vorticity field on a solid surface remains challenging. For this reason, most of the finite volume based codes solve the Navier-Stokes equations in a formulation involving the velocity and the pressure as variables and a rectangular mesh for which all the boundaries are well identified.

If the fluid domain is assumed unbounded, special care must be dedicated to the respective locations of the boundary. The ratio of the cylinder diameter to the distance between the lateral boundaries defines a numerical blockage ratio, which has a similar influence on the flow as in the case where physical walls confine the flow [23] (see also chapter 2.4). With a numerical blockage ratio smaller than 1/16, lateral boundaries have little effect on the flow [25, 53]. At the inlet of a channel or a duct, the flow may be considered as fully established and one can map the velocity field at the inlet either by giving an analytical expression if any or by imposing a velocity profile extracted from preliminary numerical computations. The distance of the inlet boundary to the cylinder must only be determined so as to not influence the local acceleration of the fluid in the vicinity of the cylinder. Usually it is located at a distance of about $10d$ upstream the cylinder axis [106].

A more sensitive point is the location of the outflow boundary. Two main kinds of boundary conditions are used at the outlet in finite-volume: either a zero normal gradient boundary condition is applied which is easy to implement, or a convective boundary condition which is a bit more sophisticated. Far away from the cylinder, one may consider that the perturbations have vanished and the flow is back to streamwise invariance. This is modelled by a homogeneous Neumann condition for the velocity:

$$\partial_n \mathbf{u}|_{outlet} = 0 \tag{5.5}$$

where $\partial_n * = (\nabla *) \cdot \mathbf{n}_w$. The convective boundary condition reads:

$$\partial_t \mathbf{u}|_{outlet} + U_c \, \partial_n \mathbf{u}|_{outlet} = 0 \tag{5.6}$$

where $\partial_t *$ is the time derivative and U_c is a constant velocity, usually defined as the mean streamwise velocity.

Only the latter condition prevents pressure waves from being reflected on the outflow boundary, while it eases the convection of flow structures through the outlet. Consequently, the convective boundary condition can be located closer from the cylinder than the other one with little influence on the flow [21, 46, 106]. In case the reflective boundary condition is applied, its pernicious effects can be smoothed by inserting a buffer region before the outlet. This technique consists of significantly relaxing the mesh in a small section upstream the outlet to artificially enhance the damping of flow structures through numerical diffusion before they reach the outlet [49]. When the reflective boundary is used, it shall be located at least at 15 diameters from the cylinder [78]. A detailed comparison of both boundary conditions is available in e.g. [21, 106].

The boundary conditions for the pressure are derived from the combination of the pressure equation and the boundary conditions for the velocity. For duct and channel flows, it results in a homogeneous Neumann boundary condition imposed at all the boundaries [189]. However this configuration induces some numerical difficulties, as the problem for the pressure field in a rectangular computational domain is defined as completely symmetric. To alleviate this difficulty, one takes advantage of the fact that the pressure field in duct and channel flows is greatly determined from the streamwise pressure gradient. It is therefore usual to fix the value of the pressure at the duct or channel outlet to an arbitrary value, for example zero:

$$p|_{outlet} = 0 \tag{5.7}$$

The implementation of this boundary condition at the outlet induces however some slight flow distortion, as vortices leaving the fluid domain generate a non-uniform pressure distribution.

To minimise the flow distortion due to the implementation of condition (5.7), one may impose the mean value of the pressure across the outlet. Assuming that the outlet boundary is normal to the x-axis, one defines the pressure at the outlet as:

$$p(y, z)|_{outlet} = \bar{P} - \langle p \rangle_{outlet} + p^c(y, z) \tag{5.8}$$

where $\bar{P}$ is the imposed arbitrary mean value of the pressure across the outlet, p^c is the local value of the pressure in the cell located next to the outlet and $\langle p \rangle_{outlet} = \frac{1}{S_{outlet}} \int_{S_{outlet}} p^c(y^\star, z^\star) dS$ (S_{outlet} denotes the surface of the outlet boundary). Using condition (5.8) results in a smoothing of the pressure variations over the outlet boundary and therefore minimise flow distortion.

5.3 Pressure-velocity coupling scheme PISO

5.3.1 Scope of the scheme

The flow equations can be solved either with a coupled solver which solves all the equations at the same time or with a segregated one in which the equations are treated one after the other. A segregated solver is less demanding in CPU power and shall be used in the present numerical code. Nevertheless, as the flow equations are solved one after the other, a numerical scheme is included in the code to account for the coupling between the flow quantities.

In the finite-volume method, the most widespread pressure-velocity schemes are the SIMPLE algorithm proposed by [196] and the Pressure-Implicit with Splitting of Operators (PISO) algorithm introduced by [201]. Many variants of these schemes were elaborated afterwards [198, 207]. In the present thesis, we only use a variant of PISO which we shall describe now.

The flow equations are written under their integral formulation on a collocated mesh (see section 7.1.2 for a description of the possible mesh arrangements). In this arrangement, the flow variables are all located at the centroid of the control volume, but the velocity is not used directly into PISO.

PISO is an iterative scheme, whose each step is decomposed into a predictor step followed by a series of pressure solutions and explicit velocity corrections. In the predictor step, the momentum equation is linearised and used to derive a guess velocity u^{m*} using the pressure from the previous time step. u^{m*} does not satisfy the mass conservation and must be corrected. To this end, the fluxes of velocity are computed from u^{m*} and introduced into the mass equation. This results in an equation linking the pressure and the fluxes of velocity, from which the pressure can be calculated. The pressure is then used to correct both the velocity and its fluxes in an explicit way, which in turn are used to update the pressure equation. This initiates an iterative procedure which runs until the tolerance fixed beforehand for the respective flow variables is reached. We shall see in the next section that the numerical implementation of the SM82 model does not affect this pressure-coupling algorithm.

5.3.2 Pressure equation and PISO steps

We now describe in more detail the successive PISO steps in the non-MHD case. The flow equations are the Navier-Stokes equation:

$$\partial_t \mathbf{u} + \nabla \cdot (\mathbf{u}\mathbf{u}) + \nabla p = (1/Re)\nabla^2 \mathbf{u} \tag{5.9}$$

$$\nabla \cdot \mathbf{u} = 0 \tag{5.10}$$

The second term on the left-hand side of (5.9) is the convection term, which has been written under its divergence form [204] using (5.10).

Time and space discretization schemes are chosen and applied for each term of equations and integrated over the cell volumes using the Gauss' theorem. We denote `T`, `D` and `C` the time, diffusion and convective discretisation schemes, respectively. Equation (5.9) then reads:

$$\mathtt{T}(\mathbf{u}) = \frac{1}{Re}\mathtt{D}(\mathbf{u}) - \mathtt{C}(\mathbf{u}) - \nabla p \tag{5.11}$$

It follows then from this equation that the velocity at the centre of mesh cell M can then be written as a combinaison of the velocities at the neighbour cells N, the pressure term and a source term $\mathbf{Q}_M$ including here the velocities at the two previous time steps as we implement a backwards quadratic time scheme. Equation (5.9) is therefore expressed under the following formulation [198, 202]:

$$A_M \mathbf{u}_M^c = -\sum_N A_N \mathbf{u}_N^c + \mathbf{Q}_M^c - (\nabla p)_M^c \tag{5.12}$$

where A_M and A_N are the coefficients obtained from the time- and space-discretization of the velocities $\mathbf{u}_M$ and $\mathbf{u}_N$, respectively, and the superscript c indicates quantities taken at the cell centre. This formulation is a semi-discretized formulation as the pressure gradient term is not discretized [208] and all terms are actually divided through by the cell volume. Similarly, (5.10) can be written as:

$$\sum_{faces} \mathbf{u}_M^f \cdot \mathbf{S}^f = 0 \tag{5.13}$$

where the superscript f indicates quantities taken at the cell face.

At a given time step, the PISO algorithm reads:

1. Estimate the velocity from (5.12) taking the value of the pressure from the previous time step $(m-1)$;

   $$(\hat{\mathbf{u}}_M^c)_q = \frac{1}{A_M}\left[-\sum_N A_N (\hat{\mathbf{u}}_N^c)_q + (\mathbf{Q}_M^c)_q - (\nabla p)_{m-1}^c\right] \tag{5.14}$$

   where the subscript q indicates the value of the quantities obtained at the current PISO step.

2. Calculate the velocity $(\hat{\mathbf{u}}_M^f)_q$ at the cell faces from the interpolation at the faces of each term on the right hand side of (5.14);

3. Assemble the Poisson equation for the pressure using (5.13) and $(\hat{\mathbf{u}}_M^f)_q$ obtained at step 2;

$$\sum_{faces} \frac{1}{A_M}(\nabla p)_q^f \cdot \mathbf{S}^f = \sum_{faces} (\hat{\mathbf{u}}_M^f)_q \cdot \mathbf{S}^f \tag{5.15}$$

4. Solve equation (5.15) to obtain the pressure at current PISO step q;

5. Correct both the fluxes of velocity and the velocity with the pressure term;

$$(\mathbf{u}_M^f)_{q+1} \cdot \mathbf{S}^f = (\hat{\mathbf{u}}_M^f)_q \cdot \mathbf{S}^f - \frac{1}{A_M}(\nabla p)_q^f \cdot \mathbf{S}^f \tag{5.16}$$

$$(\mathbf{u}_M^c)_{q+1} = (\hat{\mathbf{u}}_M^c)_q - \frac{1}{A_M}(\nabla p)_q^c \tag{5.17}$$

The satisfaction of equation (5.15) ensures that the fluxes of velocity are conservative.

6. Use corrected velocity in equation (5.14) and iterate over steps (2) to (5) until tolerance reached;

$$(\mathbf{u}_M^f)_{m+1} \cdot \mathbf{S}^f = (\mathbf{u}_M^f)_{q+1} \cdot \mathbf{S}^f \tag{5.18}$$

$$(\mathbf{u}_M^c)_{m+1} = (\mathbf{u}_M^c)_{q+1} \tag{5.19}$$

$$p_{m+1}^c = p_{q+1}^c \tag{5.20}$$

5.4 Numerical implementation of the SM82 model

In the SM82 model, the flow is governed by equations (1.43) and (1.48). In the present thesis, there is no current injection at the Hartmann walls so that the forcing velocity $\mathbf{u}_f$ is uniformly zero. We furthermore consider configurations which feature 2 Hartmann walls only. The implementation of the SM82 model only involves the addition of the linear term $[-(2/Ha)\bar{\mathbf{u}}_\perp]$ in the momentum equation. This term is expressed implicitly, *i.e.* at the current time on which the iterations of the PISO algorithm are achieved [1, 159]. The additional term only modifies the coefficient A_M in (5.12) and consequently does not affect the PISO algorithm.

5.5 Influence of the choice of the solver

A segregated solver treats the flow equations one after the other. It has been stressed in [42] that the use of such a solver introduces an artificial numerical damping between the flow equations, which may eventually undermine the stability properties of the numerical code and shift the transition between two flow regimes to a higher value for Re. In contrast, a coupled solver treats all the flow equations at the same time and does not induce such a numerical damping. It comes with a higher CPU cost yet, since the matrix to be inverted is more complex and requires a numerical method involving more inner iterations at a given time step (see e.g. [199]). To assess the influence of the solver on the 2D simulations achieved with FLUENT/UNS, we have built a set of 2D meshes for the configuration with a blockage ratio $\beta = 0.25$ (see configuration sketched on figure 2.8). The main characteristics of these meshes are gathered in table 5.1.

Meshes	G1	G2	G3	G4	G5	G6
Number of nodes along the cylinder circumference	72	144	216	288	360	432
Total number of nodes	1.0×10^4	2.6×10^4	5.0×10^4	7.5×10^4	1.0×10^5	1.2×10^5

Table 5.1: Main characteristics of the different meshes used to assess the influence of the choice of the solver. The related configuration is the confined circular cylinder wake with a blockage ratio $\beta = 0.25$.

Figure 5.1 shows the critical Re for the appearance of the steady recirculation regions obtained with a segregated and a coupled solver when increasing the number of mesh nodes. The critical Re remains stable and in excellent agreement with [35] when refining the mesh and using a coupled solver, while it departs from the reference value of [35] when refining the mesh and using a segregated solver. This indicates that the artificial numerical damping introduced by the segregated solver becomes more significant when the grid is refined. The best choice would have then been to achieve the whole study using the coupled solver only. However, the CPU cost involved is too expensive if one intends to make a parametric investigation on both Re and Ha. We have therefore run our simulations using a segregated solver.

5.6 Perturbation method

The over-stabilisation of the flow can also be noticed in the vicinity of the transition to unsteadiness. The onset of vortex shedding corresponds to the transition between a symmetric and an asymmetric wake. While any experimental set-up introduces small perturbations in the flow due to e.g. surface roughness of the walls, inlet velocity slightly 3D, confining walls not perfectly parallel [31], the disturbances of the numerical set-up are mainly restricted to numerical truncation and round-off errors. In addition, the symmetry of the flow is favoured in numerical simulations by the symmetric disposition and definition of the boundary conditions. As a result, numerical computations tend to naturally yield a critical Re for the transition to unsteadiness at a much higher Re than that obtained in experimental campaigns. This feature is illustrated on figure 5.2, which reports the length of the steady recirculation regions with increasing Re obtained in simulations performed with a segregated and a coupled solver. Whereas the expected linear increase in L_b with Re is recovered with the use of a

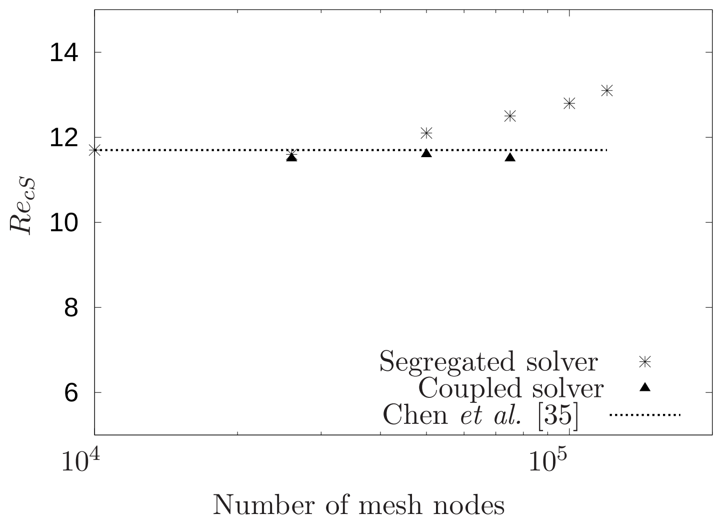

Figure 5.1: Non-MHD confined cylinder wake at $\beta = 0.25$: Critical Re for the appearance of the steady recirculation regions obtained with a segregated and a coupled solver. Calculations with the coupled solver have been performed with meshes G2, G3 and G4 only. The value for Chen [35] is obtained after interpolating the authors' data. Simulations achieved with FLUENT/UNS.

coupled solver, in the computations performed with the segregated solver, the linear increase in L_b is no longer recovered, but L_b saturates as Re gets closer of the critical threshold for the onset of vortex shedding. However whereas the use of a segregated or a coupled solver has a significant influence on the L_b-curve, its influence on the evolution of the base pressure coefficient with Re is very weak (see figure 5.2 right). This indicates that the growth of the recirculation is a very sensitive aspect of the flow dynamics.

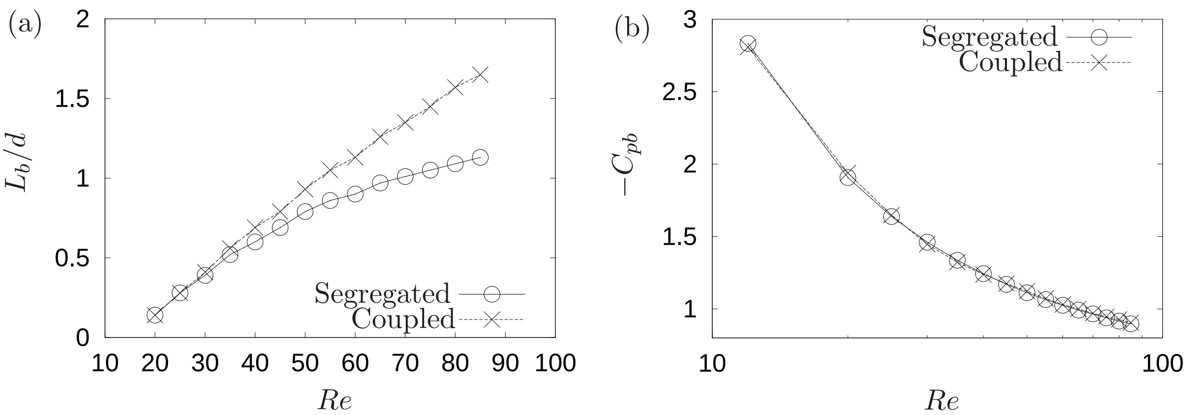

Figure 5.2: Non-MHD confined circular cylinder wake at $\beta = 0.2$: (a) length of the steady recirculation regions L_b and (b) base pressure coefficient C_{pb} versus Re obtained from simulations run with a segregated and a coupled solver. Simulations achieved with FLUENT/UNS.

In the case of the unbounded circular cylinder wake, numerical simulations performed by [31] at $Re = 10^3$ captured unsteady flow pattern at the beginning of the simulation and as the simulation time increases, only unsteadiness vanishes and only steady flow pattern can be identified in the flow. As the perturbations of the experimental set-up are hard to identify, no model can be used to reproduce them in the numerical set-up. A numerical technique consists then in adding a vorticity-like perturbation in the flow to initiate the vortex shedding in the cylinder wake. Several techniques are available in the literature. [22] introduces a small vorticity-like perturbation to the whole velocity field at the start of the simulation. The most wide-spread, efficient and easy-to-implement technique consists in rotating the cylinder about its own axis for a short while at the start of the simulation (see e.g [31, 35]). The perturbation method used by [31] has been used in our simulations, as its use has provided a critical Re for the onset of vortex shedding in agreement with existing data within the shortest establishment time. This method is described in the following equation:

$$u_\theta^{cyl} = \begin{cases} -0.14U_0 & \text{if } \; 2.8t_u < t < 4.3t_u, \\ +0.1U_0 & \text{if } \; 4.5t_u < t < 6t_u, \\ 0 & \text{otherwise.} \end{cases} \tag{5.21}$$

where u_θ^{cyl} is the tangential velocity of the cylinder surface and t_u the turnover time.

Chapter 6

Quasi-two dimensional circular cylinder wake in a square duct

In this chapter, we are concerned only with the 2D simulations of the MHD circular cylinder wake confined between two parallel walls achieved with FLUENT/UNS. We describe the different steps in the construction of the numerical set-up. The non-MHD 2D flow past a confined circular cylinder is used as a benchmark to test the components of the numerical set-up. The MHD performances of the present code are compared to the experiments of [174, 179, 180]. The results of this part have been published in [1] which is available in appendix. We shall thus focus on the results. Details of the methods and procedures used to obtain them are provided in [1].

6.1 Numerical set-up

6.1.1 Configuration and flow equations

We assume that both Hartmann and Stuart numbers are much bigger than unity so that the flow dynamics can be well modelled by the SM82 model. The geometrical configuration is presented on figure 6.1. It corresponds to the experimental set-up of [174]. We consider a flow of the electrically conducting, incompressible eutectic alloy GaInSn (density $\rho = 6360$ kg.m^{-3}, kinematic viscosity $\nu = 3.4 \times 10^{-7}$ m^2.s^{-1}, electrical conductivity $\sigma = 3.46 \times 10^6$ Ω^{-1}.m^{-1}). The duct walls and the cylinder are assumed to be electrically insulating. The cylinder of diameter $d = 0.01$m is at the centre of the duct and its axis is parallel to the side walls (z-axis) and orthogonal to the streamwise direction (x-axis). The duct has a square-cross section of width equal to 0.04m which yields a blockage ratio of $\beta = 0.25$. A steady homogeneous externally applied magnetic field $\mathbf{B}$ with intensities between 0 and 1.35 Tesla is imposed along the cylinder axis.

Using the cylinder diameter d as typical length, the flow equations (1.43) and (1.46) are now

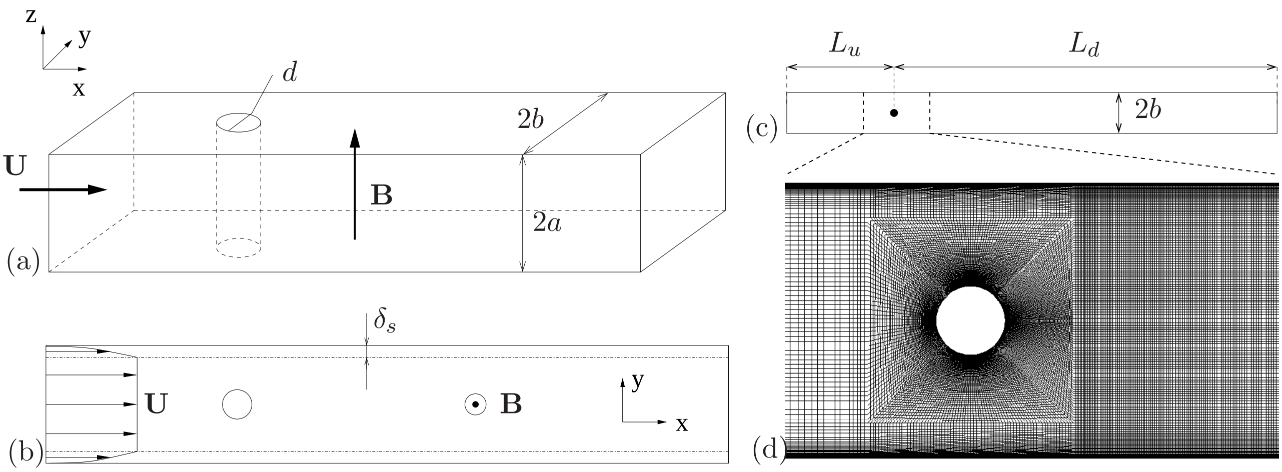

Figure 6.1: Geometrical configuration of the quasi-2D study (a). 2D equivalent problem in the average plane to which equations (6.1) and (6.2) apply (b). Computational domain (c). Detail of the mesh around the cylinder between the dash-lines indicated on the computational domain (d).

written as:

$$\nabla_\perp \cdot \mathbf{u}_\perp = 0 \tag{6.1}$$

$$\frac{\partial \mathbf{u}_\perp}{\partial t} + (\mathbf{u}_\perp \cdot \nabla_\perp)\mathbf{u}_\perp + \nabla_\perp p = \frac{1}{Re_d}\nabla_\perp^2 \mathbf{u}_\perp - 2\frac{d^2}{a^2}\frac{Ha}{Re_d}\mathbf{u}_\perp \tag{6.2}$$

where $\mathbf{u}_\perp$ is the velocity component normal to the magnetic field and averaged between both Hartmann walls located at $z = \pm a/d$, $Re_d = U_0 d/\nu$ and $Ha = aB_0\sqrt{\sigma/(\rho\nu)}$ (U_0 is the maximum velocity at the inlet).

6.1.2 Mesh

The computational domain is sketched in figure 6.1(c). The mesh is composed of a polar mesh embedded in a square of dimensions $3d \times 3d$ centred on the cylinder axis and a rectangular Cartesian mesh covering the resting computational domain. A detail of this mesh is shown on figure 6.1(d). The origin of the coordinate system is taken on the cylinder axis. The cylinder circumference ∂C is defined by the equation $x^2 + y^2 = 1/4$. The side walls confining the flow are located at $y = \pm b/d$.

Following the recommendations of [78], the inlet and outlet boundaries are located at $x = L_u/d = 12$ and $x = L_d/d = 42$, respectively. The distance $2b$ between the confining walls is deduced from the blockage ratio $2b = d/\beta$. We shall retain the configuration in which $\beta = 0.25$ since it corresponds to that of the experimental set-up of [174]. Few works in the literature considering a blockage ratio $\beta = 0.25$ are however available. We have therefore proceeded to the validation of the numerical model also with a configuration featuring $\beta = 0.2$.

6.1.3 Boundary conditions

A zero normal gradient is imposed on the pressure at all the mesh boundaries:

$$\partial_n p = 0 \quad \text{at} \quad \begin{cases} y = \pm b/d, \forall x; \\ x = -L_u/d, \forall y; \\ x = L_d/d, \forall y. \end{cases} \tag{6.3}$$

No-slip boundary condition (1.22) is applied at the side walls and cylinder surface:

$$\mathbf{u}_\perp(x, \pm b/d) = \mathbf{0} \tag{6.4}$$

$$\mathbf{u}_\perp|_{\partial C} = \mathbf{0} \tag{6.5}$$

At the inlet, we impose an analytical velocity profile obtained from the conservation of momentum when considering a steady velocity field. The velocity profile imposed at the inlet is subsequently $\mathbf{u}_\perp(-L_u/d, y) = U(-L_u/d, y)\mathbf{e}_x$ with:

$$U(-L_u/d, y) = \begin{cases} 1 - (yd/b)^2 & \text{for non-MHD computations,} \\ \frac{\cosh(yd\sqrt{2Ha}/a) - \cosh(b\sqrt{2Ha}/2a)}{1 - \cosh(b\sqrt{2Ha}/2a)} & \text{for MHD computations.} \end{cases} \tag{6.6}$$

The outlet boundary condition is designed so that the outflow is back to streamwise invariance. This is obtained with a homogeneous Neumann condition (5.5) imposed at $x = L_d/d$.

6.2 Non-MHD validation tests

The validation tests aim to tune the different aspects of the numerical set-up. The quality of the mesh is checked, the influence of the boundary conditions is assessed and the stability property of the numerical method is established. As the MHD flow configuration has been little investigated in the literature, we first achieve non-MHD simulations of the confined cylinder wake. This step also gives an important insight in the flow dynamics when no magnetic field is present. We will then refer to these non-MHD features when looking in detail at the MHD cylinder wake.

6.2.1 Influence of the mesh: simulation at $Re_d = 100$

A set of meshes is built whose characteristics are given in table 6.1. For each mesh, we have performed a simulation at $Re_d = 100$ over a long simulation time equal to $120t_u$ where t_u is the turnover time defined as:

$$t_u = d/U_0 \tag{6.7}$$

Meshes	M1	M2	M3	M4	M5
Number of nodes along the cylinder circumference	120	180	260	300	360
Number of nodes in the Shercliff layers at $Ha = 1080$	7	10	15	16	20
Number of points along the radius of the embedded polar mesh	32	56	72	80	96
Total number of nodes	2×10^4	4×10^4	7×10^4	1×10^5	1.3×10^5
$\epsilon_{st} = \|1 - St(Mi)/St(M5)\|$	3.6×10^{-2}	1.3×10^{-2}	2.6×10^{-3}	2.6×10^{-3}	/
$\epsilon_{cd} = \|1 - C_D(Mi)/C_D(M5)\|$	5.5×10^{-3}	9.1×10^{-4}	2.8×10^{-4}	2.1×10^{-4}	/

Table 6.1: Main characteristics of the different meshes and errors in drag coefficient C_D and Strouhal number St relative to M5 mesh at $Re_d = 100$. One sees that even for the highest value of Ha, M4 insures a high enough resolution in the Shercliff layers.

The perturbation method (5.21) has been used in each simulation. The respective Strouhal number St and the total drag coefficient C_D have been systematically calculated and compared to those from M5 mesh. The related errors in St and C_D, respectively defined by ϵ_{st} and ϵ_{cd}, are given in table 6.1. We have found that both ϵ_{st} and ϵ_{cd} decrease as the mesh is refined, which shows good convergence. In order to save CPU time and keep a reasonable accuracy in our computations, we shall perform both MHD and non-MHD simulations with the M4 mesh.

6.2.2 Critical Re at the onset of vortex shedding

The transition to unsteadiness has been tracked by gradually increasing Re_d by small steps. The initial conditions for the very first simulation corresponds to a fluid at rest. Then once a fully established state is reached by the flow, it is used as initial conditions for the following simulations. The critical threshold for the transition to unsteadiness in a flow configuration with a blockage ratio $\beta = 0.25$ was obtained in [35]. In the vicinity of this critical threshold, the perturbation method (5.21) is implemented in the numerical model. We have found a critical Re_d for the onset of vortex shedding in very good agreement with [35] as can be seen on figure 6.2. This proves that the stability properties of the present numerical model are very satisfactory.

6.2.3 Total drag coefficient and Strouhal number versus Re_d

[59] have carried a parametric study over both β and Re_d of the confined circular cylinder wake for $0 \leq \beta \leq 0.4$ and Re_d up to 500. In particular, they provide the respective evolutions of the total drag coefficient C_D and Strouhal number St with Re_d for each value of β. We have compared the curves that they obtained with $\beta = 0.2, 0.3$ with the ones which we have computed with $\beta = 0.25$. On this comparison shown on figure 6.3, our respective curves for C_D and St are located between the respective curves obtained with $\beta = 0.2$ and $\beta = 0.3$. Both the shape of the curves and the values

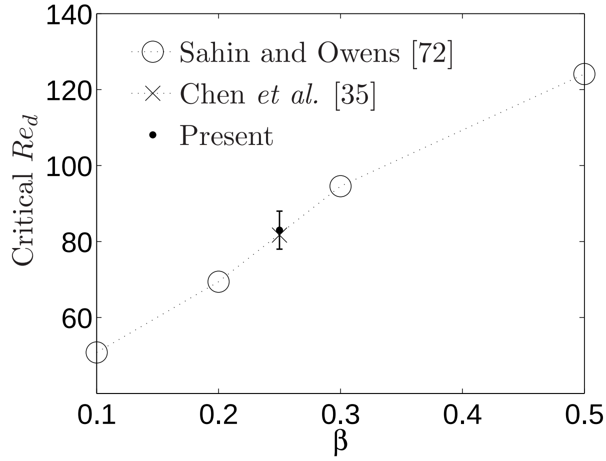

Figure 6.2: Critical Re_d for the onset of the unsteady flow regime versus the blockage ratio β. Our critical Re_d is located in the Re_d interval represented by the bar: the lower (*resp.* upper) extremity is the last (*resp.* first) simulation in the steady (*resp.* unsteady) regime.

computed for St and C_D are in excellent agreement with the existing data.

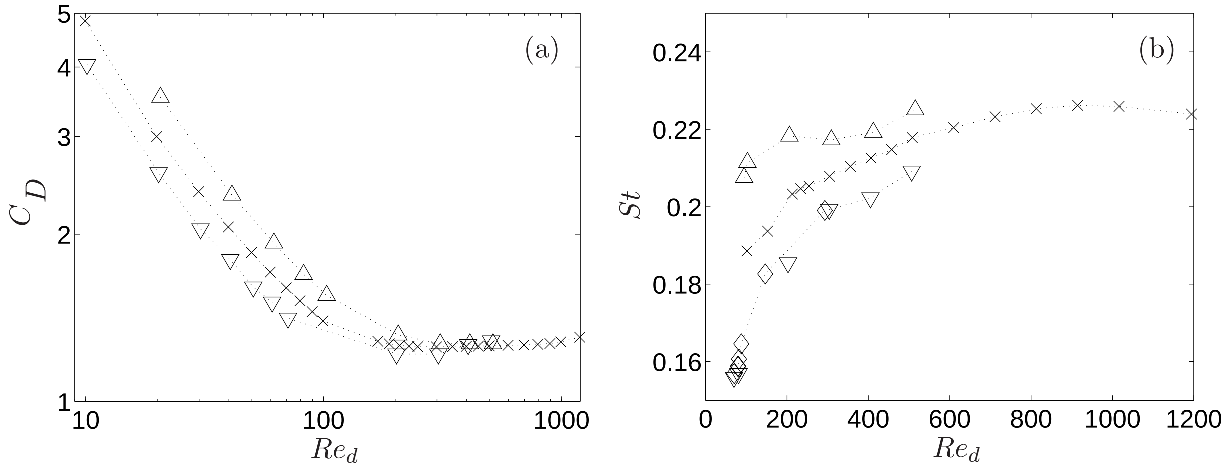

Figure 6.3: Comparative evolutions of (a) C_D and (b) St versus Re_d. $\times$ Present ($\beta = 0.25$). $\diamond$ Simulations [95] ($\beta = 0.2$). ∇ Simulations [59] ($\beta = 0.2$). Δ Simulations [59] ($\beta = 0.3$).

6.3 MHD validation test

At this stage, we have ensured that the present numerical model recovers the flow patterns of both steady and unsteady regimes in the non-MHD case. The respective critical Re_d for the appearance of the steady recirculation regions and the onset of vortex shedding are accurately predicted and the curves of global flow coefficients match well with existing data. We shall now make sure that the present numerical model is also reliable in the MHD case. To this end, we have considered the experimental set-up of [180] at $Re_d = 5000$ and $Ha = 1200$. In this configuration, the authors observed a regular Kármán vortex street in the cylinder wake. In this case, both Ha and N are much bigger than unity, so that the SM82 flow model is well adapted to capture the flow dynamics. We have simulated this flow using equations (6.1) and (6.2) using both the present numerical code and OpenFOAM. The same boundary and initial conditions have been implemented in both numerical packages and the computations have been achieved over the same simulation time. As a result, both codes yield the regular Kármán vortex street observed by [180]. We have obtained a Strouhal number equal to 0.2595 (*resp.* 0.2582) in the simulation performed with the present numerical model (*resp.* OpenFOAM). Both values compare well and the agreement with the experimental $St \simeq 0.28$ is reasonable. The discrepancy between the numerical and the experimental values reflects the unavoidable imperfections between the numerical and the experimental systems. Consequently, the present numerical model is able to reproduce the MHD flow past a circular cylinder even for both high Ha and Re_d, up to respective values of the order of 5×10^3.

6.4 Stability diagram

6.4.1 Flow regimes

We have performed a parametric study over both Re_d and Ha. Simulations have been achieved for a magnetic field with intensities $B = 0, 0.2, 0.4, 0.7, 1.0, 1.35$ Tesla which corresponds to $Ha = 0, 160, 320, 560, 800, 1080$ respectively, and for Re_d up to 6000. At a given Ha, when one gradually increases Re_d, four flow regimes can be identified resulting in the stability diagram given on figure 6.4. The three first regimes are well-known, as they correspond to the initial non-MHD flow regimes, *i.e* the creeping flow regime **I**, the regime of the steady recirculation regions **II** and the laminar periodic flow regime with the regular Kármán vortex street **III**. We denote Re_1^c and Re_2^c the respective critical Re_d for the appearance of regimes **II** and **III** respectively. For Re_d higher than a third critical threshold, denoted Re_3^c, the Kármán vortex street becomes irregular.

The regime **IV** is specific to confined cylinder wakes, in which the boundary layers at the side walls are likely to separate and generate vortex shedding [59, 67, 72]. As seen on figure 6.5, the Kármán vortices are still initiated by the rolling-up of the free shear layers as in regime **III**, but in the cylinder wake, between these vortices and the side wall layers, secondary counter-rotating vortices are generated by separation of the Shercliff layer at the side walls, shed, and eventually flow downstream. These vortices either cross the wake obliquely and interact strongly with the adjacent Kármán vortices or are quickly dissipated as soon as they detach from the Shercliff layer.

The oblique trajectory of the secondary vortices results from the combined action of the free stream that takes them away downstream and of the Kármán vortices at the origin of their formation, that thrust them towards the opposite side wall [see vortices S1 and Kc on figure 6.5(a)]. As a first consequence, the Kármán vortices dissipate a large amount of energy during the formation of the

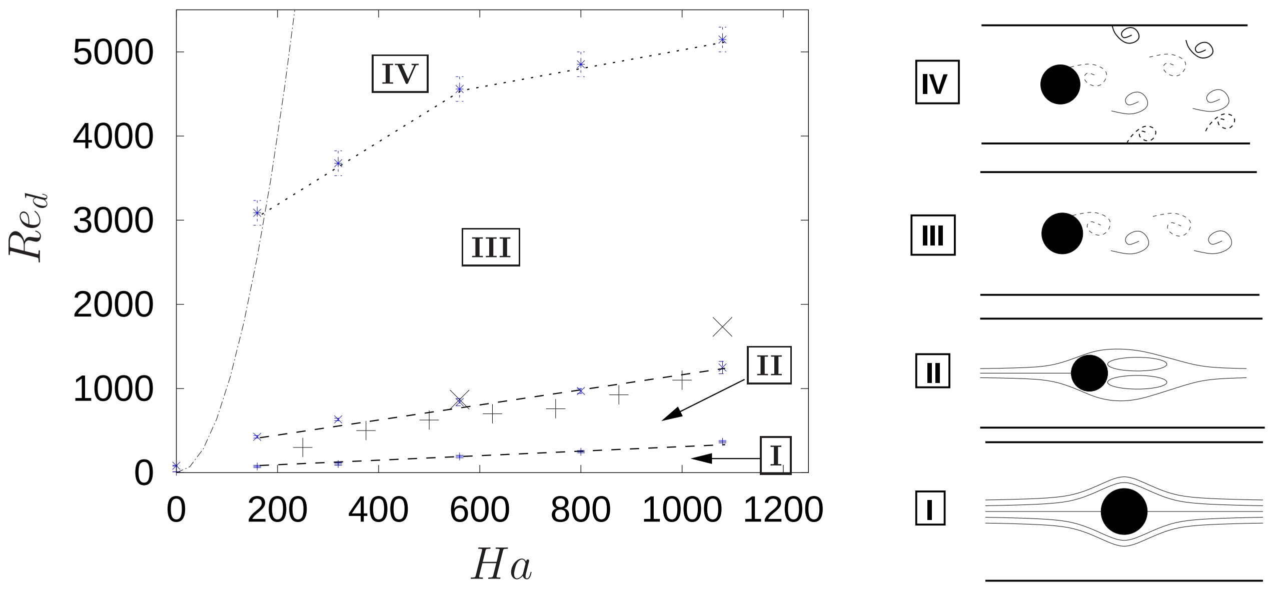

Figure 6.4: Stability diagram: sector **I** is the creeping flow regime, sector **II** the flow regime of the steady symmetric attached recirculation regions, sector **III** the laminar periodic flow regime with the regular Kármán vortex street and sector **IV** the flow regime where secondary vortices are released from the side walls. $Re_1^c < Re_2^c < Re_3^c$ are the successive critical thresholds between the flow regimes. At a given Ha, each of them is located in a Re_d interval represented by a bar: the lower (*resp.* upper) extremity is the last (*resp.* first) simulation in the subcritical (*resp.* supercritical) regime. The dashed lines are the respective linear regressions of Re_1^c and Re_2^c against Ha. $\times$ Experimental Re_2^c from [174] ($\beta = 0.25$). $+$ Experimental Re_2^c from [180] ($\beta = 0.1$). The dash-dot line is the $N = 10$ curve.

secondary vortices and the subsequent interaction with them. This lost energy misses downstream to further maintain the periodic vortex street. The second consequence is that the formation process of the secondary vortices disturbs the Kármán vortex street which no longer appears as a regular procession of vortices, but rather as an irregular one. Remarkably, the chaotic vortex street oscillates from one wall to the other [see figures 6.5(a) and 6.5(c)].

6.4.2 Dependence on Ha

We find that the appearance of the successive flow regimes are shifted at higher Re_d due to the influence of the magnetic field. Indeed, as can be seen from equation (6.2), the Hartmann friction shifts the growth rate of the flow instabilities by Ha/Re_d [155, 168]. As Ha is increased, a higher Re_d is required to reach the transition to another flow regime compared to the non-MHD configuration. This is why, both Re_1^c and Re_2^c are controlled by the friction parameter Re_d/Ha. This ratio, introduced by [163], measures the effective ratio of inertial to Lorentz forces in quasi-2D flows. Both Re_1^c and Re_2^c obey an affine dependence with Ha for $Ha \geq 160$ with $Re_1^c \propto 0.32Ha$ and $Re_2^c \propto 0.86Ha$. By contrast, such a dependence has not been singled out for the transition to regime **IV**, even if an affine asymptotic one is seen for $Ha \geq 560$ with $Re_3^c \propto 1.12Ha$. Additional computations achieved for

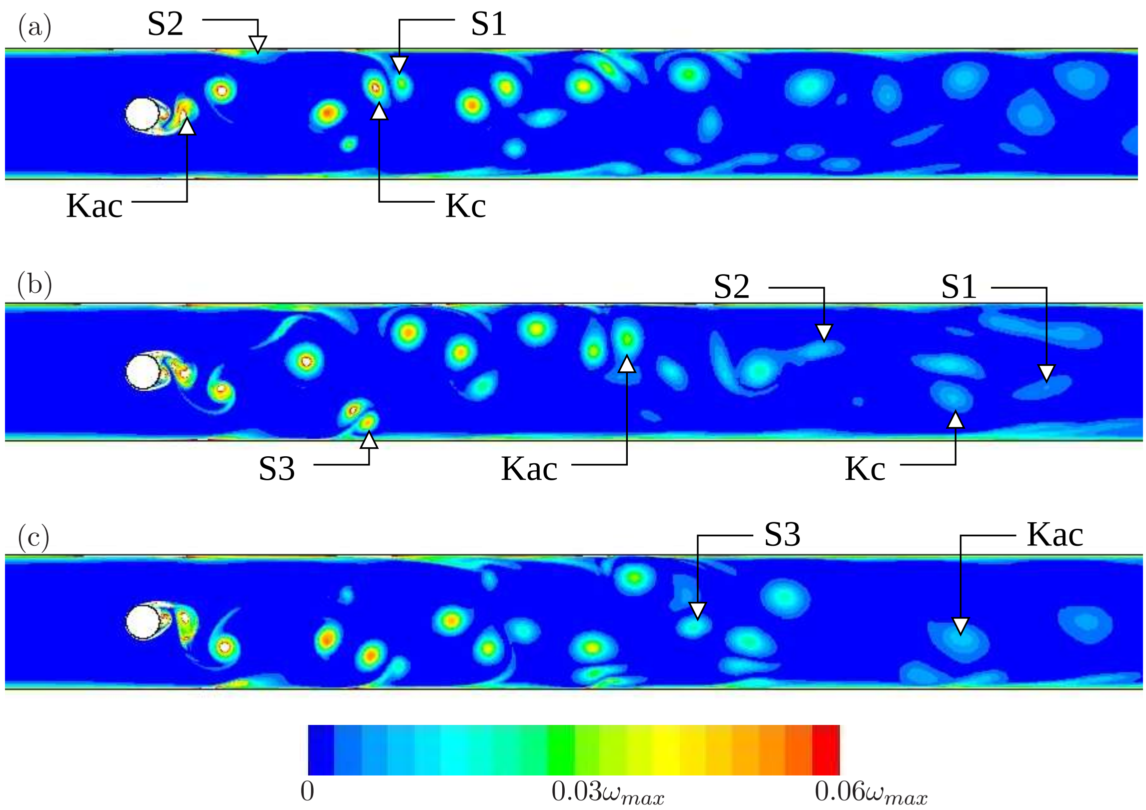

Figure 6.5: Flow regime **IV**: successive stages of the field of vorticity magnitude (s^{-1}) at $Ha = 560$ and $Re = 5000$ at: $t = 3.22t_H$ (a), $3.33t_H$ (b), $3.44t_H$ (c). S1, S2 and S3 are secondary vortices, Kc (*resp.* Kac) is a clockwise (*resp.* anticlockwise) Kármán vortex. ω_{max} is the maximum vorticity magnitude.

higher values of Ha would be required to confirm this trend.

We have also found that the onset of vortex shedding appears at the same critical threshold whether Re_d is increased from regime **II** or decreased from regime **III**. As it was established in experiments by [180], the nature of the transition to unsteadiness is thus supercritical and not hysteretical. Nevertheless, in the simulations performed in the early stages of regime **III**, the flow has never reached any fully-established state even when extending the simulations time up to $20t_H$ (see figure 6.6).

We have indicated on figure (6.4) the respective critical thresholds for the transition to unsteadiness obtained in both experiments of [174] and [180]. The agreement with [174] is excellent at $Ha = 560$, but less convincing at $Ha = 1080$. We shall however point out that the procedure used in [174] to detect the onset of vortex shedding relies on the recordings of velocity from two probes located in the near wake of the cylinder. In their experiments, the onset of vortex shedding is detected when one of the measurement probe first records an unsteady signal. The corresponding value of Re_d was then claimed to be the critical threshold for the transition to unsteadiness. It is well established that, as Re_d is increased within the unsteady flow regime, the vortex formation region shrinks and the vortices are shed closer from the cylinder. In the case the vortex shedding is initiated at a position slightly downstream of the measurement probes at a given Re_d, the transition to unsteadiness would

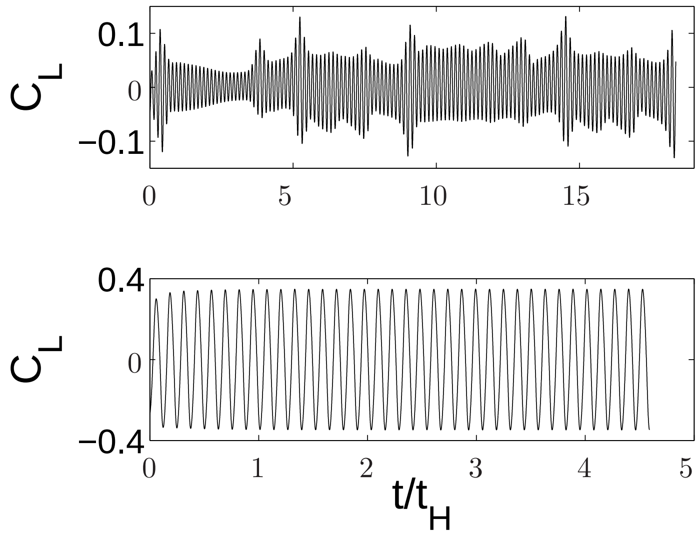

Figure 6.6: Top: Lift coefficient C_L versus t/t_H for $Ha = 1080$ and $Re_d \simeq 1.3Re_2^c$; the flow does not reach any clearly established state after almost $20t_H$. Bottom: C_L versus t/t_H for $Ha = 1080$ and $Re_d \simeq 1.5Re_2^c$; the flow is fully established after t_H.

not be detected for this value of Re_d by the procedure of [174], but at a higher value when the tail of the vortex formation region reaches the position of the measurement probe. As a consequence, the critical threshold Re_3^c detected by [174] at $Ha = 1080$ might be bigger than the real value and indeed we have found a higher Re_3^c than [174].

The transition to unsteadiness as detected by [180] systematically occurs at lower Re_d than those obtained in the present simulations. This must be due to the difference in the respective flow configurations. The blockage ratio β is higher in the configuration used in our computations than in the experimental set-up of [180]: 0.25 and 0.1 respectively. In the range $0.1 \leq \beta \leq 0.6$, non-MHD investigations [35, 37, 45, 72] found that increasing the blockage ratio resulted in a shifting of the onset of vortex shedding to higher Re_d. In the MHD case, increasing β shall enhance the stabilisation of the flow by the magnetic field, which is consistent with the fact that, for a given Ha, we have systematically detected the onset of vortex shedding at a higher Re_d than [180].

The collapse of the periodic laminar flow regime was also observed in experiments of [180]. The authors moreover established that increasing Ha shifted the break-up of the regular Kármán vortex street to a higher Re_d. Regime **IV** was observed as clockwise (*resp.* anticlockwise) vortices were detected in the lower (*resp.* upper) part of the wake, while only vortices of opposite sense of rotation were detected in regime **III**. Nevertheless, their measurement system could give information on the cylinder wake only within a 3-diameter wide stripe centred on the wake centreline. Consequently, their observations could not indicate the exact origin of the secondary vortices. In this respect, the present simulations clearly show that the latter vortices are generated from separation of the Shercliff layers at the side walls, which were outside of the observation windows of [180].

6.5 Steady flow regimes

6.5.1 Lengthening of the recirculation regions

The evolution of the non-dimensional length L_b of the steady recirculation regions versus Re_d are given in figure 6.7. In both non-MHD and MHD cases, the growth of the recirculation regions scales with Re_d with a respective slope and a maximum length that diminish as Ha increases. In addition, we have found a universal scaling law relating L_b with $Re_d/Ha^{0.8}$ in the limit $Ha \to \infty$. Only the curve with $Ha = 160$ slightly departs from this law as the transition to unsteadiness comes closer, indicating a non-asymptotic regime.

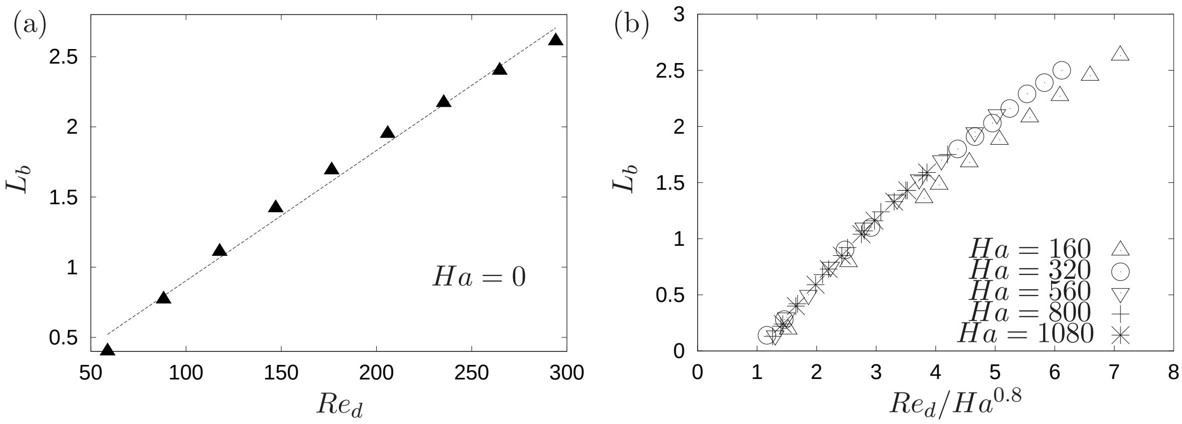

Figure 6.7: (a) Length L_b of the recirculation regions versus Re_d in the non-MHD case. The dash line is the linear regression of the data. (b) MHD universal scaling law $L_b = f_1(Re_d/Ha^{0.8})$.

It is well accepted from the non-MHD studies that in cylinder wakes, the variations of the length of the recirculation regions strongly influence those of the base pressure coefficient C_{pb}. The respective C_{pb} curves in both MHD and non-MHD cases are reported on figure 6.8. Whichever the value of Ha, $-C_{pb}$ decreases throughout the steady flow regimes, while a discontinuity in the slope is observed at the onset of the vortex shedding. For the MHD computations, a universal scaling law has been found in which C_{pb} scales with Re_d/Ha, and not $Re_d/Ha^{0.8}$. To understand why the base pressure coefficient decreases in the steady flow regime, one can analytically compute the base pressure coefficient based on the pressure drop induced by the channel flow only, *i.e.* that due to the Hartmann and viscous friction only [1]. We denote C_{pb}^{HD} (*resp.* C_{pb}^{MHD}) the resulting analytical base pressure coefficient in the non-MHD (*resp.* MHD) case and we obtain with $L_c = L_u + d/2$:

$$-C_{pb}^{HD} = 16\frac{L_c d}{h^2}\frac{1}{Re_d} \tag{6.8}$$

$$-C_{pb}^{MHD} = 4\frac{L_c d}{a^2}\frac{Ha}{Re_d} \quad \text{for } Ha \gg 1 \tag{6.9}$$

The latter base pressure coefficients govern the evolution of $-C_{pb}$ when the presence of the cylinder

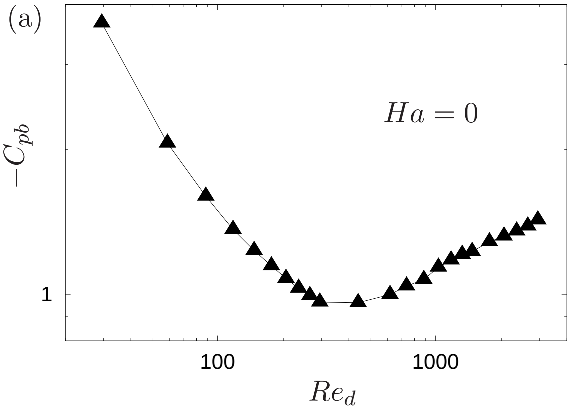

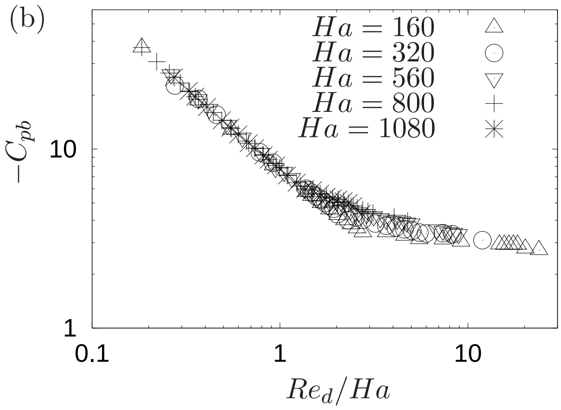

Figure 6.8: (a) Base pressure coefficient versus Re_d in the non-MHD case. (b) MHD universal scaling law $C_{pb} = f_2(Re_d/Ha)$.

has little effect on the flow, e.g. in the creeping flow regime. Indeed, from equations (6.8) and (6.9), it follows that $-C_{pb}$ decreases when Re_d increases at a given Ha, as observed in our simulations. The presence of the cylinder has an increasing influence on the flow throughout regime **II**. $-C_{pb}$ therefore drifts away from $-C_{pb}^{HD}$ in the non-MHD one, whereas it slightly departs from $-C_{pb}^{MHD}$ in the MHD one. This shows that the pressure drop induced by the cylinder only is negligible with respect to that induced by the Hartmann friction over a length L_c of the order of magnitude d in the MHD cases, whereas it is dominant when $Ha = 0$ where no Hartmann damping is present. As a result, the MHD values of $-C_{pb}$ are all the closer to equation (6.9) as Ha is larger. This explains why Re_d/Ha is the governing parameter.

6.5.2 Outer boundary layer of the steady recirculation regions

To complete our investigations of the flow dynamics in the steady flow regime, we have analysed the outer boundary layer of the steady recirculation regions and in particular their thickness δ as Re_d is increased. δ is estimated from the streamwise velocity profile across the recirculation regions. The detailed procedure is described in [1] (see appendix). The respective evolutions of δ with Re_d at $Ha = 1080$ and with Ha at constant critical parameter $r = 0.7$ [$r = (Re_d - Re_1^c)/(Re_2^c - Re_1^c)$] are given on figure 6.9.

One observes that δ is of the order of the thickness of the Shercliff layer $\delta \sim Ha^{1/2}$. The curvature of the boundary layer, which is accounted for in the derivation of δ, plays an important part in the determination of δ. In the upstream half of the recirculation regions, the boundary layer is rather parallel to the streamwise direction and roughly exhibits the same characteristics as a Shercliff layer, hence its thickness of about one δ_s. In contrast, in the downstream half, as the curvature of the boundary layer becomes more significant, δ increases for $0.5 < (x - 1/2)/L_b < 0.8$ with a maximum thickness systematically reached at $(x - 1/2)/L_b \simeq 0.7$ with a value of about $2\delta_s$ to $3\delta_s$.

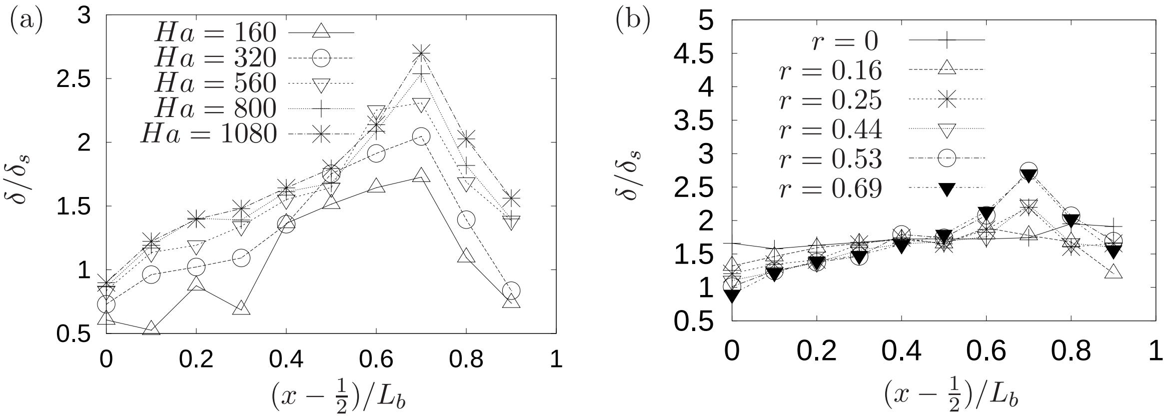

Figure 6.9: Thickness of the boundary layer of the recirculation regions for (a) increasing Ha at $r = 0.7$ and (b) for increasing r at $Ha = 1080$. $r = (Re_d - Re_1^c)/(Re_2^c - Re_1^c)$.

Eventually, a sharp decrease in δ is observed at the tail of the recirculation regions. In the latter region, the boundary layer is mostly oriented along the transverse direction and consequently under little influence from the free stream. This boundary layer then turns back to a parallel side layer so that its thickness drops down to δ_s.

For a given value of the critical parameter r, the increase in Ha does not affect much the shape of the curve, but induces a shift towards higher values of δ/δ_s. In particular, the maximum thickness increases with r until it reaches a critical thickness which the steady recirculation regions cannot sustain anymore initiating the vortex shedding and the Kármán vortex street.

6.6 Laminar periodic flow regime III

In the steady flow regimes, we have established a couple of trends regarding the evolution of various flow coefficients. We shall now consider how far the onset of vortex shedding and the periodic laminar flow regimes influence these trends. To this end, we describe how the transition to unsteadiness modify the evolutions of both the length of the vortex formations regions and the pressure drop coefficient. We will then focus on the drag coefficient.

6.6.1 Length of the vortex formation region

For the unsteady flow regime, the length of the vortex formation region is defined in subsection 2.3.1. We denote this length L_f. Figure 6.10 shows the evolution of both L_b and L_f before and after the transition to unsteadiness respectively, for $Ha = 0, 160, 560, 800$. The linear lengthening of the steady recirculation regions is followed in both the non-MHD and the MHD cases by a decrease in L_f once the flow becomes unsteady. The slope of the decrease is initially steep and L_f eventually reaches a plateau for very high values of Re_d with a final value of about $0.5d$. The drop in L_f is more significant for the highest value of Ha ($Ha = 800$). After the initial sharp decrease in L_b, the shapes of the curves are quite similar and the values are shifted to smaller L_f. In the limit of high Ha, the curves all collapse on a single one, which supports the establishment of an asymptotic state.

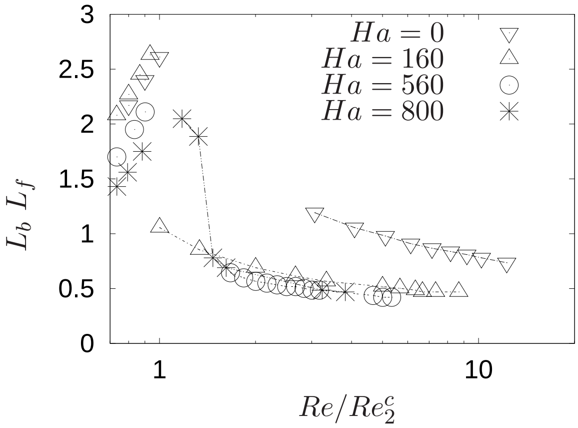

Figure 6.10: Length L_b of the steady recirculation regions in steady flow regime **II** ($Re_d < Re_2^c$) and length L_f of the vortex formation region in unsteady flow regime **III** ($Re_d > Re_2^c$)

In the periodic laminar regime, the vortices are released closer and closer from the cylinder as Re_d is increased, hence the decrease in L_f. As L_f reaches its plateau, the vortex formation region is only about half a diameter long. The free shear layers consequently roll up very close to the cylinder surface so that the boundary layer at the rear of the cylinder eventually separates and generates vortices (see [1] Fig. 13). These vortices may either shed and merge into the adjacent Kármán vortex or shed and be released together with the adjacent Kármán vortex into the cylinder wake. The mechanism of this secondary vortex shedding is similar to that induced by the Shercliff layer in regime **IV**. It has no significant influence on the formation mechanism of the Kármán vortices and especially none of the flow coefficients exhibit any change when these secondary vortices appear.

6.6.2 Base pressure coefficient in regime III

In steady flow regimes, the increase in L_b corresponds to a drop in $-C_{pb}$ in both the MHD and non-MHD cases. Surprisingly, in unsteady flow regime **III**, the decrease in L_f observed in both cases corresponds to an increase in $-C_{pb}$ only in the non-MHD case. On the contrary, as seen on figure 6.8, in the MHD computations, the onset of vortex shedding does not imply an increase in $-C_{pb}$, but only a discontinuity in its decreasing slope. To further investigate this point, we have computed a base pressure coefficient in which the pressure drop has been measured between the base point and the front stagnation point located on the wake centreline at the cylinder surface ($x = -1/2; y = 0$). We denote this base pressure coefficient C'_{pb}. The pressure drop considered in the definition of C'_{pb} is taken over a length $L'_c = d$. We report the evolutions of both C_{pb} and C'_{pb} versus Re at $Ha = 560$ in figure 6.11. One observes that, whereas $-C_{pb}$ keeps on decreasing after the transition to unsteadiness,

$-C'_{pb}$ increases in the unsteady flow regime.

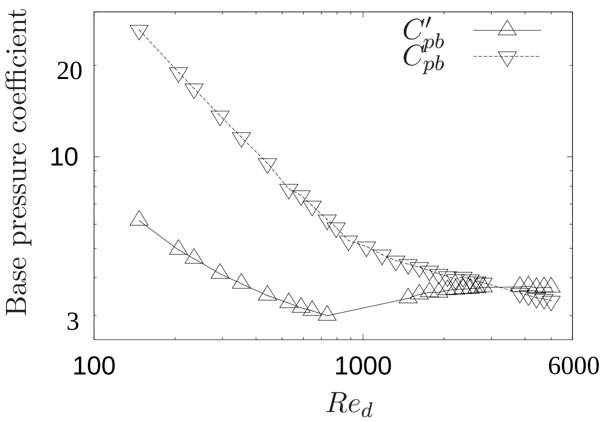

Figure 6.11: Base pressure coefficients C_{pb} and C'_{pb} versus Re_d at $Ha = 560$ for a reference pressure located at the inflow boundary and at the front of the cylinder, respectively.

Since it is measured only along one cylinder diameter, the pressure drop used in C'_{pb} is less influenced by the Hartmann friction, which has been shown to be dominant on the pressure drop in the MHD steady regime. Considering C'_{pb} as base pressure coefficient means that the variations of the length of the vortex formation region and those of the base pressure coefficient are identical in both MHD and non-MHD cases, *i.e* these quantities exhibit opposite variations in both steady and unsteady regimes. In the steady regimes, the lengthening of the steady recirculations strengthens the advert pressure gradient at the cylinder rear, hence the decrease in $-C'_{pb}$. In the unsteady regimes, the collapse of the vortex formation region weakens this advert pressure gradient and induces an increase of $-C'_{pb}$. In summary, the modification of the pressure due to the shrinkage of the vortex formation region is outweighed by the pressure drop inherent to the Hartmann damping, unless the pressure drop is measured over a length of the order of one cylinder diameter.

6.6.3 Drag coefficient

Whereas the base pressure coefficient reflects a local aspect of the flow, the drag coefficient gives a global insight of the flow in the vicinity of the cylinder circumference. Figure 6.12 shows the evolutions of the total drag coefficient C_D versus $Re_d/Ha^{0.8}$ in the MHD and non-MHD cases.

In both non-MHD and MHD cases, C_D decreases within the steady flow regimes and then increases in the unsteady ones. A slight discontinuity can be observed at the transition to unsteadiness in the non-MHD cases, whereas a clear one is seen in the MHD computations. The transitions to regime **II** and **IV** does not involve any discontinuity, nor any modification in the respective slopes. Finally, we have found a universal law in the MHD cases linking C_D to $Re/Ha^{0.8}$, *i.e.* a similar law as the one found for the length of the steady recirculation regions. This law furthermore indicates that an asymptotic regime is reached for high values of Ha.

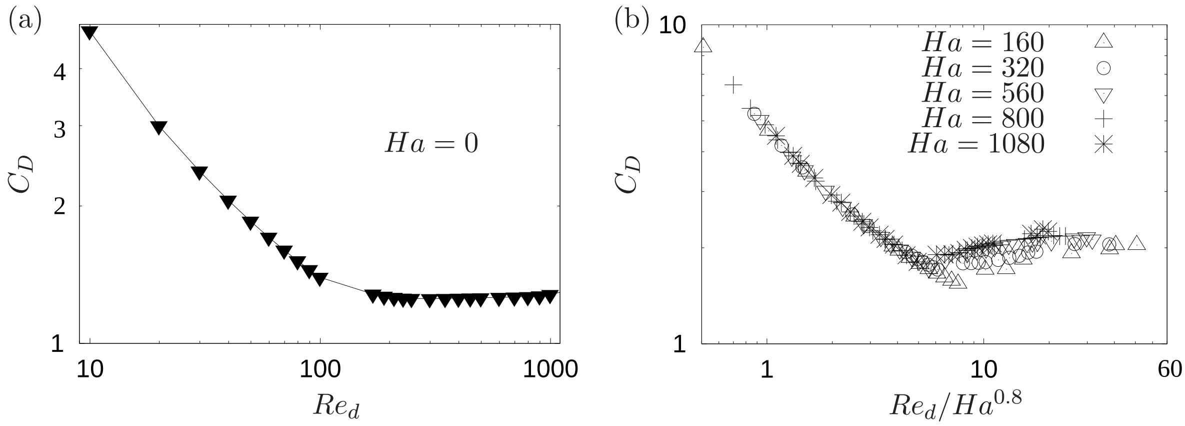

Figure 6.12: (a) Total drag coefficient C_D versus Re_d in the non-MHD case and (b) MHD universal law $C_D = f_3(Re/Ha^{0.8})$

As explained in section 2, the transition to unsteadiness implies a change in the variations of the pressure-based drag coefficient, which stops decreasing and begins to increase. This change then induces a discontinuity in the decreasing slope of the total drag coefficient C_D in unbounded cylinder wakes. In confined flows, as the transition to unsteadiness is shifted to higher Re, it induces a change in the variations of C_D which starts increasing after the onset of vortex shedding, even though this increase is very smooth. In the present MHD simulations, the transition to unsteadiness is further shifted to higher Re so that the discontinuity seen on the C_D curve is more pronounced at the onset of vortex shedding.

6.7 Higher Re_d flows

6.7.1 Drop in St at the transition to flow regime IV

The Strouhal number St is a flow coefficient which specifically reflects the process of vortex shedding in the cylinder wake. The evolution of St versus Re_d obtained in the present MHD and non-MHD simulations are shown on figure 6.13(a-b).

In the MHD computations, St increases up to a first value, then decreases down to a minimum value from which it increases once again up to an absolute maximum and eventually drops. The latter dramatic drop in St corresponds to the transition to regime **IV** and the break-up of the regular Kármán vortex street. Indeed, the development of a secondary vortex is seen by the incoming Kármán vortex as an obstacle, which impedes its motion downstream in the cylinder wake [see, e.g. vortices Kc and S1 in figures 6.5 (a) and (c)]. This causes a sudden drop in the vortex shedding frequency and subsequently a drop in St. The collapse of the regular Kármán vortex street was also correlated to a sudden drop in St in [180] although only a few values of St were measured in their experiments (see figure 4.2). Interestingly, at both $Ha = 500$ and $Ha = 1200$, the sudden drop is observed for

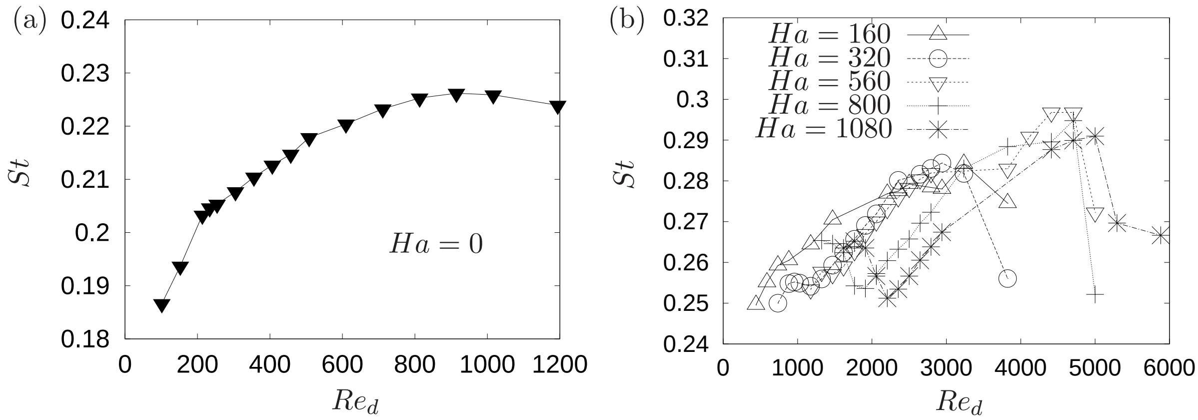

Figure 6.13: Strouhal number St versus Re_d in the non-MHD (a) and MHD cases.

$5.10^3 < Re_d < 10^4$ and the critical St reached before the break-up of the regular Kármán vortex street is about 0.29, *i.e.* at Re_d and St values of the same order of magnitude as in the present simulations. In contrast, as the development and release of the secondary vortices occur downstream of the cylinder, away from the near wake of the cylinder, it has little influence on the evolution of C_{pb}, L_f and C_D (see figures 6.8, 6.10 and 6.12, respectively).

6.7.2 Kelvin-Helmholtz instability in the free shear layers

We now consider the flow at $Re_d = 3 \times 10^4$ and $Ha = 1080$. With regards to the assumptions at the basis of the SM82 model, this simulation represents a borderline case and the corresponding results should be regarded as qualitative only, all the more so as no data neither numerical nor experimental are available in the literature for comparison. The goals are here to introduce a flow regime where instabilities take place in the free shear layers and check the validity of the quasi-2D assumption when such instabilities settle in the flow.

This simulation shows that the free shear layers on both sides of the cylinder turn unstable and are subject to the development and release of small-scale Kelvin-Helmholtz (KH) vortices (see figure 6.14). These vortices feed a chain which rolls up at the rear of the cylinder, merge into a large vortex that is eventually released downstream in the cylinder wake.

$Re_d = 3 \times 10^4$ still yields a large enough Stuart number ($N \simeq 2.5$) to safely assume that the large structures are quasi-2D. The KH vortices are however of a much smaller scale of the order of δ_s, the thickness of the Shercliff layer. Such small structures are 2D provided that $N(U_0/U_v)(\delta_s/a)^3 \gg 1$, where U_v is the structure's velocity [165]. The latter velocity is infinitesimal at the initial stages of development of the structure so that it can be fairly assumed that the structure is initially 2D and little affected by 3D inertial effects. As the structure grows and gains in energy taken from the flow, the present simulation shows that U_v becomes of the order of U_0 and $N(U_0/U_v)(\delta_s/a)^3 \simeq 6.10^{-4}$. This strongly suggests that the KH vortices are likely to experience some disruptions because of 3D

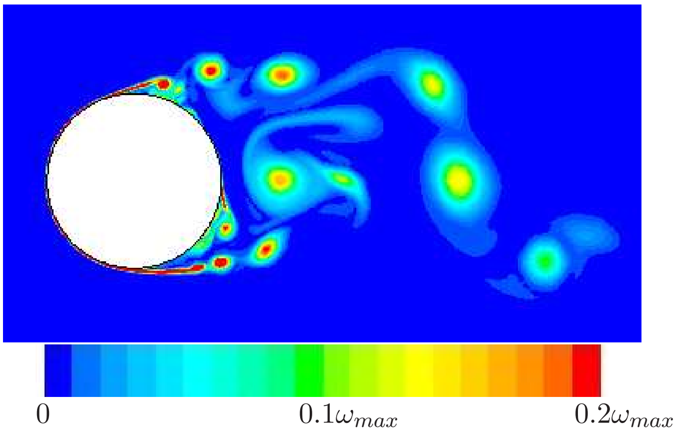

Figure 6.14: Kelvin-Helmholtz instability: snapshot of the field of vorticity magnitude at $Ha = 1080$, $Re_d = 3 \times 10^4$ and $t = 4.6t_H$. ω_{max} is the maximum vorticity magnitude.

inertial effects, which the SM82 model is unable to render.

In the non-MHD case, where the KH vortices are 3D, it is fairly accepted that the latter vortices are generated from a 2D mechanism [32, 75]. On this basis and following the same method described in [15], we have performed a simplified linear stability analysis on the MHD free shear layers to determine the critical Re_d at which a linear perturbation causes the KH vortices to turn 3D. The detailed computations are given in [1] (see in appendix). At $Ha = 560$, the corresponding critical Re_d is around 20, which is obviously much smaller than the observed one. This shows that additional effects such as the stabilizing influence of the curvature [58] and the non-constant thickness of the free shear layer play a crucial part and ought to be accounted for in more complex analyses.

6.8 Conclusions

In this part of the thesis, we have investigated the flow of an electrically conducting fluid past a circular cylinder under an intense, externally applied axial magnetic field. We have considered the case where both Ha and N are much bigger than unity so that the flow structure is quasi-2D. In this context, the SM82 model is well adapted to capture the flow dynamics within a very good approximation. We have performed a parametric study over both Ha and Re_d. We have identified a sequence of flow regimes which exhibits many similarities with the non-MHD case. In steady flow regime **II**, we have shown that high Ha values yielded shorter recirculation region and that the thickness of their external boundary layer scaled with the thickness of the Shercliff layer. Furthermore, this thickness has been shown to be non-constant along the boundary layer. Also, we have described an unsteady flow regime in which the Kármán vortex street became irregular. The latter regime was beforehand described in experiments by [180], but the mechanism leading to its appearance has been explained by the present simulations. We have eventually performed a simulation at very high Re_d in which Kelvin-Helmholtz vortices developed in the free shear layer, even though the outcomes of this simulation should be regarded as qualitative only.

The magnetic field shifts the appearance of respective flow regimes to higher Re_d as Ha is higher. The transitions to regimes **II** and **III** are governed by the friction parameter Re_d/Ha. We have obtained the evolution of a set of flow coefficients versus Re_d and Ha and identified the variations of these coefficients with the flow dynamics. In particular, for the MHD cases, we have found a universal scaling law linking C_{pb} with Re_d/Ha and both L_b and C_D with $Re_d/Ha^{0.8}$.

In a larger extent, this study shows that the SM82 flow model can be efficiently used to acquire extensive information over a wide variety of flow aspects. The SM82 model is simple, easy to implement into a numerical code and leads to a dramatic gain in CPU time in comparison with fully 3D numerical simulations. Some flow features can however not be captured by the SM82 model. As this model forbids any fluid transfer between the Hartmann layers and the core flow, it might overlook possible Ekman recirculation flow inside a vortex normal to the Hartmann layer. In addition, although it has been shown that the error involved was small [159], the SM82 model considers the Shercliff layer as perfectly 2D. It could be of interest to assess how far the three-dimensionality of the Shercliff layer influences the process of vortex shedding identified in flow regime **IV**. Also, there is still no agreement in the literature on the respective lower boundary values of Ha and N at which the flow cannot be modelled by the SM82 flow model anymore. In an attempt to give some insight on the limits of the SM82 model, we shall later present the comparative results of a cylinder wake from simulations achieved with the SM82 model on the one hand and from 3D computations on the other hand.

Part III

Three-dimensional numerical computations

Chapter 7

Numerical set-up in the three-dimensional simulations

In this chapter, we describe the numerical set-up used in the 3D numerical simulations. In the first section, we briefly review the aspects of 3D numerical set-ups used in the simulations of the non-MHD flow past a cylinder which have been shown to have a significant influence on the results of the simulations. We also review the different options to arrange the flow variables in a given cell of the mesh. The second section is dedicated to the construction of the numerical model used in the 3D MHD simulations. We assess whether the full MHD equations or the simplified ones of the low Rm approximation shall be used. We explain how far MHD flows affect the mesh design and the arrangement of the mesh variables. We shall also describe the treatment of the current density and the Lorentz force. At the end of this chapter, the detailed steps of the present 3D MHD numerical code are given. The latter has been built from the open source code OpenFOAM [202, 205, 206, 210]. FLUENT/UNS has not been used in any 3D simulations.

7.1 Numerical set-up of non-MHD flows past cylinders

The reliability of early 3D computations of non-MHD cylinder wakes has been undermined by the same issues which have affected early 2D simulations, *i.e.* poor mesh resolution, convergence problems and/or restricted numerical domain [66]. We shall introduce thereafter the problems relative to the boundary conditions and the arrangement of the flow variables in a given mesh cell.

7.1.1 Boundary conditions

In 3D simulations of cylinder wakes, special care has to be dedicated to the definition of the boundary conditions for the velocity at both cylinder ends. Since the flow patterns in the early stages of three-dimensionality have strong periodic properties (see section 2.2), a periodic boundary condition is likely to noticeably influence the results of the simulations [54, 66]. For example, [66] showed how periodic boundary conditions affected the time history of the Strouhal number. In addition, this choice presupposes that only spanwise periodic structures exist in the flow, which remains controversial [189]. Also, when using a periodic boundary condition, the spanwise distance along the cylinder axis between the planes where this condition is applied has to be chosen with care. The respective flow patterns of modes A and B have indeed very different characteristic spanwise lengths: $\lambda_A = 4d$ and $\lambda_B = d$. Consequently, a numerical domain with a spanwise length smaller than λ_A and a periodic boundary condition imposed at the boundaries normal to the cylinder axis promotes the appearance of mode-B flow pattern at the expense of mode-A structures [54, 66]. Further inaccuracies on the values of the flow coefficients may also appear if the spanwise length is ill-defined [66]. Instead of imposing periodic boundary conditions, one may apply a slip boundary condition (1.23) that has a lesser influence on the flow [76, 102, 103, 189]. Also, to our knowledge, all existing 3D numerical simulations in finite-volume [102, 107, 189] have been achieved on a mesh with a regular spanwise spatial step.

7.1.2 Arrangement of the flow variables

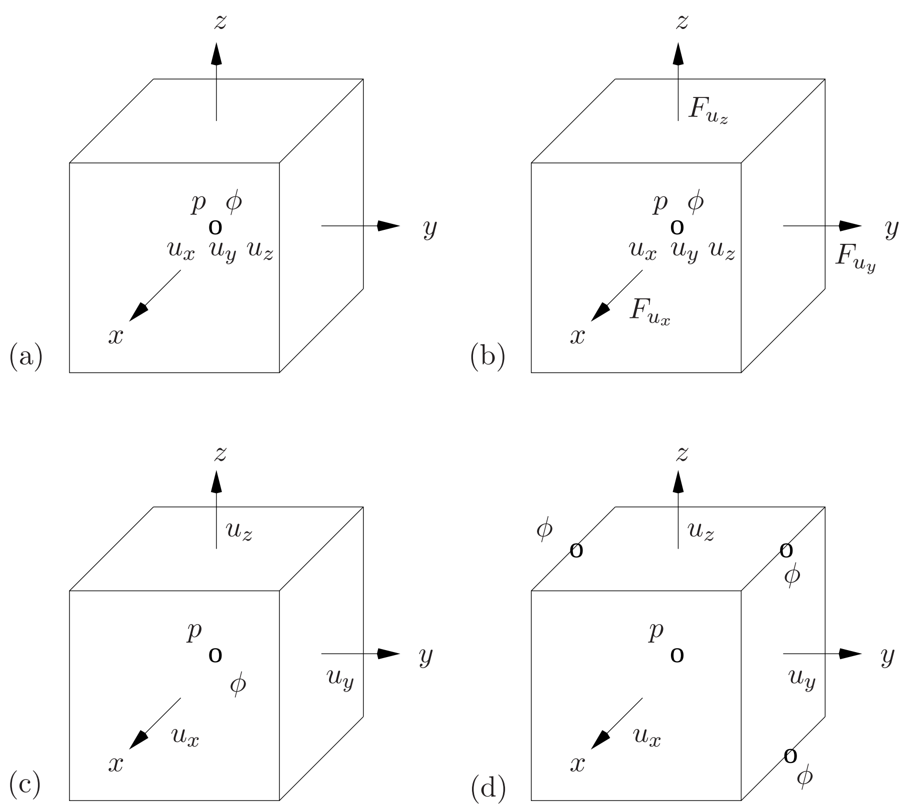

Figure 7.1: Arrangement of the flow variables in a cell of a structured mesh: Regular mesh (a) Collocated mesh (b); Staggered mesh (c); Fully staggered mesh (d). F_{u_x}, F_{u_y} and F_{u_z} are the fluxes of velocity along the x, y and z-axis respectively.

The determination inside a mesh cell of the respective locations where the variables are stored has significant implications on the complexity of the discretised numerical equations and on the number of interpolations required throughout the algorithm.

In non-MHD numerical simulations, three possible kinds of mesh arrangement are given in figures 7.1(a-c). In a regular mesh shown on figure 7.1(a), all the variables are stored at the cell centroid. Using this arrangement, the pressure field, though correct from a numerical point of view, is likely to exhibit non-physical checkerboarding patterns as the result of the formulation of the discretised pressure equation (5.15) [198, 202, 204]. [200] shifted the location of the velocity components onto the cell faces and defined the staggered mesh given on figure 7.1(c). In this configuration, the control volumes centred respectively on the velocity and the pressure nodes, are no longer identical, but overlap each other. As a result, the expression of the pressure equation exhibits a strong coupling between both odd and even mesh node numbers. This subsequently promotes non-oscillatory pressure solutions [198, 204]. Although this arrangement limits the number of interpolations required in the numerical algorithm, the formulation of the discretised equations is more complex [198, 200, 204].

[208] reformulated the pressure equation to involve the fluxes of velocity at the faces of the mesh cell. These fluxes are obtained by the interpolation of the velocity field onto the cell faces and defined as conservative by construction [202, 204]. In this configuration, the velocity is used at a pseudo-variable as the pressure-velocity coupling is formulated with the pressure and the fluxes of velocity. This corresponds to the collocated mesh shown on figure 7.1(b), which is provided in OpenFOAM and FLUENT/UNS. This mesh arrangement benefits from the advantages of both the regular mesh, as the formulation of the discretised numerical equations remains rather simple, and the staggered mesh, as the fluxes of velocity are actually located at the cell faces and used to solve the pressure equation in a similar fashion as in a staggered mesh (see PISO algorithm in section 5.3).

7.2 Numerical set-up of MHD flows at low R_m

In this section, we describe the issues encountered in the construction of a 3D MHD numerical code: the choice of the flow equations to be numerically solved, the mesh requirements, the arrangement of the flow variables in the mesh cell, the implementation of the Lorentz force, the coupling between the flow variables and the definition and implementation of the electric boundary conditions. The above issues shall be addressed one after the other. Following their respective implications and the recommendations found in the literature, we shall describe the successive steps of the construction of our 3D MHD numerical code.

7.2.1 Flow equations

We have derived in section 1 the full set of the MHD equations composed of both the Navier-Stokes equations (1.1) and (1.2) and the Maxwell equations (1.3), (1.4), (1.5) and (1.13). Under this formulation, these equations involve strong limitations on the numerical methods designed to solve them. In particular, the coupling between the velocity field $\mathbf{u}$ and the magnetic field $\mathbf{B}$ exhibited in the induction equation is highly non-linear and the respective characteristic time-scales of both fields are very different. The time scale of the diffusion mechanism of the velocity field and that of the magnetic field are therefore very different too. A very small computational time step is eventually required to ensure that the numerical results are obtained within a good accuracy [147].

In the frame of this thesis, we are concerned with MHD phenomena at the laboratory scale for most of which the magnetic Reynolds number R_m is much smaller than unity [18]. One can then consider the flow equations within the low-R_m approximation in which the coupling between the velocity and the magnetic field is weak. If furthermore the magnetic field is uniform and externally applied, its time variations can be neglected and the set of flow equations further simplified to involve only the Navier-Stokes equations and the conservation of the electric current including Ohm's law. These equations are thereafter written under their non-dimensional form assuming that the fluid is incompressible and the imposed magnetic field is $\mathbf{B}_0 = B_0\mathbf{e}_z$:

$$\partial_t \mathbf{u} + (\mathbf{u}\cdot\nabla)\mathbf{u} = -\nabla p + \frac{1}{Re}\nabla^2\mathbf{u} + \frac{Ha^2}{Re}[(-\nabla\phi + \mathbf{u}\times\mathbf{e}_z)\times\mathbf{e}_z] \tag{7.1}$$

$$\nabla\cdot\mathbf{u} = 0 \tag{7.2}$$

$$\nabla^2\phi = \nabla\cdot(\mathbf{u}\times\mathbf{e}_z) \tag{7.3}$$

The implementation of this set of equations involves a significant gain in efficiency of the numerical code since the coupling between $\mathbf{u}$ and $\mathbf{B}_0$ is negligible and the requirement on the computational time step is less prohibitive [146].

[147] performed simulations of the damping of vortices in a conducting fluid by a uniform magnetic field using two different numerical codes solving the full MHD equations and those within the low-R_m approximation, respectively. They compared the respective time histories of the circulation of the vortex obtained at $Rm = 0.1$ and $R_m = 1$. In both cases, the application of the magnetic field induces a decay of the vortex circulation. The discrepancy between the curves obtained from both codes at $R_m = 0.1$ is very weak, whereas it is more significant at $R_m = 1$. This study indicates thus that the condition $R_m \ll 1$ theoretically required to use the low-R_m approximation remains valid for R_m up to about 0.1 without undermining much the reliability of the results. The present 3D numerical code is therefore designed to solve the MHD equations within the low-R_m approximation composed of equations (7.1), (7.2) and (7.3).

7.2.2 Mesh requirements

Block-structured meshes require a special care at the interface between the mesh blocks. If two adjacent mesh blocks do not match at their common interface, interpolation schemes must be implemented to ensure the flow quantities and gradients smoothly and accurately propagate at the interface. Also, mesh skewness at the interface between two adjacent mesh blocks shall be assessed, as mesh skewness may be a significant source of numerical error [202].

Mesh refinement is necessary in the boundary layers. In MHD duct flows (see section 1), they correspond to both the Hartmann and Shercliff boundary layers. The grid refinement required in these layers must then be carefully propagated in the core flow to have a smooth mesh transition between the boundary layers and the core flow. As a result, the thickness of the Hartmann layers greatly influences the number of mesh cells required in the numerical domain to accurately simulate the flow. For high values of Ha, the Hartmann layers are very thin so that the resolution of the flow inside these layers demands large CPU effort and storage capacity.

Numerical methods are more efficient and cheaper if the mesh is uniform, *i.e.* if the mesh spacing in each direction is constant. Nevertheless, for high Ha, a uniform mesh requires such a high number of cells that the limits in CPU storage may eventually become prohibitive. For example, [167] achieved 3D Direct Numerical Simulations (DNS) of MHD duct flows using uniform meshes in the early 1990's. Since computer performance was still rather poor at this time, that author was unable to achieve computations for $Ha > 100$ due to the limitations in CPU storage. Also, in unsteady cases, the numerical time step scales with the typical size of the smallest mesh cell. As a consequence, the CPU cost of fully 3D DNS at high Ha is very expensive not only because the Hartmann layers have to be resolved, but also because the simulation time soars dramatically due to the shrinkage of the numerical time step. A decade after [167], 3D DNS unsteady simulations of a cylinder wake were made on a uniform mesh by [189]. A wall function, which is introduced in section 8.2, was used to prevent the numerical code to deal with the flow inside the Hartmann layers and provide gain in CPU efficiency. Those authors could compute the flow for Ha up to about 400, but had to make do with a low mesh resolution in the Shercliff layers involving a risk of overlooking important features in these layers.

Besides, in the case of MHD duct flows past a truncated cylinder whose axis is parallel to the magnetic field, an additional Hartmann layer arises at the cylinder free end and instead of only two Hartmann layers, three such layers are present in the flow. Although this Hartmann layer is only located in the vicinity of the cylinder free end, in a structured mesh, the refinement propagates over the whole numerical domain.

Also, unlike the previous quasi-2D computations, the electric potential is an additional flow variable and its distribution must be determined at each time step. In particular, in MHD flows in electrically insulating ducts, the electric current streamlines exhibit a sharp curve at the intersection between the Shercliff and the Hartmann layers (see e.g. figure 10.6). Besides, although the current density is only of order Ha^{-1} in the core flow, the mesh should be fine enough in the vicinity of the duct symmetry plane to render properly the change of direction of the electric streamlines.

It is usual in non-MHD computations of cylinder wakes to gradually relax the mesh downstream of the cylinder. A compromise shall then be found to capture accurately the flow dynamics over the largest possible distance downstream the cylinder and save both CPU and storage capacity. [189] claimed the artificial diffusion of the flow structures generated by the gradual coarsening of the mesh dominated the MHD damping of these structures. We have seen in the quasi-2D flow simulations that, over a distance of the order of 10 cylinder diameters, the MHD damping significantly overweighs the viscous damping when $Ha \gg 1$ (see the analytical expression for the base pressure coefficient given by equation (6.9)). In contrast, over a distance of the order of 1 cylinder diameter, the MHD damping is not as dominant, but still rules over the viscous damping (see subsection 6.6.2). We think therefore that the artificial damping of the flow structures by the coarsening of the mesh is not likely to influence the flow significantly for $Ha > 50$ and the mesh can be gradually relaxed provided the flow structures in the near-wake of the cylinder are accurately captured.

7.2.3 Arrangement of the flow variables

MHD computations bring further numerical issues, since the conservation of the electric current and the subsequent treatment of the Lorentz force must be addressed in an accurate, conservative and consistent way. Both definitions of the current density and the Lorentz force involve a cross product [see equations (7.1) and (7.3)]. Consequently, a component of e.g. the Lorentz force along a given direction is obtained with the components of the gradients of the electric potential in the other two directions. The interpolation required to obtain the gradients and the position of the flow variables influences the stability and the accuracy of the numerical scheme as well as the conservation of the current density [145, 152]. Using a staggered mesh, [145] performed a stability analysis to obtain a set of conditions necessary to yield a monotonic, and hence stable, method, although a non-monotonic numerical method may also be stable. This analysis results in prohibitive limitations on the mesh spacing along the transverse direction, *i.e.* the direction perpendicular to both the magnetic field and the streamwise direction. [145] eventually shifted the position of the electric potential variable onto the cell edges to obtain a fully staggered mesh sketched in figure 7.1(d). That author then elaborated an accurate, conservative and consistent numerical code on this mesh arrangement. The resulting numerical method was monotonic and did not involve any restriction on the mesh spacing along the transverse direction. A fully staggered mesh was also successfully used in the simulations of MHD duct flows by [162, 170].

[152] stressed that the use of a fully staggered mesh enhances the numerical complexity of the discretised equations already pointed out when using an ordinary staggered mesh. The complexity is further increased if one imposes a multi-directional magnetic field. Although 3D simulations of MHD flows at high Ha are cheaper with non-uniform meshes, [152] also showed that the calculation of the gradient of electric potential required at least 6 neighbouring cells to be conservative and consistent with respect to the current density and therefore demanded large storage capacities.

So far, we have reviewed the implications of the use of three different mesh arrangements: the regular mesh, the staggered mesh and the fully-staggered mesh. The choice of a regular mesh was rejected because the resulting pressure field may be unphysical. When using a staggered mesh, the stability and accuracy of the numerical method with respect to the current density may be at risk. Finally, a fully staggered mesh implies the resolution of very complex discretised equations and a larger storage capacity. We have already seen that the use of a collocated mesh allows the building of an accurate and consistent numerical scheme for non-MHD computations (see section 7.1.2). We shall now explain how this mesh arrangement can also be successfully used in 3D MHD simulations.

7.2.4 Treatment of the current density and Lorentz forces on a collocated mesh

Until recently, 3D MHD-capable numerical codes built on a collocated mesh have failed to address in an accurate and consistent fashion the conservation of the current density and the subsequent treatment of the Lorentz force in the momentum equation. In a breakthrough work, [152] explained how the inaccurate treatment of the current density and/or the Lorentz force undermined the reliability of previous simulations achieved on a collocated mesh. The authors then introduced a simple method to alleviate this issue on a structured collocated mesh. The method was further expanded to arbitrary collocated meshes in [153]. We shall summarise the findings of these authors without going too far into the details of the calculations.

For convenience, we assume that a steady, uniform magnetic field is externally applied along the z-axis so that Ohm's law is written as:

$$\mathbf{j} = \mathbf{j}_\phi + \mathbf{j}_u \tag{7.4}$$

with $\mathbf{j}_\phi = -\nabla\phi$ and $\mathbf{j}_u = \mathbf{u} \times \mathbf{e}_z$.

The discretisation of the current conservation (7.3) must be consistent and must thus be implemented by taking the term-by-term divergence of Ohm's law:

$$\nabla \cdot (\nabla\phi) = \nabla \cdot (\mathbf{u} \times \mathbf{e}_z) \tag{7.5}$$

Consequently, as in the numerical treatment of the pressure equation, the consistent way to discretise the left-hand side of (7.5) consists in applying the discretisation scheme of the divergence operator to that of the gradient of the electric potential.

The finite-volume method treats the flow equations under their integral formulation. The integration of the current conservation ($\nabla \cdot \mathbf{j} = 0$) over a given mesh cell is thus equal to the sum of the fluxes of current density over the cell faces. It is then natural to locate the components of the current density at the cell faces, *i.e.* at the same position of the fluxes of velocity as shown on figure 7.1 (b). The current conservation also means that $\mathbf{j}$ is defined as conservative and the interpolation schemes required to compute $\mathbf{j}$ must preserve this property.

The mesh is considered as structured so that a system of indices (a, b, c) along the $x-$, $y-$ and $z-$axes may be defined. The respective conservative discretised divergence operators of $\mathbf{j}_u$ and $\mathbf{j}_\phi$ for a given cell centred on (a, b, c) are then given by:

$$(\nabla \cdot \mathbf{j}_u)_{a,b,c} = \frac{(j_{u,x})_{a+\frac{1}{2},b,c} - (j_{u,x})_{a-\frac{1}{2},b,c}}{x_{a+\frac{1}{2}} - x_{a-\frac{1}{2}}} + \frac{(j_{u,y})_{a,b+\frac{1}{2},c} - (j_{u,y})_{a,b-\frac{1}{2},c}}{y_{b+\frac{1}{2}} - y_{b-\frac{1}{2}}} \tag{7.6}$$

$$\begin{aligned}(\nabla \cdot \mathbf{j}_\phi)_{a,b,c} = &\frac{(j_{\phi,x})_{a+\frac{1}{2},b,c} - (j_{\phi,x})_{a-\frac{1}{2},b,c}}{x_{a+\frac{1}{2}} - x_{a-\frac{1}{2}}} \\ &+ \frac{(j_{\phi,y})_{a,b+\frac{1}{2},c} - (j_{\phi,y})_{a,b-\frac{1}{2},c}}{y_{b+\frac{1}{2}} - y_{b-\frac{1}{2}}} + \frac{(j_{\phi,z})_{a,b,c+\frac{1}{2}} - (j_{\phi,z})_{a,b,c-\frac{1}{2}}}{z_{c+\frac{1}{2}} - z_{c-\frac{1}{2}}}\end{aligned} \tag{7.7}$$

where $j_{u,x}$, $j_{u,y}$ (*resp.* $j_{\phi,x}$, $j_{\phi,y}$ and $j_{\phi,z}$) are the respective components of $\mathbf{j}_u$ (*resp.* $\mathbf{j}_\phi$). By definition, $\mathbf{j}_u = \mathbf{u} \times \mathbf{e}_z$ has no component along $\mathbf{e}_z$. We shall insist here on the fact that both (7.6) and (7.7) are calculated at the cell centre from a combination of values defined at the cell faces.

Both (7.6) and (7.7) are involved in the assembling of (7.5) and require the interpolation of respectively the velocity and the electric potential from the cell centre to the cell faces. The order of accuracy of the implemented interpolation schemes has to be higher or equal than that of the discretisation schemes of the different operators involved in (7.5).

Once the treatment of the current density has been accurately handled, the next step consists in dealing with the Lorentz force. In the flow equations, the latter appears in the momentum conservation (7.1), but it may be involved at several stages within the numerical algorithm. [152] described two possible algorithms. In a first one, the Lorentz force is computed only once at the cell centre in the very first step of the algorithm, while it is computed several times both at the cell centre and faces throughout the second algorithm. The first method is the better choice because the involved interpolation schemes required for the calculation of the Lorentz force are less prone to numerical errors and the expression of the subsequent pressure boundary condition is simpler [152]. Consequently we shall use the first method, whose detailed steps are given in the next subsection, and describe how the Lorentz force is derived at the centre of a given mesh cell.

With a unidirectional magnetic field along the z-axis, the non-dimensional Lorentz force $\mathbf{F}_L$ at cell centre (a, b, c) is written as:

$$(\mathbf{F}_L)_{a,b,c} = \mathbf{j}_{a,b,c} \times \mathbf{e}_z = (\mathbf{j}_\phi)_{a,b,c} \times \mathbf{e}_z + (\mathbf{j}_u)_{a,b,c} \times \mathbf{e}_z \tag{7.8}$$

Since the components of the current density are located at the cell faces, the computation of the Lorentz force requires the interpolation of $\mathbf{j}$, *i.e.* of $\mathbf{j}_\phi$ and $\mathbf{j}_u$, from the cell faces to the cell centre. Whether the interpolation scheme is both conservative and consistent or neither conservative nor consistent has dramatic consequences on the accuracy of the simulations. Let us first consider the interpolation of the x-component of $\mathbf{j}_\phi$ from the cell faces onto the cell centre. From the direct calculation of $\mathbf{j}_\phi$ at cell centre (a, b, c), it follows:

$$(\mathbf{j}_\phi)_{a,b,c} \cdot \mathbf{e}_x = -\frac{\phi_{a+1,b,c} - \phi_{a-1,b,c}}{x_{a+1} - x_{a-1}} \tag{7.9}$$

The interpolation scheme used in this equation is of second order of accuracy. Another one with the same order of accuracy reads:

$$(\mathbf{j}_\phi)_{a,b,c} \cdot \mathbf{e}_x = \frac{1}{2}\left(\frac{\phi_{a+1,b,c} - \phi_{a,b,c}}{x_{a+1} - x_a} + \frac{\phi_{a,b,c} - \phi_{a-1,b,c}}{x_a - x_{a-1}}\right) \tag{7.10}$$

On a uniform mesh, the mesh spacings are constant and equations (7.9) and (7.10) are subsequently identical. On a non-uniform mesh, which is required to perform MHD simulations at high Ha, only (7.10) is both consistent and conservative. Using Taylor series to expand (7.9) and (7.10), [152] showed that the error involved in (7.9) was twice as big as that related to (7.10) at the first order and bigger at the second order too. As a result, for a structured mesh, the second interpolation scheme applied in (7.10) must be chosen.

Let us now discuss the interpolation required in the computation of $\mathbf{j}_u = \mathbf{u} \times \mathbf{e}_z$ that is obtained at the cell faces. The consistent and conservative interpolation scheme implemented to compute the velocity at the cell centre from its values at the cell faces is given for the x-component of the velocity at cell centre (a, b, c):

$$(u_x)_{a,b,c} = \frac{1}{2}\left[(u_x)_{a+\frac{1}{2},b,c} + (u_x)_{a-\frac{1}{2},b,c}\right] \tag{7.11}$$

The direct use of the velocity components, as stored at the cell centre, characterises a non-consistent treatment of the Lorentz force.

7.2.5 Interpolation schemes in an arbitrary collocated mesh

So far, we have reviewed interpolation schemes designed for structured meshes. In an unstructured one, the mesh cells may exhibit a skewed shape. The discretisation schemes of the respective operators have to address the mesh skewness, as the latter may induce a significant error within the simulations resulting in a loss of up to one order of accuracy [202]. Although the present 3D MHD numerical code is not specifically developed to simulate MHD flows in very complex geometrical configurations in which no structured mesh can be constructed, its elaboration has been achieved in the view for it being as robust and versatile as possible. In this spirit, we have implemented a more robust interpolation scheme for the treatment of the current density and the Lorentz force. Its characteristics are provided in [153]. It simply takes advantage of the current conservation ($\nabla \cdot \mathbf{j} = 0$) from which it follows:

$$\mathbf{j} = \nabla \cdot (\mathbf{j}\mathbf{r}) \tag{7.12}$$

where $\mathbf{r}$ denotes the distance vector and $\mathbf{j}$ is set conservative by construction. Equation (7.12) is at the basis of the interpolation scheme used to calculate the current density at the cell centroid from its value at the cell faces. Using (7.12), we can deduce:

$$\mathbf{j}^c = \frac{1}{V^c}\int_{V^c} \mathbf{j}dV = \frac{1}{V^c}\int_{V^c} [\nabla \cdot (\mathbf{j}\mathbf{r})]dV = \frac{1}{V^c}\sum_{f=1}^{nf} j_n^f \mathbf{r}^f S^f \tag{7.13}$$

where the superscript c (*resp.* f) indicates that the value at the cell centroid (*resp.* face) is considered, V^c is the cell volume, nf the number of cell faces, j_n the current density normal to the cell face, $\mathbf{r}^f$ the distance vector at the cell face and S^f the surface of the cell face. This interpolation scheme is a volume average of the fluxes of current density over a given cell. The Lorentz force at the cell centroid can then be simply computed with (7.13) as:

$$\mathbf{F}_L^c = \mathbf{j}^c \times \mathbf{B} \tag{7.14}$$

Also, the discretisation scheme of the gradient operator shall be modified to account for the mesh skewness. Expressions of schemes including linear skewness corrections are detailed in [153], while a volume skewness correction is implemented in [171].

7.2.6 Detailed steps of the present 3D MHD numerical algorithm

In the build-up of the present numerical code, we have reviewed the influence of the most important components of the code. Since this thesis deals with MHD phenomena at low magnetic Reynolds number Rm, the code has been designed to solve the 3D MHD equations within the low-Rm approximation, *i.e.* equations (7.1), (7.2) and (7.3) together with Ohm's law (1.20). To meet the requirements on the mesh, we make sure that at least 3 to 4 mesh cells are present within both the Hartmann and the Shercliff layers (tests in section 8.3.1). We have developed the code from an open source OpenFOAM 1.4.1 framework [205, 206] on a collocated mesh. Using the findings of [152, 153], we have implemented both conservative and consistent interpolation schemes to deal with the current density and the Lorentz force.

The pressure-velocity coupling is treated using the same PISO algorithm introduced in section 5.3 in which the $\mathbf{Q}$ term (see equations (5.12) and following) includes the Lorentz force term. The Poisson equation for the pressure is obtained by taking the divergence of (5.12) term-by-term. The divergence of the Lorentz force does not depend on the electric potential so that the latter can be ignored in the treatment of the pressure-velocity coupling. Nevertheless, although it has never been achieved in any numerical computation to our knowledge so far, the present numerical code addresses the coupling between the kinematic and the electric variables by going through the numerical loop at least twice per time step in the unsteady computations. We also insist that both steady and unsteady cases were simulated with the same numerical procedure and in particular, no steady solver was used. We shall now detail the sequence of steps performed by our code. The corresponding OpenFOAM code is provided in appendix.

The numerical procedure performed within one time step eventually reads:

1. Estimate the velocity at the cell centre from the momentum equation deprived of the pressure term;

$$\hat{\mathbf{u}}_q^c = \mathbf{u}_m^c + \Delta t \left[\frac{1}{Re}\mathtt{D}(\mathbf{u}) - \mathtt{C}(\mathbf{u}) + N\mathtt{F}_\mathtt{L}(\mathbf{u}, \phi) \right]_q^c \tag{7.15}$$

   where $\mathtt{D}$, $\mathtt{C}$ and $\mathtt{F}_\mathtt{L}$ denote respectively the diffusion, convective and Lorentz force terms once the time and space discretisation has been performed. The superscript c indicates quantities taken at the cell centre; the subscript m (*resp.* q) is the time (*resp.* PISO) iteration counter at the previous time (*resp.* PISO) step. Δt is the time step.

   For simplicity, we suppose here that an Euler discretisation scheme is used to update the term of the velocity time derivative $\partial_t \mathbf{u}$, hence the term u_m^c on the right-hand side. In fact, we use a backward quadratic scheme of second-order accuracy.

2. Interpolate to obtain the fluxes of velocity ($\hat{\mathbf{u}}_q^f \cdot \mathbf{S}^f$) at the cell faces where the superscript f denotes quantities at cell faces.

3. Assemble and solve the Poisson equation for the pressure;

$$\sum_{faces} \frac{1}{A_M} (\nabla p)_q^f \cdot \mathbf{S}^f = \sum_{faces} \hat{\mathbf{u}}_q^f \cdot \mathbf{S}^f \tag{7.16}$$

where A_M is defined in section (5.3).

4. Explicit correction of both the fluxes of velocity and the velocity with the pressure term;

$$\mathbf{u}^f_{q+1} \cdot \mathbf{S}^f = \hat{u}^f_q \cdot \mathbf{S}^f - \frac{1}{A_M}(\nabla p)^f_q \cdot \mathbf{S}^f \tag{7.17}$$

$$\mathbf{u}^c_{q+1} = \hat{\mathbf{u}}^c_q - \frac{1}{A_P}(\nabla p)^c_q \tag{7.18}$$

5. Implicit correction: update non-linear terms of (7.15) using the corrected velocity and fluxes of velocity and solve (7.15) to obtain a new velocity;

6. PISO loop: repeat steps (2) to (5) until tolerance is reached, then;

$$u^f_{m+1} = u^f_{q+1} \tag{7.19}$$

$$\mathbf{u}^c_{m+1} = \mathbf{u}^c_{q+1} \tag{7.20}$$

$$p^c_{m+1} = p^c_{q+1} \tag{7.21}$$

7. Assemble and solve the Poisson equation for the electric potential using the fluxes of velocity;

$$\sum_f^{Nf} (\nabla\phi)^f_{m+1} \cdot \mathbf{S}^f = \sum_f^{Nf} (\mathbf{u}^f_{m+1} \times \mathbf{e}_z) \cdot \mathbf{S}^f \tag{7.22}$$

where the magnetic field is assumed to be unidirectional along the $z-$axis.

8. Calculate the fluxes of current density at the cell faces;

$$\mathbf{j}^f_{m+1} \cdot \mathbf{S}^f = -(\nabla\phi)^f_{m+1} \cdot \mathbf{S}^f + (\mathbf{u}^f_{m+1} \times \mathbf{e}_z) \cdot \mathbf{S}^f + \mathtt{SK}(\phi_{m+1}) \tag{7.23}$$

where $\mathtt{SK}(\phi_{m+1})$ is a correction term added to address the possible mesh skewness.

9. Interpolate the current density from the cell faces to the cell centre;

$$\mathbf{j}^c_{m+1} = \frac{1}{V^c} \sum_f^{Nf} (\mathbf{j}^f_{m+1} \cdot \mathbf{S}^f)(\mathbf{r}^f - \mathbf{r}^c) \tag{7.24}$$

10. Calculate the Lorentz force term at the cell centre;

$$(\mathbf{F}_L)^c_{m+1} = \mathbf{j}^c_{m+1} \times \mathbf{e}_z \tag{7.25}$$

11. Implement the kinematic-electric coupling: iteration of loop from steps (1) to (10).

Chapter 8

Validation of the 3D MHD numerical code and physical models

In this chapter, we review the different steps performed to validate the present 3D MHD numerical code. The successive tests shall be achieved for MHD flows in configurations of increasing complexity. Firstly, we show the ability of the code at capturing the 3D non-MHD flow dynamics. 3D simulations of MHD cylinder wakes by [189] included the use of a wall function. We shall introduce this one in detail and describe its implementation into our numerical code. We then consider the Shercliff flow for which analytical expressions for the velocity and pressure drops are available (see section 1.4). We shall subsequently compare our numerical solutions obtained from 3D full DNS and 3D simulations using wall functions. In the final validation test, we compute the MHD flow past a square cylinder in the configuration investigated by [189]. As a conclusion on this chapter, we compare the solutions obtained from two different numerical methods in two simple examples at $N < 1$ and $N > 10$, respectively.

8.1 Non-MHD validation test: Square cylinder wake

The first validation test aims at checking the ability of the present code to deal with the non-MHD 3D flow dynamics. We consider the flow past an infinitely long square cylinder placed at the wake centreline between two infinite planar impermeable parallel walls as depicted on figure 8.1. The cylinder width is denoted W and the distance between both walls $2b$. The origin of the frame of reference is taken at the cylinder axis at the exact cylinder mid-span. The Reynolds number is defined as $Re_W = WU_0/\nu$ where U_0 is the maximum of the inlet velocity profile. The flow regimes and related patterns of the non-MHD square cylinder wake are described in details in section 3.1. Following [189], we consider the flow at $Re_W = 200$. At this Re_W, the flow is 3D unsteady with the presence of mode-A streamwise vortices in the cylinder wake. The Kármán vortices may also exhibit disruption at the vicinity of the midspan region. Testing our code to this configuration shall therefore bring valuable information on its ability to capture 3D structures accurately. The resulting values of both the pressure drag coefficient C_{Dp} and the Strouhal number St shall be compared to those provided in [189].

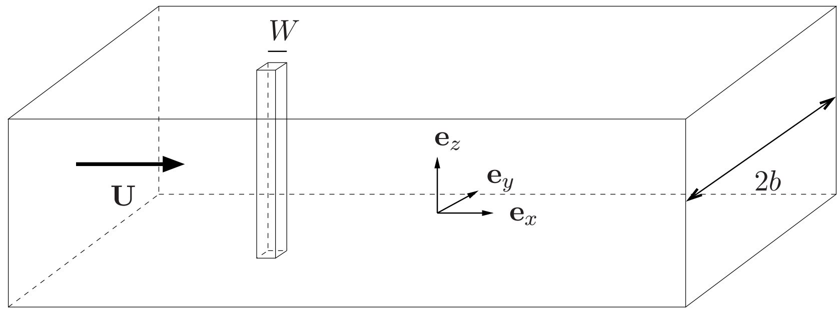

Figure 8.1: Configuration of the non-MHD flow past a square cylinder between two parallel walls.

8.1.1 Numerical set-up

The non-MHD flow motion is governed by the Navier-Stokes equations (7.1) and (7.2) in which the fluid is assumed incompressible and the magnetic field is zero. The inlet and outlet boundaries are located at $x = -10$ and $x = 30$, respectively, whereas in [189], they are located at $x = -5$ and $x = 15$, respectively. The duct side walls are located at $y = \pm 5$ and the upper and lower boundaries normal to the cylinder axis at $z = \pm 5$, as in [189]. The duct side walls and the cylinder surface are impermeable: a no-slip condition (1.22) and a homogeneous Neumann boundary are applied to the velocity and pressure fields respectively at these boundaries. At the upper and lower boundaries of the computational domain, a slip (1.23) and homogeneous Neumann conditions are imposed to the velocity and the pressure fields, respectively. At the inlet, we prescribe the velocity profile over the whole cross-section. The profile is a uniform block profile with intensity U_0 as in [189]. At the outlet, a homogeneous Neumann condition is implemented for the velocity field and the pressure is set to an arbitrary value fixed to zero.

We have designed a non-uniform mesh Cartesian in all three directions. The mesh has been refined at the vicinity of the duct walls and cylinder surface, while it has been relaxed at the vicinity of both the centre-plane $z = 0$ and the outlet boundary. The details of this mesh are provided in table 8.1. In agreement with [189], special care has been dedicated to the resolution of the mesh in the near-wake of the cylinder. Our mesh exhibits a total number of points close to that of [189]. Nevertheless, the computational method of the latter requires a fully uniform mesh and the CPU resources available to those authors have limited the maximum number of mesh points. Compared to ours, the mesh of [189] is then over-resolved in some regions of the domain and under-resolved in some others, especially in the boundary layer at the cylinder lateral faces. Also, their computational domain extends over a

	Present	Mück *et al.* [189]
Number of grid points $n_x \times n_y \times n_z$	$200 \times 90 \times 80$	$200 \times 100 \times 80$
Non-dimensional distance between the nearest grid point and the cylinder surface	0.03	0.05
Total number of points	1.4×10^6	1.6×10^6

Table 8.1: Main characteristics of the meshes used respectively in the present code and [189] to simulate the non-MHD channel flow past a square cylinder at $Re_W = 200$.

shorter distance both upstream and downstream the cylinder. The feedback effect of the downstream boundary in [189] is accurately compensated for by the use of a non-reflective boundary condition at the outlet.

8.1.2 Results

We have simulated the flow at $Re_W = 200$. The initial flow conditions and simulation time are set as in [189]. The initial velocity field inside the domain is set to a uniform and unidirectional vector field along the streamwise direction with an intensity equal to U_0, the maximum of the inlet velocity profile. The computations have been run over a total time equal to 1000 turnover times $t_u = W/U_0$. Snapshots of the resulting flow are shown in figure 8.2. Disrupted Kármán vortices and mode-A streamwise vortices are observed in the wake as pointed out in the simulations of [189]. We furthermore have singled out the presence of secondary recirculation regions at the lateral faces of the cylinder as seen on figure 8.3. This feature shall indeed appear before the flow becomes unsteady and remain at higher Re_W [101, 104]. This was however overlooked in [189] probably due to under-resolved boundary layers at the cylinder lateral faces.

We have determined both the pressure drag coefficient $C_{Dp} = 1.70$ and the Strouhal number $St = 0.164$. These values compare very well with those of [189] exhibiting a discrepancy of 3% and 1% for respectively C_{Dp} and St. Slight differences between our numerical set-up and that of [189] might explain the small discrepancy between the respective values of C_{Dp} and St. The inlet boundary is only 5 cylinder widths away from the cylinder axis in [189] and it is located twice as far from the cylinder axis in our numerical set-up. Also, the boundary layers at the lateral cylinder faces are better resolved in our computations than in those of [189]. From this validation test it follows that the present numerical code effectively captures the 3D non-MHD flow dynamics and the flow coefficients are recovered within a very satisfactory accuracy.

8.2 High Ha flows: implementation of a wall function

Finite-volume based numerical computations of high Ha flows have been limited so far by the prohibitive demand in both CPU storage and resources required to resolve the flow in the very thin

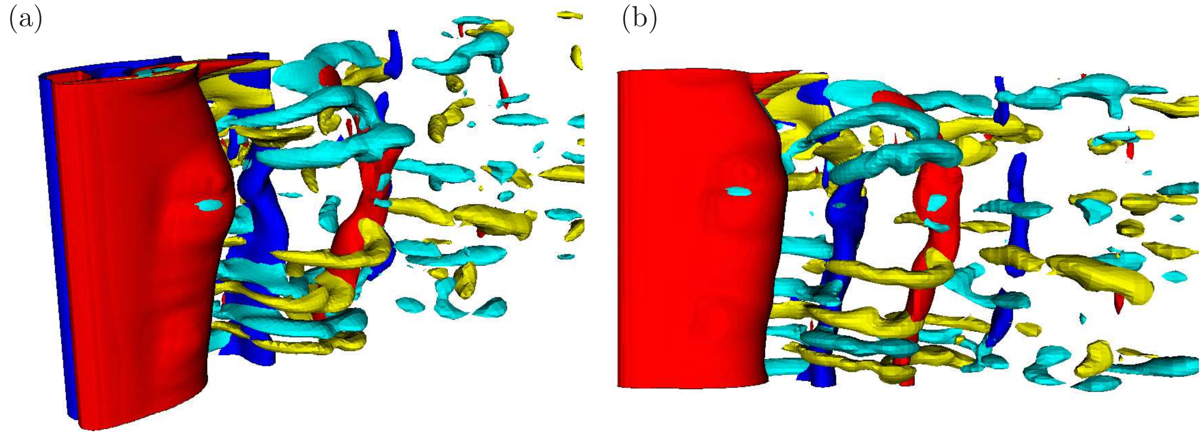

Figure 8.2: Vortex street for $Re = 200$ and $Ha = 0$ at $t = 746t_u$: (a) 3D and (b) side views. Degenerated mode-A streamwise vortices are depicted by iso-surfaces of $x-$vorticity [$\omega_x^\star = -1.2$ (*resp.* $\omega_x^\star = -1.2$) in cyan (*resp.* yellow)] and Kármán vortices by iso-surfaces of $z-$vorticity [$\omega_z^\star = -2.4$ (*resp.* $\omega_z^\star = 2.4$) in blue (*resp.* red)]. $\omega_i^\star$ is the i-component of the non-dimensional vorticity with $\omega_i = (U_0/W)\omega_i^\star$.

Hartmann layers. To tackle this issue, numerical methods [189, 145, 167, 173] have relied on theoretical approaches describing the flow at high Ha in the Hartmann layers [181, 165, 172]. Later [158] have derived more accurate expressions for the velocity and current density field inside these layers. Since the flow can be dealt with analytically within the Hartmann layers, a specific boundary condition has been designed to accurately treat the flow at an interface located at some distance away from the Hartmann layers. This boundary condition is a *wall function* and its implementation allows the simulation of very high Ha flows without the need to resolve the flow inside the very thin Hartmann layers. We shall now describe the wall function which was used in [189, 145, 167]. Its implementation in the present code is required as it was used in the 3D computations of the MHD flow past a square cylinder under the influence of an externally applied magnetic field parallel to the cylinder axis achieved by [189]. We shall validate the present code using the results of these computations.

8.2.1 Description of the wall function

We assume that both Ha and N are much bigger than unity so that all quantities are expressed using Taylor series with respect to both Ha^{-1} and N^{-1} [157, 154]. We shall derive two conditions, one for the velocity and one for the electric potential at an interface located at some distance off the Hartmann layer. We denote Γ_H this interface. The Hartmann wall is considered as electrically insulating and no current injection is present at the wall. We decompose the velocity and electric potential gradient into the sum of their component along the direction of the magnetic field and their component in the plane normal to the magnetic field. The former (*resp.* latter) component is

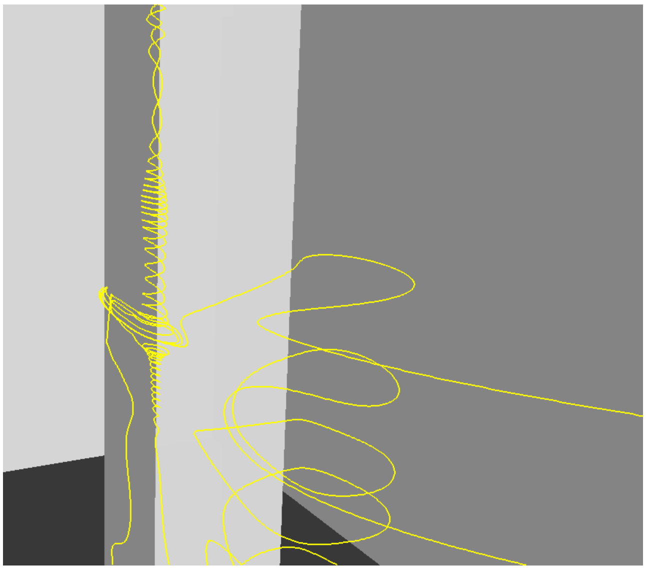

Figure 8.3: Snapshot of the vortex street at $t = 1000t_u$. Kinematic streamlines showing the presence of a secondary recirculation region at the mid-span of the cylinder lateral face. Flow from left to right.

indicated by the subscript n (*resp.* $\perp$) and $\mathbf{n}$ is the unit vector parallel to the magnetic field.

$$\mathbf{u} = \mathbf{u}_\perp + u_n\mathbf{n} \tag{8.1}$$

$$\nabla\phi = \nabla_\perp\phi + (\partial_n\phi)\mathbf{n} \tag{8.2}$$

Under the condition $Ha \gg 1$, inside the Hartmann layer, the normal derivative dominates the tangential ones and the normal coordinate can be replaced by a stretched coordinate $\eta = nHa$. The non-stretched normal coordinate n is of order Ha^{-1} in the Hartmann layer, while the stretched one is of order one in this layer. One must therefore distinguish two sets of variables whether the flow is considered inside the Hartmann layer (tangential coordinates and stretched normal coordinate η) or outside it in the core flow (tangential coordinates and non-stretched normal coordinate n). Using these two sets of coordinates, one can derive two sets of flow equations and subsequently two sets of solutions inside and outside the Hartmann layer, respectively. Finally a condition matches the respective solutions at an intermediate scale between the order Ha^{-1} and the order one, *i.e.* between the solutions in the core flow and that in the Hartmann layer. This condition might involve some tedious mathematics as for example a variable defined at a given order inside the Hartmann layer might be linked to one defined at a different order in the core flow. Detailed calculations are available in [154]. In the following explanations we shall only provide the results of these calculations to derive the expression of the wall function.

Under the condition $Ha \gg 1$, the velocity in plane normal to the magnetic field decays exponentially within the Hartmann layers to zero at the wall and the profile is given by equation (1.31). The exponential decay of the velocity to a constant inside the Hartmann layer implies a simple matching condition at Γ_H:

$$\lim_{n \to 0} \mathbf{u}^{OUT} = \lim_{\eta \to \infty} \mathbf{u}^{IN} \tag{8.3}$$

where the origin of the frame of reference is taken at the Hartmann wall and $\mathbf{u}^{OUT}$ and $\mathbf{u}^{IN}$ denote the velocity outside and inside the Hartmann layer, respectively.

The expression of the velocity component parallel to the magnetic field at Γ_H follows from the integration of the mass conservation (7.2) using the analytical expression of the velocity profile inside the Hartmann layer (1.31) and the matching condition (8.3) at Γ_H:

$$u_n^b = \frac{-1}{Ha}(\nabla_\perp \cdot \mathbf{u}_\perp^b) \tag{8.4}$$

where the b superscript indicates quantities in the bulk flow. Similarly a condition on the normal gradient of $\mathbf{u}_\perp$ is derived by taking the curl of the Ohm's law at Γ_H:

$$\partial_n \mathbf{u}_\perp^b = 0 \tag{8.5}$$

The condition on the electric potential is obtained from the integration of the conservation of electric current (7.3) across the Hartmann layers and using both (1.31) and the matching condition for the velocity (8.3) at Γ_H [181, 158]:

$$\nabla_n \phi^b = \frac{-1}{Ha}[(\nabla_\perp \times \mathbf{u}_\perp^b) \cdot \mathbf{n}] \tag{8.6}$$

Note that this expression is valid only if no current is injected through the Hartmann walls. Otherwise, an additional current source term shall be included on the right-hand side of (8.6) [158].

Equation (8.6) shows that the current entering the Hartmann layer is of order Ha^{-1}. Since $Ha \gg 1$, one can neglect the variations of the electric potential along the direction normal to the Hartmann wall and reformulate the expression of the normal gradient of electric potential at the order Ha^{-1} as:

$$\nabla_n \phi^b = \frac{-1}{Ha}\nabla_\perp^2 \phi^b \tag{8.7}$$

This equation means that the current entering inside the Hartmann layer at Γ_H diffuses in this layer, *i.e.* (8.7) expresses the conservation of current at the interface Γ_H.

At the order Ha^{-1}, the wall function consists of the following system of boundary conditions at

Γ_H:

$$u_n = 0 \tag{8.8}$$

$$\partial_n u_\perp = 0 \tag{8.9}$$

$$\nabla_n \phi = \frac{-1}{Ha}\nabla_\perp^2 \phi \tag{8.10}$$

The system of equations (8.8) and (8.9) corresponds to the slip condition. It means that any fluid transfer between the Hartmann layers and the core flow is neglected by this wall function. It is therefore unable to capture possible Ekmann secondary recirculation flows at the interface Γ_H. In contrast, the quadratic shape of the vortices at the vicinity of Γ_H is accurately rendered by the condition on the electric potential (8.10) [154] (see also the simulations of [189]).

Weak inertial effects in the Hartmann layers are responsible for the fluid transfer between the Hartmann layer and the core flow. [158] improved the previous wall function by extending the Taylor series up to terms of order $(Ha^{-1}N^{-1})$. This provides a non-zero velocity normal to Γ_H which replaces condition (8.8) and describes the fluid transfer across the interface Γ_H. The present code does not include this improved version of the wall function, only the one described by equations (8.8), (8.9) and (8.10). We shall now explain how the latter is implemented into the code.

8.2.2 Numerical implementation of the wall function

The interface Γ_H, where the wall function has been derived, is defined at an intermediate scale between the orders one and Ha^{-1}. This definition does not provide a clearly identified physical location of Γ_H and a test on this location shall therefore be performed to assess its influence on the flow and how it shall be determined (see section 8.3.2).

Both boundary conditions on the velocity (8.8) and (8.9) are implemented in a straightforward way at Γ_H. In contrast, the boundary condition on the electric potential (8.10) requires special care. Indeed, the electric potential has to satisfy both the current conservation (7.3) and condition (8.10) so that an iterative procedure is implemented to ensure both requirements are fulfilled at any time step.

The implementation of the wall function only results in a modification of step 7 of the numerical algorithm described in section 7.2.6. At the end of step 6, the PISO loop addressing the pressure-velocity coupling is over. Before solving the Poisson equation for the electric potential at step 7, the normal gradient of the electric potential ϕ defined in equation (8.10) is derived using the value of ϕ at previous iteration k. The Poisson equation derived from the current conservation is then solved to determine the new distribution of ϕ at current iteration $(k+1)$. The two previous steps are iterated until both (7.3) and (8.10) are satisfied within the predefined tolerance. The numerical algorithm then goes through steps 8 to 11 as stated in section 7.2.6.

[145, 189, 167] implemented an under-relaxation scheme to improve the convergence rate of the iteration loop between (7.3) and (8.10). Such scheme has been also tested in the present numerical code for Ha up to about 300 without much effect on the CPU time. We have therefore not included it in the present code. Its influence is expected to be more sensitive for very high Ha simulations. We have found that the most spectacular improvements in numerical stability and convergence were obtained by ensuring that the treatment of the current density and Lorentz forces was consistent [152].

8.3 MHD flow in an electrically insulating duct

We consider the configuration of the Shercliff flow sketched in figure 8.4. This classical MHD problem is presented in section 1.4.2. The analytical expression for the velocity profile is given by equation (1.37).

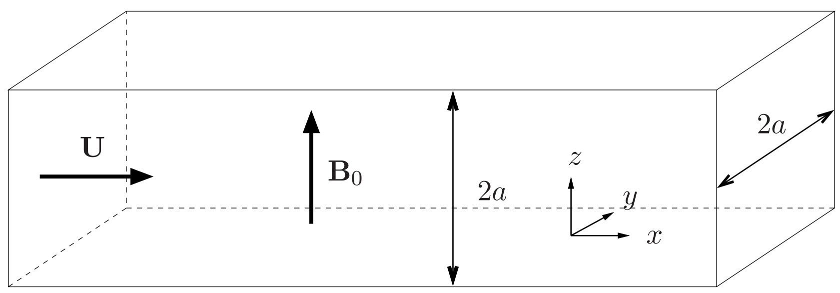

Figure 8.4: Configuration of the Shercliff flow.

The Shercliff flow has been investigated using the 3D numerical code with the use of wall functions and without it (full DNS). We shall compare the results provided by each method. For these simulations, the duct has a square cross-section of width $2a$. The origin of the frame of reference is at the centre of the duct cross-section located at equal distance to the inlet and the outlet. The streamwise direction is set along the $x-$axis and an external, steady, homogeneous, uniform and unidirectional magnetic field $\mathbf{B}_0$ is applied along the $z-$axis. Using a as characteristic length, the Hartmann walls are consequently located at $z = \pm 1$ and the Shercliff walls at $y = \pm 1$, while the inlet and outlet are located at $x = -10$ and $x = 10$, respectively. At the Shercliff walls, the no-slip condition (1.22) is imposed for the velocity and a homogeneous Neumann one is applied for both the pressure and electric potential. At the inlet, a homogeneous Neumann condition is imposed for all field. At the outlet, a homogeneous Neumann condition is applied for the velocity and electric potential, while a homogeneous Dirichlet condition is imposed for the pressure.

The boundary conditions at the Hartmann walls for the full DNS are:

$$\begin{aligned} \mathbf{u} &= \mathbf{0}, \\ \partial_n \phi &= 0, \\ \partial_n p &= 0; \end{aligned} \tag{8.11}$$

and for the simulations using wall functions:

$$\begin{aligned} u_n = 0 \quad &\text{and} \quad \partial_n \mathbf{u}_\perp = 0, \\ \partial_n \phi &= -Ha^{-1} \nabla_\perp^2 \phi, \\ \partial_n p &= 0. \end{aligned} \tag{8.12}$$

A constant and uniform streamwise pressure gradient is applied in the duct to drive the flow. The latter is added as a constant source term in the momentum equation (7.1). In the numerical algorithm, this term is added on the right-hand side of equation (7.15).

8.3.1 Full DNS

Full DNS have been achieved to investigate the flow at $Ha = 50$, 100 and 200 at a fixed $Re = 50$. The simulations have been run on a Cartesian mesh featuring 100, 80 and 80 points along the x-, y- and z-axes, respectively. The mesh is refined in the Hartmann and Shercliff layers. In all cases, at least 4 mesh nodes are present inside these layers with a smooth mesh transition between the boundary layers and the core flow. The respective velocity profiles in the cross-section $x = 0$ along the y- and z-axes are shown in figures 8.5(a-b). One observes that the discrepancy between the numerical and analytical velocity profiles is very small of the order of 1%. This shows that the present code deals very accurately with the boundary layers.

We have also made sure that the code properly recovers the streamwise pressure drop in the duct. To this end, we have performed two extra computations of the case at $Ha = 100$ with a mesh featuring 5 (*resp.* 2) nodes in the Hartmann layer and 2 (*resp.* 5) nodes in the Shercliff layer. We denote these meshes m_1 and m_2, respectively. The reference mesh used in the previous test at $Ha = 100$ is denoted m_3 and meshes m_1 and m_2 are based on mesh m_3. Mesh m_1 is obtained by decreasing the total number of points along the $y-$axis from 80 down to 40 and keeping a constant spatial step along this axis. Mesh m_2 is obtained by transferring more mesh nodes from the Hartmann layers into the core flow while keeping constant the number of mesh nodes along the z-axis. The shape of the velocity profiles is accurately recovered whatever the mesh, but an error appears on the pressure drop as shown in table (8.2). A good resolution is indeed required in the Hartmann layers to render

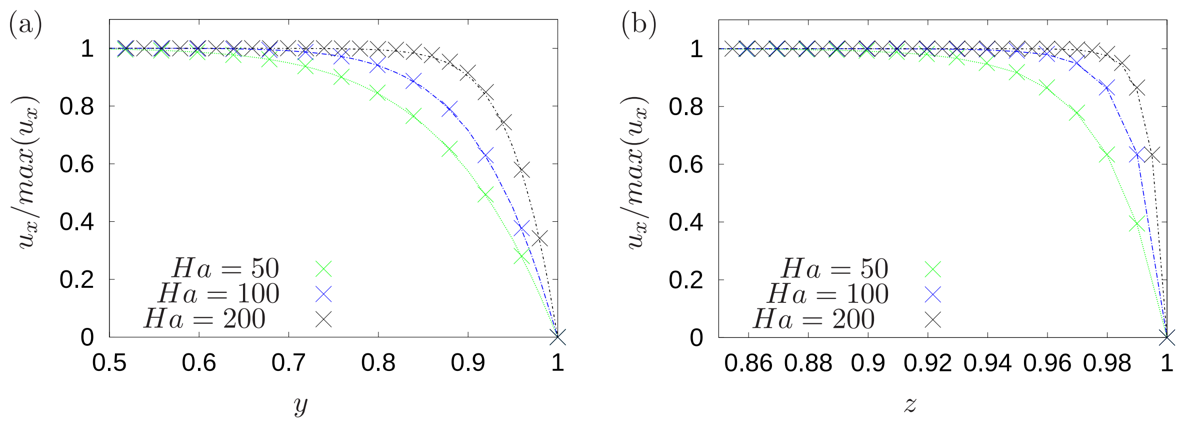

Figure 8.5: Shercliff flow at $Re = 50$ from full DNS: numerical (line) and analytical ($\times$) streamwise velocity profiles in the cross-section ($x = 0$) (a) across the magnetic field for ($|y| \leq 1, z = 0$) and (b) along the magnetic field for ($y = 0, |z| \leq 1$).

	Mesh m_1	Mesh m_2	Mesh m_3
$n_H \times n_S$	5×2	2×4	5×4
$\epsilon_K = \|1 - K(m_i)/K_{sh}\|$	1.01%	2.80%	0.61%

Table 8.2: Error in the pressure drop ϵ_K relative to the analytical value K_{sh} (1.40). n_H (*resp.* n_S) is the number of mesh nodes inside the Hartmann (*resp.* Shercliff) layer. Full DNS at $Ha = 100$ and $Re = 50$.

accurately the distribution of current density inside these layers, as the circulation of current in the Hartmann layers controls the flow in the core.

8.3.2 Simulations using wall functions

Simulations using wall functions have been performed to investigate the Shercliff flow at $Ha = 50$, 100 and 1000 for $Re = 50$. The simulations have been run on a Cartesian mesh featuring 10, 80 and 80 points along the x-, y- and z-axes. In the cases $Ha = 50$ and 100, the mesh is completely uniform with the same mesh spacing in all the directions. This mesh ensures that at least 4 points are present in the Shercliff layers. For $Ha = 1000$, the mesh has been refined in the Shercliff layers with a smooth transition between these layers and the core flow and the same distributions of mesh nodes along both the $y-$ and z-axes. The respective velocity profiles in the cross-section $x = 0$ along the y- and z-axes are reported in figures 8.6(a-b).

One observes that the analytical velocity profile across the magnetic field is recovered with an excellent accuracy. The order of accuracy of the wall function is $O(Ha^{-1}N^{-1})$ and its performances are therefore expected to be better for $Ha \gg 1$, even though the numerical velocity profile at $Ha = 50$ is already in excellent agreement with the analytical solution. The use of wall functions at the Hartmann walls results in a constant velocity along the magnetic field due to the use of the slip boundary condition for the velocity. An error is therefore committed in the vicinity of the Hartmann

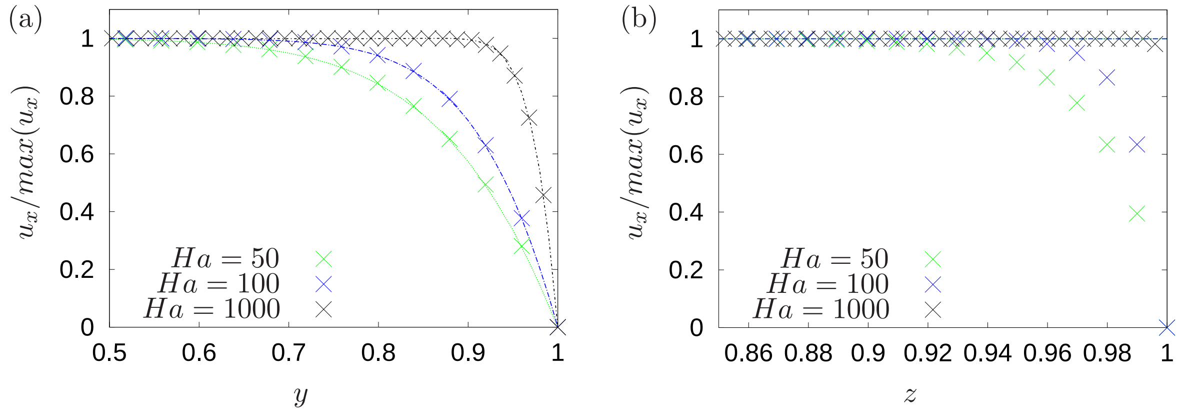

Figure 8.6: Shercliff flow from simulations at $Re = 50$ using wall functions: numerical (line) and analytical ($\times$) streamwise velocity profiles in the cross-section ($x = 0$) (a) across the magnetic field for ($|y| \leq 1, z = 0$) and (b) along the magnetic field for ($y = 0, |z| \leq 1$). The numerical profiles on (b) all collapse along the same line with $u_x(x)/max(u_x) = 1$.

	Mesh w_1	Mesh w_2	Mesh w_3
Location of the wall function	$z = \pm(1 - 2Ha^{-1})$	$z = \pm(1 - Ha^{-1})$	$z = \pm 1$
$\epsilon_K = \lvert 1 - K(m_i)/K_{sh} \rvert$	2.01%	1.62%	1.90%

Table 8.3: Error ϵ_K in the pressure drop relative to the analytical value K_{sh} (1.40). Simulations with wall functions at $Ha = 100$ and $Re = 50$.

layers in comparison with the analytical profile. The increase in Ha improves the accuracy of the wall function and the error committed thus decreases. In particular, the use of the wall function is recommended to simulate the flow at very high values of Ha for which the CPU cost of full DNS is prohibitive, as shown here for the flow at $Ha = 1000$.

We have investigated the influence of the location of the wall function on the streamwise pressure drop. The mesh used for the previous test is denoted w_3 in which the wall function is imposed at $z = \pm 1$. Meshes w_1 and w_2 have then been designed by placing the wall function at $z = \pm(1 - 2Ha^{-1})$ and $z = \pm(1 - Ha^{-1})$, respectively. Meshes w_1, w_2 and w_3 all feature the same numbers of mesh nodes along each axis. The respective errors on the streamwise pressure drop are given in table (8.3). They are all around 2%, but the best agreement is obtained with mesh w_2. The implementation of the wall function results in a flat velocity profile along the magnetic field. In the vicinity of the wall, the velocity is slightly overestimated and under-estimated in the region between the plane where the wall function is implemented and the Hartmann wall. It is therefore recommended to implement the wall function at a distance off the Hartmann wall equal to the thickness of the Hartmann wall so that the respective errors made on either sides of the boundary compensate each other.

Finally, we have investigated the influence of the number of points along the y-axis. Again we have considered the results at $Ha = 100$ and $Re = 50$ obtained from mesh w_3. This mesh has been modified by doubling the number of points along the y-axis to yield an additional mesh featuring then

$10 \times 160 \times 80$ mesh nodes along $\mathbf{e}_x \times \mathbf{e}_y \times \mathbf{e}_z$. The subsequent error made on the pressure drop is 1.71%, *i.e.* lower than that committed with the use of mesh w_3. The agreement of the velocity profile along the y-axis is also better than that reached with mesh w_3. As stated in [167], due to the use of the wall function, the flow is almost invariant along the direction of the magnetic field and the coupling between the velocity and the electric potential therefore depends only on the y-direction. A better resolution of the mesh along this direction thus improves the accuracy of the numerical solution.

8.4 MHD flow past an insulating square cylinder

8.4.1 Configuration and numerical set-up

We now consider the MHD flow past an electrically insulating square cylinder in a rectilinear duct. The configuration under investigation is sketched in figure 8.7. The cylinder of square cross-section is placed at equal distance to both duct side walls and spans over the full height of the duct. The cylinder width is W, the duct height (*resp.* width) along the $z-$axis ($y-$axis) is denoted $2a$ (*resp.* $2b$). An externally applied, homogeneous, steady, uniform magnetic field $\mathbf{B}_0 = B_0\mathbf{e}_z$ is imposed along the cylinder axis. This configuration is taken over from [189] and features $2a = 2b = 10W$. We shall assess the performances of the present 3D code by comparing our results to those provided in [189].

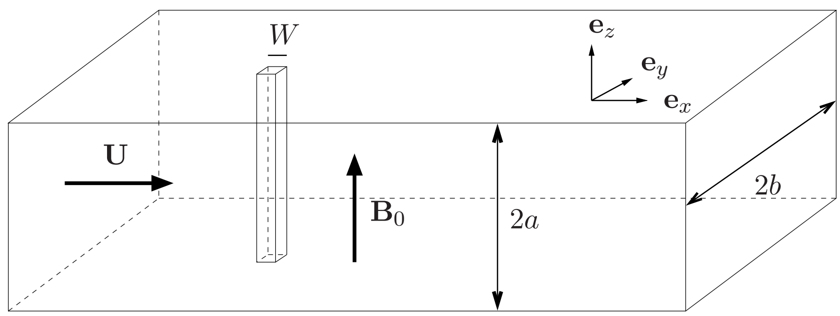

Figure 8.7: Configuration of the MHD flow past a square cylinder in a duct under an axial magnetic field as investigated in [189].

The flow has been computed at a fixed $Re_W = 200$ for $Ha = 50$ ($N = 0.5$), $Ha = 100$ ($N = 2$) and $Ha = 265$ ($N = 14$). As in [189], we have implemented wall functions at the top and bottom boundary planes normal to the magnetic field. In the present computations, for each case, the flow is at rest at the start of the simulation. [189] achieved successive computations at $Re_W = 200$ by gradually increasing Ha from 0 up to 425 and using the resulting flow at a given Ha as initial conditions for the simulation at the next value of Ha. [189] performed all the simulations with the same mesh, while the meshes used in the present computations have been designed so as to feature at least 4 mesh nodes in the Shercliff and Hartmann layers. The non-MHD case is treated in section 8.1.

The boundary conditions at the Shercliff walls located at $y = \pm 1$ are identical to those used in the simulations of the Shercliff flow (see previous section). The wall function described in section 8.2 is used at the upper and lower boundaries. Following [189], the wall functions are implemented at the physical location of the Hartmann walls at $z = \pm 1$. The conditions at these boundaries are given by (8.12). At both the inlet and outlet located at $x = -10$ and $x = 30$ respectively, the boundary conditions for the pressure are identical to those described in the previous simulations of the Shercliff flow and so is the boundary condition for the electric potential at the inlet. Following [189], we have implemented the following boundary condition for the electric potential at the outlet:

$$\partial_n \phi = (\mathbf{u} \times \mathbf{e}_z) \cdot \mathbf{n} \tag{8.13}$$

This boundary condition is exact only when averaged across the outlet, but it is here applied locally as if the currents normal to the outlet would be absent. This is not the case in general, but as these currents are of the order of Ha^{-1}, they are considered as negligible with respect to the normal component of the current in the limit $Ha \gg 1$. Since the latter condition on Ha is fulfilled in the present test, we shall use this boundary condition for the electric potential at the outlet.

The velocity profile obtained from the computations of the Shercliff flow is imposed at the inlet and a homogeneous Neumann condition is imposed at the outlet. Finally, at the cylinder surface, a homogeneous Neumann condition is applied for both the potential and the pressure while a no-slip condition (1.22) is imposed for the velocity.

8.4.2 Results

In each Ha case, the simulations have been run over a total time higher than $4t_H$ (1.47) and a snapshot of the resulting cylinder wake is shown on figure 8.8. All computations have yielded an unsteady flow and our observations are in full agreement with those made by [189]. At $Ha = 50$, counter-rotating streamwise vortices are present in the flow, although they are dissipated soon after they are released in the wake. The pattern of these streamwise vortices bears many similarities with the non-MHD mode-A pattern (see section 2.2). Only one pair of streamwise vortices is observed in the flow so that it is not possible to determine its exact spanwise wavelength. The Kármán vortices exhibit disruption at their mid-span in between the pair of streamwise vortices and their spanwise shape is therefore strongly distorted. The gap generated by the disruption then broadens as the vortices travel downstream. The ends of the Kármán vortices are perpendicular to the Hartmann layers, in agreement with the theory described in section 1.4.3.

At $Ha = 100$, only Kármán vortices are observed in the wake without any disruption of their spanwise shape. Streamwise vorticity is detected only in the very close vicinity of the cylinder walls, but no streamwise vortex is released in the wake. The lateral free shear layers on both sides of

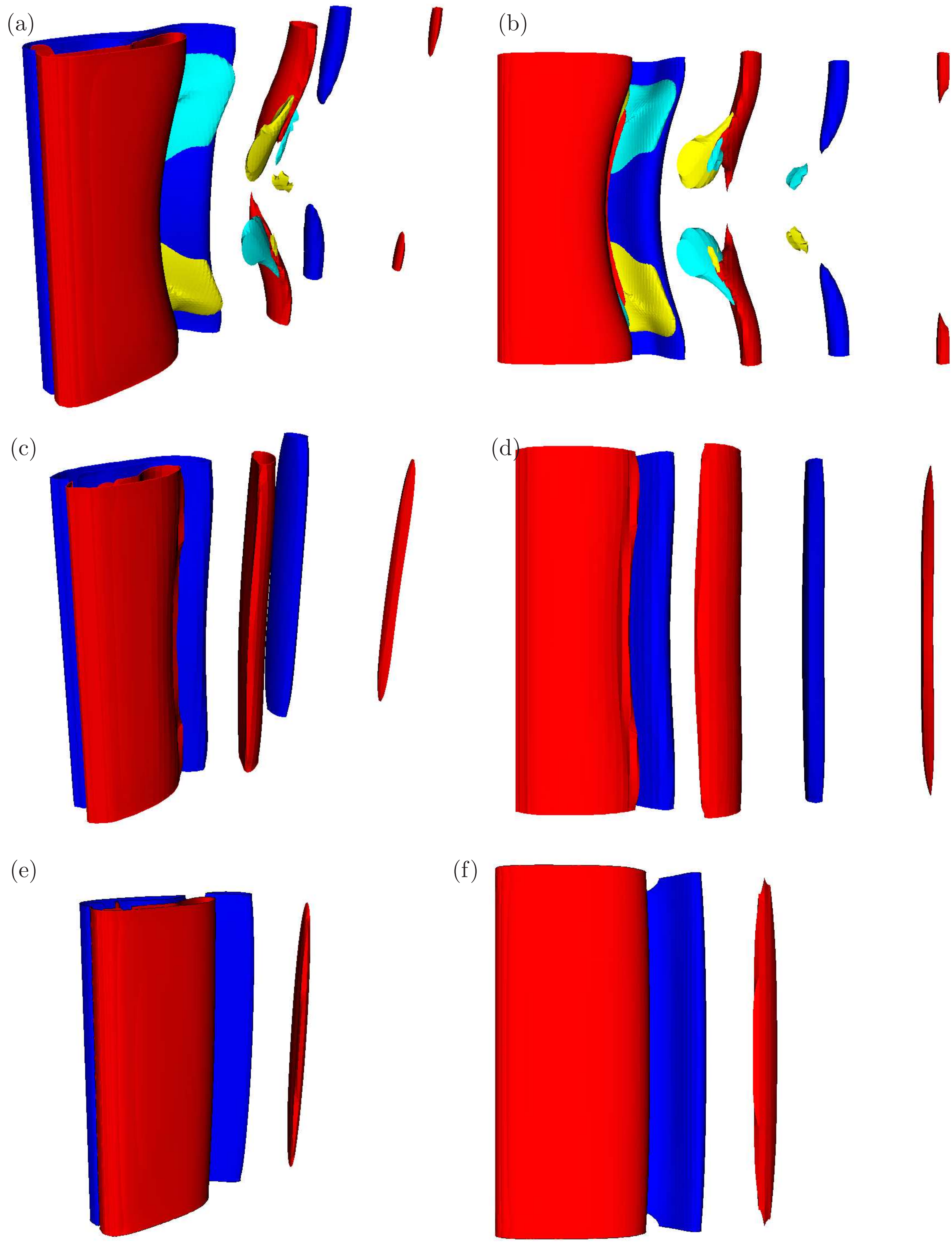

Figure 8.8: Snapshot of the vortex street at $Re_W = 200$ from simulations with wall functions at both upper and lower boundaries at $Ha = 50$ ($N = 0.5$) and $t = 3t_H$ (a-b), $Ha = 100$ ($N = 2$) and $t = 5t_H$ (c-d) and $Ha = 265$ ($N = 14$) and $t = 9t_H$ (e-f). 3D (left) and side (right) views. Colours have the same meaning as in figure 8.2. Iso-surfaces $\omega_x^\star = \pm 0.7$ are not present at $Ha = 100$ and 265.

the cylinder exhibit an almost invariant spanwise shape. The increase of Ha results indeed in a more uniform stretching of the shear layers and spanwise vortices and a suppression of the vortices perpendicular to the magnetic field. Also, the ends of the Kármán vortices are perpendicular to the Hartmann layers and further downstream a cigar-like shape is observed at their ends. The latter feature is due to the generation of a vertical current density from the Hartmann layer outwards linearly dependent with the vertical coordinate. This causes differential rotation at the vortex ends and gives them a quadratic shape (see section 1.5 or e.g. [157, 158]).

The trend described in the flow at $Ha = 100$ is enhanced in the case $Ha = 265$. The flow is still unsteady, but the Kármán vortices detach at a greater distance from the cylinder than in the previous Ha cases indicating that at $Ha = 265$, $Re_W = 200$ is closer to the critical threshold of the transition to unsteadiness. The stretching of the flow structures along the direction of the magnetic field is enhanced and the shedding of the Kármán vortices is achieved along a line almost fully parallel to the magnetic field.

We have computed the time-average pressure drag coefficient C_{Dp} and the Strouhal number St for each case. A curve of the time-average C_{Dp} is provided in [189], but the values shown on the graph are in contradiction with the text. We shall then focus rather on the variations of the curve than on the values of C_{Dp}. The values of C_{Dp} and St versus N obtained in our simulations are reported in figure 8.9. The variations of C_{Dp} with N are identical to those found by [189]. The same trend has been recovered in MHD circular cylinder wakes under the influence of a streamwise magnetic field in experiments by [182] and 2D numerical simulations by [195]. The increase in C_{Dp} observed for $N \geq 0.5$ (*i.e.* for $Ha \geq 50$) follows from the mechanism described in section 6.6.3 for the quasi-2D MHD flow past a circular cylinder. An increase in Ha enhances the pressure drop due to the Hartmann friction and therefore induces an increase in C_{Dp}, but this mechanism is only valid for the quasi-2D flows, which is the case for $N \geq 2$ ($Ha \geq 100$). At $N = 0.5$, three-dimensionality is still significant in the flow as shown by the presence of mode-A streamwise vortices. For low values of N, the pressure drop due to the Hartmann friction does not outweigh that due to the presence of the cylinder. As the influence of the streamwise vortices wanes, the formation region of the Kármán vortices lengthens and exhibits less variations along the spanwise direction. This results in an increase of the adverse pressure gradient due to the presence of this formation region and consequently a decrease in C_{Dp}.

This discrimination between the quasi-2D and the 3D regimes is also noticed on the variations of St with N. For low values of N, $N \leq 0.5$, three-dimensionality is present and St decreases with N, whereas it increases with N in the quasi-2D flow regime for $N \geq 0.5$. In the 3D regime, the increase in N induces the gradual disappearance of mode-B vortices and promotes the formation of mode-A ones. As can be seen from the comparison of figures 8.2 and 8.8(a-b), the increase in N from 0 to 0.5 induces the gradual disappearance of mode-B vortices and strengthening of mode-A ones. Disruptions of the Kármán vortices occurs soon after their release and the shedding mechanism deteriorates, hence the decrease in St. When investigating the MHD circular wake under the influence of a streamwise magnetic field, 2D simulations [195] and experiments [188] also reported a decrease in St as N was increased from 0 up to 0.4. By contrast, for $N \geq 1$, Kármán vortices become strongly two-dimensional and all the available energy contributes to their downstream transport, hence the increase in St.

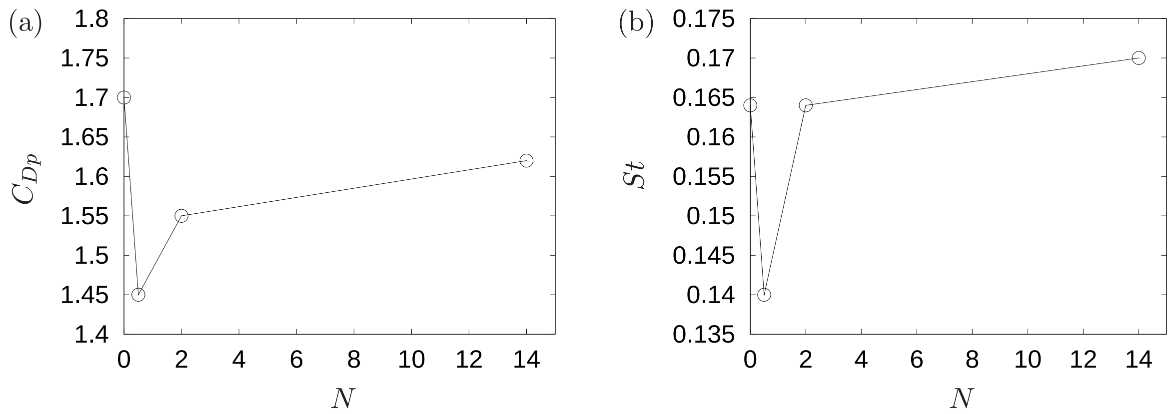

Figure 8.9: (a) Pressure drag coefficient C_{Dp} and (b) Strouhal number St versus Stuart number N.

8.5 MHD flow past a square cylinder: comparison between numerical methods

At this stage of the thesis, three different numerical methods are thus available: full 3D DNS, 3D simulations involving a wall function between the Hartmann layer and the core flow and quasi-2D computations using the SM82 model. Although full DNS are by definition the most reliable method, their CPU cost may be deterrent and promote the use of a wall function or the SM82 model to simulate the flow. One may thus wonder which of the three methods is the most adequate to investigate a given configuration. To our knowledge however, no work in the literature has provided a set of guidelines to assess the frame of application of each method. We shall now give some clues on this point as we will compare the solutions provided by the full 3D DNS and 3D simulations using wall functions on the one hand and those obtained from the 3D computations using wall functions and from 2D simulations using the SM82 model. In both cases, we consider the configuration investigated in [189] at $Re = 200$.

8.5.1 Comparison full DNS and simulations using the wall functions

We have taken over the configuration of [189] and simulated the case at $Ha = 50$, $Re = 200$ ($N = 0.5$) with full DNS and with simulations using the wall functions at both Hartmann walls. The description of the numerical set-up and settings of the case run with the solver using the wall functions is given in the previous section. The full DNS have been performed using exactly the same configuration and settings. Only the Hartmann layers at the top and lower duct walls have been fully resolved at each time step and the boundary conditions at the related Hartmann walls satisfy (8.11).

A snapshot of the cylinder wake obtained at $t = 3t_H$ from full DNS is shown on figure 8.10 and can be directly compared to the snapshot of the flow simulated with the use of wall functions at the same time instant $t = 3t_H$ presented on figure 8.8(a-b). One observes that the structures present in

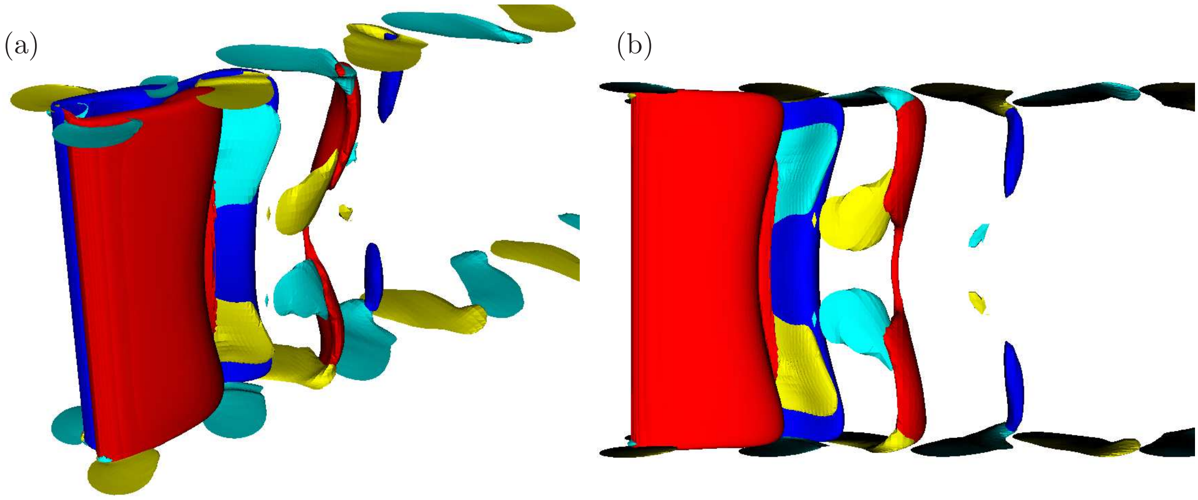

Figure 8.10: Snapshot of the vortex street at $Re_W = 200$, $Ha = 50$ and $t = 3t_H$ from full DNS: (a) 3D and (b) side views. Streamwise vortices are depicted by iso-surfaces of $x-$vorticity and Kármán vortices by iso-surfaces of $z-$vorticity. Colours have the same meaning as in figure 8.2. For clarity, the extension of the streamwise vortices in the vicinity of the Hartmann walls is truncated.

the vortex street are very similar whether they are obtained from full DNS or from the simulations using the wall functions. In both cases, the Kármán vortices present disruptions at their mid-span and their spanwise shape is very distorted due to the presence of the streamwise vortices. Also the time average values of the flow coefficients are in excellent agreement. In the full DNS, the total drag coefficient is $C_D = 1.44$ and the Strouhal number $St = 0.14$, while in the simulation using the wall functions, $C_D = 1.45$ and $St = 0.142$.

The main difference is obviously seen inside and in the vicinity of the Hartmann layers. With full DNS, streamwise vorticity is present inside the Hartmann layers and are connected to the Kármán vortices. Also there is some fluid exchange between the Hartmann layers and the core flow, which is forbidden in the simulations using wall functions.

To refine our analysis, we have computed the average of the velocity along the direction of the magnetic field at the time instant $t = 3t_H$ in both cases. We have then derived the associated error with respect to the $z-$averaged velocity provided by the full DNS. Figure 8.11 presents the spatial distribution of this error in the cylinder wake for $-1 \leq x \leq 10$. One observes that the error is very

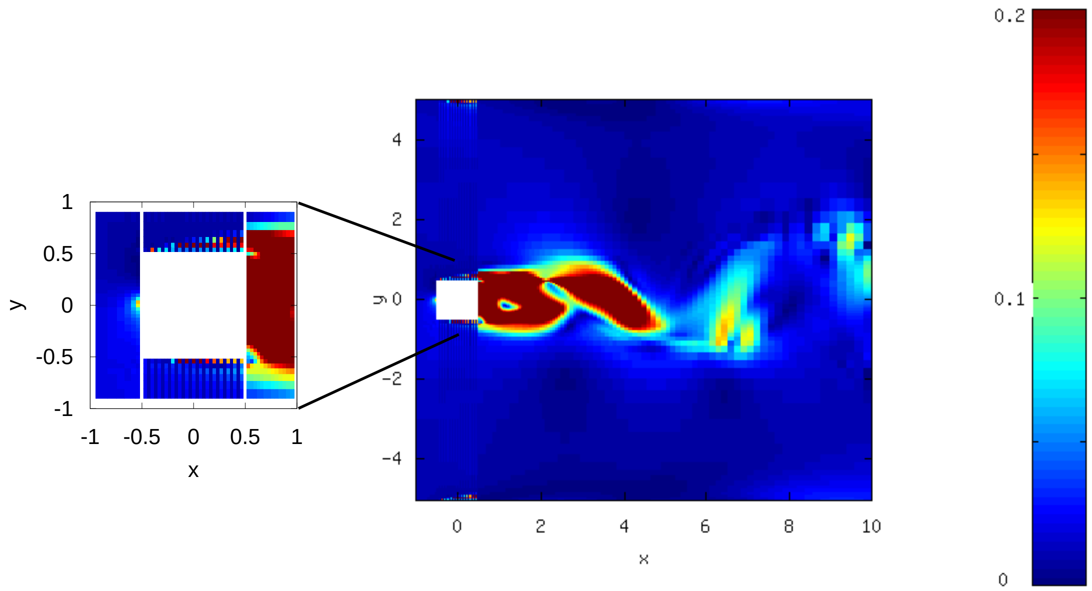

Figure 8.11: Error in the L_2-norm of the $z-$averaged velocity $\epsilon_u = ||\langle u_{DNS} - u_{WF}\rangle_z||/||\langle u_{DNS}\rangle_z||$ between the full DNS and the simulations using wall functions at $Ha = 50$, $N = 0.5$ and $t = 3t_H$.

high in the near wake of the cylinder, while it is still significant further downstream in the vicinity of the vortices. The fluid exchange between the Hartmann layers and the core flow as well as the presence of strong streamwise vorticity inside the Hartmann layers are accounted for only in the full DNS. This may explain the strong discrepancy observed in these regions. One may also question the definition of the error chosen to assess the quality of the respective solutions. We have indeed compared the z-average of the velocities and therefore ignore their variations along the z-axis. Further work on this point is required to draw some more complete conclusions.

Also some discrepancy between both velocity field, though much lower, is spotted in the Shercliff layers at the cylinder lateral faces (see insert on figure 8.11) and at the duct walls opposite to these cylinder faces. This results from the sudden confinement imposed by the presence of the cylinder.

Although deeper investigations are required, in the case chosen for comparison, it is recommended to use full DNS, as the Stuart number is lower than 1. The fluid exchange between the Hartmann layers and the core flow needs to be accurately addressed and the use of this wall function is clearly not adapted as it does not allow such exchange. The wall function designed by [158] includes weak inertial effects inside the Hartmann layers and therefore describes the fluid exchange between these layers and the core flow. The implementation of this wall function should compare better to the full DNS for $N \simeq 1$.

8.5.2 Comparison 3D code with wall functions and 2D code with the SM82 model

We now consider the case at $Re = 200$ and $Ha = 265$ ($N = 14$). We have simulated the 3D flow with a solver using the wall functions (see previous section). On the other hand, we have used the SM82 model to run 2D simulations in the plane normal to the direction of the magnetic field using the mesh as designed in this plane for the 3D simulations. The numerical set-up in the 2D simulations is similar to that elaborated in the investigations of the MHD circular wake from chapter 6, only the shape of the cross-section of the cylinder differs. Both simulations have been started with a flow initially at rest and the total simulation time is about $10t_H$. Figure 8.12 presents a snapshot of the cylinder wake at $t = 10t_H$ obtained from the 2D simulations using the SM82 model. One observes that they

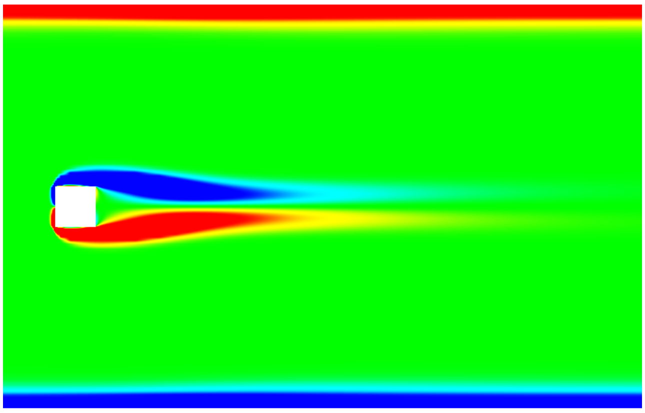

Figure 8.12: Snapshot of the vortex street at $Re_W = 200$, $Ha = 265$ and $t = 10t_H$ from 2D simulations using the SM82 model. Iso-surfaces of $z-$vorticity. Blue and red colours have the same meaning as in figure 8.8.

result in a steady flow, while 3D simulations yield unsteady flow patterns as seen on figure 8.8(e-f). We have perturbed the flow by artificially adding unsteady vorticity in the flow over a short while at the beginning of the run, but the flow has still eventually recovered the steady regime. Doubling the total simulation time has also not brought any change in the flow. It should be stressed that the case chosen for this comparison meets the conditions of reliability of the SM82 model as both Ha and N are much bigger than unity. The 3D simulations show that the flow is actually just unsteady as the formation region of the Kármán vortices is longer and the vortices are quickly dissipated in their motion downstream. The SM82 model relies on averaging the flow over the direction of the magnetic field. It therefore partly ignores the flow variations over this direction and causes an overstabilisation of the flow. In the vicinity of the transition between two flow regimes, here transition to unsteadiness, the use of the SM82 model may induce a shifting of the critical threshold of the onset of vortex shedding to higher Re. This is probably the reason why the 3D simulations and the 2D ones yield a different flow regime.

In summary, both cases chosen in this section are extreme ones that have highlighted the drawbacks of the use of wall functions and that of the SM82 model, respectively. A better review of the possibilities offered by each numerical method to investigate a given configuration requires additional work and adequate definition of criteria to assess the performances of the respective numerical approaches.

8.6 Conclusions and perspectives

Throughout this series of validation tests, we have shown that our numerical code is able to render within an excellent accuracy 3D MHD flow dynamics. We have first made sure that complex 3D non-MHD flow structures are well captured. We have insisted on including a sufficient number of mesh nodes inside both Hartmann and Shercliff layers, as the boundary layers in MHD flows play a crucial role in the dynamics. For example, due to a coarse resolution of the Shercliff layer at the lateral cylinder faces, [189] overlooked secondary recirculations. In addition, in an effort to reduce the CPU cost of high Ha flows, we have also implemented a wall function at the interface between the Hartmann layers and the core flow. Using this approach, we have successfully validated the MHD flow past a square cylinder to [189].

Although the advances in CPU technology keep on pushing the limits of feasibility of full DNS at high Ha, the use of wall function for high Ha flows may further broaden the possibilities to simulate high Ha flows in more complex configurations. Also, the quasi-2D flow model by [165] used to investigate the MHD flow past a circular cylinder in chapter 6 can also be used at least to gain valuable information on the flow at a very low CPU cost. The need to bring forward some guidelines which would suggest the benefits and the drawbacks on a given numerical approach to investigate a given problem remains to be fulfilled. For $N \simeq 1$, 3D full DNS are highly recommended, since the wall function as implemented in our code does not include the possible fluid exchange between the Hartmann layers and the core flow. Revamping the definition of the wall function to account for this fluid transfer as described in [158] could correct this flaw. Finally, we have singled out the overstabilising effect of the SM82 model which may overestimate the critical threshold of transition between two flow regimes.

Chapter 9

Three-dimensional non-MHD flow past a truncated square cylinder

In this chapter, we describe the simulations of the 3D flow around a truncated square cylinder in a duct in the case where no magnetic field is present. The scope of this non-MHD study is to provide a thorough review of both the steady and unsteady flow patterns, identify the mechanism of vortex shedding and detail the evolutions of the flow coefficients and how they reflect the flow dynamics. The non-MHD results finally represent a good basis on which we shall refer to as we will investigate the MHD case to identify the effects of the Lorentz forces by direct comparison. The main results of this chapter are given in [2].

9.1 Configuration and flow equations

We consider the flow of an incompressible fluid (density ρ and kinematic viscosity ν) past a truncated cylinder of square cross-section in a rectilinear duct of rectangular cross-section. Figure 9.1 presents the configuration under consideration in the present study. The cylinder is mounted on the duct bottom wall at equal distance from both duct side walls. It is oriented so that its upstream face is normal to the streamwise direction taken along the $x-$axis. It spans over half of the duct height along the $z-$axis. The origin of the frame of reference is located at the centre of the cylinder upper face. The duct height is $2a$ and its width $2b$. The cylinder has a square cross-section of width W and a height h. The present configuration features $h = 4W$, $2a = 8W$ and $2b = 10W$, which yields a transverse (*resp.* spanwise) blockage ratio $\beta = W/(2b) = 0.1$ (*resp.* $\beta_z = h/(2a) = 1/2$) and a cylinder aspect ratio $\gamma = h/W = 4$. β_t is low so that it does not have any noticeable effect on the flow dynamics [109], while the effects of the spanwise flow confinement shall be discussed throughout our investigations.

We investigate the flow using 3D Direct Numerical Simulations (DNS) with the code described

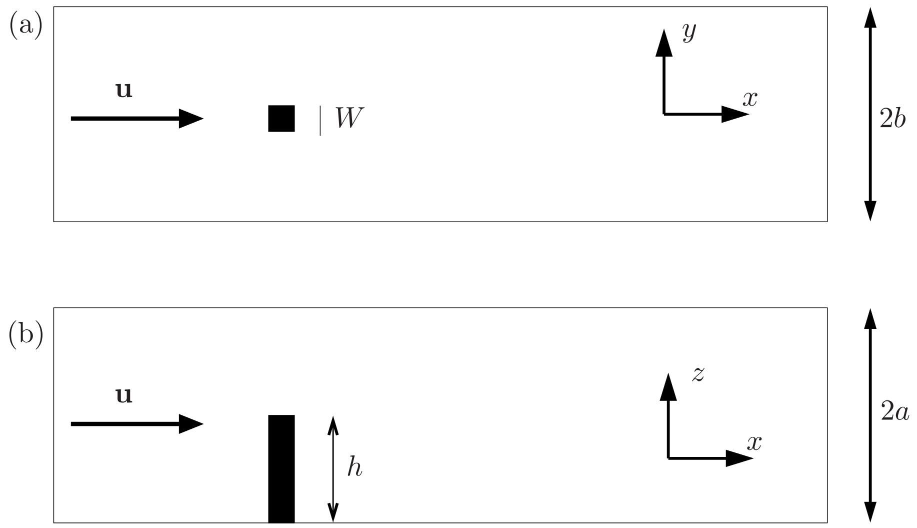

Figure 9.1: Configuration of the flow past a truncated square cylinder in a duct: (a) top view; (b) side view.

in the previous part. The flow motion is governed by the Navier-Stokes equations (1.1) and (1.2). The cylinder width W and the maximum of the inlet velocity profile U_0 are used to obtain the non-dimensional formulation of the latter equations:

$$\nabla \cdot \mathbf{u} = 0 \tag{9.1}$$

$$\frac{\partial \mathbf{u}}{\partial t} + (\mathbf{u} \cdot \nabla)\mathbf{u} = -\nabla p + \frac{1}{Re_W}\nabla^2 \mathbf{u} \tag{9.2}$$

where $Re_W = WU_0/\nu$.

9.2 Numerical model

9.2.1 Numerical set-up

The numerical domain is $15W$ (*resp.* $30W$) long upstream (*resp.* downstream) the cylinder. The remaining dimensions are fixed by the configuration described above. A no-slip impermeable boundary condition is imposed at all walls, *i.e.* at $y = \pm b/W$, $z = \pm a/W$ and at the cylinder surface ∂C_T defined as the reunion of the cylinder upper face ($|x| \leq 1/2; |y| \leq 1/2; z = 0$), the upstream and downstream faces ($|x| = 1/2; |y| \leq 1/2; -\gamma \leq z \leq 0$) and the lateral faces ($|x| \leq 1/2; |y| = 1/2; -\gamma \leq z \leq 0$):

$$\mathbf{u} = \mathbf{0} \;\text{ at } \begin{cases} -15 \leq x \leq 30, |y| = b/W, |z| \leq \gamma; \\ -15 \leq x \leq 30, |y| \leq b/W, |z| = \gamma; \\ \partial C_T \end{cases} \tag{9.3}$$

Meshes	M1	M2	M3
$n_x \times n_y \times n_z$	$135 \times 120 \times 32$	$135 \times 120 \times 64$	$135 \times 120 \times 96$
$\delta_x \times \delta_y \times \delta_z$	$0.03 \times 0.06 \times 0.06$	$0.03 \times 0.06 \times 0.03$	$0.03 \times 0.06 \times 0.02$
Total number of nodes	7.4×10^5	1.5×10^6	2.2×10^6
$\epsilon_{st} = \lvert 1 - St(Mi)/St(M3)\rvert$	0.10	0.03	/
$\epsilon_{cd} = \lvert 1 - C_D(Mi)/C_D(M3)\rvert$	3.51×10^{-3}	3.05×10^{-3}	/

Table 9.1: Main characteristics of the different meshes and errors in drag coefficient C_D and Strouhal number St relative to M3 mesh at $Re = 200$. n_i is the number of mesh nodes along the i-axis and δ_i is the non-dimensional distance between the cylinder face normal to the $i-$axis and the grid point nearest to the latter face.

A homogeneous Neumann boundary condition is applied at the outlet for the velocity:

$$\partial_n \mathbf{u} = 0 \text{ at } x = 30 \tag{9.4}$$

Following the recommendations of [106], the outlet is located at a distance downstream the cylinder greater than $25W$ to damp out the feedback effect of the outlet boundary onto the upstream flow.

Preliminary 3D computations of the duct flow with the cylinder absent are performed at a prescribed Re_W until the fully-established state is reached. The resulting velocity profile in the duct cross section is then extracted and applied as the inlet boundary condition for the velocity field in the 3D simulations with the cylinder present. A homogeneous Neumann boundary condition is applied for the pressure field at all boundaries but at the outlet:

$$\partial_n p = 0 \text{ at } \begin{cases} -15 \leq x \leq 30, |y| = b/W, |z| \leq \gamma; \\ -15 \leq x \leq 30, |y| \leq b/W, |z| = \gamma; \\ \partial C_T \end{cases} \tag{9.5}$$

To minimise flow distortion at the outlet, we impose a zero mean value of the pressure at the outlet (5.8).

9.2.2 Mesh validation

We design a Cartesian non-uniform mesh. The mesh used in the validation test of the 3D non-truncated cylinder wake as investigated by [189] has been partially taken over in this study. Since the test have been very successful at rendering the 3D flow dynamics, we have only tested the influence of the number of nodes along the cylinder axis while keeping the mesh structure in the plane normal to the cylinder axis. Three different meshes have been tested, their characteristics are provided in table 9.1. We have simulated the flow at $Re = 200$ over 1000 turnover times $t_u = d/U_0$ and derived the total drag coefficient C_D and the Strouhal number St in each case. We have found that both the errors in C_D and St relative to mesh M3 decrease with the number of nodes, which shows good convergence. In order to save CPU time and keep a reasonable accuracy in our computations, we shall perform all our simulations with the M2 mesh.

9.2.3 Vortex identification

It is usual to use vorticity field and kinematic current streamlines to isolate vortical structures in the flow. These approaches are however not rigorous and may result in wrong interpretations of flow structures. Establishing an objective definition of a vortex was discussed in several studies in the literature. [203] assessed different techniques of identification and tracking of vortical structures. One of them is based on the analysis of the eigenvalues of the symmetric tensor $\mathbf{S}^2 + \mathbf{\Omega}^2$, where $\mathbf{S}$ and $\mathbf{\Omega}$ are the respective symmetric and antisymmetric part of the velocity gradient tensor $\nabla\mathbf{u}$. In this approach, a vortex core corresponds to a pressure minimum not induced by viscous effects nor unsteady straining. It is defined as a connected region with two negative eigenvalues of $\mathbf{S}^2 + \mathbf{\Omega}^2$. A vortex is therefore detected at a given location in the fluid domain if the median eigenvalue, denoted λ_2, is locally negative. This approach is particularly efficient at spotting ring-type vortices [203]. Unfortunately, it delivers no information on the rotation directions of the vortical structures. For this reason, flow patterns will also be characterised by iso-surfaces of vorticity, especially in the unsteady flow regime. In the steady one, we will analyse the streamlines, since they match the flow trajectories [197].

9.3 Steady flow regime

We have performed a series of nine successive simulations by increasing Re_W at $Re_W = 10$, 20, 50, 100, 150, 200, 250, 300 and 400. Computations have been run over a total simulation time higher than $1000t_u$ where $t_u = W/U_0$ is the turnover time.

A steady flow regime has been detected for $Re_W \leq 150$ with appearance of secondary recirculation regions on both the top and lateral cylinder faces at $Re_W = 150$. Vortex shedding is observed for $Re_W \geq 200$ and fuels a symmetric vortex street for $Re_W = 200$ and 250, while an asymmetric one establishes for $Re_W = 300$ and 400. We shall now thoroughly assess the steady flow patterns at $Re = 100$. Then we will review the evolution of the latter structures as Re_W is increased throughout the steady flow regime. We will then show how the destabilization of the steady structures eventually leads to the shedding of regular hairpin vortices at $Re_W = 200$. The formation and release mechanism of these vortices will be described and the reasons of the transition to an asymmetric vortex street will be given.

9.3.1 Flow patterns at $Re_W = 100$

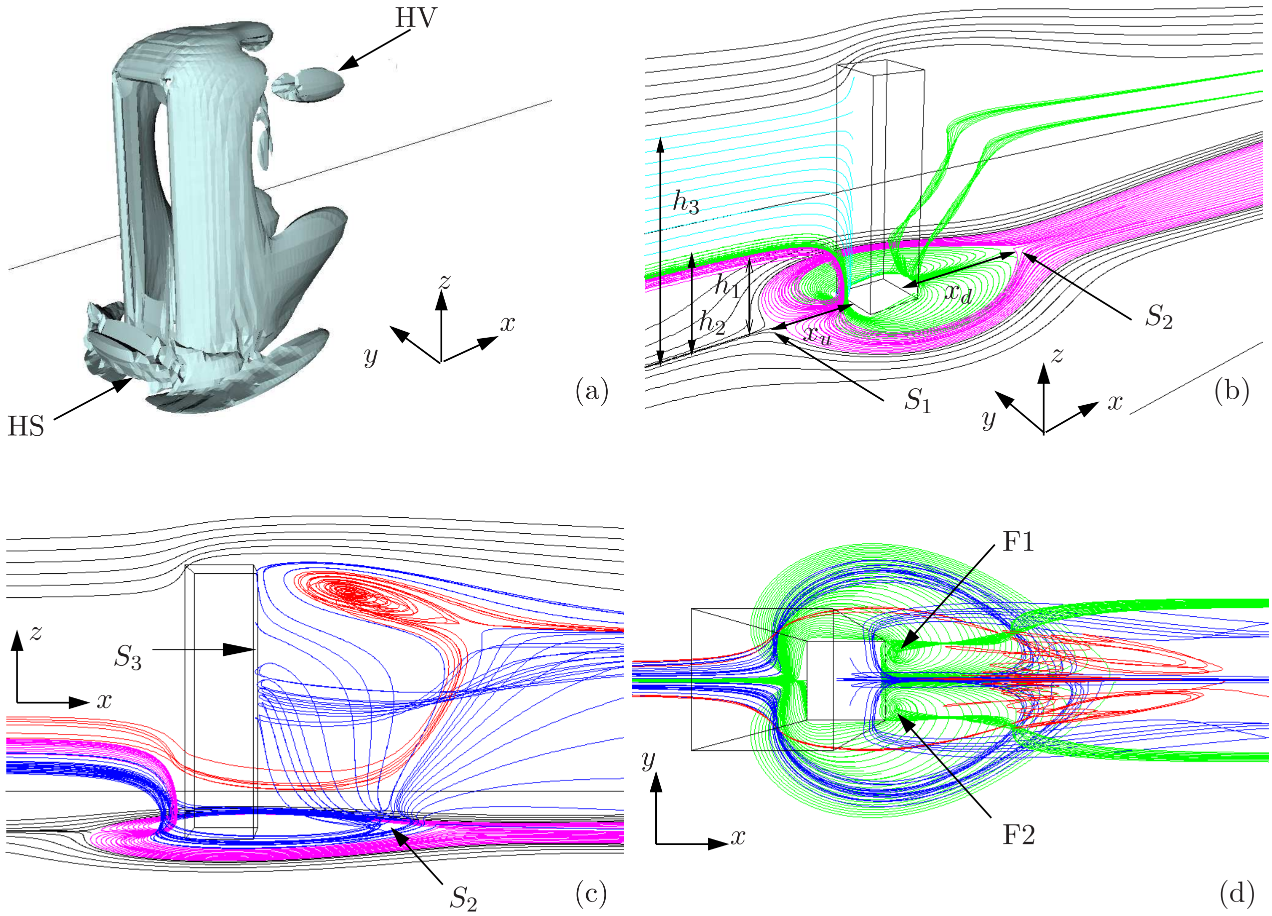

Figure 9.2: Steady flow patterns at $Re = 100$. Iso-surfaces of $\lambda_2 = -0.05$ (a) and kinematic streamlines with horseshoe pattern in pink, trailing vortices in green, streamlines rejoining the stagnation points on the upstream cylinder face in cyan, head vortex in red, spanwise vortices in blue, black streamlines are only deflected by the cylinder wake without noticeably influencing it: three-dimensional (b), side (c) and top (d) views.

Figure 9.2(a) shows the steady flow patterns at $Re = 100$ depicted by iso-surfaces of $\lambda_2 = -0.05$, *i.e.* less than 0.2% of the absolute minimum in λ_2, and by kinematic streamlines in figures 9.2(b-d) The horseshoe system is depicted by the pink streamlines. The front swirl region of the horseshoe pattern located at $x = -0.5$ is indicated by HS in figure 9.2(a). A second set of streamlines (in green) originating upstream at the vicinity of the centre-plane ($y = 0$), just above the previous streamlines, impacts the bottom duct wall between the cylinder upstream face and the front of the horseshoe system. It then recirculates around the cylinder base and below the lateral free shear layers to rejoin two foci, denoted F1 and F2 in figure 9.2(d). It subsequently spirals upwards underneath the lateral layers and tilts along the streamwise direction to create a pair of counter-rotating trailing vortices. This description corresponds to that of the base vortices as given in [112] and [123]. The foci have also been detected in numerical simulations by [114] and [129] but have not been linked to the formation of base vortices. At $Re = 100$, these vortices are very weak so that they do not induce a significant pressure minimum likely to be captured by the iso-surfaces of λ_2. Far upstream, in the centre-plane ($y = 0$), the border between the previous sets of streamlines is located at ($z = h_1 - \gamma$) and the upper border of the second set at ($z = h_2 - \gamma$).

Interestingly, no pair of tip vortices have been detected in the steady flow regime neither from iso-surfaces of λ_2, nor from kinematic streamlines. This absence relies probably on two factors. Firstly, the spanwise flow confinement imposes a spanwise velocity gradient as that induced in boundary layers and [127] have shown that the thickening of the bottom boundary layer results in an enhancing of the base vortices at the expenses of the tip ones. Secondly, the present cylinder aspect ratio is rather low and no tip vortices have been observed in simulations run with a low aspect ratio [123, 129].

A third set of streamlines (in cyan) originating within the centre-plane ($y = 0$), just above the second set at ($h_2 - \gamma \leq z \leq h_3 - \gamma$) ends at the front stagnation points on the upstream cylinder face along the wake centreline. A fourth set of streamlines (in black) are just deflected by the cylinder wake without taking any part in the flow dynamics. Figure 9.2 (b) also reveals the presence of front (S_1) and rear (S_2) saddle points located in the boundary layer at the bottom duct wall on the wake centreline respectively upstream the horseshoe pattern at ($x = -x_u - 1/2$) and at the downstream border between the first two sets of streamlines at ($x = x_d + 1/2$) as seen in [113, 123].

Both sets of blue and red streamlines on figure 9.2 (b-c) rejoin the centre-plane ($y = 0$) behind the cylinder. Blue streamlines also move around the cylinder base and inbetween the lateral free shear layers from their bottom up. On the one hand, the streamlines located just upstream S_2 head upwards and back upstream along the wake centre-plane behind the cylinder and separate into two substreams at saddle point S_3 on the cylinder downstream face. The lower substream is deflected by the cylinder rear face along the $y-$axis, reaches the trailing edges of the cylinder lateral faces and is carried away by the free stream to form a pair of weak counter-rotating spanwise vortices. The upper substream heads towards the cylinder tip where the free stream takes it away along the wake centreline. On the other hand, the blue streamlines located just downstream S_2 head upwards and downstream until they reach the free stream and align along the streamwise direction.

A gap between the blue streamlines moving downstream and upstream is observed at the rear of the cylinder below the cylinder tip where a transverse vortex is seen [red lines in figure 9.2 (c-d)]. This head vortex consists of a pair of symmetric transverse vortices located at short distance off the centreplane ($y = 0$) and connected to a single transverse vortex within this centreplane. Only the right part of the head vortex, denoted HV, is seen on figure 9.2(a). The streamlines enter this three-vortex structure at the periphery of the symmetric vortices, spiral towards the axis and exit at the periphery of the centre vortex onto the wake centreline. Like all the structures described so far, the transverse vortex is fuelled by streamlines flowing around the cylinder base and inbetween the lateral free shear layers from their bottom up as in [123, 129]. By contrast, the head vortex observed in [113, 124, 126] is generated by streamlines curling from the cylinder free end.

Two free shear layers arise at the lateral downstream edges of the cylinder and stretch on both sides of the wake [see $z-$vorticity contours on figure 9.4]. Due to the presence of the bottom duct wall and the free shear layer stretching from the top trailing edge of the cylinder, their streamwise length is reduced at both their ends and reaches its maximum in the vicinity of the base vortices.

9.3.2 Effect of increasing Re_W within the steady regime

The flow patterns involved in the steady regime appear at different Re_W. At $Re_W = 10$, no swirl is detected at the front of the horseshoe system. Only a weak one is observed at $Re_W = 20$, that gains in strength for $Re_W \geq 50$ and generates a second vortex by flow separation at the bottom wall. As Re_W is increased, saddle point S_1 moves upstream and S_2 barely moves, so that x_u increases and x_d remains almost constant. The dynamics of the horseshoe pattern is similar to that described in e.g. [108, 114, 117, 123]. Also, upstream the cylinder, the set of streamlines fuelling the horseshoe pattern is pushed downwards when Re_W is increased, *i.e.* h_1 shrinks. The set of streamlines at the origin of the trailing vortices experiences the same evolution and h_1 diminishes with increasing Re_W. In contrast, the upper border of the set of streamlines rejoining the front stagnation points on the cylinder upstream face hardly moves throughout the steady flow regime and h_3 remains almost constant.

Due to the presence of the cylinder, a pair of opposite transverse jets and an upwards one are generated at the cylinder upstream face. At low Re_W, these jets are weak and the flow separates at the trailing edges of the lateral and top faces. At $Re_W = 150$, the jets are stronger and flow separation is observed at the front edges of the latter faces. Downstream these edges, at the faces, secondary flow recirculations are observed, as shown on figures 9.3(a-b). The lateral recirculation regions result from the stretching of the spanwise vortices along the lateral faces. The top one is generated by a swirl on the cylinder upper face which reattaches at short distance off the trailing edge. Also, the spanwise vortices do no longer exist, but are entangled within the base vortices [see figure 9.3(a)]. The head vortex appears at $Re_W = 50$. For higher Re_W, it gradually drifts both downstream and upwards. The latter move is favoured by both the appearance of the top secondary recirculation, which enhances the upwards deflection of the top free stream, and the upwards jet generated by the pair of streamwise vortices from their mutual interactions at the centre-plane ($y = 0$).

In the late stages of the steady flow regime, the situation behind the cylinder is the following: a pair of strong counter-rotating streamwise vortices is surrounded on both its sides and top by the free shear layers stretching from the cylinder top and sides. We shall now describe how this set of structures becomes unstable and drives the onset of vortex shedding.

(a) (b)

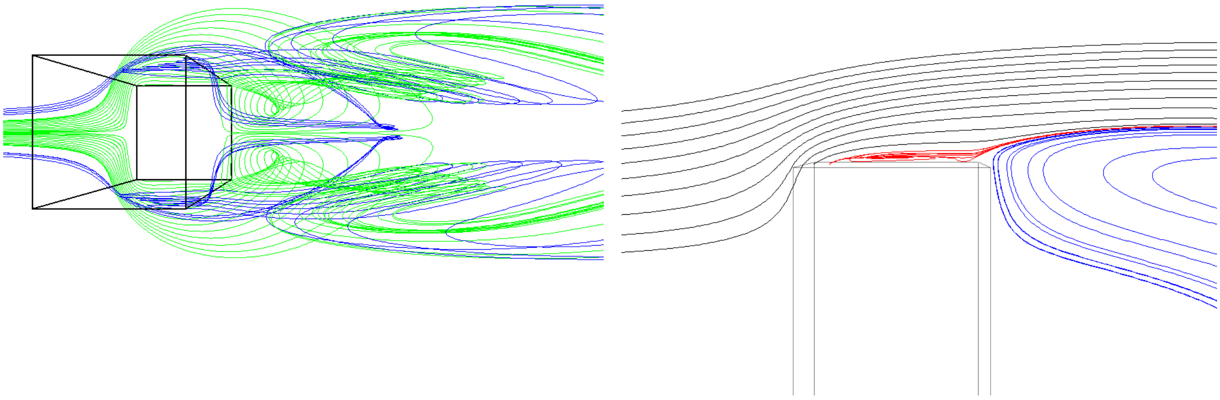

Figure 9.3: Secondary recirculation regions at $Re_W = 150$: (left) top view of the lateral secondary recirculation resulting from the stretching of the blue streamlines; (right) side view of the top secondary recirculation (in red) generated by a swirl reattaching close to the trailing edge of the cylinder upper face.

9.4 Unsteady flow regime

9.4.1 Formation and release of hairpin vortices

At $Re_W = 200$, one observes a regular, laminar, symmetric vortex street consisting of a single row of hairpin vortices along on the wake centreline. The formation and release of hairpin vortices at $Re = 200$ at three successive time instants depicted by iso-surfaces of both vorticity field and $\lambda_2 = -0.5$ (0.5% of its absolute minimum) are provided in figures 9.4(a-c).

At $t = 1349t_u$, one observes a hairpin vortex in the early stage of its formation in the near cylinder wake and a freshly released hairpin vortex in the far wake. The presence of three distinct vortical structures, denoted as TV, LV and RV and originating from respectively the top, left and right free shear layers are distinguished in figure 9.4 (a). Under their mutual interactions, the base vortices, shown in cyan and yellow in figure 9.4(b), generate an upwards jet between them which lifts the tail of the top free shear layer. This results in an inversion of the curvature of the latter which becomes unstably curved [58] leading to the breakaway of its tail. At $t = 1349t_u$, two secondary counter-rotating streamwise vortices, denoted SR and SL on figure 9.4(b), then rise just upstream the structure shed from the top free shear layer and wrap around the base vortices, while TV, LV and RV have gathered into a single bow of vorticity. The subsequent pairing between both base and secondary streamwise vortices eventually triggers the symmetric shedding of structures from both lateral free shear layers [in blue and red in figure 9.4(c)] observed at $t = 1351t_u$. At this moment, the head of the hairpin vortex is completely formed and taken away by the free stream, while the base vortices split and join the head of the hairpin vortex to form the legs of this vortex, as shown by the

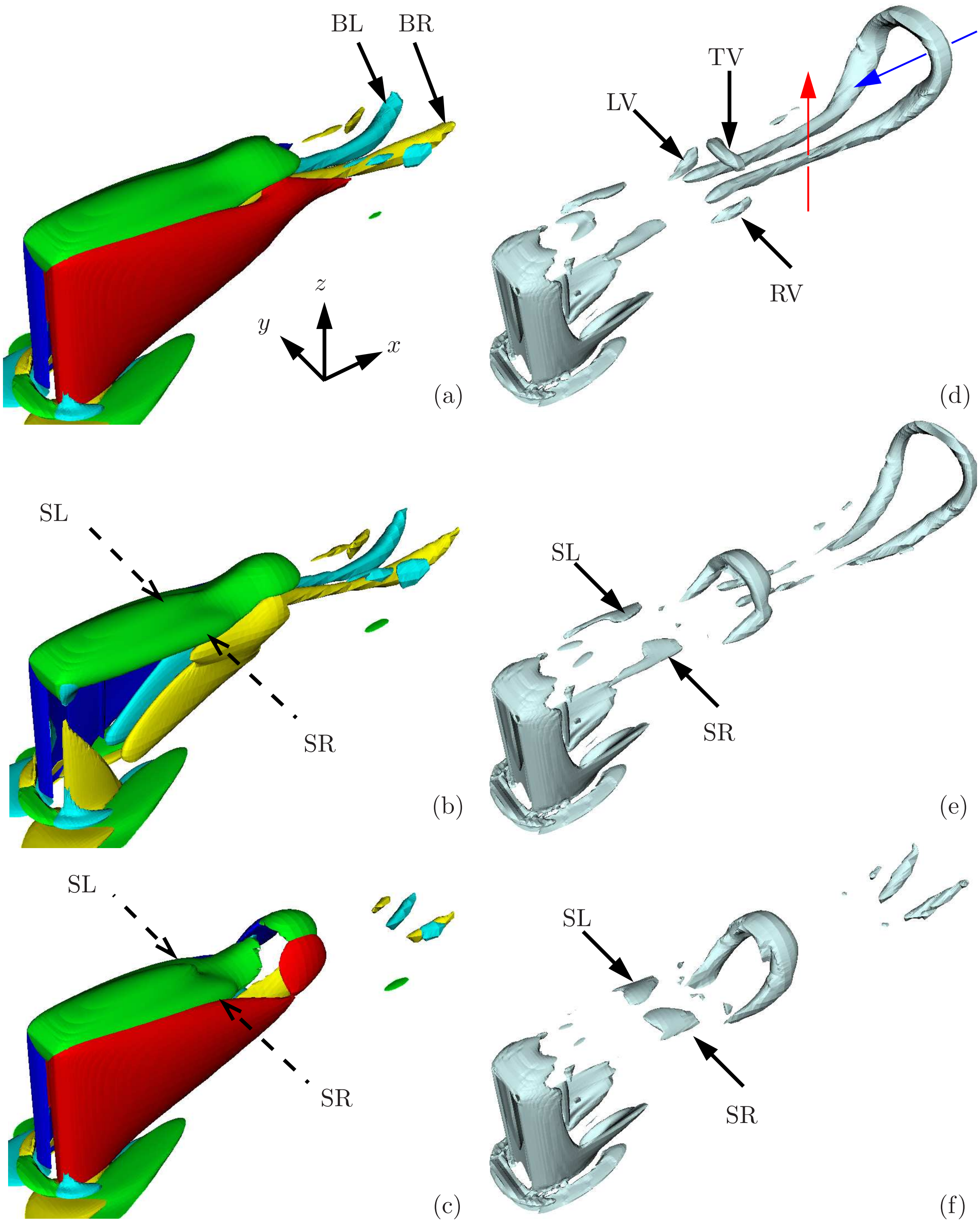

Figure 9.4: Vortex street at $Re = 200$ depicted by iso-surfaces of (a-c) non-dimensional vorticity ω and (d-f) $\lambda_2 = -0.5$ at $t = 1349t_u$ (top), $1351t_u$ (middle) and $1353t_u$ (bottom). $\omega_x = 2.5$ (*resp.* -2.5) in yellow (*resp.* cyan); $\omega_y = 5$ in green; $\omega_z = 5$ (*resp.* -5) in red (*resp.* blue). The red lateral free shear layer is not shown in (b). TV, LV and RV are vortical structures shed from the top, left and right free shear layers, respectively; BR and BL the base vortices; SR and SL the secondary streamwise vortices clearly visible (e-f) but not (b-c) where their locations are indicated by dashed arrows. Red and blue arrows on (d) indicate the jets induced by the base and hairpin vortices respectively.

hairpin vortex present in the far wake on figure 9.4(a).

This shedding is symmetric and has been observed in experiments [121, 122], but the present formation scenario comes at odds with those provided in previous works. Our computations show that the hairpin vortices are not generated only by the destabilization of the top free shear layer as suggested in [114] and [129]. The head of the hairpin vortex are formed from the smooth assembling of a structure shed from the top and lateral free shear layers. The hairpin vortices observed in the present simulations differ from the arch-type vortices observed in experiments by [121] and [126]. Firstly, their head is located at the downstream end of the hairpin structure. This may be due to the spanwise velocity gradient imposed by the spanwise flow confinement. The free stream velocity is higher in the vicinity of the cylinder tip so that the hairpin head, located in this region, shall be carried away downstream more efficiently than the rest of the hairpin structure. Secondly, the hairpin legs are almost parallel to the streamwise axis and not aligned along the spanwise direction. In our configuration, the hairpin legs are the base vortices which are oriented along the streamwise axis, whereas in those of the arch-type vortices are the spanwise vortices shed from the lateral free shear layers. This shows that the base vortices play an active part in the vortex shedding mechanism, which shall therefore not be reduced only to the interactions between both top and lateral free shear layers as in [121] and [126]. The active part of the base vortices in the formation of hairpin vortices has been stressed in the flow past a trapezoidal tab [111, 130].

9.4.2 Formation and release of secondary Ω-shaped vortices

We have described how the hairpin vortices are generated and released in the cylinder wake. A chain of secondary Ω-shaped vortices appears following the release of the hairpin vortices. We shall now describe these secondary vortices and their formation mechanism.

Figure 9.5 (a) shows the vortex street at $t = 1353t_u$ depicted by iso-surfaces of $\lambda_2 = -0.03$, *i.e* a lower threshold than that used in figure 9.4(a-c). This figure reveals the presence of a chain of Ω-shaped vortices between two successive hairpin vortices. The strength of the Ω-shaped vortices decreases as they are further away from the hairpin vortex. The Ω-shaped vortices are located in the plane (y, z) [see figure 9.5 (c)] and their bottom ends rejoin the secondary streamwise vortices [see figure 9.5 (d)]. The Ω-shaped vortices are the mirror image of the hairpin vortex as they all rotate in the sense opposite to the hairpin vortex as shown by figures 9.5 (b-d). Vortex streets involving hairpin vortices and secondary reverse vortices, *i.e.* rotating a sense opposite to that of the hairpin head, have been observed on the flow past a trapezoidal tab in experiments [130] and numerical simulations [111]. The latter simulations have furthermore shown that the reverse vortices were part of Ω-shaped vortices. Also, reverse vortices vortices were observed between and below two successive hairpin vortices, while they are aligned along the streamwise axis in the present configuration.

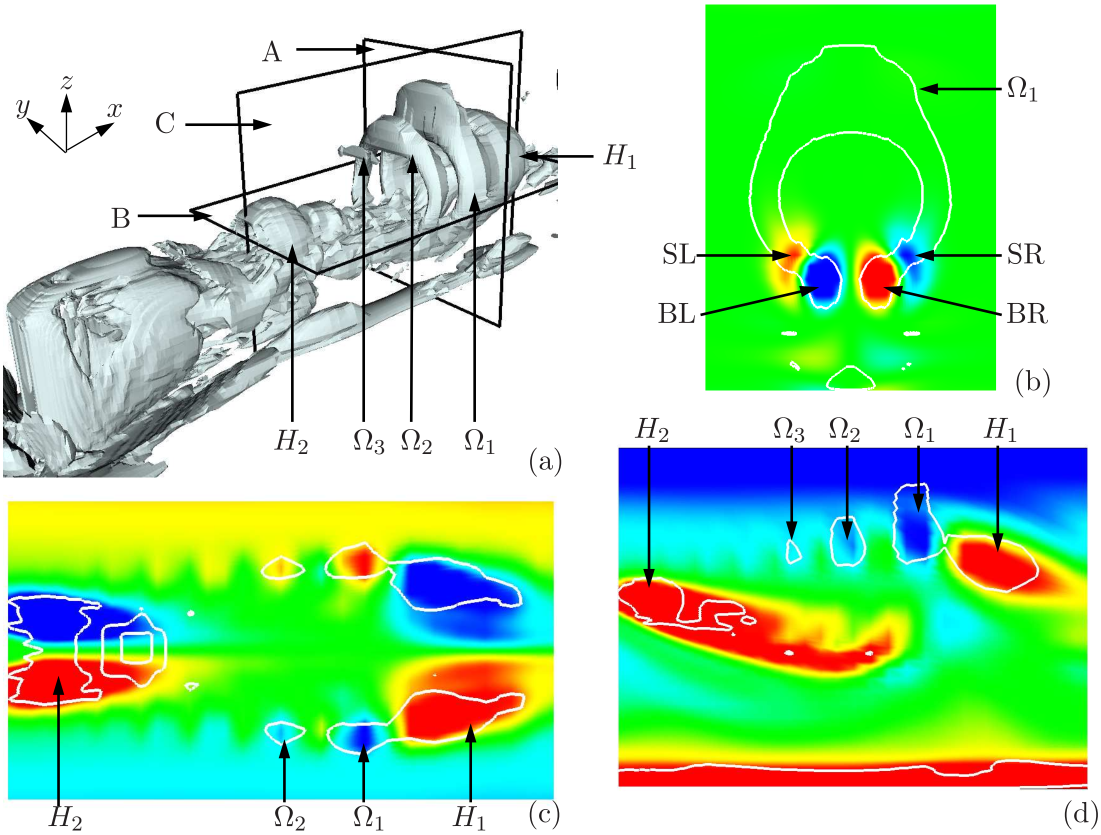

Figure 9.5: (a) Iso-surfaces of $\lambda_2 = -0.03$ at $Re = 200$ and $t = 1353$. Fields of non-dimensional (b) x-vorticity in plane A ($x = 12.9$) with $|\omega_x| \leq 2$, (c) $z-$vorticity in plane B ($z = 0$) with $|\omega_z| \leq 1.5$ and (d) $y-$vorticity in plane C ($y = 0$) with $|\omega_y| \leq 1.8$ (minimum and maximum values in blue and red, respectively). Thick white lines on (b-d) are the intersected λ_2-iso-surfaces. H_1 and H_2 are two successive hairpin vortices, Ω_1, Ω_2 and Ω_3 three Ω-shaped vortices, SR and SL the respective left and right secondary streamwise vortices and BR and BL the respective left and right base vortices.

The formation of Ω-shaped vortices follows from a mechanism encountered in turbulent boundary layers in channel flows described in e.g. [131]. In its motion downstream, the head of the hairpin vortex broadens and induces a backwards streamwise jet inside the head. The pair of streamwise vortices forming the legs of the hairpin vortex generates an upwards jet between them. The shearing between the latter jet and the one induced by the head of the hairpin vortex causes the formation of a bridging shear layer between both streamwise vortices. The shear layer eventually rolls up into an Ω-shaped vortex in the plane (y, z). This mechanism is active all along the legs of the hairpin vortex and leads to the formation of several Ω-shaped vortices between two successive hairpin vortices.

9.4.3 Effect of increasing Re_W on the vortex street

We shall now detail how the hairpin vortices are affected when Re_W is increased up to 400. The vortex street at $Re_W = 250$ and $Re_W = 300$ is shown in figure 9.6. At $Re_W = 250$, the shedding mechanism described above remains unchanged, although the shape of the hairpin vortices becomes irregular and the primary streamwise vortices undergo weak spanwise oscillations. The latter induce a

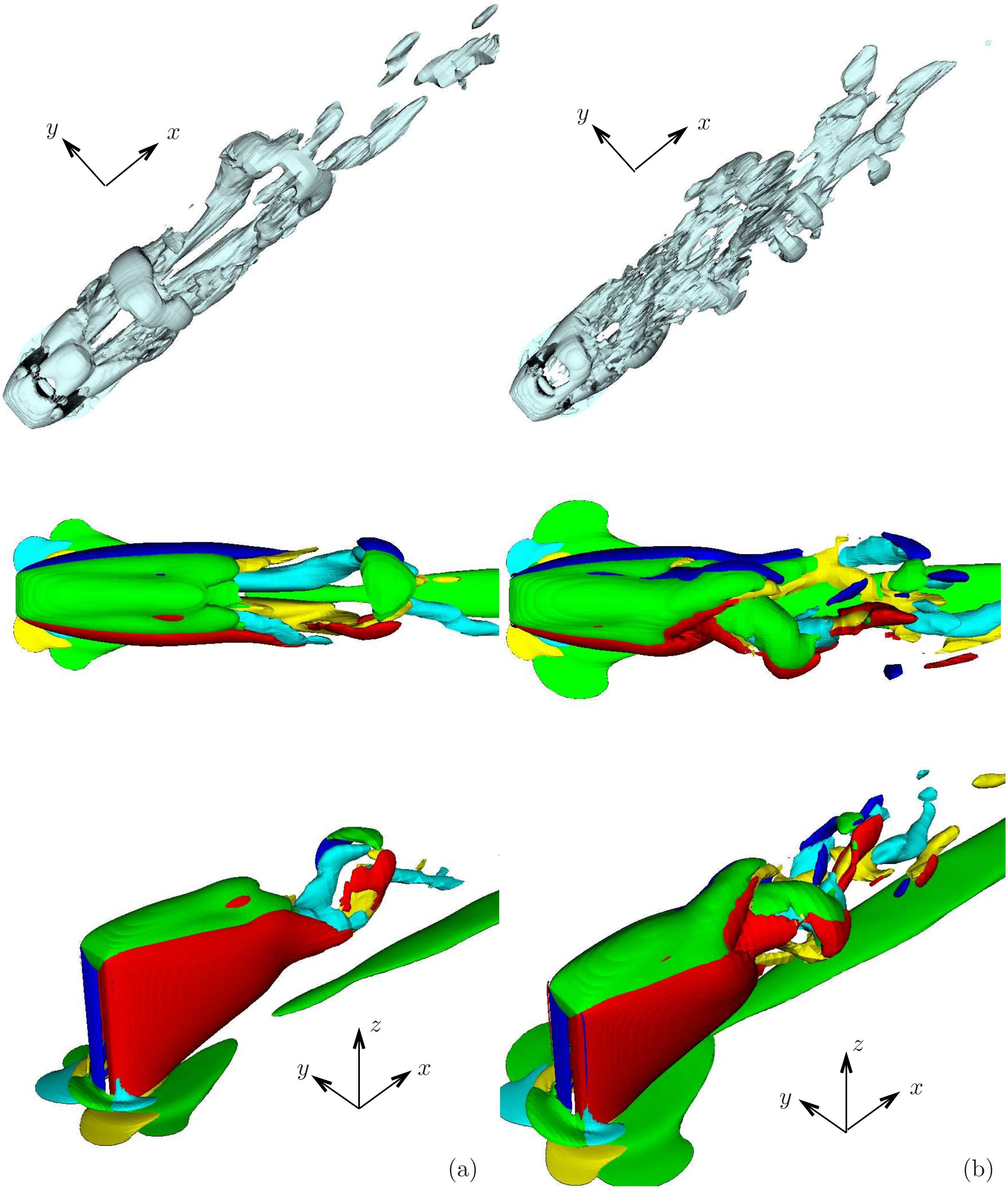

Figure 9.6: Vortex street at (a) $Re_W = 250$ and $t = 1420t_u$ and (b) $Re = 300$ and $t = 1044t_u$. (top) Iso-surfaces of λ_2 = (a) -0.5 and (b) -0.7; iso-surfaces of vorticity: (middle) top and (bottom) 3D views. Colours have the same meaning as in figure 9.4.

slight asymmetry in the vortex street. For $Re_W \geq 300$, the latter oscillations have gained in intensity. The legs of the hairpin vortices do not split at the same $z-$coordinate, while their head turn into a chaotic aggregate of structures shed from the free shear layers. Hairpin vortices are therefore released alternately on either side of the wake centreline and a fully asymmetric vortex street is therefore observed as seen on figure 9.6(b). The chain of Ω-shaped vortices is still observed, but their shape is also irregular and their orientation follows that of the hairpin vortices at the origin of their formation. A similar evolution of the vortex street with increasing Re has been described by [128] in experiments of the flow past a square plate.

To summarize the flow dynamics, we report in figure 9.7 the main features observed in the present non-MHD investigations.

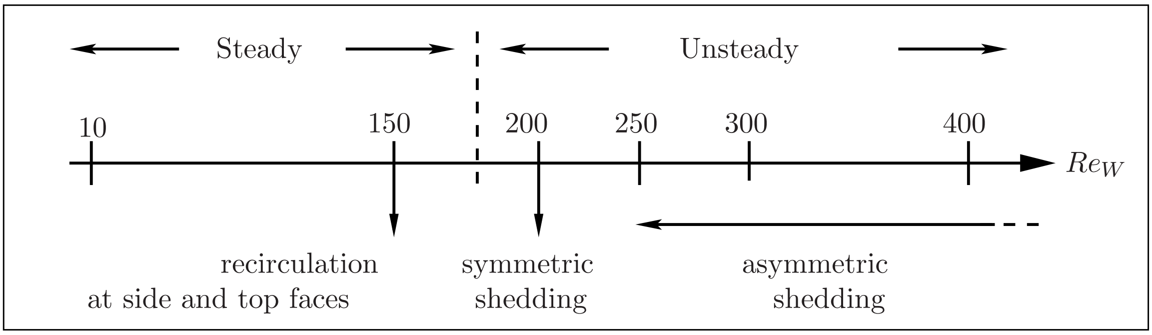

Figure 9.7: Summary of the outcomes of the simulations

9.5 Flow coefficients

We shall now give a deeper insight into the flow dynamics through the scrutiny of the variations with Re_W of a set of flow coefficients. The latter have all been introduced in section 2.3 but the spanwise lift coefficient C_z which shall be defined in this section. The first part is dedicated to the evolutions with Re_W of the flow coefficients averaged over both cylinder span and time. These evolutions shall reflect the global flow dynamics. In the second part of this section, we will present the respective spanwise distributions of the flow coefficients at different Re_W within both the steady and the unsteady flow regimes. The examination of the relevant curves shall give valuable insight on some local aspects of the flow and bring better understanding of the physical mechanisms underlying the global flow dynamics.

9.5.1 Average values

Figure 9.8 presents the variations of the length of the recirculation regions with Re_W. L_b is defined in section 2.3: in the steady (*resp.* unsteady) flow regime, it is the length of the steady recirculation

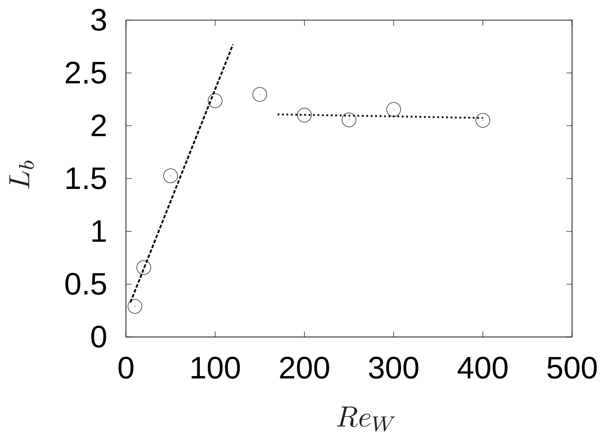

Figure 9.8: Length L_b of the recirculation region versus Re_W. For $Re_W \geq 200$, the respective time averages of L_b are reported. The dash-lines are the respective linear regressions in the steady and unsteady flow regimes.

regions (*resp.* vortex formation region). One observes that L_b increases within the steady regime and slightly decreases with the unsteady one. The maximum length reached by the recirculation regions is about $2.3W$. The subsequent decrease is very smooth as L_b eventually drops down to about $2W$ at $Re_W = 400$.

The linear lengthening of the recirculation regions in the steady regime is also observed in the case of the non-truncated cylinder and relies on the action of the free stream at the outer boundary of the lateral free shear layers. The appearance of secondary recirculation regions at the cylinder lateral faces induces a sudden changes in the curvature at the vicinity of the cylinder and consequently alters the action of the free stream on the outer boundary of the lateral free shear layers. As a result, the latter still lengthen, but not at the same pace as in the early stages of the steady regime. The decrease in L_b in the unsteady flow regime results from the shortening of the lateral free layers induced by the vortex shedding. This shortening is however not uniform along the span, as the formation of the hairpin vortices triggers the shedding of the lateral free shear layers in the upper part of the latter layers only. Consequently, the spanwise average of L_b decrease is weak.

The dynamics of the recirculation regions determines the variations of all the drag coefficients. The respective evolutions of the base pressure coefficient C^i_{pb}, the pressure drag coefficient C_{Dp}, the viscous drag coefficient C_{Dv} and the total drag coefficient C_D with increasing Re_W are shown in figure 9.9. C^i_{pb} is computed with the reference pressure taken at the inlet.

The base pressure coefficient $-C^i_{pb}$ decreases throughout the steady regime and increases within the unsteady one. The variations of $-C^i_{pb}$ are then opposite to those of L_b as in the non-truncated case. The recirculation regions correspond indeed to a region of adverse pressure gradient which opposes the streamwise pressure gradient in the duct. As the recirculation regions lengthen, this adverse gradient becomes more significant and the pressure difference between the inlet and the base

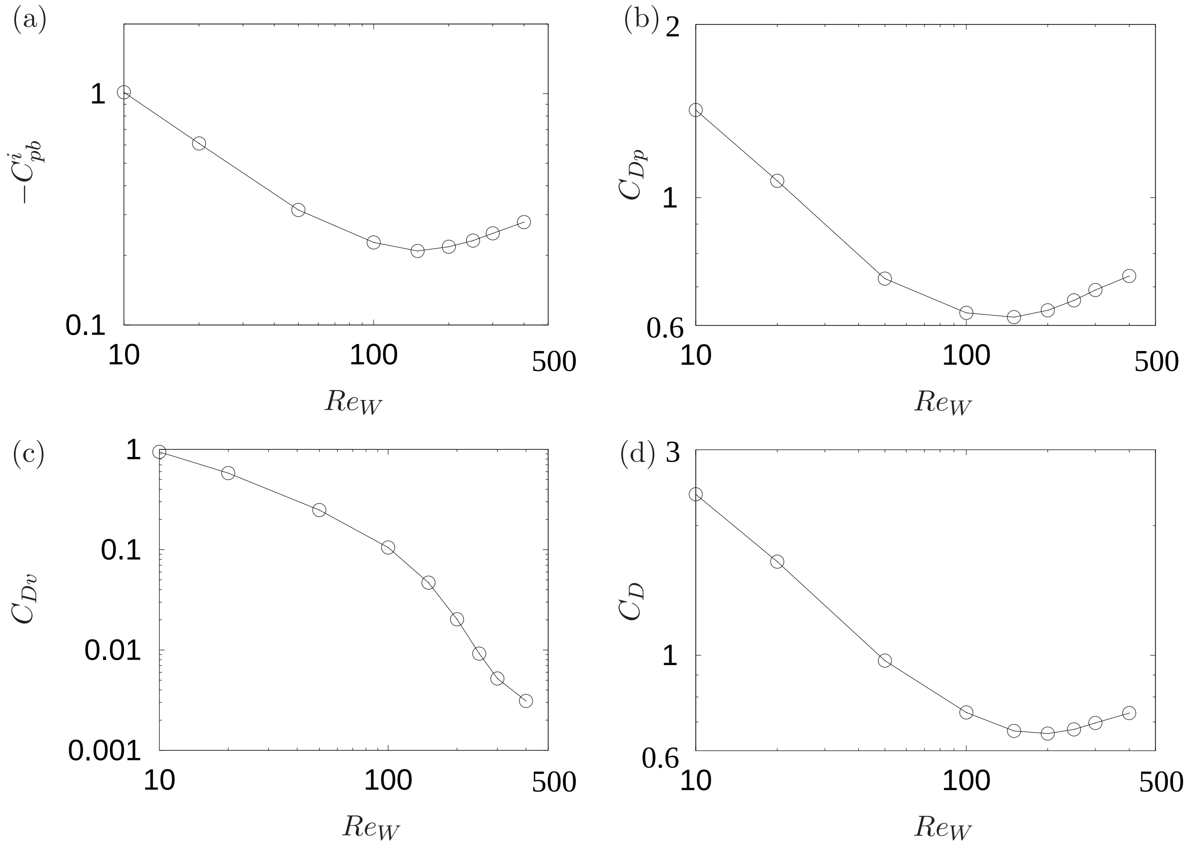

Figure 9.9: (a) Base pressure coefficient C^i_{pb}, (b) pressure drag coefficient C_{Dp}, (c) viscous drag coefficient C_{Dv}, (d) total drag coefficient C_D versus Re_W. C^i_{pb} is computed with the reference pressure taken at the inlet. For $Re_W \geq 200$, the time average of the coefficients is reported.

point shrinks, hence the decrease in $-C^i_{pb}$ within the steady regime. In return, when the recirculation regions shorten in the unsteady regime, the adverse pressure gradient reduces and $-C^i_{pb}$ increases.

The variations in the pressure drag coefficient C_{Dp} follow from the same mechanism so that C_{Dp} exhibits the same evolution as $-C^i_{pb}$. As the viscous drag coefficient C_{Dv} continuously decreases throughout the steady regime, the total drag coefficient C_D also decreases in this regime. At $Re_W =$ 200, after the onset of vortex shedding, C_{Dv} is one order of magnitude lower than C_{Dp} ($C_{Dv} \simeq 0.02$ and $C_{Dp} \simeq 0.7$) and keeps on decreasing in the unsteady flow regime. As a result, the evolution of C_D follows from that of C_{Dp} and since the latter increases in the unsteady flow regime due to the shrinking of the mean recirculation regions, C_D also increases within the unsteady flow regime. Remarkably the values of C_D are about half as high as that of the non-truncated cylinder [102, 104, 107].

Similarly to the drag and lift coefficient, a third flow coefficient based on the z-component F_z of of the force exerted by the flow on the cylinder is defined as the spanwise lift coefficient C_z [114]:

$$C_z = \frac{2F_z}{\rho U_0^2 W^2} \tag{9.6}$$

We shall distinguish two parts in the spanwise lift coefficient: C_{zt} is the contribution of the cylinder

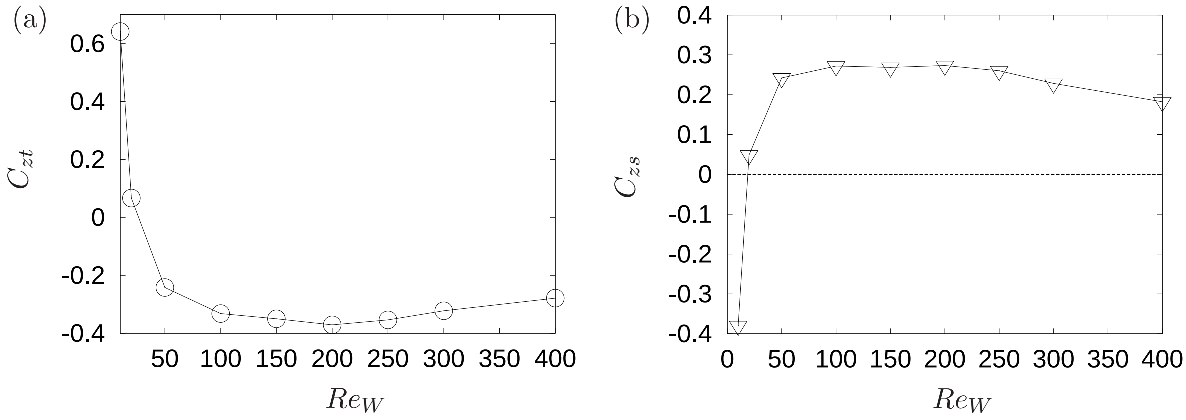

Figure 9.10: Spanwise lift coefficient versus Re_W: C_{zt} is computed over the cylinder top face only (a) and C_{zs} over the whole cylinder surface but the top face (b).

upper face only and C_{zs} that of the cylinder lateral, front and rear faces. The variations with Re_W of both C_{zt} and C_{zs} are shown on figure 9.10.

By definition, on the cylinder top face, C_{zt} results exclusively from the integration of the pressure force and is defined up to a constant determined by the value of the reference pressure. As a consequence, only the variations of C_{zt} reflect the flow dynamics, while its absolute values shall be regarded relatively to the reference pressure. In particular, the sign of C_{zt} bears no significance. C_{zt} decreases in the steady regime and slightly increases in the unsteady one. As for the drag coefficient, the decrease of C_{zt} results from the lengthening of the spanwise recirculation regions at the back of the cylinder. The reason for its increase is the appearance of the secondary recirculation over the cylinder upper face that induces an adverse pressure gradient. The destabilization of the top free shear layer in the unsteady regime for $Re_W \geq 200$ slightly enhances this trend throughout the unsteady regime.

On the other hand, C_{zs} results only from the z-component of the viscous friction at the cylinder stem faces, *i.e.* from the variations of the z-component u_z of the velocity at these faces. At $Re_W = 10$, u_z is very weak in the vicinity of the lateral cylinder faces. The value of C_{zs} therefore relies mainly on the flow downwash from the cylinder free end. The latter results in negative values for C_{zs}. When Re_W is increased up to 150, three aspects of the flow dynamics in the cylinder wake have been identified. Firstly, the appearance and dynamics of the head vortex shown by red streamlines on figures 9.2(c-d) causes the flow downwash to be shifted further from the cylinder free end at the downstream end of the head vortex. Secondly, the upper substream of blue streamlines (see figure 9.2(c) and section 9.3.1) induces an upwards jet along the upper part of cylinder rear face. Finally, as the foci F_1 and F_2 shown on figure 9.2(d) are located closer to the cylinder rear face when Re_W is increased, the upwards spirals feeding the base vortices also induces an upwards jet along the upper lower of cylinder rear face. These three effects thus combine to result in an increase of C_{zs} which subsequently turns positive for $Re_W \geq 20$. Secondary recirculations appear at the lateral cylinder faces at $Re_W \geq 150$ and feed an advert friction, which eventually causes a decrease in C_z.

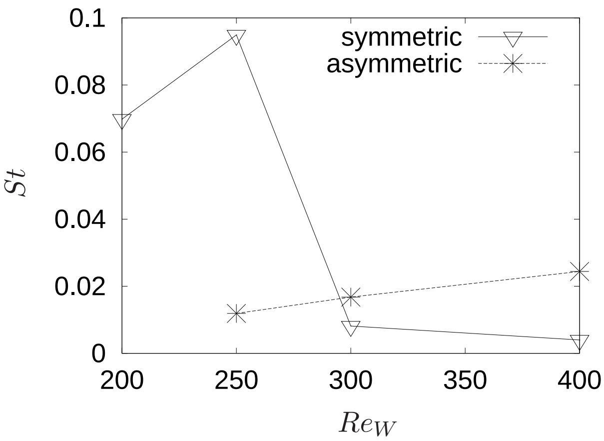

Figure 9.11: Strouhal number St versus Re_W.

The frequency of the symmetric (*resp.* asymmetric) mode was obtained from the time history of the total drag coefficient C_D (*resp.* lift coefficient C_L). We were then able to calculate the Strouhal numbers associated to the respective frequencies of the symmetric and asymmetric modes. Their dependence on Re_W is presented on figure 9.11. At $Re_W = 200$, the vortex street is indeed perfectly symmetric so the asymmetric mode is absent. At $Re_W = 250$, a slight asymmetry is observed in the wake due to the appearance of the slight vertical oscillations of the base vortices. These oscillations are enhanced when Re_W is further increased until the wake becomes chaotic and completely asymmetric. When the wake is symmetric at $Re_W = 200$, only the symmetric mode is present with an associated $St = 0.07$. When the asymmetric mode appears at $Re_W = 250$, its associated St is much lower ($St = 0.01$) but increases with Re. As the wake becomes more asymmetric, the Strouhal number associated to the symmetric mode collapses down to values below those of the asymmetric one.

9.5.2 Spanwise distribution

We shall now consider the spanwise distribution of the respective flow coefficients at different Re within both the steady and unsteady flow regimes.

Figure 9.12 presents the curves relative to the length of the recirculation regions at different Re_W from 10 up to 400. At $Re_W = 10$, L_b is more or less constant over the cylinder span except at the vicinity of the bottom wall where it gradually increases as the latter wall gets closer. Also, the recirculation regions extends over the whole cylinder span and is zero at the cylinder tip. At $Re_W = 50$, a peak region is observed slightly above the cylinder mid-span. This region widens along the spanwise direction, lengthens along the streamwise one and drifts upwards for higher Re_W. The maximum of this peak region is slightly less than $4.5W$ reached at $z \simeq -0.2h$ for $Re_W = 200$. For $Re_W \leq 100$, the spanwise extension of the recirculation matches exactly the cylinder span. When

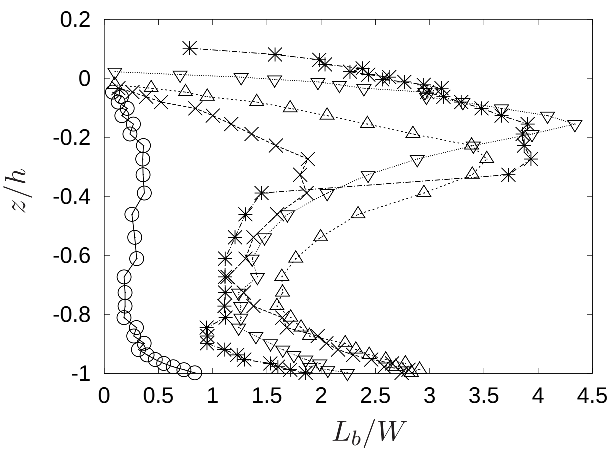

Figure 9.12: Spanwise distribution of the length of the recirculation regions L_b at $Re_W = 10$ (○), 50 (×), 100 (△), 200 (▽) and 400 (∗).

further increasing Re_W, the latter extension exceeds the cylinder height h. At $Re_W = 400$, the maximum spanwise extension is about $1.1h$ reached at $L_b \simeq 0.75W$ downstream the cylinder. On the other hand, when increasing Re_W from 10 on, the bottom end of the recirculation region stretches up to about $3W$ at $Re = 100$ and then decreases down to about $2W$ at $Re_W = 400$.

From these observations it follows that the variations in the spanwise averaged stretching of the recirculation regions in the steady regime results mainly from those of the bottom and upper peak regions. The lower peak region is present at the lowest Re_W, unlike the upper one which appears only at $Re_W = 50$. The lower one reflects the dynamics of the horseshoe pattern and the upper one that of the head vortex. In the steady flow regime, these two structures lengthens along the streamwise direction, hence the increase in L_b in the corresponding regions. In the unsteady regime, the upper fluid jet fuelled by the primary streamwise vortices deteriorates the downstream shape of the horseshoe so that L_b slightly shrinks. The similar mechanism applies for the head vortex and leads to the same variations in L_b in the upper peak region. In addition, the upwards drift of the head vortex and the presence of secondary recirculation for $Re_W \geq 150$ causes the recirculation regions to eventually overcome the cylinder tip from $Re_W = 150$ onwards. In other words, the top of the recirculation regions coincides with the top free shear layer. As already mentioned previously, one observes that this layer washes down behind the cylinder tip at low Re_W and gradually moves upwards for increasing Re_W.

The streamwise distributions of the pressure base coefficients C^i_{pb} and C^f_{pb}, computed respectively with the pressure reference at the inlet and at the front stagnation point, is reported in figures 9.13 (a) and (b), respectively. Note that, in the determination of $C^{i,f}_{pb}(z)$, the base pressure and the reference pressure are taken at the same z-coordinate and the variations in the coefficient are shown relatively to the spanwise and time average.

The streamwise distribution of C^i_{pb} exhibits an invariant point at $z \simeq -0.4h$. On the one hand,

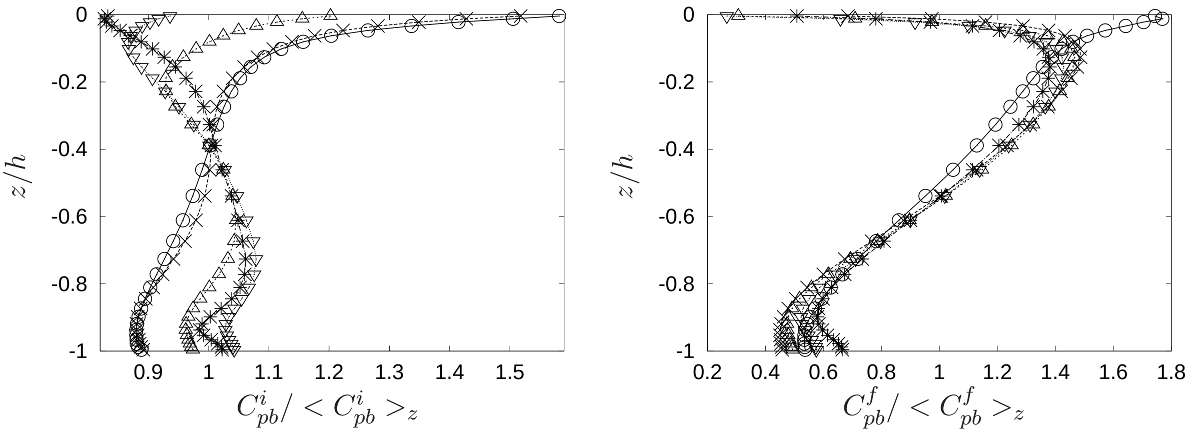

Figure 9.13: Spanwise distribution of the base pressure coefficient relatively to the spanwise and time average at $Re_W = 10$ ($\circ$), 50 ($\times$), 100 ($\triangle$), 200 (∇) and 400 ($*$). C^i_{pb} (*resp.* C^f_{pb}) is computed with the reference pressure taken at the inlet (*resp.* front cylinder face). $< \cdot >_z$ is the spanwise average.

above this point, C^i_{pb} decreases sharply over the whole span for $10 \leq Re_W \leq 200$ and a slight increase is observed at $Re_W = 400$ for $-0.005h \leq z \leq -0.4h$. On the other hand, below the invariant point, C^i_{pb} smoothly increases and then barely varies for $Re_W \geq 100$. An invariant point is also detected on the streamwise distribution of C^f_{pb} at $z \simeq -0.7h$. The sharp drop in C^f_{pb} above this point is though limited to a narrow spanwise interval close to the cylinder tip. Also, below the invariant point, a slight increase in C^f_{pb} is also observed over the whole Re_W interval.

From figure 9.12 it follows that the invariant point present on the C^i_{pb} curve corresponds to the bottom end of the head vortex, while that exhibited on the C^f_{pb} curve has to do with the upper border of the horseshoe pattern. On the one hand, the adverse pressure gradient relative to the head vortex grows and gains in strength within the steady flow regime so that C^i_{pb} decreases in the upper part of the cylinder. As the head vortex drifts upwards, the minimum of C^i_{pb} also shifts closer to the cylinder tip. The transition to the unsteady regime induces a shrink in the head vortex, in terms of time average, and the subsequent increase in C^i_{pb} observed at $Re_W = 400$. On the other hand, the bottom region of the cylinder is immersed within the horseshoe pattern and the evolution of C^f_{pb} reflects the dynamics of the latter structure. Since the horseshoe pattern remains steady for the Re_W interval considered in this study, the relative variations in C^f_{pb} are weak.

Figures 9.14 (a-c) presents the respective spanwise distributions of the pressure (C_{Dp}), viscous (C_{Dv}) and total (C_D) drag coefficients at different Re_W within both the steady and the unsteady flow regimes. The variations are shown relatively to the respective spanwise and time averages. Three regions are identified on this set of curves: two narrow ones at both cylinder ends and a large one between them [118]. The C_{Dp} curves are very similar to the C^f_{pb} ones. The spanwise variations of C_{Dv} show that both end regions are associated to a peak of C_{Dv} which increases with higher Re_W, while the large mid-span one is rather plateau-shape with a minimum value decreasing with higher

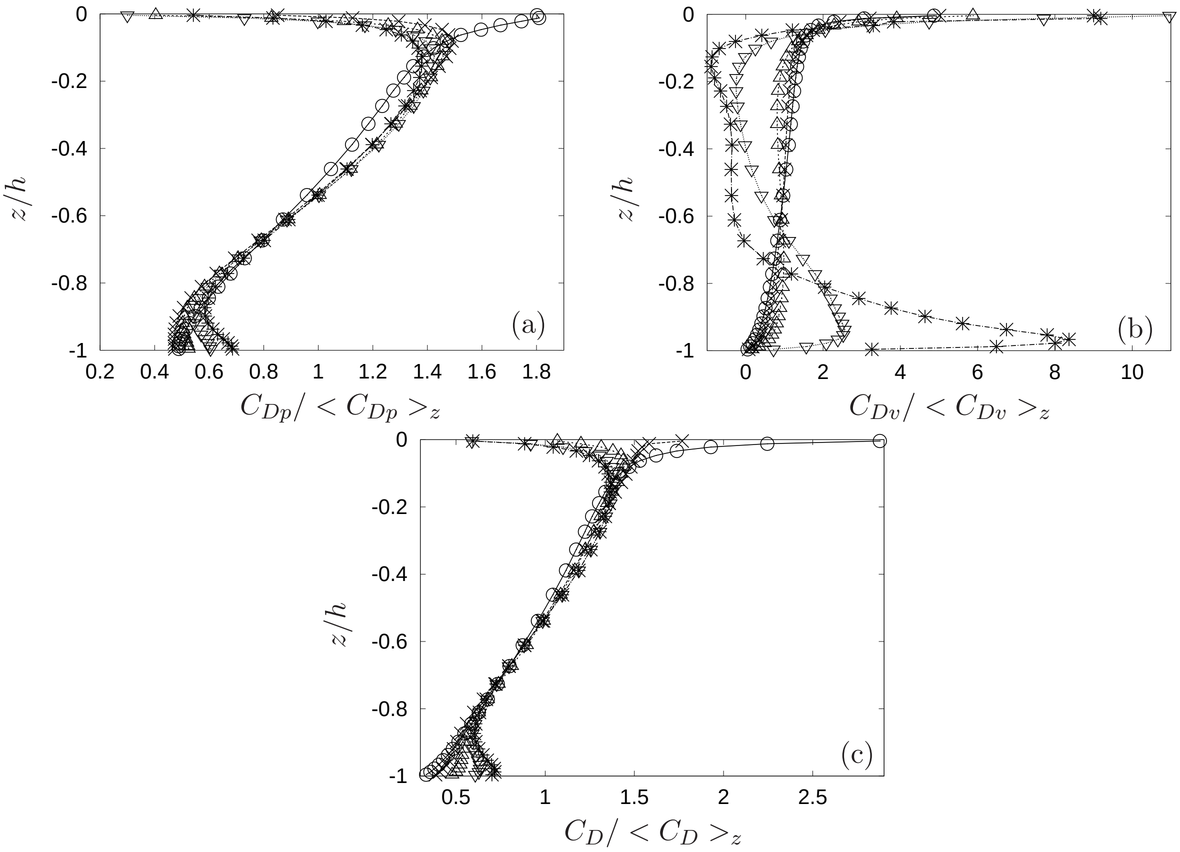

Figure 9.14: Spanwise distributions of (a) the pressure drag coefficient C_{Dp}, (b) the viscous drag coefficient C_{Dv}, (c) the total drag coefficient C_D at $Re_W = 10$ (∘), 50 (×), 100 (△), 200 (∇) and 400 (∗). $< \cdot >_z$ is the spanwise average.

Re_W. In addition, C_{Dv} turns negative over a narrow spanwise interval at $Re_W = 200$, which is wider at $Re_W = 400$. Finally the total drag coefficient C_D exhibits variations only in both end regions, whereas the mid-span barely changes. Also, these curves look very much alike those relative to C_{Dp}.

The spanwise variations of C_{Dp} rely on the same effects as those described for the C_{pb}^f curves. A remarkable feature is seen on the evolutions of C_{Dv} which turns negative on some extent of the cylinder span. This is caused by the appearance and subsequent growth of secondary recirculation at the cylinder lateral faces for $Re_W \geq 150$. The counter-flow induced by the latter recirculation opposes the main stream and eventually pushes C_{Dv} into negative values. As a consequence, in the region where C_{Dv} is negative, the total drag coefficient C_D is higher than the pressure one C_{Dp}. This has been observed in 2D square cylinder wakes [104]. In contrast, in the end regions, the fluid circulates at a higher velocity than in the mid-span region and generates the peaks in C_{Dv}, although this has a weak influence on the variations in C_D. The latter are governed by the pressure drag coefficient whose values significantly overweigh those of C_{Dv} at high Re_W, hence the strong similarity between both curves of C_{Dp} and C_D. Although the general shape of the C_D and C_{Dp} curves do not change much with Re_W, their respective spanwise and time averages vary as shown on figures 9.9 (b) and (d).

9.6 Conclusions and perspectives

9.6.1 Summary of the outcomes

In this chapter, we have investigated the non-MHD flow past a truncated square cylinder in a duct of rectangular cross-section for Reynolds numbers up to 400.

Through a thorough scrutiny of the steady flow regime, we have identified the steady flow patterns and their dynamics in this regime. We have shown that all the structures are generated by streamlines circulating underneath the lateral free shear layers. The high spanwise blockage ratio promotes the development of the base vortices at the expenses of the tip ones. In the late stages of the steady regime, we have detected the appearance of secondary recirculation at both upper and lateral faces of the cylinder. The appearance of the top secondary recirculation combined with the upwards flow jet induced by the base vortices gradually shift the head vortex to higher spanwise positions.

These dynamics are the key to understanding the transition to the unsteady flow regime. The upwards jet between the base vortices lifts the tail of the top free shear layer which eventually turns unstable and initiates the formation of hairpin vortices at $Re_W = 200$. Those vortices have been detected in many experimental works involving an obstacle of different shapes with an aspect ratio γ such that $1 \leq \gamma \leq 4$ [121, 122, 128, 129]. We have singled out a formation mechanism undiscovered so far which has little in common with those introduced in former works [114, 121, 129]. In our computations, the hairpin vortices result from the smooth assembling of structures shed from initially steady patterns, *i.e.* from the top and lateral free shear layers and the base vortices. Again, due the strong spanwise confinement, the shedding mechanism yields a vertical head connected to two almost streamwise legs, in contrast with the arch-type vortices observed in [121, 126]. Also, we have detected the formation of a chain of Ω-shaped vortices as a consequence of the release of the hairpin vortices. The Ω-shaped vortices are well known in turbulent boundary layers and their formation follows from the same mechanism [131]. For $Re_W \geq 250$, the vortex street gradually turns asymmetric. We have observed that growing spanwise oscillations of the base vortices are linked to the transition to the asymmetric wake.

The different stages of both flow regimes and the dynamics of the different flow patterns have been related to the evolution of the set of flow coefficients. Basically, many similarities with the non-truncated cylinder wakes have been recovered. The variations of the spanwise and time averaged flow coefficients are very similar and reflect the same mechanisms. We have observed on the spanwise distribution of the viscous drag coefficient C_{Dv} the effect of the presence of secondary recirculation which induces negative values of C_{Dv}. On the other hand, the secondary recirculation appearing at the upper cylinder face causes an increase of the spanwise lift coefficient C_z. Finally, we have shown that the Strouhal number collapses when the wake turns asymmetric indicating the vanishing of the symmetric frequency mode associated with the hairpin vortex vortex singled out at $Re_W = 200$.

9.6.2 Perspectives

The non-MHD wake past a truncated cylinder is a reference case. We shall later refer to the physics described in this configuration as we consider the MHD case in the following chapter. We shall however bring forward some comments on the present outcomes.

Although the chosen configuration is relevant from a physical point of view, the cylinder wake is subject to the influence of the duct walls. The transverse blockage ratio $\beta = d/(2b)$ featured in this configuration is equal to 0.1. Such a ratio has little effect in the flow dynamics of the non-truncated cylinder wake and we shall expect the same negligible influence in the truncated case. [109] showed that a ratio lower than 0.25 had no effect on the horseshoe pattern. A parametric study on β may indicate whether the transverse blockage ratio might promote the stability of the hairpin vortices and enhance the symmetric properties of the wake. A similar parametric investigation performed on the spanwise blockage ratio $\beta_z = h/(2a)$ could also address these issues. The present spanwise confinement is however high and explains the shape of the hairpin vortices and why the base vortices prevail in the flow. Also, there is a significant discrepancy between the critical values of the aspect ratio separating the regimes involving the shedding of hairpin vortices and Kármán vortices provided by different experimental works [115, 121, 128]. A further parametric study over the cylinder shape and aspect ratio should bring a good insight on this question.

Chapter 10

Three-dimensional MHD flow past a truncated square cylinder

We now investigate the MHD flow past an insulating square cylinder in an insulating duct in an externally applied magnetic field aligned with the cylinder axis using 3D full DNS. The non-MHD case is treated in the previous chapter. We shall show the effects of the magnetic field on the flow dynamics. We describe the steady flow patterns, their dynamics and the paths of the electric current in the steady regime. We then consider the unsteady flow patterns and give the mechanism of vortex shedding. The evolutions of the respective flow coefficients and their spanwise distribution at increasing Re_W and Ha are provided. Finally, we consider the case where the insulating square cylinder is replaced by a perfectly conducting cylinder. The consequences on the flow dynamics and coefficients are discussed and systematically compared with the case with an insulating cylinder.

The results provided in this chapter are to be included in an article currently in preparation [3].

10.1 Configuration and flow equations

We consider the flow of an electrically conducting fluid around a truncated cylinder of square cross-section under an externally applied, steady, homogeneous magnetic field in a duct of rectangular cross-section. The geometric configuration sketched in figure 10.1 is exactly the same as that of the previous non-MHD study, *i.e.* $h = 4W$, $2a = 8W$ and $2b = 10W$. The magnetic field $\mathbf{B}_0$ is oriented along the cylinder axis and points upwards such that $\mathbf{B}_0 = B_0\mathbf{e}_z$.

The magnetic Reynolds number Rm is assumed to be much smaller than unity so that the flow is governed by the MHD equations written in the low-Rm approximation. The 3D MHD numerical code described in section 7.2 is used to investigate the flow dynamics. Using the cylinder width W, the duct half-height a, the maximum of the inlet velocity U_0 and the intensity of the magnetic field B_0 as respective characteristic length of the velocity field, diffusion length of the magnetic field, velocity

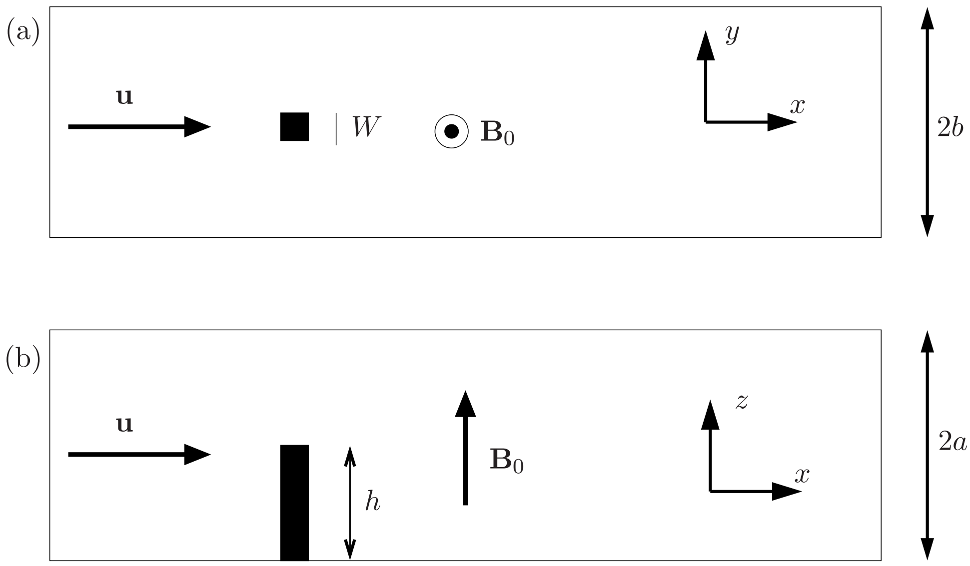

Figure 10.1: Configuration of the MHD flow past a truncated square cylinder: top (a) and side (b) views

and magnetic field, the non-dimensional flow equations are the momentum conservation (10.1), the mass conservation (10.2) and the electric current conservation (10.3) together with Ohm's law (1.20):

$$\frac{\partial \mathbf{u}}{\partial t} + (\mathbf{u} \cdot \nabla)\mathbf{u} = -\nabla p + \frac{1}{Re_W}\nabla^2 \mathbf{u} + \frac{W}{a}\frac{Ha^2}{Re_W}[(-\nabla\phi + \mathbf{u} \times \mathbf{e}_z) \times \mathbf{e}_z] \tag{10.1}$$

$$\nabla \cdot \mathbf{u} = 0 \tag{10.2}$$

$$\nabla^2 \phi = \nabla \cdot (\mathbf{u} \times \mathbf{e}_z) \tag{10.3}$$

The Reynolds number is based on the cylinder width $Re_W = WU_0/\nu$ and the Hartmann number on the half-height of the duct $Ha = aB_0\sqrt{\sigma/(\rho\nu)}$.

10.2 Numerical set-up

The dimensions of the computational domain and the boundary conditions for the pressure are identical to those of the non-MHD configuration. Figure 10.2 shows an overview of the mesh designed for the case at $Ha = 100$.

For the velocity, only the velocity profile imposed at the inlet to drive the flow differs from the non-MHD study. It is obtained from preliminary 3D MHD computations in the duct with the cylinder absent, *i.e.* from 3D simulations of the Shercliff flow (see section 8.3).

The duct walls and the cylinder are considered as electrically insulating and impermeable and no wall function is implemented at any of the Hartmann walls. Consequently, the boundary conditions for the electric potential at the duct and cylinder walls are identical and given by (8.11). At the inlet,

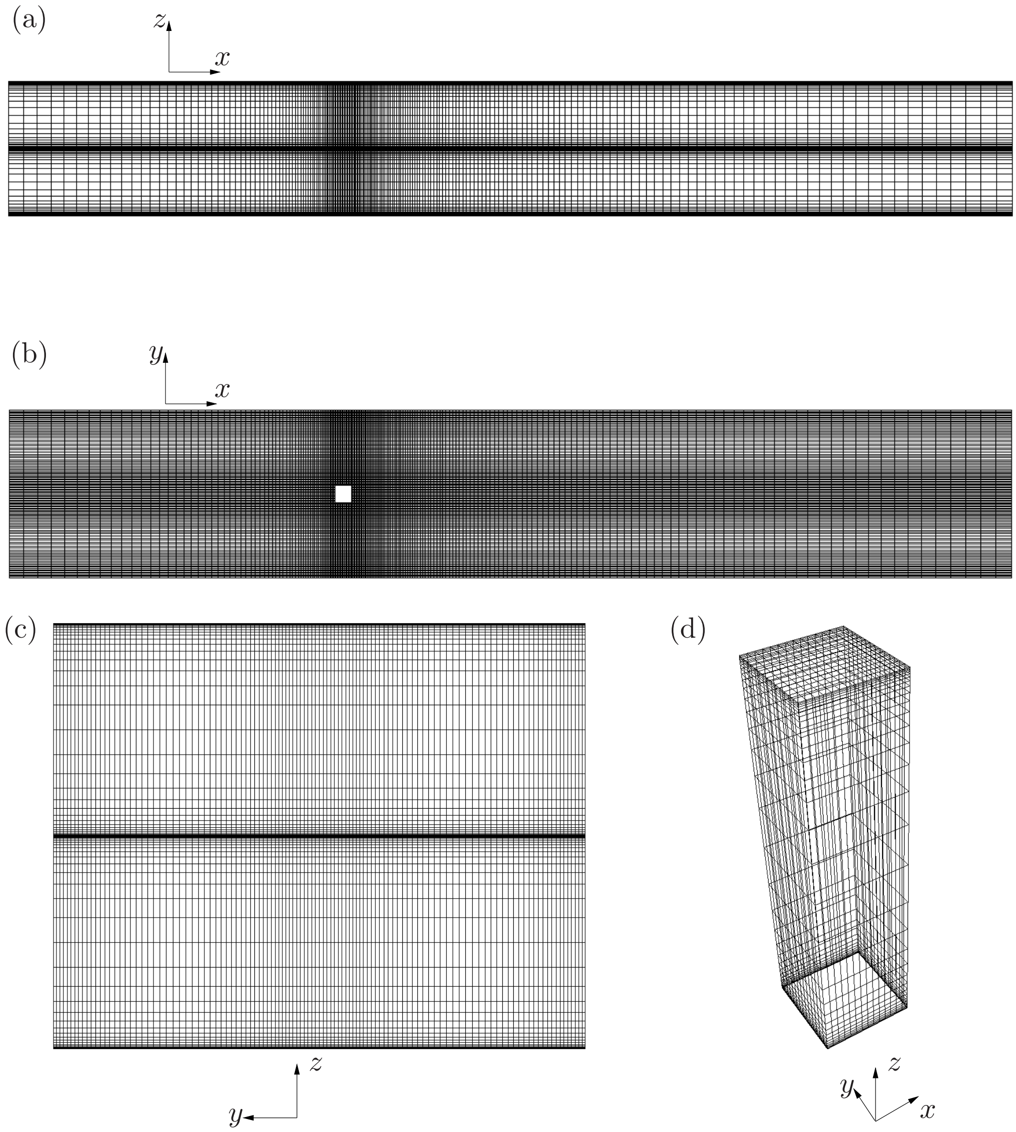

Figure 10.2: Overview of the mesh designed for the case $Ha = 100$ in the planes $y = b/W$ (a), $z = -\gamma$, $x = -20$ (c) and at the cylinder surface (d).

a homogeneous Neumann condition is imposed:

$$\partial_n \phi = 0 \text{ at } x = -15, |y| \leq b/W, |z| \leq \gamma \tag{10.4}$$

At the outlet boundary, we impose equation (8.13) as we assumed that the condition $Ha \gg 1$ is met in our simulations. Equations (8.13) and (10.4) enforce a zero normal component of the electric current to prevent any leak of electric current through these boundaries and guarantee the current conservation inside the computational domain [189].

We have achieved two sets of computations by increasing Re_W at $Ha = 100$ for Re_W =1, 10, 20, 50, 100, 300, 400, 600 and 800 and at $Ha = 200$ for $Re_W = 1$, 10, 20, 50, 100, 400, 600, 800 and 1000. Each series has been started at $Re_W = 1$ for which the fluid is considered at rest in the initial conditions. The flow is computed over a total simulation time higher than $5t_H$ (1.47). The final state of the flow at a given Re_W is used as initial conditions for the next value of Re_W.

10.3 Steady flow regime

10.3.1 Hunt's wake

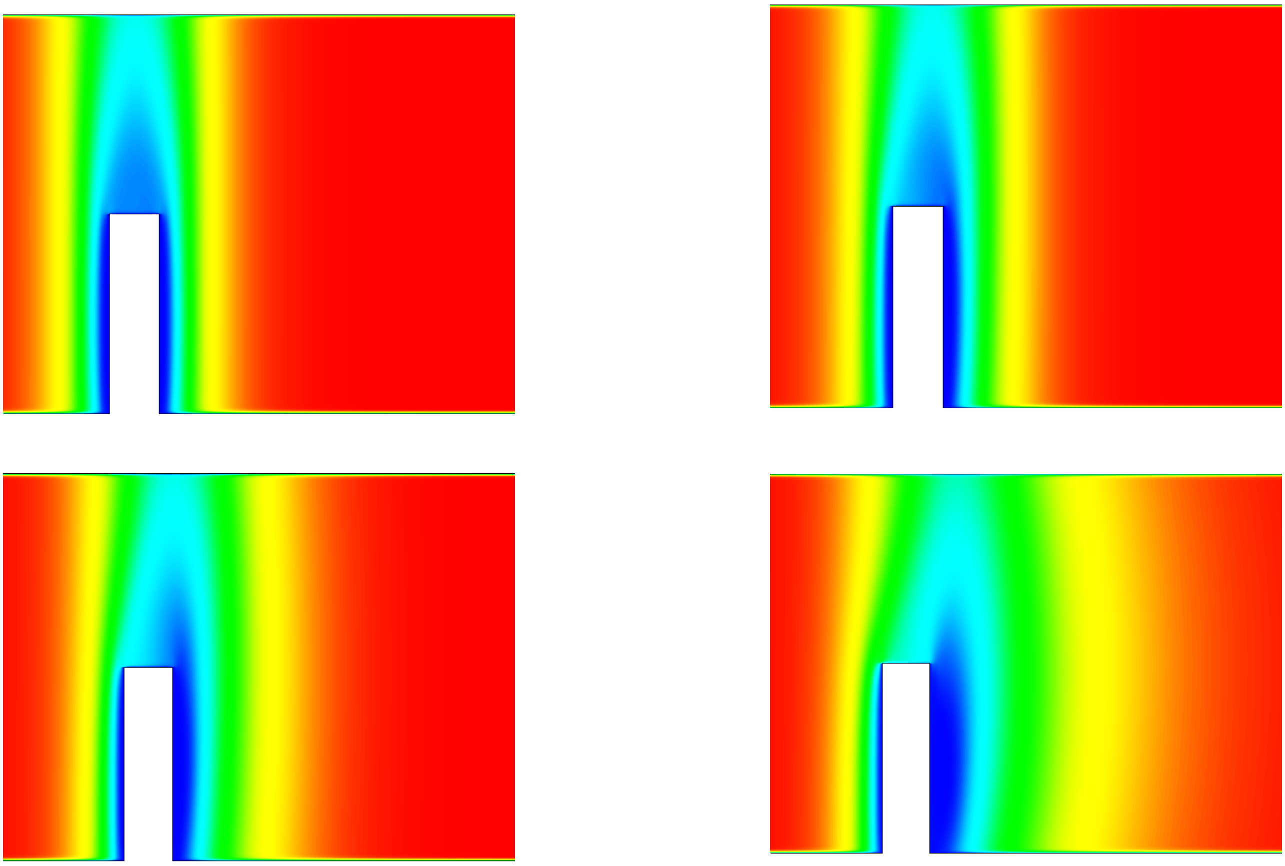

Figure 10.3: Streamwise velocity magnitude in the plane $y = 0$ at $Ha = 200$: $Re_W = 1$, 10, 20 and 50 (top to bottom, left to right).

Figure 10.3 shows the magnitude of the streamwise velocity in the centre-plane $y = 0$ at $Ha = 200$ for $1 \leq Re_W \leq 50$. No flow separation could be detected at anywhere in the fluid domain at $Re_W = 1$ and 10. This corresponds to the creeping flow regime. One observes an almost zero velocity region above the cylinder upper face up to the top Hartmann walls. Outside this region, the flow is quasi-2D: it is fully two-dimensional in the core flow and three-dimensional in the Hartmann and Shercliff layers. Above the cylinder tip, the flow structures imposed by the presence of the cylinder are stretched along the direction of the magnetic field leading to the formation of a *ghost* half-cylinder on the top of the existing one. This feature has been predicted in the analytical investigations of the MHD flow past an obstacle in a strong magnetic field by Hunt and co-workers [181, 140]. We shall therefore denote the latter as *Hunt's wake*. The present flow visualisations have however been the first evidence shown of the existence of such a feature, since the experiments of [133] that detected it above an electrically conducting disk placed in a trough inside an electrically insulating duct. When Re_W is increased, the low-velocity flow region above the cylinder is gradually pushed downstream by the free stream.

10.3.2 Steady recirculation regions

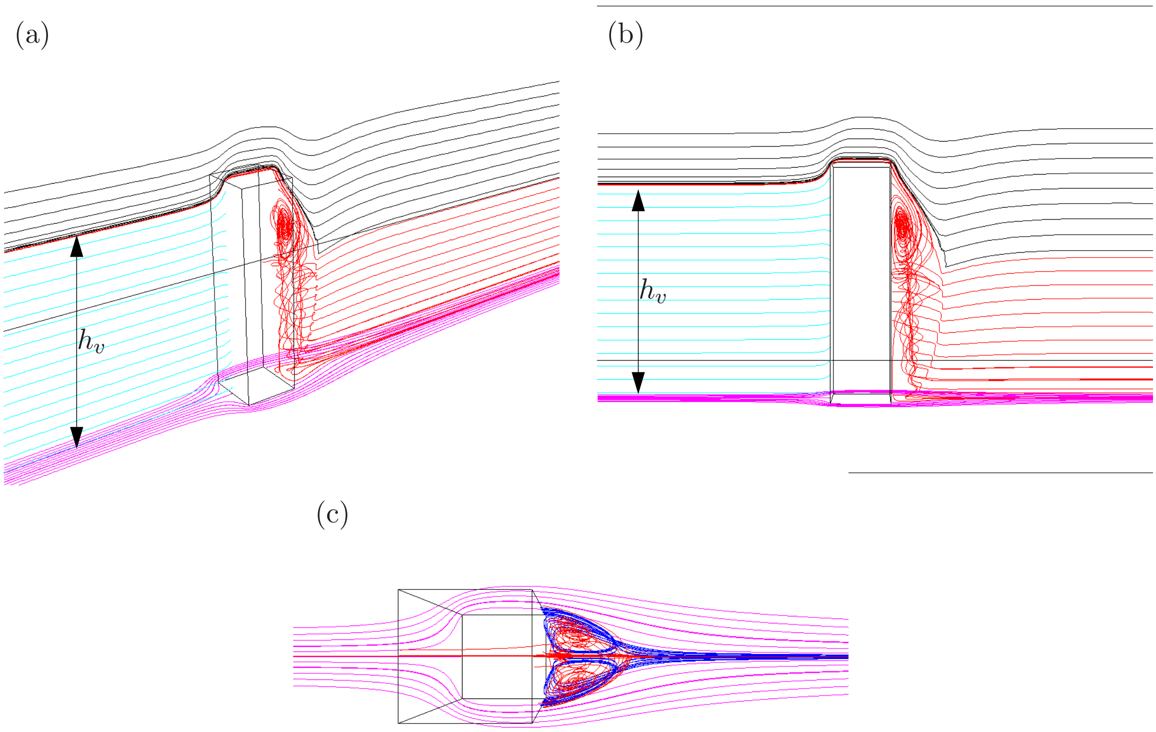

Figure 10.4: Kinematic streamlines at $Re_W = 100$ and $Ha = 200$: (a) 3D view; (b) side view and (c) top view. Red lines depict the head vortex degenerating into two columnar spanwise vortices. Blue lines show the spanwise vortices initiated by the red spanwise vortices. Pink streamlines originate upstream the cylinder in the plane $z/h = -0.998$ immersed within the bottom Hartmann layer. Cyan streamlines rejoin the stagnation points along the upstream cylinder face. Black streamlines are only deflected by the cylinder wake without any noticeable influence on the latter.

Flow separation is observed at the rear of the cylinder at $Re_W = 10$ and 20 for $Ha = 100$ and 200, respectively. The resulting steady flow patterns seen in the cylinder wake are shown in figure 10.4 in the case $Re_W = 100$ and $Ha = 200$. Red streamlines originate upstream the cylinder in the centre-plane $y = 0$ at ($z \simeq -\gamma + h_v$) and pass within the Hartmann layer at the cylinder upper face. They separate at the rear of the cylinder and give rise to a transverse vortex extending from the mid-span up to the tip of the cylinder. The streamlines enter this vortex from the outside and get out at its centre to generate two symmetric counter-rotating spanwise vortices spiralling downwards along the rear cylinder face. The red streamlines then circulate downstream along the streamwise direction in the vicinity of the bottom Hartmann layer. At the rear of the cylinder, the red spanwise vortices give rise to bigger but weaker spanwise vortices depicted by blue streamlines in 10.4(c). Pink streamlines originate upstream the cylinder in the plane $z/h = -0.998$ immersed within the bottom Hartmann boundary layer. These streamlines strictly remain in this plane in the whole fluid domain. A set of streamlines in cyan also originates upstream the cylinder in the centre-plane $y = 0$ and rejoins the line of stagnation points at the upstream cylinder face. The black streamlines are just deflected by the cylinder wake without affecting much the flow patterns. Note how deep they dive behind the cylinder on figure 10.4 (b).

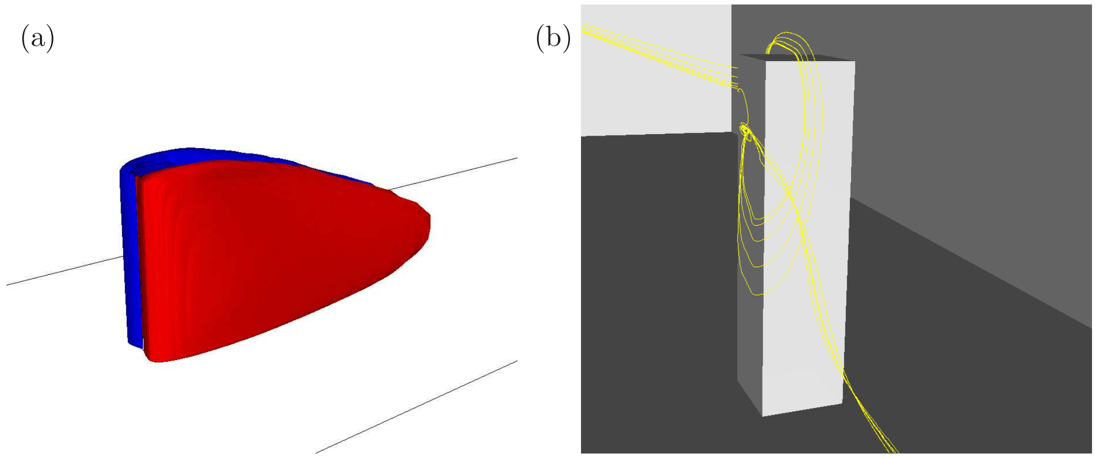

Figure 10.5: Steady flow patterns at $Re_W = 400$ and $Ha = 100$. (a) Lateral free shear layers: iso-surfaces of $z-$vorticity $\omega_z^\star = -20$ (*resp.* 20) in blue (*resp.* red). (b) Steady secondary recirculation region at the lateral cylinder face: kinematic streamlines.

A striking difference with the non-MHD steady flow patterns is the absence of any horseshoe structure at the bottom wall around the cylinder basis. In the non-MHD case, the horseshoe pattern results from the interaction of the boundary layers arising at the upstream cylinder face and at the bottom wall. From this destabilisation a system of swirls is generated at some distance upstream the upstream cylinder face which then spiral around the cylinder basis to form a remarkable horseshoe-like structure. In the MHD case, the bottom boundary layer is a Hartmann layer. This boundary layer is much more stable than the non-MHD one [144, 151]. For the values of Re_W and Ha considered in this study, the Hartmann layers remain stable. No swirl forms at the upstream cylinder face and therefore no horseshoe pattern develop around the cylinder basis. As a consequence, the flow streamlines originating in a plane immersed into the bottom Hartmann layer remain in this plane.

A second striking difference with the non-MHD steady flow patterns is the shape of the lateral free shear layers. Figure 10.5(a) shows the lateral free shear layers at $Re_W = 400$ and $Ha = 100$. In the vicinity of the cylinder, these shear layers are almost invariant along the $z-$axis. Their spanwise extension gradually shrinks from their upper extremity down as they extend downstream due to erosion by the free stream. The magnetic field strongly dissipates the vortices perpendicular to the direction of the magnetic field. In addition, it stretches the lateral free shear layers along the $z-$axis so that the characteristic V-shape seen in the non-MHD case is no longer observed in the MHD one. In particular, these shear layers are so long at the vicinity of the Hartmann layers that no fluid can enter the cylinder wake underneath these shear layers as observed in the non-MHD case. The MHD flow structures are made of streamlines circulating above the cylinder tip and washing down behind the cylinder.

10.3.3 Effect of increasing Re_W at a given Ha on the steady flow patterns

Increasing Re_W within the steady regime at a given Ha has several noticeable effects. Firstly, the lateral free shear layers stretch further downstream while keeping an almost invariant spanwise shape. Secondly, the spanwise vortices gain in strength and broaden. They are not only generated by the head vortex, but also by streamlines passing above the cylinder tip and spiralling from the cylinder tip down. Finally, in the late stages of the steady regime, we have detected the presence of steady secondary recirculation regions at the lateral faces of the cylinder: for $Re_W \geq 300$ at $Ha = 100$ and for $Re_W \geq 400$ at $Ha = 200$. Figure 10.5(b) shows the steady secondary recirculation at a lateral cylinder face observed at $Re_W = 400$ and $Ha = 100$. As in the non-MHD case, these secondary recirculations are generated by the stretching of blue streamlines from the spanwise vortices along each lateral cylinder faces and spiral upwards. A secondary recirculation has been also detected at the upper cylinder face at $Re_W = 600$ and $Ha = 100$. In this case and as already observed in the non-MHD study, it emanates from flow separation at the front edge of the upper cylinder face. No secondary recirculation at this face has been detected in the steady regime at $Ha = 200$.

10.3.4 Electric current streamlines

The streamlines of the electric current at $Re_W = 100$ and $Ha = 100$ are shown in figure 10.6 in three different duct cross-sections located upstream, across and downstream the cylinder.

Upstream of the cylinder, the current streamlines remain in the cross-section ($x = -10$) and one observes the characteristic patterns of the Shercliff flow. In this region, the presence of the cylinder has indeed little influence on the flow. Similarly, downstream of the cylinder, as the perturbations induced the cylinder gradually dissipate, the electric streamlines gradually recover the typical patterns of the undisturbed Shercliff flow.

Across the cylinder, the electric current accumulates in the region above the cylinder tip as the cylinder is electrically insulating. The flow braking induced by the Lorentz forces is therefore greatly enhanced in this region. The flow is significantly decelerated above the cylinder tip and when reaching the trailing edge of the cylinder upper face, it just washes down into the rear of the cylinder.

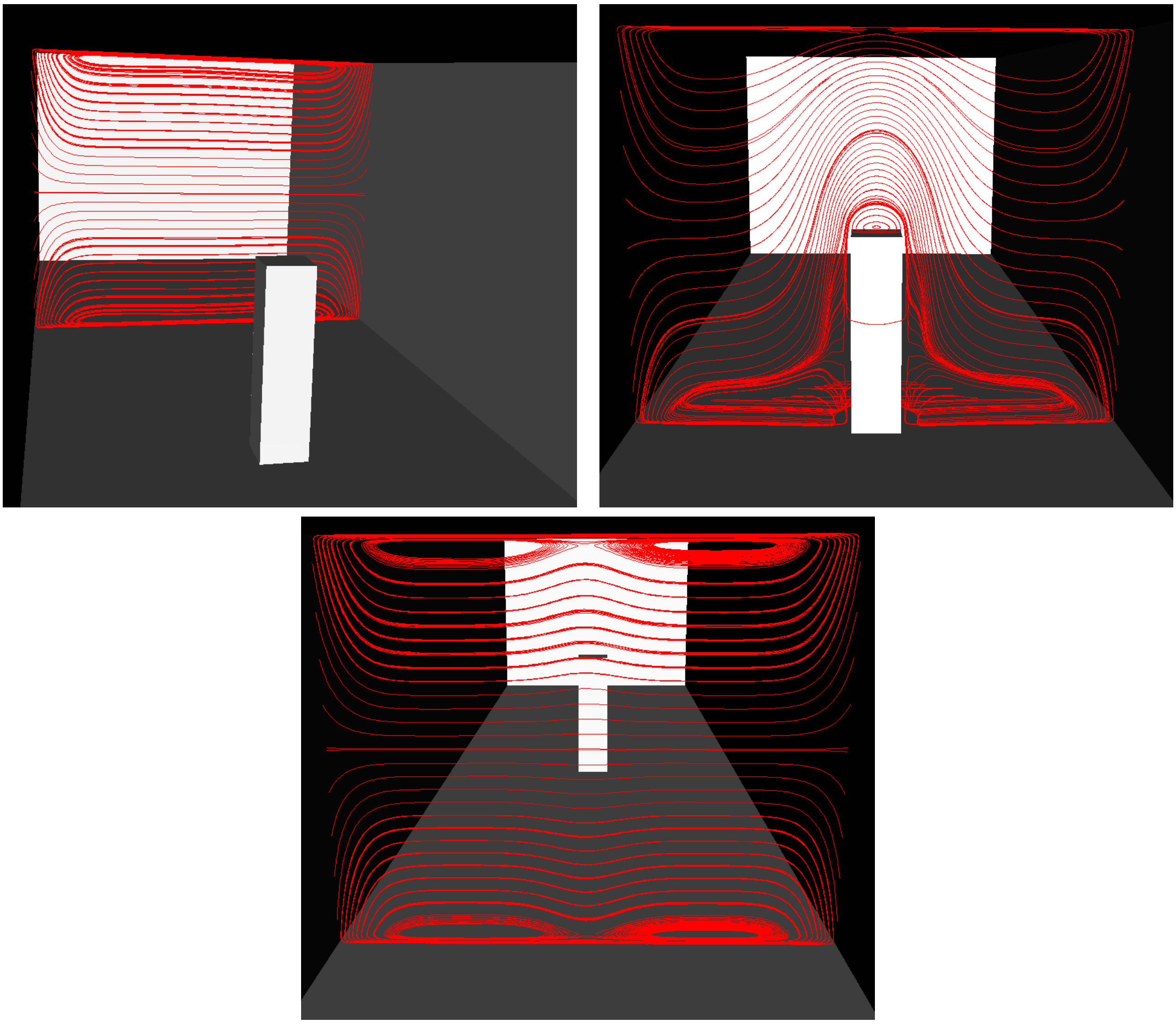

Figure 10.6: Electric streamlines in the cross-section at (top left) $x = -10$, (top right) $x = 0$ and (bottom) $x = 15$ for $Re_W = 100$ and $Ha = 100$. Flow from back to front.

In the vicinity of the cylinder faces, the current streamlines get out of the cross-section ($x = 0$) indicating that the x-component of the current density is non-zero in these regions. The presence of the cylinder actually induces a deflection of the flow along both y- and z-axes. The current density is not unidirectional in these regions and the electric streamlines are thus more intricate.

10.3.5 Lengthening of the steady recirculation regions

We shall now take a deeper look at the dynamics of the recirculation regions within the steady regime through the scrutiny of the evolutions of their length L_b with Re_W, Ha and z/h.

Figure 10.7 shows the variations of the spanwise average of L_b, denoted $\langle L_b \rangle_z$, versus Re_W at $Ha = 100$ and 200. At both $Ha = 100$ and 200, $\langle L_b \rangle_z$ lengthens with Re_W in the steady flow regime. The slope of the curve is steeper and at a given Re_W, $\langle L_b \rangle_z$ is bigger for $Ha = 200$ than for $Ha = 100$.

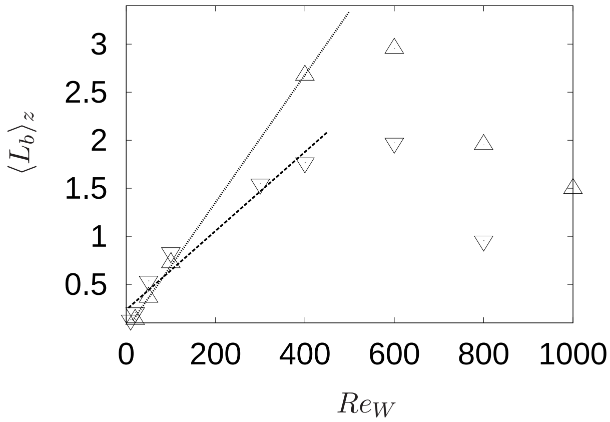

Figure 10.7: Spanwise averaged non-dimensional length of the recirculation region $\langle L_b \rangle_z$ versus Re_W at $Ha = 100$ (∇) and $Ha = 200$ ($\triangle$). In the unsteady regime, L_b is the length of the vortex formation region. The dash-lines are the linear regressions in the steady flow regimes.

The magnetic field little influences the streamwise elongation of the lateral free shear layers: it only shifts the critical Re_W at which they become unstable to a higher value. The linear streamwise extension of the free shear layers already observed in the non-MHD case is thus also observed in the MHD one. The magnetic field however stretches the free shear layers along the spanwise direction so that the spanwise shape of these layers exhibits less variation along the z-axis for $Ha = 200$ than for $Ha = 100$ and $\langle L_b \rangle_z$ is bigger. This latter feature is clearly observed on the respective spanwise distributions of $L_b(z)$ at $Ha = 100$ and 100 for $20 \leq Re_W \leq 1000$ shown on figures 10.8(a-b).

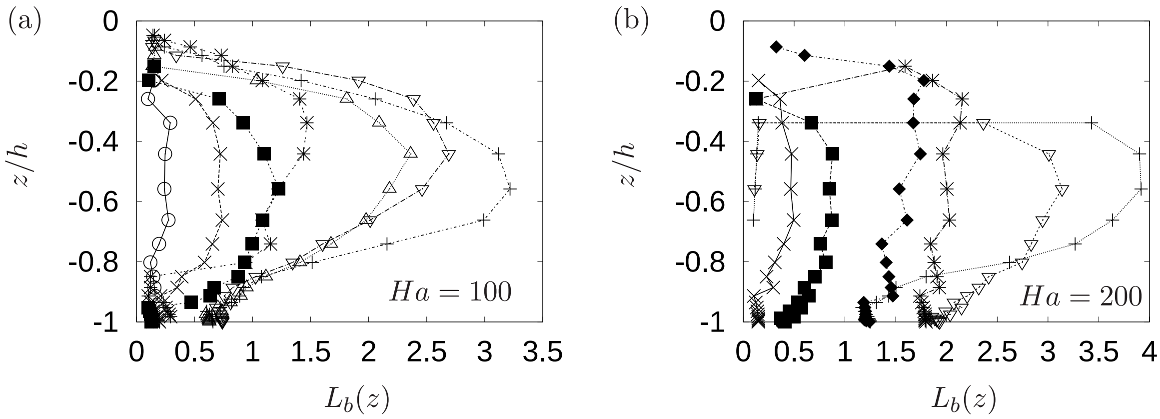

Figure 10.8: Spanwise distribution of the length of the recirculation regions L_b at $Re_W = 20$ ($\circ$), 50 ($\times$), 100 ($\blacksquare$), 300(Δ), 400 (∇), 600($+$), 800($*$) and 1000 ($\blacklozenge$). (a) $Ha = 100$ and (b) $Ha = 200$.

The steady recirculation regions do not extend over the full cylinder span, but only from the bottom Hartmann wall up to $z/h \simeq -0.2$ (*resp.* -0.3) for $Ha = 100$ (*resp.* $Ha = 200$). At a given Re_W, the maximum streamwise elongation of the recirculation regions is almost the same for both values of Ha. Also, at $Re_W = 400$, $L_b(z)$ is significantly bigger inside the bottom Hartmann layer for $Ha = 200$ than for $Ha = 100$.

The steady spanwise vortices at the origin of the recirculation regions are initially fuelled by the head vortex. The latter is located below the cylinder tip at the downstream cylinder face and the spanwise vortices are generated from the centre of the head vortex down. The maximum height reached by the recirculation regions corresponds to the position of the centre of head vortex. At a given Re_W, the latter is closer to the cylinder mid-span at $Ha = 200$ so that the spanwise extension of the recirculation regions is smaller for this value of Ha. By comparison with the non-MHD, as no horseshoe pattern is present around the cylinder basis in the MHD case, the spanwise distribution of L_b exhibits little variations in this region.

Finally, we shall stress that, at both Ha, the last occurrence of the steady regime in our computations exhibits a value of $\langle L_b \rangle_z$ below the one which can be extrapolated from the linear regression in the steady regime (see figure 10.7). For values of Re_W close to the critical threshold of the transition to unsteadiness, the flow dynamics are more sensitive to numerical errors and such a sensitive feature as the maximum streamwise elongation of the recirculation regions is prone to biased estimation.

10.3.6 Consequences on the base pressure coefficient

As already mentioned several times so far, the variations of L_b are directly connected to those of the base pressure coefficient. The reference pressure used in the definition of this coefficient has been taken in two different duct cross-sections. It is denoted C^i_{pb} when it is formed using the reference pressure in the cross-section ($x = -20$), *i.e.* at the inlet boundary and C^f_{pb} if it is computed using the reference pressure in the cross-section ($x = -0.5$), *i.e.* at the upstream cylinder face. At a given spanwise coordinate $-\gamma \leq z \leq 0$, these coefficients are then defined as:

$$C^i_{pb}(z) = \frac{p(x = 0.5, y = 0, z) - p(x = -20, y = 0, z)}{0.5\rho W U_0^2} \quad (10.5)$$

$$C^f_{pb}(z) = \frac{p(x = 0.5, y = 0, z) - p(x = -0.5, y = 0, z)}{0.5\rho W U_0^2} \quad (10.6)$$

Figures 10.9 (a) and (b) show the respective evolutions of the spanwise averaged C^i_{pb} and C^f_{pb} with Re_W/Ha. Both $-C^i_{pb}$ and $-C^f_{pb}$ decrease within the steady flow regime. This decrease is linked to the lengthening of the steady recirculation regions and the subsequent enhancing of the advert pressure gradient (see e.g section 9.5.1).

A good agreement with the scaling in Re/Ha is obtained between both $-C^i_{pb}$ curves at $Ha = 100$ and $Ha = 200$ and the discrepancy between both curves of $-C^f_{pb}$ is still low for $Re/Ha \leq 0.3$ but deteriorates for higher values of Re/Ha. In the MHD case, the pressure gradient imposed by the Hartmann friction dominates that induced by the presence of the cylinder. We have shown in section 6.5.1 that a good estimation of the base pressure coefficient in laminar flows due to the Hartmann

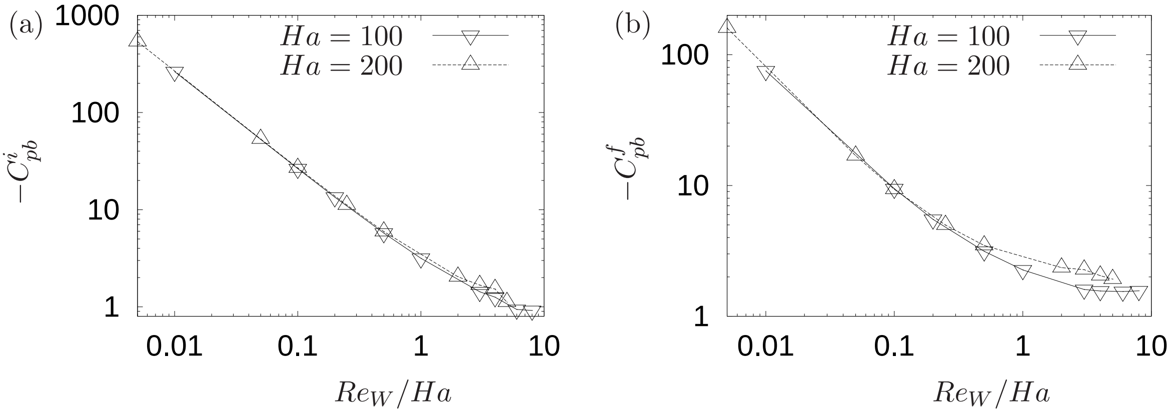

Figure 10.9: Spanwise averaged base pressure coefficient versus Re_W/Ha at $Ha = 100$ and 200: (a) C_{pb}^i computed with the reference pressure taken at the inlet and (b) C_{pb}^f computed with the reference pressure taken at the upstream cylinder face. In the unsteady regime, time averaged values are reported.

friction only is given by (6.9) in which the base pressure coefficient scales with $(Re/Ha)^{-1}$. As the pressure difference used in C_{pb}^i is computed over a larger distance than that used in C_{pb}^f, the pressure drop due to the Hartmann friction has a greater influence on the values of C_{pb}^i than on those of C_{pb}^f. The scaling in Re/Ha is therefore better with $-C_{pb}^i$ than with $-C_{pb}^f$. The friction parameter Re/Ha is an effective measure of the ratio between the inertial and the Lorentz forces in quasi-2D MHD flows. Since a good agreement is obtained with a scaling with this parameter, it is a first indication that, at the values of Ha considered in these investigations, the flow dynamics are mostly quasi-two-dimensional in the far wake region but not in the near wake.

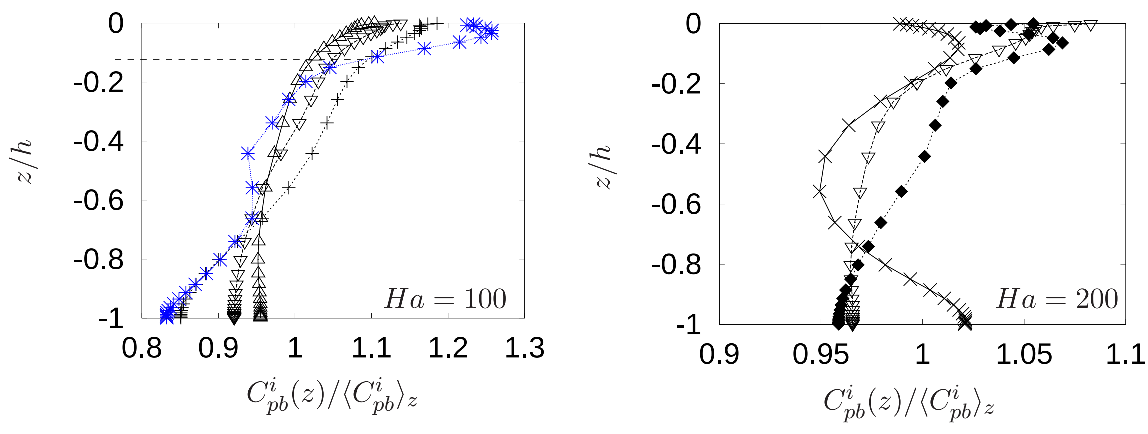

Figure 10.10: Spanwise distribution of the base pressure coefficient C_{pb}^i with the reference pressure at the inlet at $Re_W = 50$ ($\times$), 300(Δ), 400 (∇), 600($+$), 800($*$) and 1000 ($\blacklozenge$). For $Ha = 100$, the z-range for which $C_{pb}^i(z)$ is higher at $Re_W = 800$ (blue curve) than at $Re_W = 600$ is located above the horizontal dashed line. $< C_{pb}^i >_z$ is the spanwise averaged value.

Figure 10.10 shows the spanwise distributions of $-C_{pb}^i$ with respect to its spanwise average at $Ha = 100$ and 200 for $50 \leq Re_W \leq 1000$. The shape of the respective distributions for $Ha = 100$ and

200 at a given stage of the steady regime is similar, but the amplitude of their variations is smaller at $Ha = 200$ than $Ha = 100$. In the steady regime, the spanwise variations reflect the spanwise variations of the length of the recirculation regions. The $z-$coordinate at which the streamwise elongation of the recirculation regions is maximum corresponds to an absolute minimum of $-C^i_{pb}$, while the shrinking of the recirculation regions on either side of this maximum results in an increase in $-C^i_{pb}$. The spanwise variations are smoother at $Ha = 200$ than at $Ha = 100$, as a higher magnetic field enhances the uniformisation of the flow along its lines.

10.3.7 Outer boundary layer of the steady recirculation regions

We shall now investigate the outer boundary layer of the steady recirculation regions depicted by the blue streamlines in figure 10.4. The thickness δ of the steady recirculation regions is estimated from the streamwise velocity profile following the method described in [1]. We shall review the respective influences of Re_W, z/h and Ha on δ.

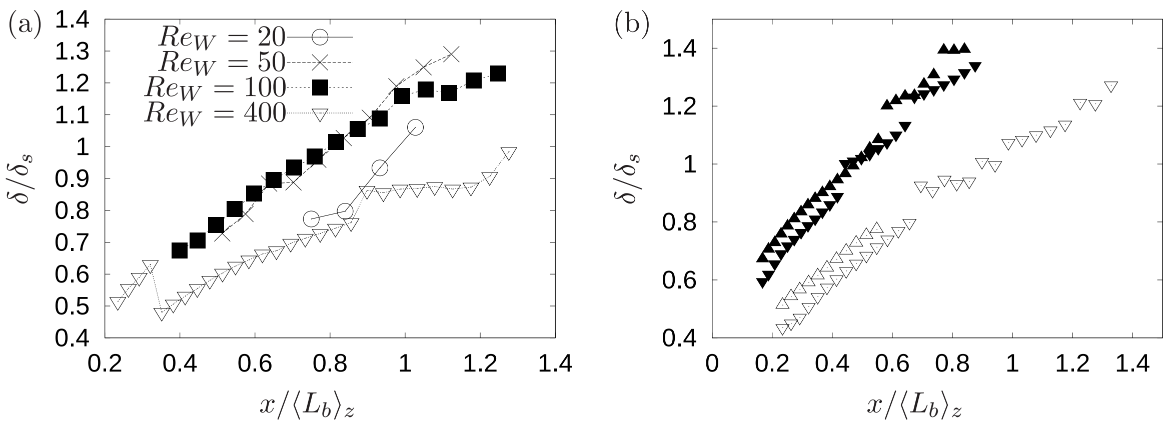

Figure 10.11: Thickness of the outer boundary layer of the recirculation region (a) for increasing Re_W at $Ha = 100$ and $z/h = -0.56$ and (b) at $Re_W = 400$ for $Ha = 100$ (open symbols) and 200 (solid symbols) with $z/h = -0.34$ (∇) and $z/h = -0.91$ (Δ). δ_s is the thickness of the Shercliff layer.

Figure 10.11(a) presents the influence of Re_W on the thickness δ at $Ha = 100$ and $z/h = -0.56$. One observes that δ is of the order of the thickness δ_s of the Shercliff layer. The boundary layer is parallel to the magnetic field so that it involves the same balance between the Lorentz forces and viscosity that results in a thickness δ of the order of $Ha^{-1/2}$. The outer boundary layer of the steady recirculation regions is however subject to strong viscous and inertial effects that make its thickness more or less depart from this value.

δ_s increases linearly with the streamwise coordinate with some slight variations at the tail of the recirculation regions. This linear dependence was not observed in the quasi-2D flow past a circular cylinder (see figure 6.9). This is partly due the shape of the cylinder cross-section, which has some influence on the streamwise profile of the lateral free shear layers. Firstly, the point at which the flow separates at a circular cylinder moves along the circumference when Re is increased, whereas it remains fixed at the cylinder front edge in the case of a square cylinder. Secondly, the free shears layers wrap around the cylinder before they separate and a circular cylinder thus imposes an initial curvature of these layers unlike in the case of a square cylinder. Finally, in the laminar regime, the shape of the cylinder is one of the parameters governing the width of the wake [102] and therefore the distance between both free shear layers. Investigations by [58, 102] showed that the curvature of the free shear layers and a greater vicinity between them promote the formation of vortices inside these layers, that results from a greater instability of these layers.

As Re_W is increased, the slope of the curves slightly decreases and the internal boundary layer becomes thinner. One also notices a striking discontinuity of the curve for $Re_W = 400$ at $(x/\langle L_b \rangle_z \simeq 0.35)$ where δ suddenly drops from $0.65\delta_s$ down to $0.45\delta_s$. This discontinuity appears at the same Re_W as the secondary recirculations at the lateral cylinder faces. The presence of these recirculations imposes a local curvature of the free shear layer and therefore a discontinuity in the δ-curve is observed at the root of the free shear layer. Away from the secondary recirculation, the shape of the curve is similar to that observed at lower Re_W and the thickness of the boundary layer increases linearly with x. Also, variations of δ are noticed at the tail of the recirculation regions. In this region, the parallel layers are very elongated and very thin. Consequently, the computation of δ is more sensitive in this region.

Finally, the influence of Ha on δ is presented on figure 10.11(b) for $Re_W = 400$ at two different spanwise coordinates $z/h = -0.91$ and -0.34 for $Ha = 100$ and 200. The general shape of the δ-curves is not affected by Ha as a linear increase in δ is seen for all the curves. The normalised thickness δ/δ_s is however bigger at $Ha = 200$ than at $Ha = 100$. This is in line with the observations made previously for the influence of Re_W on δ.

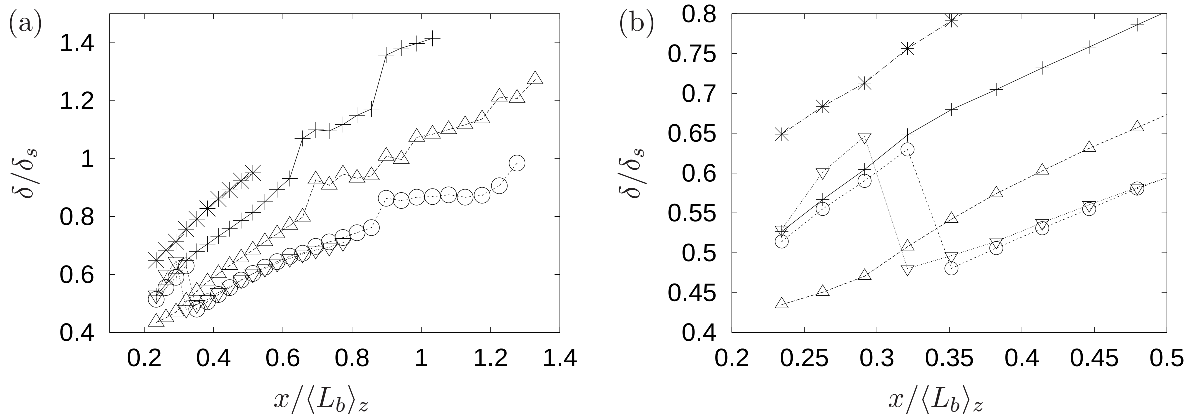

Figure 10.12: Spanwise distribution of the thickness of the outer boundary layer of the recirculation region at $Ha = 100$ and $Re_W = 400$ for $z/h = -0.20$ (+), -0.34(Δ), -0.56($\circ$), -0.80 (∇) and -0.99 ($*$). A magnified view for $x/\langle L_b \rangle_z < 0.5$ is shown on (b).

Figure 10.12 shows the variations of δ at $Re_W = 400$ and $Ha = 100$ as a function of the spanwise coordinate along the cylinder height for $-0.99 \leq z/h \leq -0.20$. It is maximum in the upper part of the recirculation regions with a maximum of $1.4\delta_s$ measured at the tail of the recirculation regions at $z/h = -0.20$. Again, the presence of a secondary recirculation has a noticeable effect on δ for $z/h = -0.56$ and -0.80, as a sudden drop in δ is seen at $x = 0.3\langle L_b \rangle_z$ after a initial increase. As the secondary recirculations extend mostly over the bottom half of the lateral cylinder face, a sudden drop in δ is therefore observed only for $z/h \leq -0.5$.

10.4 Unsteady flow regime

10.4.1 Unsteady flow features

The unsteady flow regime appears as spanwise vortices shed from the lateral free shear layers. Vortex shedding is observed at $Re_W \geq 800$ at both $Ha = 100$ and $Ha = 200$. Note however that, in the case $Re_W = 600$ and $Ha = 100$, unsteadiness is observed in the flow during the transient phase, but dies out in the established regime when the simulation time exceeds several t_H. This indicates that the critical Re_W for the transition to unsteadiness at $Ha = 100$ is closer to 600 than 800 and therefore very likely to be lower than in the case $Ha = 200$.

The vortex street observed at $Re_W = 1000$ and $Ha = 200$ at three different time steps is shown in figures 10.13(a-c). The shedding mechanism feeds a Kármán-like vortex street, *i.e.* an alternate procession of counter-rotating vortices is observed in the cylinder wake. As Re_W is increased within the unsteady regime, the lateral free shear layers shrink and vortices shed closer to the cylinder. If one identifies the formation region of the Kármán vortices and measure its streamwise elongation following the method described in [88], the increase of Re_W thus induces a decrease of the length of this formation region as shown on figures 10.7 and 10.8.

The vortices do not shed uniformly from the free shear layers and once released, they break down into a set of smaller spanwise vortices, which form a trailing chain. This chain follows the motion of the initially shed vortex and thus exhibits a wavy streamwise shape as seen on e.g. figure 10.13(a).

The vortex street is therefore asymmetric, unlike the one which develops at the onset of vortex shedding in the non-MHD case. As the magnetic field is oriented along the cylinder axis, it dissipates all the structures perpendicular to its direction and promotes the development of the spanwise recirculation regions and the lateral free shear layers. The pair of counter-rotating streamwise vortices (base vortices) detected in the non-MHD case are therefore absent in the MHD flow. The non-MHD shedding mechanism relies heavily on this pair of streamwise vortices (see section 9.4.1). Their suppression by the magnetic field in the MHD case thus implies that the MHD unsteady regime is initiated by a different mechanism that is based on the destabilisation of the lateral free shear layers. In that sense,

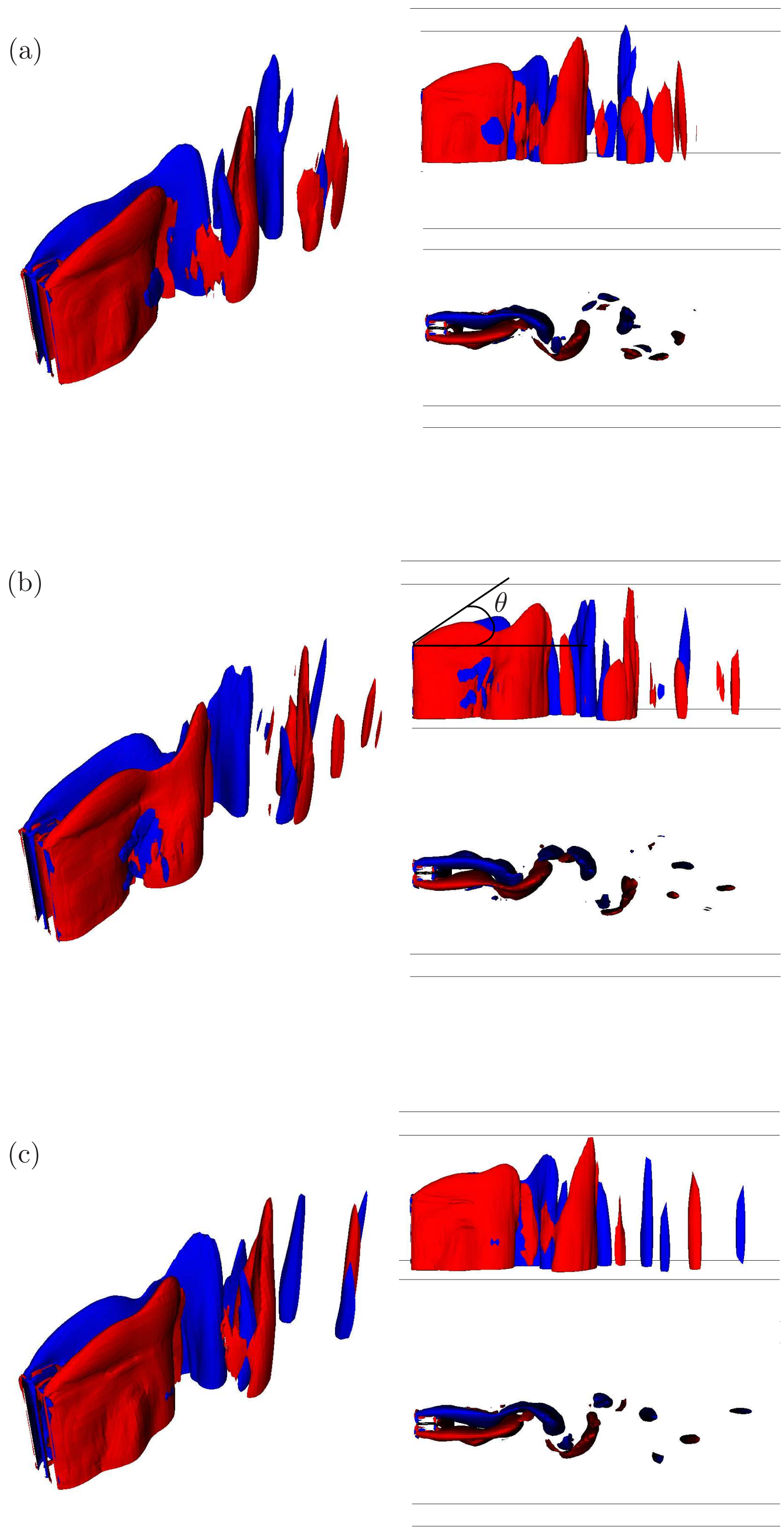

Figure 10.13: Vortex street at $Re_W = 1000$ and $Ha = 200$. Iso-surfaces of $z-$vorticity: $\omega_z^\star = -50$ (*resp.* 50) in blue (*resp.* red): (a) $t = 11.76 t_H$; (b) $t = 11.78 t_H$ and (c) $t = 11.80 t_H$. (Clockwise from left): 3D, side and top views.

the flow dynamics are reminiscent of that of the laminar non-truncated cylinder wakes described in chapter 2 . The transition to unsteadiness results from the destabilisation of the recirculation regions and the formation of an asymmetric Kármán vortex street. By contrast, in the non-MHD case, no structure is favoured at the expense of others so that the transition to unsteadiness is a consequence of the complex interaction between the vortical structures present in the wake.

The front edge of the lateral free shear layers forms an angle θ at their top end as indicated on figure 10.13(b). The effect of the magnetic field is to stretch the free shear layers along its direction, whereas that of the free stream is to erode them along the x-axis. Angle θ shall then depends on the Stuart number N that means the ratio of the two effects. In the extreme case $N \to \infty$, in which θ would be equal to 90 degrees, a Hunt's wake would be observed.

Also, the secondary vortices fuelled by the recirculation regions rising at both lateral cylinder faces entwine with the Kármán vortices. These secondary vortices are fed by streamlines spiralling from the bottom of the lateral cylinder faces upwards. Their upper part is taken downstream by the adjacent Kárman vortex, whereas their bottom part lags behind. As the result, the lateral free shear layers exhibit a convex, slant shape in the vicinity of the cylinder bottom as seen on e.g. figure 10.13 (c). Since the secondary vortex and the adjacent Kármán vortex are co-rotating, the pairing effect between both vortices is likely to play a part in the break-down of the Kármán vortex into smaller vortices after its shedding.

Finally, we shall point out that a secondary recirculation region is detected at the upper cylinder face in the steady regime at $Ha = 100$ for $Re_W = 600$, but in the unsteady one at $Ha = 200$ for $Re_W = 1000$. It is generated by separation of the upper boundary layer slightly behind the upstream edge of the upper face as in the non-MHD case. This top recirculation thus appears at a higher Re_W than the lateral recirculations in both Ha cases. The boundary layer at the upper cylinder face is a Hartmann layer. Experimental [151] and numerical [144] investigations agreed that the critical Reynolds number at which the Hartmann layer turns unstable is proportional to Ha. This is why the top recirculation appears at a higher Re_W at $Ha = 200$ than at $Ha = 200$.

In summary, we have indicated the main features of the MHD flow dynamics on figure 10.14.

10.4.2 Base pressure coefficient

We have already indicated that the onset of vortex shedding induces a collapse of the formation region of the Kármán vortices. We shall now see how this collapse influences the evolutions of the base pressure coefficient.

Again, we consider two definitions of the base pressure coefficient whether the reference pressure is taken at the duct inlet used to define C^i_{pb} (10.5) or at the line of stagnation points on the upstream cylinder face used to define C^f_{pb} (10.6). Figure 10.9 gives the respective evolutions of the spanwise-

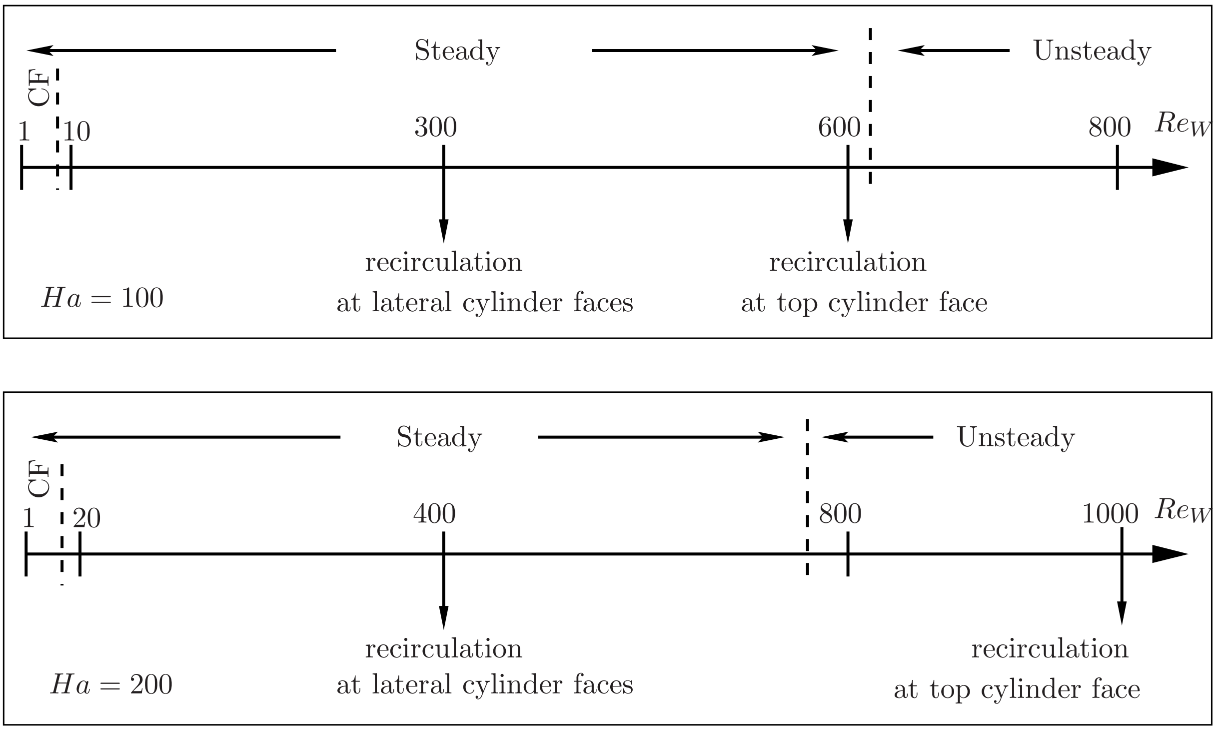

Figure 10.14: Summary of the simulations on the MHD flow past a truncated square insulating cylinder. CF denotes the creeping flow regime.

and time-averaged values of $-C^i_{pb}$ and $-C^f_{pb}$ with Re_W/Ha.

The decrease of both $-C^i_{pb}$ and $-C^f_{pb}$ observed in the steady regime is due to the lengthening of the steady spanwise recirculation regions (see section 10.3.6). After the onset of vortex shedding, $-C^i_{pb}$ keeps on decreasing in both Ha, although a slight change in the decreasing slope is observed. The same evolution is observed for $-C^f_{pb}$ at $Ha = 200$, whereas the $(-C^f_{pb})$-curve at $Ha = 100$ exhibits a slight increase after the transition to unsteadiness. The evolution of all four curves is linked to the shrinkage of the formation region of the Kármán vortices that causes a decrease of the adverse pressure gradient in the cylinder near wake. For this reason, $-C^f_{pb}$ at $Ha = 100$ starts increasing after the onset of vortex shedding. This modification of the pressure distribution is however weak in comparison to the pressure drop imposed by the Hartmann friction. When this friction is accounted for along a length of several cylinder widths, the related pressure drop outweighs significantly the modification of the advert pressure gradient due to the shrinkage of the vortex formation region, hence $-C^i_{pb}$ keeps on decreasing in both Ha cases after the transition to unsteadiness. Even in the case of C^f_{pb} where the pressure drop is computed over a length equal to one cylinder width, the modification of the advert pressure gradient is too weak to counter-balance the pressure drop induced by Hartmann friction at $Ha = 200$. In the non-MHD case, no Hartmann friction is present and consequently the base pressure coefficient starts increasing after the onset of vortex shedding as shown on figure 9.9.

The importance of the choice of the location at which the reference pressure is taken is further underlined by comparing the spanwise variations of $-C^f_{pb}$ shown on figure 10.15 to those of $-C^i_{pb}$

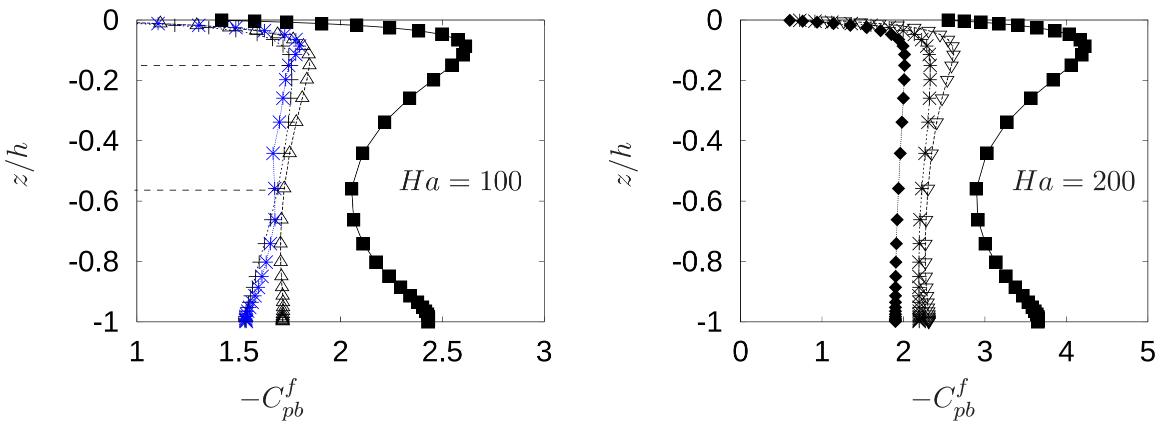

Figure 10.15: Spanwise distribution of the base pressure coefficient C^f_{pb} with the reference pressure at the upstream cylinder face at $Re_W = 100$ (■), 300(∆), 400 (∇), 600(+), 800(∗) and 1000 (♦). At $Ha = 100$, the z-range for which $-C^f_{pb}$ is higher at $Re_W = 800$ (blue curve) than at $Re_W = 600$ is located above (*resp.* below) the upper (*resp.* lower) horizontal dashed line.

reported on figure 10.10. As Re_W is increased in the unsteady regime, the shape of the spanwise distribution of $-C^f_{pb}$ varies little, but the curves are shifted to lower values. After the onset of vortex shedding, the decrease in the counter pressure gradient induced by the collapse of the vortex formation region does not reverse this trend at $Ha = 200$. At $Ha = 100$ however, this decrease induces higher values of $-C^f_{pb}$ in regions close to both cylinder ends at $Re_W = 800$ than at $Re_W = 600$. This is observed for $-0.15 \leq z/h \leq 0$ and $-1 \leq z/h \leq -0.5$. By comparison, on the respective spanwise distributions of $-C^i_{pb}$ for $Ha = 100$ at $Re_W = 600$ and $Re_W = 800$ shown on figure 10.10, this is only observed in the region close to the cylinder free end for $-0.11 \leq z/h \leq 0$. Since the shrinkage of the vortex formation region is weak in the region close to the cylinder tip, it has little effect on the pressure distribution in this region and the spanwise averages value of $-C^i_{pb}$ is little affected and keeps on decreasing. On the other hand, the shrinkage is very significant in the bottom half of the wake: its length is up to three times as small at $Re_W = 800$ than at $Re_W = 600$ for $-0.75 \leq z/h \leq -0.5$ [see figure 10.8(a)]. This has dramatic consequences on the advert pressure gradient in the bottom half of the wake. It results in higher $-C^f_{pb}$ at $Re_W = 800$ than at $Re_W = 600$ in this region and by extension on the spanwise average of $-C^f_{pb}$ which starts increasing after the onset of vortex shedding.

10.4.3 Consequences on the drag coefficients

Figures 10.16 (a-c) present the respective evolutions of the pressure drag coefficient C_{Dp}, viscous drag coefficient C_{Dv} and total drag coefficient C_D versus Re_W/Ha at $Ha = 100$ and 200. Their respective spanwise distributions are presented on figure 10.17.

In both Ha cases, for $Re_W/Ha \leq 1$, C_{Dv} decrease with a slope scaling with Re_W/Ha. The values of C_{Dv} subsequently depart significantly from this initial scaling as a sudden drop is noticed at $Re_W/Ha = 3$ for $Ha = 100$ and $Re_W/Ha = 2$ for $Ha = 200$. This corresponds to the appearance

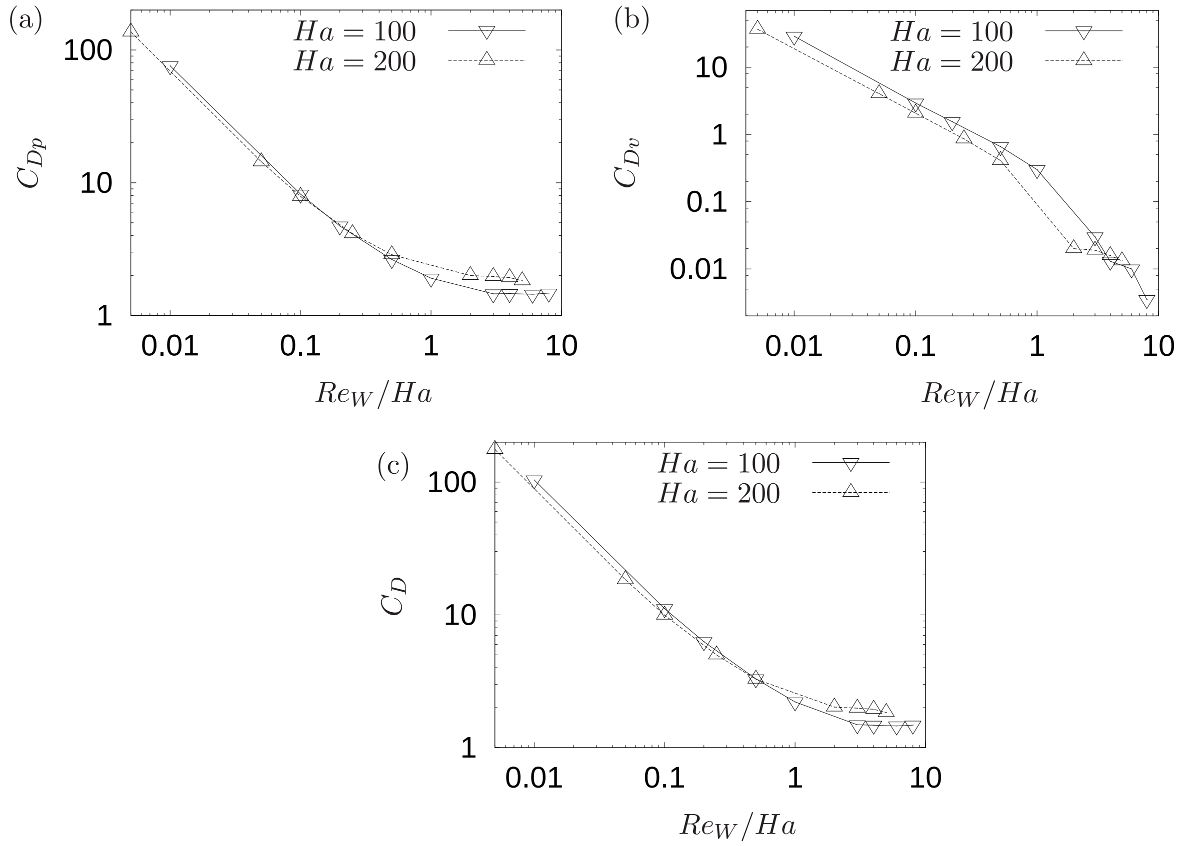

Figure 10.16: (a) Pressure drag coefficient C_{Dp}, (b) viscous drag coefficient C_{Dv} and (c) total drag coefficient C_D versus Re_W/Ha. In the unsteady regime, time-averaged values are reported.

of secondary recirculations at the lateral cylinder faces. These recirculations induce negative C_{Dv} along a portion of the lateral faces as shown on the spanwise distribution of C_{Dv} reported on figures 10.17(c-d). Negative values of C_{Dv} cause a sudden drop of its spanwise average. The variations of C_{Dv} in the MHD case are in line with those of the non-MHD case (see section 9.5.1).

The pressure and the total drag coefficients decrease throughout the steady flow regime. At $Ha = 100$, after the onset of vortex shedding, both C_{Dp} and C_D exhibit a change of slope as they increase between $Re_W/Ha = 6$ and 8, unlike for $Ha = 200$ where no increase is observed for any of these two coefficients. The variations of C_{Dp} are very similar to those of C^f_{pb} as C_{Dp} results from the integration of the pressure over the upstream and downstream cylinder faces and therefore reflects on the same mechanism as C^f_{pb}. The spanwise distributions of C_{Dp} shown on figures 10.17(a-b) also exhibit strong similarities to those of C^f_{pb}. As the contribution of C_{Dv} to the total drag coefficient C_D decreases with increasing Re_W, the variations of C_D follow from those of C_{Dp}. This is also true for the spanwise distributions of C_D visible on figures 10.17(e-f). We have shown in section 10.3.6 that the streamwise pressure drop scales with Re_W/Ha in the early stages of the steady regime. The C_{Dp}-curves at different values of Ha tend to merge at low Re_W/Ha. This scaling is less relevant for C_{Dv} as the Hartmann friction has little influence on the viscous forces. Relatively high values of

C_{Dv} at low Re_W/Ha are responsible for the slight discrepancy of the C_D-curves at low Re_W/Ha. In the late stages of the steady regime and after the onset of vortex shedding, the dynamics of the recirculation regions and then that of the formation region of the Kármán vortices are responsible for more significant variations in pressure at the rear of the cylinder. As a result, the curves of both C_{Dp} and C_D depart from the scaling law in Re_W/Ha in this regime. Finally, we shall stress that the variations of the drag coefficients in the MHD cases are very similar to those observed in the non-MHD case. Only in the latter case, the transition to unsteadiness causes a spectacular reversal of the slope of the respective curves of C_{Dp} and C_D, as no Hartmann friction softens the effect of the pressure change at the rear of the cylinder (see section 9.5.1).

10.4.4 Spanwise lift coefficient

We now look at the spanwise lift coefficient C_z (9.6). Again, as explained in section 9.5.1, pressure forces contribute to C_z only on the cylinder upper face, while viscous forces contribute to it only on the lateral, upstream and downstream cylinder faces. We consider therefore the pressure and the viscous spanwise lift coefficients, denoted C_{zt} and C_{zs}, respectively. The variations of C_{zt} with the Stuart number N is reported on figure 10.18(a) and those of C_{zs} with Re_W/Ha on figure 10.18(b).

By definition, the values of C_{zt} strongly depend on the value of the reference pressure and the location of the mesh cell where it is allocated (see section 9.5.1). In particular, the sign of C_{zt} bears no significance. One observes that C_{zt} increases monotonically with N, *i.e* at a given Ha, it decreases monotonically with Re_W in both steady and unsteady flow regimes. The scaling with N is excellent for $N \gg 1$ and slightly deteriorates for $N \lesssim 1$ when the flow is unsteady. In the limit $N \to \infty$ and within the steady regime, it follows from the momentum conservation (7.1) that the pressure gradient is proportional to N within a good approximation and negative along the streamwise direction, hence the linear dependency between C_{zt} and N. In the unsteady regime, N gets closer to one and inertia effects counter-balance those of the Lorentz force. The pressure gradient scaling with N is therefore less relevant in this regime. C_{zt} however keeps on decreasing after the onset of vortex shedding, whereas, in the non-MHD case, the transition to unsteadiness causes a switch to increasing values of C_{zt} as shown on figure 9.10(a). In the non-MHD case, C_{zt} starts increasing as a consequence of the appearance of secondary recirculation at the upper cylinder face that induces a significant enough modification of the pressure to trigger an increase of C_{zt}. By contrast, in the MHD case, although secondary recirculation also appears at the upper cylinder face, the induced pressure modification is not able to counter-balance the pressure drop due to the Hartmann friction. The appearance of this secondary recirculation at $Re_W = 600$ ($N = 1$) for $Ha = 100$ and $Re_W = 1000$ ($N = 2.5$) for $Ha = 200$ though causes the deterioration of the scaling with N.

No monotonic trend is observed for C_{zs}. No flow separation is present in the creeping flow regime

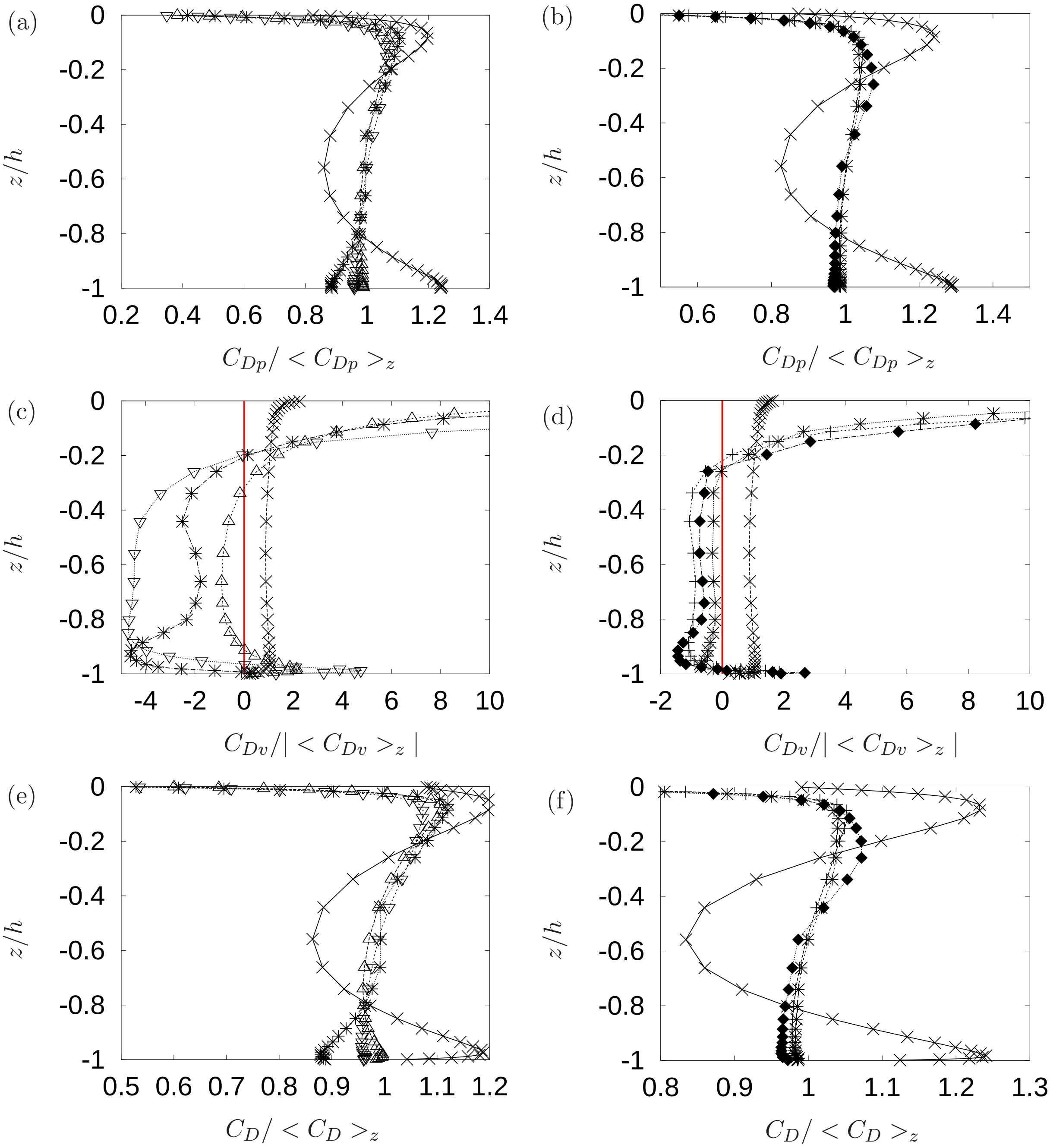

Figure 10.17: Spanwise distributions of (a-b) the viscous drag coefficient C_{Dv}, (c-d) the pressure drag coefficient C_{Dp} and (e-f) the total drag coefficient C_D at $Ha = 100$ (left column) and 200 (right column) for $Re_W = 50$ ($\times$), 300 ($\triangle$), 400 (∇), 600 ($+$), 800 ($*$) and 1000 ($\blacklozenge$). $<\cdot>_z$ is the spanwise averaged value. In the unsteady regime, time-averaged values are reported.

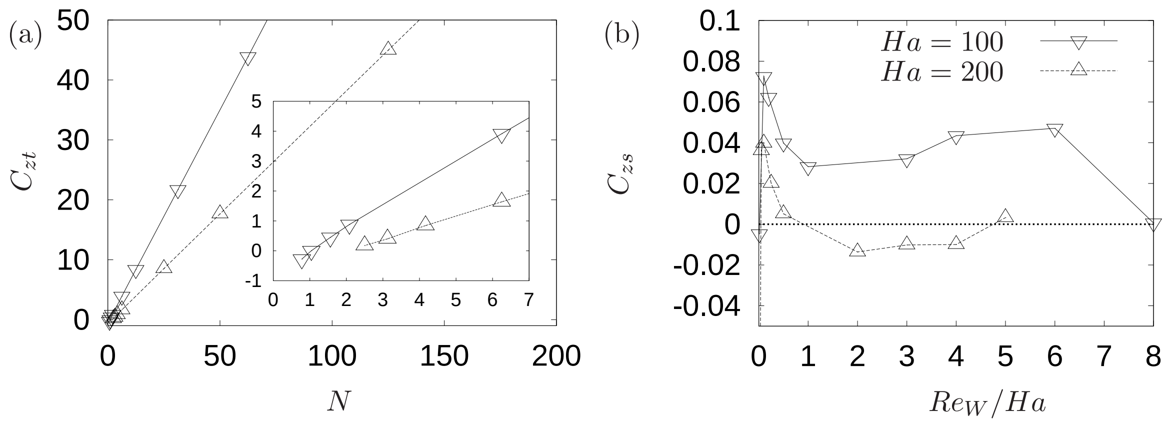

Figure 10.18: Spanwise lift coefficients (a) C_{zt} computed over the cylinder upper face only versus the Stuart number N and (b) C_{zs} computed over the cylinder lateral, downstream and upstream faces only versus Re_W/Ha. A magnified view for $N < 7$ is shown in the insert on (a).

and the spanwise velocity component is close to zero at the lateral cylinder faces. At very low Re_W, $Re_W = 1$, for which a Hunt's wake is observed, the flows on the upstream and downstream cylinder faces are antisymmetric with respect to the plane ($x = 0$). Consequently the spanwise viscous frictions at the upstream and downstream faces compensate each other and C_{zs} is close to zero for $Re_W/Ha \to 0$. Increasing Re_W within the creeping flow regime breaks the flow antisymmetry as the Hunt's wake is pushed slightly downstream. This induces a slight imbalance between the spanwise frictions at the upstream and downstream faces. The flow is decelerated as it passes above the cylinder tip so that the spanwise velocity is slightly higher at the upstream face than at the downstream one and C_{zs} increases and turns positive. The initial change of slope at $Re_W/Ha = 0.1$ corresponds to the appearance of the head vortex at the rear cylinder face. On the one hand, as shown by the red streamlines on figure 10.4, the head vortex induces an upwards flow at the rear cylinder face. The spanwise velocity resulting from this upwards flow is however weak and located only in the centre-plane $y = 0$. On the other hand, the head vortex generates two downwards spiralling vortices on either sides of the centre-plane $y = 0$. As a consequence, the spanwise wall friction at the downstream faces counter-balances that at the upstream face and C_{zs} decreases. This trend is enhanced as the rear spanwise vortices (blue streamlines on figure 10.4) are generated from the cylinder tip in the late stages of the steady regime. The appearance of secondary recirculation at $Re_W/Ha = 3$ (*resp.* 2) for $Ha = 100$ (*resp.* 200) at the lateral cylinder faces causes an increase in C_{zs} due to the upwards spiralling flow feeding these recirculations.

10.4.5 Strouhal number

We have simulated three unsteady flows: one at $Ha = 100$ and two at $Ha = 200$. For each case, we have computed the Strouhal number from the time-history of the lift coefficient. Their values are

	$Ha = 100$	$Ha = 200$
$Re_W = 800$	$St = 0.1235$	$St = 0.1218$
$Re_W = 1000$	/	$St = 0.1474$

Table 10.1: Strouhal number St versus Re_W and Ha.

reported in table 10.1. At $Ha = 200$, St increases from 0.1218 to 0.1474 between $Re_W = 800$ and $Re_W = 1000$. At $Re_W = 800$, St is higher at $Ha = 100$ is higher than at $Ha = 200$. In comparison with the non-MHD case (see figure 9.11), the MHD values of St are one order of magnitude higher than the non-MHD ones calculated from the asymmetric mode, thus reflecting two entirely different mechanisms of vortex shedding.

The increase in St relies on the same mechanism described in e.g. subsection 2.3.2: when Re_W increases, the velocity of the Kármán vortices reaches that of the free stream and the distance between two successive vortices with the same sense of rotation diminishes. The stabilising effect of the Hartmann friction results in Kármán vortices with a smoother spanwise shape. In contrast, the vortex street observed in the non-MHD flow past a truncated square cylinder is fuelled by complex interactions between spanwise, streamwise and transverse structures. The non-MHD shedding mechanism is truly laminar only within a narrow Re_W interval beyond the onset of vortex shedding. In this case, the value of St is quite high and as the shedding mechanism deteriorates for higher Re_W, the vortex street turns chaotic and St drops sharply.

10.5 Perfectly conducting cylinder

We consider now the MHD flow past a perfectly conducting, square truncated cylinder placed in an insulating duct. The main goal of these investigations is to indicate the general influence of the conductivity of the cylinder on the flow dynamics. Further calculations and analyse are required to have a better understanding of its precise effects.

We take over the configuration used in the previous section and we replace the insulating truncated square cylinder by a perfectly conducting one with the same dimensions. The boundary condition for the electric potential at the cylinder surface ∂C_T (defined in subsection 9.2.1) has been changed accordingly. The cylinder is considered as perfectly conducting so that the electric potential is uniform on its whole surface. It is then fixed to an arbitrary value equal to zero:

$$\phi = 0 \quad \text{at} \quad \partial C_T \tag{10.7}$$

The mesh characteristics are given in table 10.2. We have performed four simulations at $Ha = 100$ for increasing Re_W with $Re_W = 10$, 100, 400 and 600. The flow is steady for $10 \leq Re_W \leq 400$ and unsteady at $Re_W = 600$. The flow patterns are very similar to those with an insulating cylinder. We

$n_x \times n_y \times n_z$	$\delta_x \times \delta_y \times \delta_z$	$n_H \times n_S$	Total number of mesh nodes
$200 \times 50 \times 80$	$0.12 \times 0.12 \times 0.012$	4×7	1.16×10^6

Table 10.2: Main characteristics of the mesh used in the simulations performed with a perfectly conducting cylinder. n_i is the number of mesh nodes along the $i-$axis. δ_i is the non-dimensional distance between the cylinder face normal to the $i-$axis and the grid point nearest to the latter face. n_H and n_S are the numbers of mesh nodes in each Hartmann and Shercliff layers, respectively.

shall consequently only point out the changes in the following comments.

10.5.1 Flow patterns, dynamics and electric current streamlines

Due to the presence of a perfectly conducting cylinder is the existence of the creeping flow over a greater range of Re_W than with an insulating cylinder, since, at $Re_W = 10$, no flow separation is detected in the former case in contrast with an insulating cylinder.

The steady flow patterns detected at $Re_W = 100$ are shown on figure 10.19. The most spectacular change with respect to the case with an insulating cylinder is the absence of any transverse vortex at the downstream cylinder face. The flow streamlines (in red) originating in the centre-plane $y = 0$ reattach in the same plane along a line from the trailing edge of the upper cylinder face downwards over a distance h_d. A pair of counter-rotating spanwise vortices are still observed in the near-wake on either side of the centre-plane $y = 0$. They are generated by streamlines (in blue) passing over the cylinder tip at some distance off the centre-plane $y = 0$. A saddle point denoted S_P is detected at the confluence between the set of red streamlines, the upper end of the spanwise vortices and the black streamlines. The latter set of streamlines does not play any part in the formation of any of the wake features. The cyan streamlines rejoin the line of stagnation points at the upstream cylinder face in the centre-plane $y = 0$ and span over a height h_v.

By increasing Re_W from 100 to 400 within the steady regime, the reattachment line at the top rear of the cylinder lengthens downwards, *i.e.* h_d increases, saddle point S_p in the cylinder wake moves significantly downstream and slightly downwards and height h_v shrinks. Also, the spanwise vortices lengthen along the x-axis. The lateral free shear layers stretch further downstream in the cylinder wake. Secondary recirculations are observed at $Re_W = 400$ at both the lateral and top cylinder faces from the stretching of the streamlines generating the spanwise vortices and flow separation at the front edge of the top face, respectively. The paths of electric current are depicted in three cross-sections at $Re_W = 100$ in figure 10.20. In the cross-section upstream the cylinder and far away downstream the cylinder, the electric current streamlines exhibit the characteristic patterns observed in the Shercliff flow. The infinite conductivity of the cylinder however induces a slight attraction of the current streamlines to the cylinder. In the cross-section across the cylinder, one observes that most of the current circulates from the bottom Hartmann layer to the Shercliff layer at the lateral cylinder face.

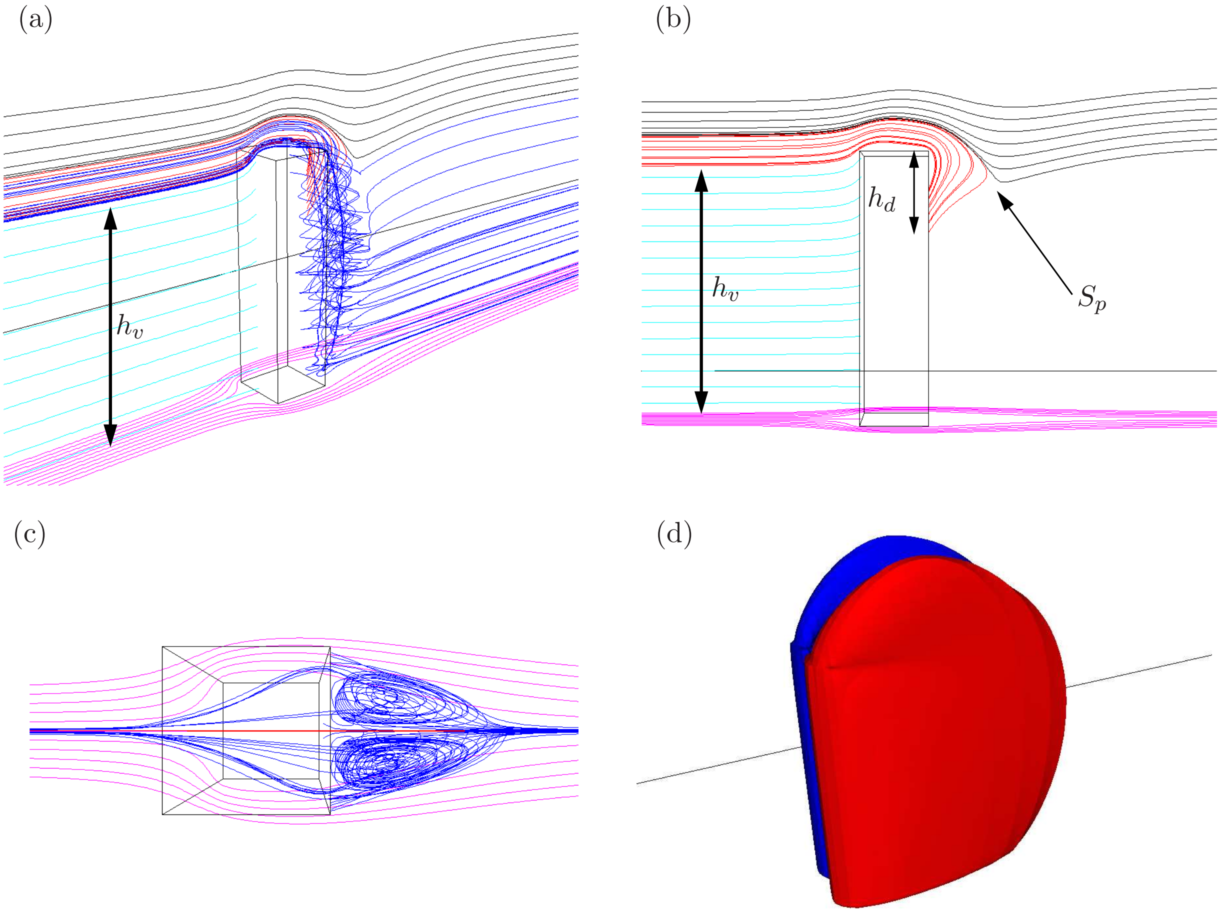

Figure 10.19: Simulations with a perfectly conducting cylinder: steady flow patterns at $Re_W = 100$ and $Ha = 100$. Kinematic streamlines: (a) 3D view; (b) side view and (c) top view. Red streamlines show that no head vortex is present at the cylinder rear face, but reattach at the rear of the cylinder. Spanwise vortices are depicted by the blue streamlines which originate from the region above the cylinder tip, but off the centre-plane $y = 0$. Pink streamlines originate upstream the cylinder in the plane $z/h = -0.998$ immersed within the bottom Hartmann layer. Cyan streamlines rejoin the line of stagnation points at the upstream cylinder face. Black streamlines are only deflected by the cylinder wake without noticeable influence on the latter. (d) Lateral free shear layers depicted by the iso-surfaces of $z-$vorticity: $\omega_z^\star = -10$ and 10 in blue and red, respectively.

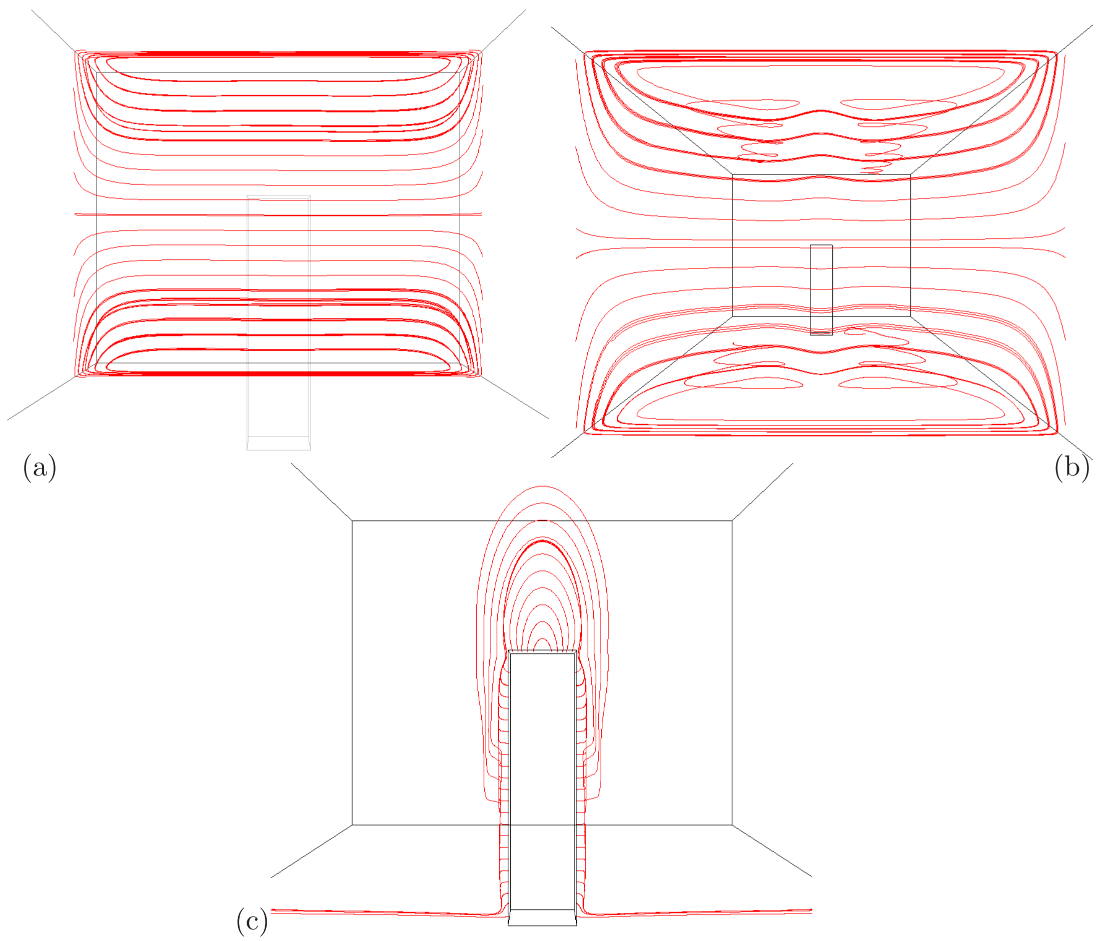

Figure 10.20: Simulations with a perfectly conducting cylinder: electric current streamlines in the cross-section at (a) $x = -8W$, (b) $x = 20W$ and (c) $x = 0$ at $Re_W = 100$ and $Ha = 100$. Flow from back to front

In addition, current loops are seen in the region above the cylinder tip that recirculate inside the bulk of the cylinder leading therefore to a much higher braking of the flow than in the case with an insulating cylinder [134]. This is well illustrated by the comparison of the streamwise velocity profiles along the $y-$axis in the plane ($x = 0.49$) at $z = 1/2$ at $Ha = 100$ and $Re_W = 100$ shown on figure 10.21. The flow passing along the wake centreline is more decelerated in the presence of a perfectly conducting cylinder than in that of an insulating one. As a result, a head vortex is generated only in the case where the flow washing down behind the cylinder is fast enough to separate at the trailing edge of the upper cylinder face, *i.e.* only in the case with an insulating cylinder.

A snapshot of the vortex street seen at $Re_W = 600$ is shown on figure 10.22. The vortex shedding fuels an asymmetric Kármán vortex street as in the case with an insulating cylinder. The vortices shed from the lateral free shear layers and break away into smaller vortices. The bottom end of the vortices exhibits a cigar-shape. The flow is fully unsteady at $Re_W = 600$, while it is still steady in the computations with an insulating cylinder. In the latter case, the spanwise vortices are weak since the streamlines at their origin first generate a transverse vortex. On the contrary, the spanwise vortices

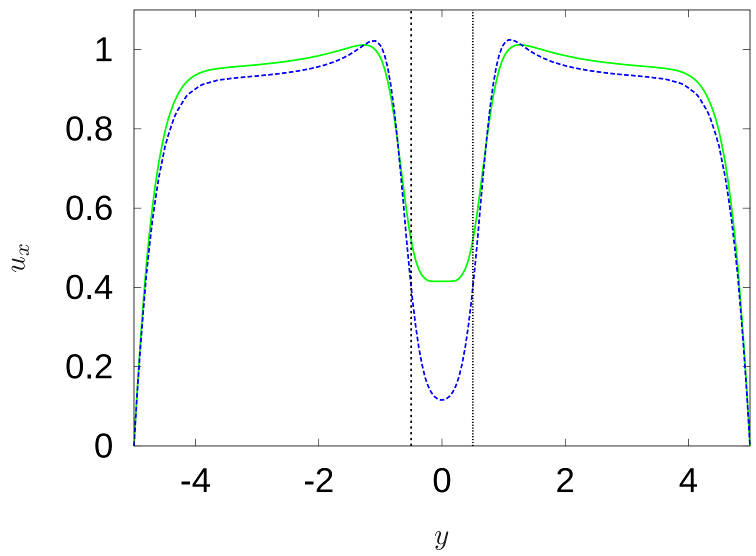

Figure 10.21: Streamwise velocity profile along the y-axis above the cylinder tip at $z = 1/2$ in the cross-section $x = 0.49$ at $Ha = 100$ and $Re_W = 100$ in the case with an insulating cylinder (green line) and in that with a perfectly conducting one (blue line). The vertical black lines indicate the extremities of the upper cylinder faces.

in the case with a perfectly conducting cylinder are promptly generated by streamlines passing over the cylinder tip. At a given Re_W, they are consequently stronger than the ones in the case with an insulating cylinder and the collapse of the steady recirculation regions occurs at a lower Re_W. It shall however be noted that extra computations are required to characterise the mechanism trigeering the onset of vortex shedding.

10.5.2 Flow coefficients

As already stressed several times so far, the dynamics of the recirculation regions at the rear of the cylinder determine greatly the evolutions of the flow coefficients with Re_W. Figure 10.23 presents the comparative spanwise distributions of the length of the steady recirculation regions at $Ha = 100$ for $Re_W = 100$ and 400 in the simulations run with an insulating and a perfectly conducting cylinder. In the case with a perfectly conducting cylinder, one observes that both the spanwise and streamwise extensions of the recirculation regions is bigger than in the case with an insulating cylinder. Again, in the latter case, the head vortex is at the origin of the spanwise vortices and therefore limits their spanwise extension. No such head vortex is present in the case with a perfectly conducting cylinder and the spanwise vortices are formed by streamlines spiralling from the cylinder tip downwards so that the recirculation regions extend up to the cylinder tip. The difference in the streamwise elongation results from the difference in strength of the spanwise vortices already pointed out previously. Stronger spanwise vortices induce longer recirculation regions. This causes a greater instability of these regions and therefore the onset of vortex shedding occurs at a lower Re_W than in the case with an insulating

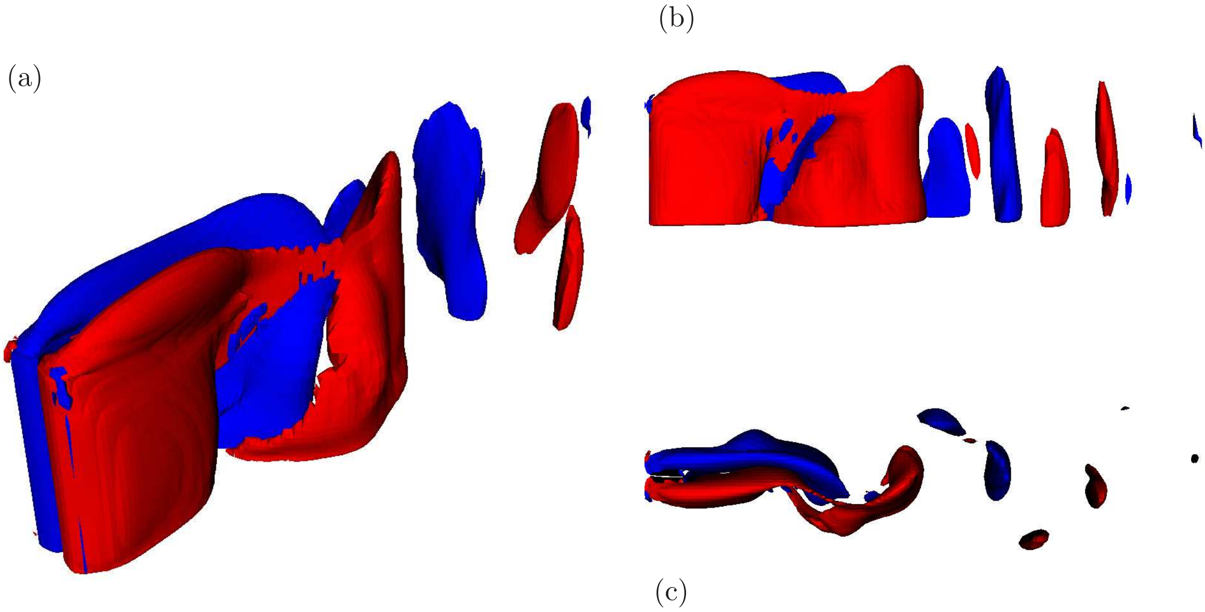

Figure 10.22: Simulations with a perfectly conducting cylinder: snapshot of the vortex street at $Re_W = 600$, $Ha = 100$ and $t = 9.1t_H$. Iso-surfaces of $z-$vorticity $\omega_z^\star = -18$ (*resp.* 18) in blue (*resp.* red). (a) 3D view; (b) side view and (c) top view.

cylinder.

We report the comparative evolutions of the spanwise- and time-averaged values of the force coefficients resulting from computations involving either an insulating or a perfectly conducting cylinder on figure 10.24. For the viscous drag coefficient C_{Dv}, the discrepancy between the two curves is small. In contrast, for the pressure drag coefficient C_{Dp} and subsequently for the total one C_D, the discrepancy between the respective curves is much more significant. For all three drag coefficients, the curves relating to the perfectly conducting cylinder are below those relating to the insulating cylinder, although the respective shapes of the curves are similar.

The variations of C_{Dp} are linked to the dimensions and the dynamics of the recirculation regions located in the near-wake of the cylinder. These recirculations are longer in the case with a perfectly conducting cylinder, *i.e.* the counter pressure gradient fed by the recirculations is greater in this case and C_{Dp} is lower than in the case with an insulating cylinder. Also, one observes that C_{Dp} is higher at $Re_W = 400$ than at $Re_W = 100$, *i.e.* the increase of C_{Dp} is initiated within the steady flow regime by contrast with the case with an insulating cylinder and the non-truncated cylinder wake in general. In these cases, the switch from decreasing to increasing C_{Dp} is due to the onset of vortex shedding that causes the collapse of the vortex formation region. This explains why the unsteady flow regime

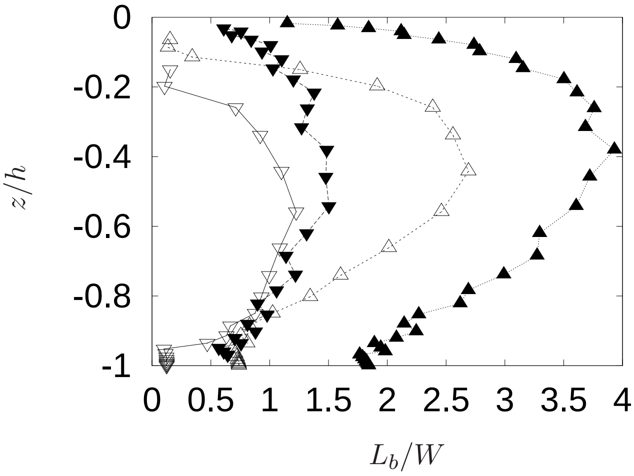

Figure 10.23: Spanwise distributions of the length L_b of the steady recirculation regions at $Ha = 100$ for $Re_W = 100$ (∇) and $Re_W = 400$ (Δ). Insulating (open symbols) and perfectly conducting (solid symbols) cylinder.

at $Re_W = 600$ does not affect the variations of C_{Dp} in the case of the perfectly conducting cylinder, for which the shrinkage of the vortex formation region strengthens the increase of C_{Dp} initiated in the steady regime. Further analysis and computations are however required to explain what induces this increases within the steady regime.

Figures 10.25(a-d) present the spanwise distributions of the pressure, viscous and total drag coefficients and of the viscous component of the spanwise lift coefficient C_{zs} obtained from simulations involving either an insulating or a perfectly conducting cylinder. The spanwise distributions of C_{Dv} are little affected by the conductivity of the cylinder. The presence of a secondary recirculation at the lateral cylinder faces results in both cases in negative values of C_{Dv}. In contrast, the respective spanwise distributions of C_{Dp} differ in the region near the cylinder tip. In the simulations run with a perfectly conducting cylinder, C_{Dp} is very low at the cylinder tip and then increases monotonically up to the cylinder mid-span. In the computations performed with an insulating cylinder, C_{Dp} is also very low at the cylinder, but then it increases up to a maximum value reached at $z/h \simeq -0.1$ from which it decreases down to the cylinder mid-span. In the case with an insulating cylinder, the presence of the head vortex at the rear of the cylinder tip induces a local pressure minimum that generates an extremum of C_{Dp}. With a perfectly conducting cylinder, the head vortex is absent and no extremum of C_{Dp} is detected close to the cylinder tip. Also, the existence of the creeping flow regime at $Re_W = 10$ in the case with a perfectly conducting cylinder unlike in that with an insulating one induces a negative value for the viscous component of the spanwise lift coefficient C_{zs} [see figure 10.25(d)], whereas $C_{zs} > 0$ at $Re_W = 10$ with an insulating cylinder due to the presence of both the head vortex and the spanwise recirculations behind the cylinder.

We have also computed the value of the Strouhal number St at $Re_W = 600$ and we have found

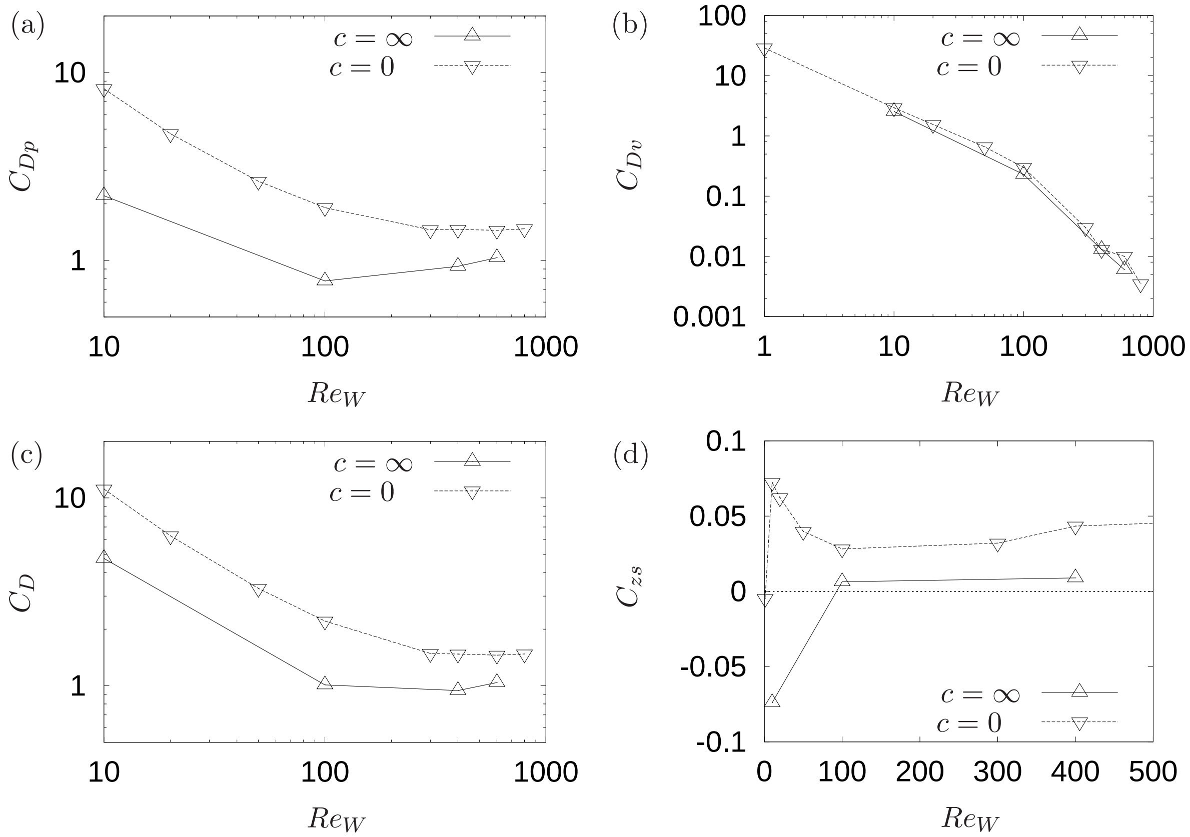

Figure 10.24: Spanwise and time-averaged values of the (a) pressure C_{Dp}, (b) viscous C_{Dv}, (c) total C_D drag coefficients and (d) viscous spanwise lift coefficient C_{zs} versus Re_W at $Ha = 100$. Insulating cylinder ($c = 0$) and perfectly conducting cylinder ($c = \infty$).

$St = 0.1183$. In the simulations with an insulating cylinder, the flow is still steady at $Re_W = 600$, but at $Re_W = 800$, $St = 0.1235$. As only one unsteady case was simulated, little can be inferred on the influence of the cylinder conductivity on St. Nevertheless, since the Kármán vortices are higher and longer than in the case with an insulating cylinder, the inertia of the vortices should be greater and therefore so should be the shedding period. Consequently, one would expect slightly lower values of St with a perfectly cylinder than with an insulating one. Further unsteady computations would be required to confirm this reasoning.

10.6 Conclusions and perspectives

10.6.1 Summary of the outcomes

In this chapter, we have investigated the MHD flow past a truncated square cylinder in an electrically insulating rectangular duct under an externally applied axial magnetic field using 3D full DNS. The cylinder has been considered, firstly, as fully insulating and, secondly, as perfectly conducting. The latter case has been investigated only briefly to give insight on the influence of the cylinder conductivity on the flow dynamics. The study with an insulating cylinder has been our reference case and therefore

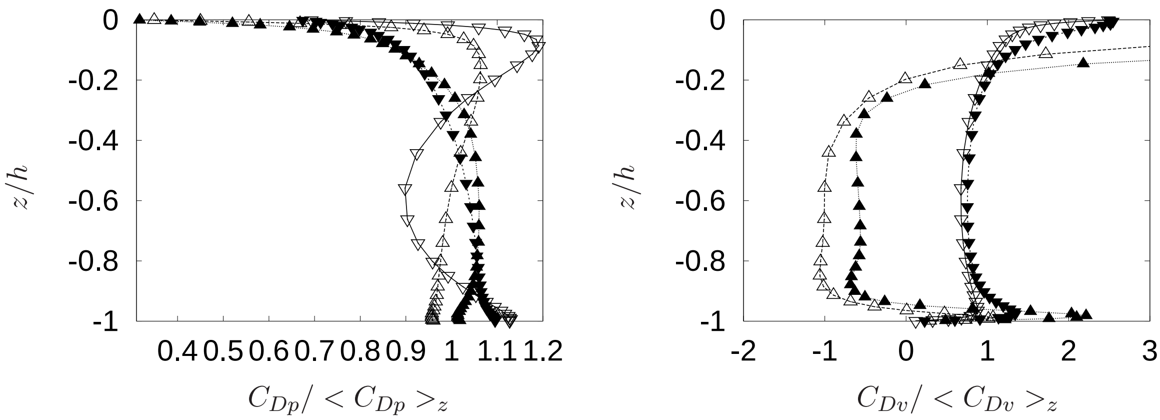

Figure 10.25: Spanwise distributions of the (left) pressure drag coefficient and (right) viscous drag coefficient at $Ha = 100$. $Re_W = 10$ (∇) and $Re_W = 400$ (Δ). Insulating (open symbols) and perfectly conducting (plain symbols) cylinder.

treated in more detail. We shall now summarise the outcomes of this study.

Two sets of computations have been performed at $Ha = 100$ and 200 for $1 \leq Re_W \leq 1000$. At very low Re_W, we have provided some visualisations of Hunt's wake in which the flow passes round the region above the cylinder tip as if the cylinder would span over the full height of the duct. It theoretically exists for $Ha \gg 1$ and $N \gg 1$. For the values of Ha set in this study, such a wake has been detected only in the creeping flow regime. Simulations at $Ha > 1000$ are likely to provide Hunt's wake including the steady recirculation regions and even the initial part of the Kármán vortex street.

Beyond the creeping flow regime, steady recirculation regions appear and lengthen in the cylinder wake. In the early stages of this regime, we have shown that the spanwise vortices are generated by a transverse vortex located at the rear cylinder face slightly below the cylinder tip. Unlike the non-MHD case, the magnetic field stretches the lateral free shear layer and prevents any fluid from entering the cylinder wake beneath these shear layers so the MHD wake structures are formed by streamlines passing over the cylinder tip. We have demonstrated that the outer boundary layer of the steady recirculation regions has a thickness δ of the order of that of the Shercliff layer. Also, imposing a magnetic field changes the nature of the boundary layers. At the bottom duct wall, there is a very stable Hartmann layer and no horseshoe pattern is therefore observed. Finally, the appearance of secondary recirculation at the lateral cylinder faces has a dramatic effect on the viscous drag coefficient.

In the steady regime, the electric current streamlines are fully 2D upstream the cylinder and far away downstream it. In the vicinity of the cylinder, as the latter is insulating, the current density accumulates in the region above the cylinder tip. This implies a significant increase of the Lorentz forces in this region and consequently a greater braking of the flow. The latter is decelerated when reaching this region and then washes down behind the cylinder with low velocity. This explains why the flow remains steady at much higher Re_W than in the non-MHD case.

The onset of vortex shedding leads to the formation of an asymmetric Kármán vortex street. The magnetic field indeed promotes the development of the lateral free shear layers and strongly dissipates structures orientated across its direction. The transition to unsteadiness results only from the instability of these shear layers and the recirculation regions which has been thoroughly investigated in e.g. 2D cylinder wakes. Under the influence of the magnetic field, the mechanism of vortex shedding is strongly laminar and the subsequent values of St are much higher than the ones obtained in the non-MHD cases.

Several simulations have been performed at $Ha = 100$ and $10 \leq Re_W \leq 600$ after replacing the insulating truncated square cylinder by a perfectly conducting one. It has induced a greater braking of the flow above the cylinder tip. As a result, the creeping flow regime exist over a wider Re_W-range than in the case with an insulating cylinder. Also, in the regime of the steady spanwise recirculations, no transverse vortex is present at the rear cylinder face as the spanwise recirculations are generated from streamlines spiralling from the cylinder tip down. At a given Re_W, the latter recirculations are longer in the case with the perfectly conducting cylinder. They are also more unstable at higher Re_W and the onset of vortex shedding thus occurs at a lower Re_W than in the case with an insulating cylinder. The flow dynamics of the perfectly conducting truncated cylinder however require extra simulations and analysis to explain e.g. the switch of the pressure drag coefficient from a decrease to an increase within the steady flow regime and the mechanism of transition to unsteadiness.

10.6.2 Perspectives

As in non-MHD study, the results obtained in the MHD investigations also depend on the choice of the configuration. The aspect ratio of the cylinder, the shape of its cross-section, the blockage ratio $\beta = W/2b$ and the gap between the cylinder tip and the top wall are likely to have a more or less noticeable influence. For example, higher values of β may result in the flow separation of the boundary layers at the side duct walls for Re_W values in the range of that considered in the previous investigations. The orientation of the magnetic field is however expected to have a more spectacular impact on the flow dynamics. Since a spanwise magnetic field prevents the fluid from passing behind the cylinder from under the lateral free shear layers, an interesting study would be to impose a magnetic field along a direction perpendicular to the spanwise one. A streamwise magnetic field would promote streamwise vortices which play a crucial part in the non-MHD vortex shedding.

The values of Ha considered in this study are moderate. 3D full DNS of MHD flows at higher Ha would require greater CPU resources. The latter problem could be partially tackled by using wall functions to avoid solving the flow inside the bottom and top Hartmann layers. One issue would however remain about the treatment of the Hartmann layer located at the upper cylinder face. Using a structured mesh implies a propagation of the local mesh refinement required inside this Hartmann layer over the whole fluid domain. Nevertheless, the flow dynamics at very high Ha can be fairly well described by asymptotic models, whereas the dynamics of low to moderate Ha flows are more subtle, especially if ones considers the very different flow patterns observed at $Ha = 0$ and $Ha = 100$.

Finally, the case of a partially conducting cylinder would bring even more information on the influence of measurement probes. Meshing and solving the distribution of the electric potential inside the cylinder are also likely to improve the reliability of the measurement methods by suggesting some corrections to the measured signals. Also, controlling the boundary condition at the cylinder end located outside the duct shall have a sensitive influence on the flow dynamics and deserve to be investigated.

Summary and perspectives

One main concern of this thesis has been the development of a numerical code able to simulate 3D MHD flows within the low-Rm approximation. Our code has been elaborated within the OpenFOAM 1.4.1 framework that relies on the finite-volume method and is free of any license agreement. We have carefully reviewed the literature and devised the requirements to design an accurate, consistent and conservative numerical algorithm. In particular, by contrast with previous codes which were undermined by a poor treatment of the current density and Lorentz forces, we have taken advantage of the work of [152, 153] to implement a current-conservative and consistent scheme. Although our code has been developed to be robust and flexible, further work is however required to optimise the efficiency of the code. The code would greatly benefit from a thorough assessment of the discretisation schemes and the numerical techniques on its stability and CPU cost. Several modifications of the code are also likely to broaden its range of application. For example, there is a large interest to gain insight on the effects of a space- and/or time-dependent externally applied magnetic field on the flow dynamics. Also, the understanding of the effects of a fringing magnetic field in regions where the flow enters or leaves the magnetic field is another major issue in the designs of blankets for ITER fusion reactor. Secondly, a time- and space-dependent magnetic field with a low frequency of the order of 1 Hz is used in continuous casting process to control the flow of molten metal. These kinds of modifications into our code do not apparently present much difficulty, although a detailed scrutiny is required to assess their exact numerical implications.

Throughout this thesis, we have successfully implemented three different numerical approaches: full 3D DNS, 3D simulations using wall functions and 2D simulations based on the SM82 model. Full 3D DNS are the most reliable, as they do not involve any model nor approximation other than the low Rm one. For high Ha MHD flows, they however demand very large CPU power and memory storage capacity. Although the recent advances in CPU technology have made it possible to investigate MHD flows with full DNS for Ha up to about 5000 in simple geometrical configuration [171], alternative numerical methods based on the use of wall functions or the SM82 model can be used to obtain an initial assessment of the flow or even fully investigate the flow using parametric studies at a lower CPU cost. Additional work is though required to devise a set of guidelines to provide recommendations on the most adequate numerical method according the geometric configuration and the range of Ha and N under consideration.

The second objective of this thesis has been to achieve an extensive review of MHD flows past a cylindrical obstacle under an axial magnetic field. For both high Ha and N, we have investigated the MHD flow past a circular cylinder with 2D simulations. Using the SM82 model, it has been possible to perform a parametric study on both Ha and Re. We have recovered the flow regimes observed in experiments by [180] and explained the collapse of the regular Kármán vortex street as the consequence of the interaction between the Kármán vortices and secondary ones released from separation of the Shercliff layers at the duct side walls. We have also found two types of scaling law linking the base pressure coefficient C_{pb} to the friction parameter Re/Ha on the one hand and the length of the steady recirculation regions and all drag coefficients to $Re/Ha^{0.8}$.

We have then considered a configuration featuring strong 3D effects in the flow and we have therefore investigated the flow past a truncated square cylinder inside a duct. In the non-MHD investigations, we have indeed highlighted complex 3D flow dynamics with intricate interactions between vortical structures for Re up to 400. After a thorough analyse of the steady flow patterns regime, we have identified an very original scenario for the formation and release of hairpin vortices feeding a symmetric vortex street at $Re = 200$. We have stressed that the high spanwise flow confinement enhances the role of the pair of streamwise vortices spiralling upwards from the bottom of the wake and induces a more efficient entrainment of the head of the hairpin.

The flow dynamics is completely modified when the magnetic field is present. We have performed two sets of computations with an insulating cylinder at $Ha = 100$ and 200 for Re up to 1000. At very low Re for $N \gg 1$, we have provided visualisations of a Hunt's wake. For higher Re, the steady structures are generated from streamlines circulating above the cylinder tip by contrast with the non-MHD study where they are all induced by streamlines passing underneath the lateral free shear layers In the unsteady flow regime, one observes an asymmetric Kármán vortex street where vortices form from the rolling-up of the lateral free shear layers.

Replacing the electrically insulating cylinder by a perfectly conducting one at $Ha = 100$ enhances the braking of the flow by Lorentz forces. Striking differences are the suppression of the transverse vortex and an increase of the pressure drag coefficient in the middle of the steady regime. This study requires however further computations and analyse.

To conclude, we shall stress that our study raises serious questions on the interest of promoting turbulence and thus heat transfer in blankets by placing obstacles. Indeed, for $Ha = 100$ and $N < 10$, we have shown that the flow dynamics is dominated by quasi-2D effects and mostly laminar. In fusion reactor blankets, typical values of both Ha and N are several orders higher and placing obstacles is therefore very unlikely to promote turbulence in the flow.

Part IV

References

Author's publications: peer-reviewed journals

[1] V. Dousset and A. Pothérat. Numerical simulations of a cylinder wake under a strong axial magnetic field. *Phys. Fluids*, 20:017104, 2008.

[2] V. Dousset and A. Pothérat. Formation mechanism of hairpin vortices in the wake of a truncated square cylinder in a duct. *J. Fluid Mech.*, 653:519–536, 2010.

[3] V. Dousset and A. Pothérat. Three-dimensional numerical simulations of the MHD flow past a truncated square cylinder under an axial magnetic field. *J. Fluid Mech.*, 2010. (In preparation).

Author's publications: peer-reviewed conferences

[4] V. Dousset and A. Pothérat. Numerical simulations of a cylinder wake under a strong axial magnetic field. 6th Intl. Congress Ind. Applied Maths., Zurich, Switzerland, July 2007.

[5] V. Dousset and A. Pothérat. Numerical computations of a cylinder wake inside a rectangular duct in a strong axial magnetic field. 7th PAMIR Intl. Conf. Fund. Applied MHD, Giens, France, September 2008.

Author's publications: other conferences

[6] V. Dousset and A. Pothérat. Numerical simulations of a cylinder wake under an imposed magnetic field. German MHD days, Potsdam, Germany, November 2005.

[7] V. Dousset and A. Pothérat. Numerical simulations of a quasi-2d cylinder wake in a high magnetic field. EUROMECH, Ilmenau, Germany, March 2006.

[8] V. Dousset and A. Pothérat. Numerical simulations of a cylinder wake in a strong external axial magnetic field. Julius Hartmann meeting, Coventry, UK, February 2007.

[9] V. Dousset and A. Pothérat. Numerical simulations of a cylinder wake under a strong axial magnetic field. International Workshop on Numerical Simulations of Magnetohydrodynamic flows, Karlsruhe, Germany, November 2007.

[10] V. Dousset and A. Pothérat. 3D numerical simulations of a duct mhd flow past a truncated square cylinder. German MHD days, Ilmenau, Germany, December 2008.

[11] V. Dousset and A. Pothérat. 3D numerical simulations of MHD cylinder wake in a rectangular duct. UK MHD days, Salford, UK, June 2008.

[12] V. Dousset and A. Pothérat. Numerical simulations of MHD flow past a circular cylinder in a rectangular duct. MHD fundamentals from liquid-metals to astrophysics, Brussels, Belgium, April 2008.

[13] V. Dousset and A. Pothérat. 3D numerical simulations of a duct MHD flow past a truncated square cylinder. UK MHD days, Coventry, UK, June 2009.

General books

[14] G.K. Batchelor. *An introduction to fluid dynamics.* Cambridge University Press, 1974.

[15] S. Chandrasekhar. *Hydrodynamic and hydromagnetic stability.* Dover, New-York, 1981.

[16] P.A. Davidson. *An introduction to magnetohydrodynamics.* Cambridge University Press, 2001.

[17] H. Lamb. *Hydrodynamics, 6th edition.* Cambridge University Press, 1975.

[18] R. Moreau. *Magnetohydrodynamics.* Kluwer Academic Publisher, 1990.

[19] U. Müller and L. Bühler. *Magnetofluiddynamics in channels and containers.* Springer, 2001.

[20] P.H. Roberts. *Introduction to magnetohydrodynamics.* Longmans, 1967.

Non-MHD circular cylinder wake

[21] H. Abbassi, S. Turki, and S. Ben Nasrallah. Channel flow past bluff-body: outlet boundary condition, vortex shedding and effects of buoyancy. *Comp. Mech.*, 28:10–16, 2002.

[22] G. Alfonsi and A. Giorgini. Nonlinear perturbation of the vortex shedding from a circular cylinder. *J. Fluid Mech.*, 222:267–291, 1991.

[23] P. Anagnostopoulos, G. Iliadis, and S. Richardson. Numerical study of the blockage effects on viscous flow past a circular cylinder. *Int. J. Numer. Meth. Fluids*, 22:1061–1074, 1996.

[24] D. Barkley and R.D. Henderson. Three-dimensional Floquet stability analysis of the wake of a circular cylinder. *J. Fluid Mech.*, 322:215–241, 1996.

[25] M. Behr, D. Hastreiter, S. Mittal, and T.E. Tezduyar. Incompressible flow past a circular cylinder: dependence of the computed flow field on the location of the lateral boundaries. *Comp. Meth. Appl. Mech. Eng.*, 123:309–316, 1995.

[26] H. Bénard. Formation de centres de giration à l'arrière d'un obstacle en mouvement. *C. R. Acad. Sci. Paris*, 147:839–842, 1908.

[27] H. Bénard. Sur la marche des tourbillons alternés derrière un obstacle. *C. R. Acad. Sci.*, 156:1225–1228, 1913.

[28] H. Bénard. Sur la zone de formation des tourbillons alternés derrière un obstacle. *C. R. Acad. Sci.*, 156:1003–1005, 1913.

[29] R. Bouard. Détermination de la traînée engendrée par un cylindre. *Z. angew. Math. Phys*, 48:584–596, 1997.

[30] R. Bouard and M. Coutanceau. Etude théorique et expérimentale de l'écoulement engendré par un cylindre en translation uniforme dans un fluide visqueux en régime de Stokes. *Z. angew. Math. Phys*, 37:673–684, 1986.

[31] M. Braza, P. Chassaing, and H. Ha Minh. Numerical study and physical analysis of the pressure and velocity fields in the near wake of a circular cylinder. *J. Fluid Mech.*, 165:79–130, 1986.

[32] M. Braza, P. Chassaing, and H. Ha Minh. Prediction of large-scale transition features in the wake of a circular cylinder. *Phys. Fluids A*, 2(8):1461–1471, 1990.

[33] M. Braza, D. Faghani, and H. Persillon. Successive stages and the role of natural vortex dislocations in three-dimensional wake transition. *J. F. Mech.*, 439:1–41, 2001.

[34] M. Brede, H. Eckelmann, and D. Rockwell. On secondary vortices in the cylinder wake. *Phys. Fluids*, 8(8):2117–2124, 1996.

[35] J.-H. Chen, W.G. Pritchard, and S.J. Tavener. Bifurcation for flow past a cylinder between parallel planes. *J. Fluid Mech.*, 284:23–41, 1995.

[36] K.A. Cliffe and S.J. Tavener. The effect of cylinder rotation and blockage ratio on the onset of periodic flows. *J. Fluid Mech.*, 501:125–133, 2004.

[37] M. Coutanceau and R. Bouard. Experimental determination of the main features of the viscous flow of the wake of a circular cylinder in uniform translation. Part 1: Steady flow. *J. Fluid Mech.*, 79:231–256, 1977.

[38] M. Coutanceau and J.R. Defaye. Cylinder wake configurations: a flow visualisation survey. *App. Mech. Rev.*, 44(6):255–305, 1991.

[39] S.C.R. Dennis and G.Z. Chang. Numerical solutions for steady flow past a cylinder at Reynolds number up to 100. *J. Fluid Mech.*, 42:471–489, 1970.

[40] B.E. Eaton. Analysis of laminar vortex behind a circular cylinder by aided-flow visualisation. *J. Fluid Mech.*, 180:117–145, 1987.

[41] M.S. Engelman and M.-A. Jamnia. Transient flow past a circular cylinder: a benchmark solution. *Int. J. Numer. Meth. Fluids*, 11:989–1000, 1990.

[42] B. Fornberg. A numerical study of steady viscous flow past a circular cylinder. *J. Fluid Mech.*, 98:819–855, 1980.

[43] P. Freymuth, F. Finaish, and W. Bank. Visualization of the vortex street behind a circular cylinder at low Reynolds numbers. *Phys. Fluids*, 29(4):1321–1323, 1986.

[44] J.H. Gerrard. The wakes of cylindrical bluff bodies at low Reynolds number. *Phil. Trans.*, A288:351–382, 1978.

[45] A.S. Grove, F.H. Shair, E.E. Petersen, and A. Acrivos. An experimental investigation of the steady separated flow past a circular cylinder. *J. Fluid Mech.*, 19:60–80, 1964.

[46] V.A. Gushchin, A.V. Kostomorov, P.V. Matyushin, and E.R. Pavlyukova. Direct numerical simulation of the transitional separated fluid flows around a sphere and a circular cylinder. *J. Wind Eng. Ind. Aer.*, 90:341–358, 2002.

[47] R.D. Henderson. Details of the drag curve near the onset of vortex shedding. *Phys. Fluids*, 7(9):2102–2104, 1995.

[48] R.D. Henderson. Nonlinear dynamics and pattern formation in turbulent wake transition. *J. Fluid Mech.*, 352:65–112, 1997.

[49] O. Inoue and Y. Yamazaki. Secondary vortex streets in two-dimensional cylinder wakes. *Fluid Dyn. Res.*, 25:1–18, 1999.

[50] G. Karniadakis and G. Triantafyllou. Frequency selection and asymptotic states of laminar wakes. *J. Fluid Mech.*, 199:441–469, 1989.

[51] M. Kawaguti. Numerical solution of the Navier-Stokes equations for the flow around a circular cylinder at Reynolds number 40. *J. Phys. Soc. Jpn.*, 8:747–757, 1953.

[52] W.A. Khan, J.R. Culham, and M.M. Yovanovich. Fluid flow and heat transfer from a cylinder between parallel planes. *J. Thermophys. Heat Transfer*, 18(3):395–403, 2004.

[53] B. Kumar and S. Mittal. Prediction of the critical Reynolds number for flow past a circular cylinder. *Comput. Methods Appl. Mech. Engrg*, 195:6046–6058, 2006.

[54] D.F.L. Labbé and P.A. Wilson. A numerical investigation of the effects of the spanwise length on the 3-D wake of a circular cylinder. *J. Fluids Struct.*, 23:1168–1188, 2007.

[55] C.F. Lange, F. Durst, and M. Breuer. Momentum and heat transfer from cylinders in laminar crossflow at $10^{-4} \leq Re \leq 200$. *Intl. J. Heat Mass Transfer*, 41(22):3409–3430, 1998.

[56] C. Lei, L. Cheng, and K. Kavanagh. Spanwise length effects on three-dimensional modelling of flow over a circular cylinder. *Comput. Methods Appl. Mech. Engrg.*, 19:2909–2923, 1001.

[57] T. Leweke and C.H.K. Williamson. Three-dimensional instabilities in wake transition. *Eur. J. Mech. B Fluids*, 17:571–586, 1998.

[58] W.W. Liou. Linear stability of cruved free shear layers. *Phys. Fluids*, 6:541–549, 1994.

[59] S. Mettu, N. Verma, and R.P. Chhabra. Momentum and heat transfer from an asymmetrically confined circular cylinder in a plane channel. *Heat Mass Transfer*, 42:1037–1048, 2006.

[60] S. Mittal. Computation of three-dimensional flows past circular cylinder of low aspect ratio. *Phys. Fluids*, 13(1):177–191, 2001.

[61] M. Nishioka and H. Sato. Measurements of velocity distributions in the wake of a circular cylinder at low Reynolds numbers. *J. Fluid Mech.*, 65:97–112, 1974.

[62] M. Nishioka and H. Sato. Mechanism of determination of the shedding frequency of vortices behind a cylinder at low Reynolds numbers. *J. Fluid Mech.*, 89:49–60, 1978.

[63] R.B. Payne. Calculations of unsteady viscous flow past a circular cylinder. *J. Fluid Mech.*, 4:81–86, 1958.

[64] A.E. Perry, M.S. Chong, and T.T. Lim. The vortex shedding process behind two-dimensional bluff bodies. *J. Fluid Mech.*, 116:77–90, 1982.

[65] H. Persillon and M. Braza. Physical analysis of the transition to turbulence in the wake of a circular cylinder by three-dimensional Navier-Stokes simulation. *J. Fluid Mech.*, 365:23–88, 1998.

[66] O. Posdziech and R. Grundmann. Numerical simulation of the flow around an infinitely long circular cylinder in the transition regime. *Theor. Comp. Fluid Dyn.*, 15:121–141, 2001.

[67] F. Rehimi, F. Aloui, S. Ben Nasrallah, L. Doubliez, and J. Legrand. Experimental investigation of a confined flow downstream of a circular cylinder centred between two parallel walls. *J. Fluids Struct.*, 24:855–882, 2008.

[68] A. Ben Richou, A. Ambari, M. Lebey, and J.K. Naciri. Drag force on a circular cylinder midway between two parallel plates at $Re \ll 1$ Part 2: moving uniformly (numerical and experimental). *Chem. Engng. Science*, 60:2535–2543, 2005.

[69] L. Rosenhead and M. Schwabe. An experimental investigation of the flow behind circular cylinders in channels of different breadth. *Proc. Roy. Soc. A*, 129:115–135, 1930.

[70] A. Roshko. *On the development of turbulent wakes from vortex streets*. PhD thesis, California Institute of Technology, 1952.

[71] P. Roushan and X.L. Wu. Universal wake structures of Kármán vortex streets in two-dimensional flows. *Phys. Fluids*, 17(7):073601, 2005.

[72] M. Sahin and R.G. Owens. A numerical investigation of the wall effects up to high blockage ratios on two-dimensional flow past a confined circular cylinder. *Phys. Fluids*, 16(5):1305–1320, 2004.

[73] S. Sen, S. Mittal, and G. Biswas. Steady separated flow past a circular cylinder at low Reynolds numbers. *J. Fluid Mech.*, 620:89–119, 2009.

[74] F.H Shair, A.S. Grove, E.E. Petersen, and A. Acrivos. The effect of confining walls on the stability of the steady wake behind a circular cylinder. *J. Fluid Mech.*, 17:546–560, 1963.

[75] S.P. Singh and S. Mittal. Flow past a cylinder, shear layer instability and drag crisis. *Int. J. Numer. Methods Fluids*, 47:75–98, 2005.

[76] R.M.C. So, Y. Liu, Z.X. Cui, C.H. Zhang, and X.Q. Wang. Three-dimensional wake effects on flow-induced forces. *J. Fluids Struc.*, 20:373–402, 2005.

[77] S. Taneda. Experimental investigation of the wall-effect on a cylindrical obstacle moving in a viscous fluid at low Reynolds numbers. *J. Phys. Soc. Jap.*, 19(6):1024–1030, 1964.

[78] T.E. Tezduyar and R. Shih. Numerical experiments on downstream boundary of flow past cylinder. *ASCE J. Engng Mech.*, 117(4):854–871, 1991.

[79] A. Thom. The flow past circular cylinders at low speeds. *Proc. Roy. Soc. A*, 141:651–659, 1933.

[80] M. Thompson, K. Hourigan, K. Ryan, and G.J. Sheard. Wake transition of two-dimensional cylinders and axisymmetric bluff bodies. *J. Fluids Struct.*, 22:793–806, 2006.

[81] M. Thompson, K. Hourigan, and J. Sheridan. Three-dimensional instabilities in the wake of a circular cylinder. *Exp. Therm. Fluid Sci.*, 12:190–196, 1996.

[82] Th. von Kármán. Über den Mechanismus des Widerstandes, den ein bewegter Körper in einer Flüssigkeit erfährt. 1 Teil. *Nachr. Ges. Wiss. Göttingen. Math-Physik Kl.*, 29(4):509–517, 1911.

[83] Th. von Kármán. Über den Mechanismus des Widerstandes, den ein bewegter Körper in einer Flüssigkeit erfährt. 2 Teil. *Nachr. Ges. Wiss. Göttingen. Math-Physik Kl.*, pages 547–556, 1912.

[84] C.-Y. Wen and C.-Y. Lin. Two-dimensional vortex shedding of a circular cylinder. *Phys. Fluids*, 13(3):557–560, 2001.

[85] C.M. White. The drag of circular cylinders in fluids at slow speed. *Proc. Roy. Soc.*, 186:472–279, 1946.

[86] C.H.K. Williamson. The existence of two stages in the transition to three-dimensionality of a cylinder wake. *Phys. Fluids*, 31(11):3165–3168, 1988.

[87] C.H.K. Williamson. Three-dimensional wake transition. *J. Fluid Mech.*, 328:345–407, 1996.

[88] C.H.K. Williamson. Vortex dynamics in the cylinder wake. *Ann. Rev. Fluid Mech.*, 28:477–539, 1996.

[89] M.-H. Wu, C.-Y. Wen, R.-H. Yen, M.-C Weng, and A.-B. Wang. Experimental and numerical study of the separation angle for flow around a circular cylinder at low Reynolds number. *J. Fluid Mech.*, 515:233–260, 2004.

[90] Y. Yokoi and K. Kamemoto. Initial stage of a three-dimensional vortex structure existing in a two-dimensional boundary later separation flow. *JSME Int. J. Series B*, 36(2):201–206, 1993.

[91] M.M. Zdravkovich. Smoke observations of the formation of a Kármán vortex street. *J. Fluid Mech.*, 37:491–496, 1969.

[92] M.M. Zdravkovich. *Flow around circular cylinders. Vol. 1: Fundamentals.* Oxford University Press, 1997.

[93] M.M. Zdravkovich. *Flow around circular cylinders. Vol. 2: Applications.* Oxford University Press, 2003.

[94] H.Q. Zhang, U. Fey, B.R. Noack, M. König, and H. Eckelmann. On the transition of the cylinder wake. *Phys. Fluids*, 7(4):779–794, 1995.

[95] L. Zovatto and G. Pedretti. Flow about a circular cylinder between parallel walls. *J. Fluid Mech.*, 440:1–25, 2001.

Non-MHD square cylinder wake

[96] M. Breuer, J. Bernsdorf, T. Zeiser, and F. Durst. Accurate computations of the laminar flow past a square cylinder based on two different methods: lattice-Boltzmann and finite-volume. *Int. J. Heat Fluid Flow*, 21:186–196, 2000.

[97] S. Camarri and F. Giannetti. On the inversion of the von Kármán street in the wake of a confined square cylinder. *J. Fluid Mech.*, 574:169–178, 2007.

[98] R.W. Davis, E.F. Moore, and L.P. Purtell. A numerical-experimental study of confined flow around rectangular cylinders. *Phys. Fluids*, 27(1):46–59, 1984.

[99] S.C. Luo, X.H. Tong, and B.C. Khoo. Transition phenomena in the wake of a square cylinder. *J. Fluids Struct.*, 23:227–248, 2007.

[100] A. Okajima. Strouhal numbers of rectangular cylinders. *J. Fluid Mech.*, 123:379–398, 1982.

[101] J. Robichaux, S. Balachandar, and S.P. Vanka. Three-dimensional Floquet instability of the wake of square cylinder. *Phys. Fluids*, 11(3):560–578, 1999.

[102] A.K. Saha, G.Biswas, and K. Muralidhar. Three-dimensional study of flow past a square cylinder at low Reynolds numbers. *Int. J. Heat Fluid Flow*, 24:54–66, 2003.

[103] A. Sau. Hopf bifurcations in the wake of a square cylinder. *Phys. Fluids*, 21:034105, 2009.

[104] A. Sharma and V. Eswaran. Heat and fluid flow across a square cylinder in the two-dimensional flow regime. *Numer. Heat Transfer A*, 45:247–269, 2004.

[105] A. Sharma and V. Eswaran. Effect of channel confinement on the two-dimensional laminar flow and heat transfer across a square cylinder. *Numer. Heat Transfer A*, 47:79–107, 2005.

[106] A. Sohankar, C. Norberg, and L. Davidson. Low-Reynolds-number flow around a square cylinder at incidence: study of blockage, onset of vortex shedding and outlet boundary condition. *Int. J. Num. Meth. Fluids*, 26:39–56, 1998.

[107] A. Sohankar, C. Norberg, and L. Davidson. Simulation of three-dimensional flow around a square cylinder at moderate Reynolds numbers. *Phys. Fluids*, 11(2):288–306, 1999.

Non-MHD flows past an obstacle with one free end

[108] C.J. Baker. The laminar horseshoe vortex. *J. Fluid Mech.*, 95:347–361, 1979.

[109] F. Ballio, C. Bettoni, and S. Franzetti. A survey of time-averaged characteristics of laminar and turbulent horseshoe vortices. *J. Fluids Engng.*, 120:347–361, 1998.

[110] C. Dauchy, J. Dušek, and P. Fraunié. Primary and secondary instabilities in the wake of a cylinder with free ends. *J. Fluid Mech.*, 332:295–339, 1997.

[111] S. Dong and H. Meng. Flow past a trapezoidal tab. *J. Fluid Mech.*, 510:219–242, 2004.

[112] F. Etzold and H. Fiedler. The near-wake structure of a cantilevered cylinder in a cross-flow. *Z. Flugwiss.*, 24:77–82, 1976.

[113] J.C.R. Hunt, C.J. Abell, J.A. Peterka, and H. Woo. Kinematical studies of the flows around free or surface-mounted obstacles; applying topology to flow visualization. *J. Fluid Mech.*, 86(1):179–200, 1978.

[114] J.-Y. Hwang and K.-S. Yang. Numerical study of vortical structures around a wall-mounted cubic obstacle in channel flow. *Phys. Fluids*, 16(7):2382–2394, 2004.

[115] T. Kawamura, M. Hiwada, T. Hibino, I. Mabuchi, and M. Kumada. Flow around a finite circular cylinder on a flat plate. *Bulletin of the JSME*, 27(232):2142–2151, 1984.

[116] C. Lin, P.-H. Chiu, and S.-J. Shieh. Characteristic of horseshoe vortex system near a vertical plate-base plate juncture. *Exp. Therm. Fluid Sci.*, 27:25–46, 2002.

[117] C. Lin, T.C. Ho, and S. Dey. Characteristic of steady horseshoe vortex system near junction of square cylinder and base plate. *ASCE J. Engnrg Mech.*, 134(2):184–197, 2008.

[118] Y. Liu, R.M.C. So, and Z.X. Cui. A finite cantilevered cylinder in a cross-flow. *J. Fluid Struct.*, 20:589–609, 2005.

[119] H. Nakamura and T. Igarashi. Forced convection heat transfer from a low-profile block simulating a package of electronic equipment. *J. Heat Trans.*, 126:463–470, 2004.

[120] C.-W. Park and S.-J. Lee. Free end effects on the near wake flow structure behind a finite circular cylinder. *J. Wind Engng. Ind. Aerodyn,*, 88:231–246, 2000.

[121] H. Sakamoto and M. Arie. Vortex shedding from a rectangular prism and a circular cylinder placed vertically in a turbulent boundary layer. *J. Fluid Mech.*, 126:147–165, 1983.

[122] H. Sakamoto, H. Haniu, and Y. Obata. Vortex shedding from a circular cylinder placed vertically in a laminar boundary layer. *Trans. JSME B*, 53(487):714–721, 1987. (in Japanese).

[123] A. Sau, R.R. Hwang, T.W.H. Sheu, and W.C. Yang. Interaction of trailing vortices in the wake of a wall-mounted rectangular cylinder. *Phys. Rev. E*, 68:056303, 2003.

[124] A. Slaouti and J.H. Gerrard. An experimental investigation of the end effects on the wake of a circular cylinder towed through water at low Reynolds number. *J. Fluid Mech.*, 112:297–314, 1981.

[125] D. Sumner, J.L. Heseltine, and O.J.P Dansereau. Wake structure of a finite circular cylinder of small aspect ratio. *Exp. Fluids*, 37:720–730, 2004.

[126] H.F. Wang and Y. Zhou. The finite-length square cylinder near wake. *J. Fluid Mech.*, 638:453–490, 2009.

[127] H.F. Wang, Y. Zhou, C.K. Chan, and K.S. Lam. Effect of initial conditions on interaction between a boundary layer and a wall-mounted finite-length-cylinder wake. *Phys. Fluids*, 18:065106, 2006.

[128] H. Yamada, T. Yamane, and H. Osaka. Vortex structure behind a square plate protuberance standing on a flat ground wal. *Trans. JSME B*, 59(559):677–683, 1993. (in Japanese).

[129] H. Yanaoka, T. Inamura, and S. Kawabe. Turbulence and heat transfer of a hairpin vortex formed behind a cube in a laminar boundary layer. *Numerical Heat Transfer, Part A*, 52:973–990, 2007.

[130] W. Yang, H. Meng, and J. Sheng. Dynamics of hairpin vortices generated by a mixing tab in a channel flow. *Exp. Fluids*, 30:705–722, 2001.

[131] J. Zhou, R.J. Adrian, S. Balachandar, and T.M. Kendall. Mechanisms for generating coherent packets of hairpin vortices in channel flow. *J. Fluid Mech.*, 387:353–396, 1999.

MHD flows at low R_m

[132] A. Alémany, R. Moreau, P. Sulem, and U. Frisch. Influence of external magnetic field on homogeneous MHD turbulence. *J. Méc.*, 18(2):277–313, 1979.

[133] R.A. Alpher, H. Hurwitz, R.H. Johnson, and D.R. White. Some studies of free-surface mercury magnetohydrodynamics. *Rev. Modern Phys.*, 32(4):758–769, 1960.

[134] L. Bühler. Instabilities in quasi-two-dimensional magnetohydrodynamic flows. *J. Fluid Mech.*, 326:125–150, 1996.

[135] P.A. Davidson. The role of angular momentum in the magnetic damping of turbulence. *J. Fluid Mech.*, 336:123–150, 1997.

[136] Y. Fautrelle, J. Etay, and S. Daugan. Free-surface horizontal waves generated by low-frequency alternating magnetic fields. *J. Fluid Mech.*, 527:285–301, 2005.

[137] J. Hartmann. Hg-Dynamics I. Theory of the laminar flow of an electrically conductive liquid in a homogeneous magnetic field. *Det. Kgl. Danske Vid. Sels. Mat.-Fys. Medd.*, 15(6):1–27, 1937.

[138] J. Hartmann and F. Lazarus. Hg-Dynamics II. Experimental investigations on the flow of mercury in a homogeneous magnetic field. *Det. Kgl. Danske Vid. Sels. Mat.-Fys. Medd.*, 15(7):1–45, 1937.

[139] J.C.R. Hunt. Magnetohydrodynamic flow in rectangular ducts. *J. Fluid Mech.*, 21:577–590, 1965.

[140] J.C.R. Hunt and J.A. Shercliff. Magnetohydrodynamic at high Hartmann number. *Ann. Rev. Fluid. Mech.*, 3:37–62, 1971.

[141] M. Kinet, B. Knaepen, and S. Molokov. Instabilities and transition in magnetohydrodynamic flows in ducts with electrically conducting walls. *Phys. Rev. Letters*, 103:154501, 2009.

[142] B. Knaepen and R. Moreau. Magnetohydrodynamic turbulence at low magnetic Reynolds number. *Annu. Rev. Fluid. Mech.*, 40:25–25, 2008.

[143] V. Kocourek, C. Karcher, M. Conrath, and D. Schulze. Stability of liquid metal drops affected by a high-frequency magnetic field. *Phys. Rev. E*, 74:026303, 2006.

[144] D.S. Krasnov, E. Zienicke, O. Zikanov, T. Boeck, and A. Thess. Numerical study of the instability of the Hartmann layer. *J. Fluid Mech.*, 504:183–211, 2004.

[145] L. Leboucher. Monotone scheme and boundary conditions for finite volume simulation of magnetohydrodynamic internal flows at high Hartmann number. *J. Comp. Phys.*, 150:181–198, 1999.

[146] D. Lee and H. Choi. Magnetohydrodynamic turbulent flow in a channel at low magnetic Reynolds number. *J. Fluid Mech.*, 439:367–394, 2001.

[147] J. Lim, H. Choi, and J. Kim. Control of streamwise vortices with uniform magnetic fluxes. *Phys. Fluids*, 10(8):1997–2005, 1998.

[148] C. Mistrangelo and L. Bühler. Influence of helium cooling channels on magnetohydrodynamic flows in the HCLL blanket. *Fusion Engineering and Design*, 84(7-11):1323–1328, 2009.

[149] H.K. Moffat. On the suppression of turbulence by a uniform magnetic field. *J. Fluid Mech.*, 28:571–592, 1967.

[150] J.-U. Mohring, C. Karcher, and D. Schulze. Dynamic behavior of a liquid metal interface under the influence of a high-frequency magnetic field. *Phys. Rev. E*, 71:047301, 2005.

[151] P. Moresco and T. Alboussière. Experimental study of the instability of the Hartmann layer. *J. Fluid Mech.*, 504:167–181, 2004.

[152] M.-J. Ni, R. Munipalli, N.B. Morley, P. Huang, and M.A. Abdou. A current density conservative scheme for incompressible MHD flows at a low Reynolds number. Part I: On a rectangular collocated grid system. *J. Comp. Phys.*, 227:174–204, 2007.

[153] M.-J. Ni, R. Munipalli, N.B. Morley, P. Huang, and M.A. Abdou. A current density conservative scheme for incompressible MHD flows at a low Reynolds number. Part II: On an arbitrary collocated mesh. *J. Comp. Phys.*, 227:205–228, 2007.

[154] A. Pothérat. *Etude et modèles effectifs d'écoulements quasi-2D.* PhD thesis, Institut National Polytechnique de Grenoble, September 2000.

[155] A. Pothérat. Quasi-2d perturbations in duct flows under transverse magnetic field. *Phys. Fluids*, 19(7):074104, 2007.

[156] A. Pothérat and T. Alboussière. Small scales and anisotropy in low R_m magnetohydrodynamic turbulence. *Phys. Fluids*, 15(10):3170–3180, 2003.

[157] A. Pothérat, J. Sommeria, and R. Moreau. An effective two-dimensional model for MHD flows with transverse magnetic field. *J. Fluid Mech.*, 424:75–100, 2000.

[158] A. Pothérat, J. Sommeria, and R. Moreau. Effective boundary conditions for magnetohydrodynamic flows with thin hartmann layers. *Phys. Fluids*, 14:403–410, 2002.

[159] A. Pothérat, J. Sommeria, and R. Moreau. Numerical simulations of an effective 2d model for flows with a transverse magnetic field. *J. Fluid Mech.*, 534:115–143, 2005.

[160] J. Priede, S. Aleksandrova, and S. Molokov. Linear stability of hunt's flow. *J. Fluid Mech.*, 649:115–134, 2010.

[161] J.A. Shercliff. Steady motion of conducting fluids in pipes under transverse magnetic fields. *Proc. Cam. Phil. Soc.*, 49:136–144, 1953.

[162] Y. Shimomura. Large eddy simulation of magnetohydrodynamic turbulent channel flows under a uniform magnetic field. *Phys. Fluids*, A3(12):3098–3106, 1991.

[163] J. Sommeria. Experimental study of two-dimensional inverse energy cascade in a square box. *J. Fluid Mech.*, 170:139–168, 1986.

[164] J. Sommeria. Electrically driven vortices in a strong magnetic field. *J. Fluid Mech.*, 189:553–569, 1988.

[165] J. Sommeria and R. Moreau. Why, how, and when, MHD turbulence becomes two-dimensional. *J. Fluid Mech.*, 118:507–518, 1982.

[166] B. Sreenivasan and T. Alboussière. Experimental study of a vortex in a magnetic field. *J. Fluid Mech.*, 464:287–309, 2002.

[167] A. Sterl. Numerical simulation of liquid-metal mhd flows in rectangular ducts. *J. Fluid Mech.*, 216:161–191, 1990.

[168] A. Thess. Instabilities in 2-dimensional spatially periodic flows .1. Kolmogorov flow. *Phys. Fluids A*, 4(7):1385–1395, 1992.

[169] A. Thess, Y. Kolesnikov, T. Boeck, P. Terhoeven, and A. Krätzschmar. The H-trough: a model for liquid metal electric current limiters. *J. Fluid Mech.*, 527:67–84, 2005.

[170] N. Umeda and M. Takahashi. Numerical analysis for heat transfer enhancement of a lithium flow under a transverse magnetic field. *Fusion Engrg. Design*, 51-52:899–907, 2000.

[171] S. Vantieghem, X. Albets-Chico, and B. Knaepen. The velocity profile of laminar MHD flows in circular conducting pipes. *Theor. Comp. Fluid Dyn.*, pages 1–9, 2009. (in press).

[172] J.S. Walker. Magnetohydrodynamic flows in rectangular ducts with thin conducting walls. Part I. *J. Mécanique*, 20(1):79–112, 1981.

[173] O. Widlund. Wall functions for numerical modeling of laminar MHD flows. *Eur. J. Mech. B/Fluids*, 22:221–237, 2003.

MHD cylinder wake

[174] O.V. Andreev and Y.B. Kolesnikov. MHD instabilities at transverse flow around a circular cylinder in an axial magnetic field. In *Third Intl. Conf. on Transfer Phenomena in Magnetohydrodynamics and Electroconducting Flows, Aussois, France*, pages 205–210, 1997.

[175] O.V. Andreev and Y.B. Kolesnikov. Experimental flow around a conducting cylinder in an axial homogeneous magnetic field. *Magnetohydrodynamics (N.Y.)*, 34(4):286–293, 1998.

[176] G.G. Branover, Yu. M. Gel'fgat, S.V. Turuntaev, and A.B. Tsinober. Effect of a transverse magnetic field on velocity perturbations behind a circular cylinder swept by an electrolyte. *Magnetohydrodynamics (N.Y.)*, 7(1):35–41, 1969.

[177] L. Bühler, S. Horanyi, and C. Mistrangelo. Interpretation of LEVI velocity signals in 3D MHD flows. *Fusion Eng. Des.*, 83:1822–1827, 2008.

[178] H. Choi, D. Lee, and J. Kim. Control of near-wall streamwise vortices using an electromagnetic force in a conducting fluid. *AIAA Paper*, 97:2059, 1997.

[179] M. Frank. Experimentelle Untersuchung zweidimensionaler MHD-Turbulenz. Master's thesis, Forschungszentrum Karlsruhe, Institut für angewandte Thermo- und Fluiddynamik, 2001.

[180] M. Frank, L. Barleon, and U. Müller. Visual analysis of two-dimensional magnetohydrodynamics. *Phys. Fluids*, 13(8):2287–2295, 2001.

[181] J.C.R. Hunt and G.S.S. Ludford. Three-dimensional MHD duct flows with strong transverse magnetic fields. Part 1. obstacles in a constant area channel. *J. Fluid Mech.*, 33:693–714, 1968.

[182] J. Josserand, P. Marty, and A. Alemany. Pressure and drag measurements on a cylinder in a liquid metal flow with an aligned magnetic field. *Fluid Dyn. Res.*, 11:107–117, 1993.

[183] K.E. Kalis, A.B. Tsinober, A.G. Shtern, and E.V. Shcherbinin. Flow of a conducting fluid past a circular cylinder in a transverse magnetic field. *Magnetohydrodynamics (N.Y.)*, 1(1):11–19, 1965.

[184] L.G. Kit, Yu.B. Kolesnikov, A.B. Tsinober, and P.G. Shtern. Use of a conduction anemometer in investigating the MHD wake behind a body. *Magnetohydrodynamics (N.Y.)*, 5(4):46–50, 1969.

[185] L.G. Kit, S.V. Turuntaev, and A.B. Tsinober. Investigation with a conduction anemometer of the effect of a magnetic field in the wake of a cylinder. *Magnetohydrodynamics (N.Y.)*, 6(3):331–335, 1970.

[186] R. Klein, A. Pothérat, and A. Alferenok. Experiment on a confined electrically driven vortex pair. *Phys. Rev. E*, 79(016304), 2009.

[187] Yu.B. Kolesnikov and A.B. Tsinober. Two-dimensional turbulent flow behind a circular cylindar. *Magnetohydrodynamics (N.Y.)*, 8(3):300–307, 1972.

[188] J. Lahjomri, P. Capéran, and A. Alemany. The cylinder wake in a magnetic field aligned with the velocity. *J. Fluid Mech.*, 253:421–448, 1993.

[189] B. Mück, C. Günther, U. Müller, and L. Bühler. Three-dimensional MHD flows in rectangular ducts with internal obstacles. *J. Fluid Mech*, 418:265–295, 2000.

[190] G. Mutschke, G. Gerbeth, V. Shatrov, and A. Tomboulides. Two- and three-dimensional instabilities of the cylinder wake in an aligned magnetic field. *Phys. Fluids*, 9(11):3114–3116, 1997.

[191] G. Mutschke, G. Gerbeth, V. Shatrov, and A. Tomboulides. The scenario of three-dimensional instabilities of the cylinder wake in an external magnetic field. *Phys. Fluids*, 13(3):723–734, 2001.

[192] G. Mutschke, V. Shatrov, and G. Gerbeth. Cylinder wake control by magnetic fields in liquid metal flows. *Exp. Therm. Fluid Sci.*, 16:92–99, 1998.

[193] A.B. Tsinober and P.G. Shtern. Experimental investigation of the pressure distribution for constrained MHD flow past cylinders. *Magnetohydrodynamics (N.Y.)*, 9(1):9–14, 1973.

[194] K. Ueno, K. Saito, and S. Kamiyama. Three-dimensional simulation of MHD flow with turbulence. *JSME Intl. J. Series B*, 44(1):38–44, 2001.

[195] H.S. Yoon, H.H. Chun, M.Y. Ha, and H.G. Lee. A numerical study on the fluid flow and heat transfer around a circular cylinder in an aligned magnetic field. *Int. J. Heat Mass Trans.*, 47(19-20):4075–4087, 2004.

Numerical methods

[196] L.S. Caretto, A.D. Gosman, S.V. Patankar, and D.B. Spalding. Two calculation procedures for steady, three-dimensional flows with recirculation. In *Proc. Third Conf. Numer. Methods Fluid Dyn.*, Paris, 1972.

[197] M.S. Chong, A.E. Perry, and B.J. Cantwell. A general classification of three-dimensional flow fields. *Phys. Fluids A*, 2(5):765–777, 1990.

[198] J.H. Ferziger and M. Peri̇̀c. *Computational methods for fluid dynamics - Third edition*. Springer Verlag, 2002.

[199] Fluent. *Fluent 6.2 User's Guide*. Fluent Inc., January 2005.

[200] F.H. Harlow and J.E. Welsh. Numerical calculation of the time dependent viscous incompressible flow with free-surface. *Phys. Fluids*, 8:2182–2189, 1965.

[201] R. Issa. Solution of the implicitly discretized fluid flow equations by operator-splitting. *J. Comp. Phys.*, 62:40–65, 1986.

[202] H. Jasak. *Error analysis and estimation for the finite volume method with applications to fluid flow*. PhD thesis, Imperial College London, June 1996.

[203] J. Jeong and F. Hussain. On the identification of a vortex. *J. Fluid. Mech.*, 285:69–94, 1995.

[204] Y. Morinishi, T.S. Lund, O.V. Vasilyev, and P. Moin. Fully conservative higher order finite difference schemes for incompressible flows. *J. Comp. Phys.*, 143:90–124, 1998.

[205] OpenCFD. *OpenFOAM version 1.4.1 Programmer's Guide*. OpenCFD, August 2007.

[206] OpenCFD. *OpenFOAM version 1.4.1 User Guide*. OpenCFD, August 2007.

[207] S.V. Patankar. *Numerical heat transfer and fluid flow*. McGraw-Hill, New-York, 1980.

[208] C.M. Rhie and W.L. Chow. A numerical study of the turbulent flow past an isolated airfoil with trailing edge separation. *AIAA J.*, 21:1525–1532, 1983.

[209] H.K. Versteeg and W. Malalasekera. *An introduction to computational fluid dynamics: The finite volume method*. Longman Scientific & Technical, 1995.

[210] H.G. Weller, G. Tabor, H. Jasak, and C. Fureby. A tensorial approach to computational continuum mechanics using object oriented techniques. *Comp. Phys.*, 12(6):620–631, 1998.

Appendix A

Implementation of MHD solvers in OpenFOAM

A.1 C++ script of the MHD solver used in Direct Numerical Simulations

```
/*---------------------------------------------------------------------------*\
  =========                 |
  \\      /  F ield         | OpenFOAM: The Open Source CFD Toolbox
   \\    /   O peration     |
    \\  /    A nd           | Copyright (C) 1991-2007 OpenCFD Ltd.
     \\/     M anipulation  |
\*---------------------------------------------------------------------------*/

#include "fvCFD.H"

// * * * * * * * * * * * * * * * * * * * * * * * * * * * * * * * * * * * * * //
int main(int argc, char *argv[])
{
// Settings of the simulation and the mesh
#   include "setRootCase.H"
#   include "createTime.H"
#   include "createMesh.H"
#   include "createFields.H"
#   include "initContinuityErrs.H"
```

```
#   include "readPISOControls.H"
// * * * * * * * * * * * * * * * * * * * * * * * * * * * * * * * * * * * * * //

Info<< "\nStarting time loop\n" << endl;

const vector nB = B0.value()/mag(B0.value());   // Magnetic field direction

// Arbitrary scalar included in Poisson equation for electric potential
scalar consist = 1;
// Initialization of Lorentz force
volVectorField lorentz = sigma * (-fvc::grad(PotE) ^ B0) + sigma * ((U ^ B0) ^ B0);

for (runTime++; !runTime.end(); runTime++)
{
 Info<< "Time = " << runTime.timeName() << nl << endl;

#include "CourantNo.H"

  for (int cor=0; cor<PotElnCorr; cor++)
  {
   Info << "Iteration No " << cor+1 << "\n";

   fvVectorMatrix UEqn
   (
      fvm::ddt(U) // Time variation term of velocity U
    + fvm::div(phi, U) // Convection term with flux of velocity phi
    - fvm::laplacian(nu, U) // Viscous term
    ==
     (1.0/rho) * lorentz // Lorentz force term
   );

   solve( UEqn == -fvc::grad(p)); // Pressure gradient term

   // --- PISO loop
        for (int corr=0; corr<nCorr; corr++)
```

```
        {
            volScalarField rUA = 1.0/UEqn.A();

            U = rUA*UEqn.H();
            phi = (fvc::interpolate(U) & mesh.Sf()) + fvc::ddtPhiCorr(rUA, U, phi);

            adjustPhi(phi, U, p);

           for (int nonOrth=0; nonOrth<=nNonOrthCorr; nonOrth++)
            {
                fvScalarMatrix pEqn
                (
                    fvm::laplacian(rUA, p) == fvc::div(phi)
                );

                pEqn.setReference(pRefCell, pRefValue);
                pEqn.solve();

// Correction of pressure for non-orthogonal meshes
                if (nonOrth == nNonOrthCorr)
                {
                    phi -= pEqn.flux();
                }
            }

#           include "continuityErrs.H"

            U -= (rUA*fvc::grad(p));
            U.correctBoundaryConditions();
          }

// Fluxes of cross product velocity and magnetic fields
        surfaceScalarField psiub = fvc::interpolate(U ^ B0) & mesh.Sf();

// Consistent treatment of Poisson equation for electric potential PotE
```

```
        fvScalarMatrix PotEEqn
        (
                fvm::laplacian(consist,PotE) == consist * fvc::div(psiub)
        );

        PotEEqn.setReference(PotERefCell, PotERefValue);
        PotEEqn.solve();

// Conservative treatment of the current density
surfaceScalarField jn = -(fvc::snGrad(PotE) * mesh.magSf()) + psiub ;
surfaceVectorField jnv = jn * mesh.Cf();

// Equation (42) in Ni et al. (2007, PartII)
volVectorField jfinal = fvc::surfaceIntegrate(jnv) - fvc::surfaceIntegrate(jn) * mesh.C();

jfinal.correctBoundaryConditions();

// Derivation of the Lorentz force
lorentz = sigma* (jfinal ^ B0);
}
        runTime.write();

        Info<< "ExecutionTime = " << runTime.elapsedCpuTime() << " s"
            << "  ClockTime = " << runTime.elapsedClockTime() << " s"
            << nl << endl;
    }

    Info<< "End\n" << endl;

    return(0);
}
```

A.2 Performances of the solver

We have simulated the 3D flow of an electric conducting fluid in an electrically insulating duct of rectangular cross-section under the influence of a transverse magnetic field. The configuration is described in section 8.3. In this test, the Hartmann number is 50.

The mesh is fully structured and built with 605475 points. Parallel computations were run over 2 nodes using 6 processors out of 8 available on each node. One node has 16 GBits shared memory and the public domain OpenMPI implementation of the message Passing Interface is used. The mesh was equally decomposed over each processor. Second-order discrezation schemes in time and space were used. The job was run over 79805 time steps with an execution time 605717 seconds for a clock time of 606671 seconds.

Appendix B

Article published in *Physics of Fluids* 20, 017104 (2008)

Numerical simulations of a cylinder wake under a strong axial magnetic field

Appendix C

Article published in *Journal of Fluid Mechanics* 653, pp.519-536 (2010)

Formation mechanism of hairpin vortices in the wake of a truncated square cylinder in a duct

This article has been removed due to third party copyright. The published version can be found at http://dx.doi.org/10.1017/S002211201000073X. The unabridged version of the thesis can be viewed at the Lanchester Library, Coventry University